2020

PROBING VIBRATIONAL WAVE PACKETS IN ORGANOPHOSHOROUS MOLECULES USING FEMTOSECOND TIME-RESOLVED MASS SPECTROMETRY (FTRMS)

Derrick Ampadu Boateng
Virginia Commonwealth University

Probing Vibrational Wavepacket in Organophosphorus and Nitroaromatic Molecules using Femtosecond Time Resolved Mass Spectrometry (FTRMS).

A dissertation submitted in partial fulfillment of the requirements for degree of Doctor of

Philosophy from Virginia Commonwealth University

By:

Derrick Ampadu-Boateng

Master of Science in Chemistry, East Tennessee State University (2014)

Bachelor of Science in Chemistry, Kwame Nkrumah University of Science and Technology

(2006)

Director:

Dr. Katharine Moore Tibbetts

Assistant Professor, Department of Chemistry

Virginia Commonwealth University

Richmond, Virginia

May, 2020.

Table of Contents

List of Figures

List of Tables

List of Schemes

List of Abbreviations

β-BBO	β-Barium Borate
BNC	Bayonet Neill Concelman
CMOS	Complementary metal oxide semiconductor
DEMP	Diethyl methylphosphonate
DIMP	Diisopropyl methylphoshonate
DMMP	Dimethy methylphosphonate
DNA	Deoxyribonucleic acid
FTRMS	Femtosecond time-resolved mass spectrometry
FROG-SHG	Frequency resolved optical gating second harmonic generation
MALDI	Matrix-assisted laser desorption ionization
MCP	Micro channel plate
MNT	3-Nitrotoluene
m/z	mass-to-charge ratio
NB	Nitrbenzene
Nd:YLF	Neodymium doped yttrium lithium fluoride
OPA	Optical parametric amplifier
PNT	4-Nitrotoluene
TNT	2,4,6-Trinitrotoluene
TMP	Trimethyl phosphate
TOF-MS	Time-of-flight Mass Spectrometry

Abstract

PROBING VIBRATIONAL WAVEPACKET IN ORGANOPHOSPHORUS AND

NITROAROMATIC MOLECULES USING FEMTOSECOND TIME RESOLVED MASS

SPECTROMETRY (FTRMS).

By Derrick Ampadu-Boateng

A dissertation submitted in partial fulfillment of the requirements for the degree of Doctor of

Philosophy at Virginia Commonwealth University.

Virginia Commonwealth University, 2020.

Director: Dr. Katharine Moore Tibbetts, Department of Chemistry.

The study of organophosphorus and nitroaromatic compounds is essential due to their

suitability as models for understanding the dynamics of radiation induce damage to DNA sugar-

phosphate backbone, and the detection of chemical warfare agents as well as nitroaromatic

explosives (such as TNT). The ultrafast dynamics of these polyatomic radicals were studied using

femtosecond time-resolved mass spectrometry (FTRMS), a versatile method that is capable of

monitoring the ultrafast dynamics of rapid dissociation in the gas phase after the removal of an

electron. The method uses a technique called pump-probe, which makes use of two time-delayed

laser pulses. In this work, the strong ionizing pump pulse and the weak non-ionizing probe pulse

were in the near infrared and the visible region respectively. The pump pulse ionizes the molecule

to produce a parent radical cation, which is vertically excited in the Frank Condon region to the

ground electronic state. A wave packet is generated as a result of the coherent vibrational excitation

that populates several excited vibrational states at the same time. A delayed probe pulse monitors

the wave packet as it moves over the potential energy surface giving information on a particular molecule including the vibrational frequency.

Four organophosphorus compounds, dimethyl methylphosphonate (DMMP), diethyl methylphosphonate (DEMP), diisopropyl methylphosphonate (DIMP) and trimethyl phosphate (TMP) were studied. Upon ionization, each molecular radical cation exhibited unique oscillatory dynamics in its transient ion yield resulting from coherent vibrational excitation. The results for DMMP revealed a particularly well-resolved frequency at 732 ± 28 cm^{-1} with a weak feature at 610-650 cm^{-1} and an oscillation period of 45 fs. DIMP exhibited bimodal oscillation with period of ~55 fs and two frequency features at 554 ± 28 and 670-720 cm^{-1}. A bimodal frequency oscillation at 770 and 880 cm^{-1} was observed in TMP with an oscillational period of ~ 40 fs. In contrast, the oscillations for DEMP were barely visible due to rapid decay. Based on our DFT calculations, the high- and low- frequency oscillations observed in DMMP and DIMP were assigned to coherent excitation of P-C and O-P-O stretching and bending modes respectively. The high and low frequencies in TMP were assigned to an asymmetric and symmetric P-O stretching modes respectively.

Four nitroaromatic derivatives of 2,4,6-trinitrotoluene (TNT), 4-Nitrotoluene (PNT), 3-Nitrotoluene (MNT), 2-Nitrotoluene (ONT) and nitrobenzene (NB) were studied. Oscillation frequencies of the transient ion yield were observed for these compounds upon ionization. A torsional motion of the NO$_2$ group with respect to the phenyl and benzene ring (in the case of NB) was identified as the main excited vibrational mode in three compounds, PNT (85 cm^{-1}), ONT (91 cm^{-1}) and NB (80 cm^{-1}), based on DFT calculations. The vibrational frequency in MNT was roughly two times faster than in the others and was assigned to a symmetric bending mode of the CH$_3$ and NO$_2$ with respect to the benzene ring. In ONT, the *aci*-tautomer exhibited a unique

oscillation frequency at 114 cm^{-1}, faster than the frequency of the parent ion. The *aci*-tautomer preserved the torsional coherence that was initially exhibited by the parent ion.

All the assignments of vibrational motion were supported by DFT calculations utilizing various functionals such as BPW91, B3LYP, CAM-B3LYP and the basis set Def2-tzvpp[(11s6p2d1f)/5s3p2d1f], 6-311+G* and 6-311G*.

Collectively, results obtained from this research may support several applications such as in national security. For example, procedures can be developed to specifically detect explosives, and enhanced techniques could detect and decontaminate nerve agents, which would help save lives and property. It could also help build photo-labile explosives, which could be initiated by a laser. In addition, quality of life could be enhanced via early intervention from radiation induced damage to DNA.

Chapter 1: Introduction

1.1 Historical background

The importance of polyatomic radical cations cannot be overemphasized as they play critical roles in many physical, chemical and biological processes. Examples of such processes include reactions between aromatic radical cations and hydrogen atoms that generate complex organic molecules observed in the interstellar medium,[1] decomposition of energetic molecules such as explosives initiated by radical cations or anions,[2] radical cations generated via photoexcitation of $Ru(bpy)_3^{2+}$ catalyzing reactions for organic synthesis,[3] and radiation-induced damage from radical cation formation in the sugar-phosphate DNA backbone that can lead to strand breaks and eventually may cause cancer.[4] These reactions take place on pico- or femtosecond time scales making it impossible to measure their dynamics directly until recently.

Over a century now, time resolution in chemistry has evolved from the days of Arrhenius in the 1800's who predicted the existence of transition states and how fast chemical reactions evolves with the Arrhenius equation to measure sub-second chemical reactions. Chemical reactions in the 1920's was studied using a faster technique called the stop-flow method,[5] capable of measuring reaction rate in millisecond time scale. In this method two reactants are placed in different syringes and mixed together in a reaction chamber. The reaction is monitored with a UV-Vis detector via the change in absorbance as a function of time. The stop syringe is filled with the product as the reaction progresses until it hits a block at a steady state. At this point the reaction reaches a continue flow rate therefore stopping the reaction, and allowing for the calculation of the reaction time and initial rate of reaction. Later in 1949, flash photolysis was developed based on the initiation of chemical reactions using a light source.[6] A near UV pulse is sent into a sample at

a delayed time and the change in absorption is recorded by a detector. The technique enabled chemical reactions to be studied in the microsecond time scale. Not long after in the 1960's, lasers were invented. Owing to their useful properties such as monochromaticity, coherence and unidirectionality, their popularity grew. There was rapid development in lasers technology between 1960 and 1980's with both nano- and picosecond lasers taking center stage. Later, femtosecond lasers became popular because of their short pulse duration ($10^{-13} - 10^{-15}$ s) that is capable of elucidating ultrafast dynamics. Lasers of this kind are usually generated from Ti:sapphire, a solid state medium,[7] which has desirable properties including a gain bandwidth from 700 nm to 1100 nm and a self-existing modelock to generate short laser pulses.

The availability of femtosecond lasers fostered the development of a technique called pump-probe by the group of Ahmed Zewail,[8] which is presented in Figure 1.1.
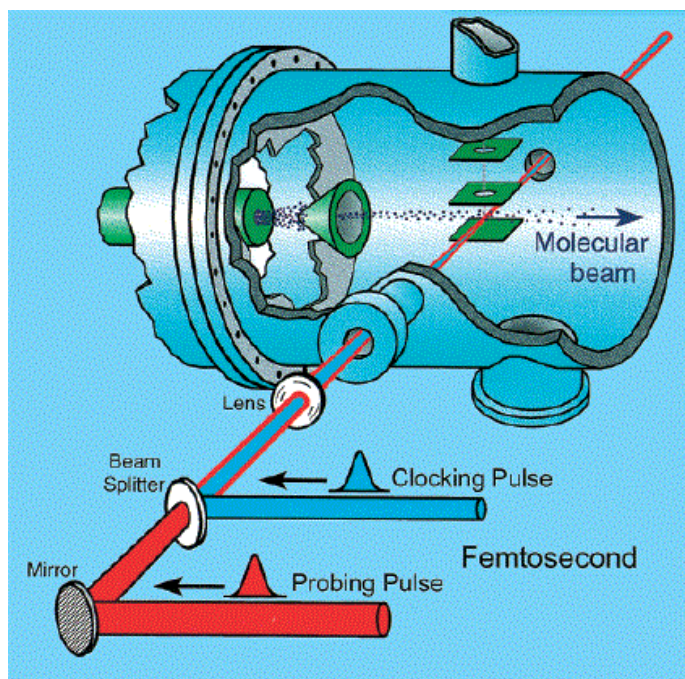
Figure 1.1. The diagram of pump-probe technique showing two laser pulses, the clocking pulse (pump pulse) in blue and probe pulse in red. The two pulses move collinearly through the lens, get focused and interact with molecular beam stream.[9]

Zewail's group performed the first pump-probe experiment in the late 1980's monitoring the dissociation of iodine cyanide (ICN) using two time-delayed laser pulses, one as the pump and the other as the probe. This allowed the first time-dependent observation of a transition state and bond breaking.[10] Since this pioneering experiment, the femtosecond time-resolved pump-probe technique has been used widely to study dissociation pathways of electronically excited neutral dynamics.[11–32] Only recently, pump-probe techniques have been used to study the excited dynamics of radical cations,[11,32–37] partly because of the difficulty of generating intact molecular parent ion. Producing a high population of parent molecular ions is key to the study of the dissociation dynamics. Experiments have shown that generating parent ions with 800 nm laser pulse is difficult because of excess fragmentation of the molecular ion through multiphoton ionization,[38–43] which causes excitation to ionic excited states and further fragmentation. In contrast, longer wavelengths (near-infrared, ∼1200-1600 nm) have been shown to enhance the population of the electronic ground state with a high percentage of parent ions via a 'tunneling' ionization.[38,39,44–52] Both mechanisms are explained in detailed in Section 1.2.

1.2 Keldysh Theory

Tunnel ionization was first explained by Keldysh in atoms where the transition from nonadiabatic to adiabatic ionization was described by the Keldysh adiabaticity parameter (γ).[53] The parameter γ in equation 1.1 is given by the ratio of the incident laser frequency (ω_0) to the electron tunneling frequency ω_t in a zero-range potential. The ionization potential is indicated by Δ, m_e is the electron mass, e is the electron charge and E_0 is the laser electric field strength.

$$\gamma = \frac{\omega_0}{\omega_t} = \omega_0 \frac{\sqrt{2\Delta m_e}}{eE_0} \qquad (1.1)$$

The parameters that determine γ are the laser wavelength, electric field strength, and the molecule's ionization potential. $\gamma > 1$ indicates a very high laser frequency that inhibits tunneling of an electron through the electrostatic potential barrier before the electric field switches signs. This results in a nonadiabatic multiphoton ionization as multiple electrons continue to absorb energy over multiple cycles of the laser pulse. Alternatively, the probability for electron tunneling is greatly increased when $\gamma < 1$, resulting in adiabatic ionization that imparts little energy to the remaining electrons.[38,39,44–46,54]

Even though the Keldysh theory was proposed for atoms, it has also been found to qualitatively characterize ionization in polyatomic molecules based on recent experiments of strong field ionization with near-infrared excitation wavelengths where $\gamma < 1$.[38,39,44–46,53] For instance, in decatetraene[50] and anthracene,[46] 800 nm excitation resulted in extensive fragmentation, but 1400 nm did not. The extensive fragmentation was attributed to cationic resonance and nonadiabatic excitation. Similar patterns were observed for wavelengths between 800 nm to 1434 nm on acetophenone, which gave a high fractional yield of small fragments for 800 nm and low yield for the wavelengths between 1240 nm and 1434 nm.[44] The variations of ion yields between the IR wavelengths were small with the exception of an ionic resonance at 1370 nm confirming the dominance of tunneling ionization as compared to multiphoton ionization at 800 nm.[44] The experimental results were supported by the Keldysh parameters ranging from 0.59 at 1550 nm to 0.73 at 1240 nm as compared to 1.25 at 800 nm, validating the Keldysh theory.[44–46,53] Data from our laboratory confirms the difference in a mass spectra fragmentation patterns upon multiphoton and tunneling ionization, as can be observed in Figure 1.2.
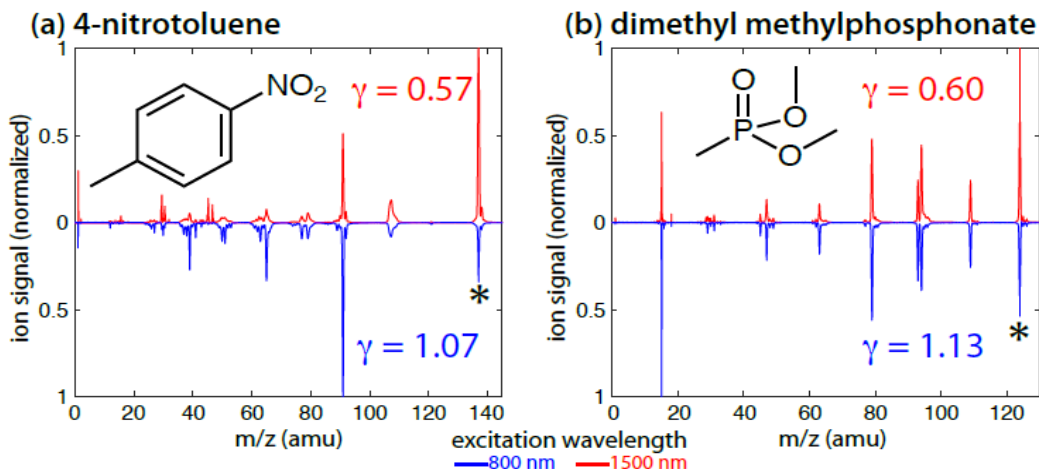
Figure 1.2. Mass spectra of (a) 4-nitrotoluene and (b) dimethyl methylphosphonate taken with 800nm (blue) and 1500nm (red) with peak intensity $\sim 7 \times 10^{13}$ W cm^{-2}. The * denotes the parent molecular ion.[55]

Figure 1.2 displays the mass spectra taken for 4-nitrotoluene and dimethyl methylphosphonate with a peak intensity $\sim 7 \times 10^{13}$ W cm^{-2}. The parent molecular ions are marked with * and multiple fragments were generated with 800 nm (blue) and 1500 nm (red) for both molecules. The parent molecular ion is the base peak in both molecules for 1500 nm while showing less fragments with $\gamma \sim 0.6$. In contrast, the parent ion in 800 nm is significantly depleted and fragment yields are enhanced when $\gamma \sim 1.1$. Even though the same set of fragments are shown in each molecule, the parent yield increases about two folds with 1500 nm compared to 800 nm.

1.3 Coherent Control and Wave Packet dynamics

Understanding the dissociation dynamics of a molecule starts with the fundamental principles of wave packet generation. To generate a wave packet, very short pulse duration as compared to the molecule's vibrational period is needed. Since the uncertainty principle states that the energy

5

and time of a particle cannot be determine simultaneously, a short pulse must have a broad bandwidth. The broad bandwidth of a short pulse results in simultaneous population of multiple excited vibrational states with accessible Franck–Condon factors in the cation, which creates a coherent superposition, or vibrational "wave packet" [9] as shown in Figure 1.3. For vibrational wave packets to be lunched vertically upon ionization, according Frank Condon's principle, the minima on S_0 and D_0 potential energy surface (PES) do not overlap. The localized wavefunction, called a wave packet, moves along the internuclear axis on the timescale of the classical vibrational period of the molecule. The ability to generate wave packets facilitates selective bond breaking, where a wave packets can be targeted at a particular position on the PES to induce a particular bond breakage.[56–58] The Young's double silt experiment (Figure 1.3, inset) could be related to the wave packet phenomenon where dark and bright fringes are observed due to an interference pattern caused by superposition of light waves coming from two slits.
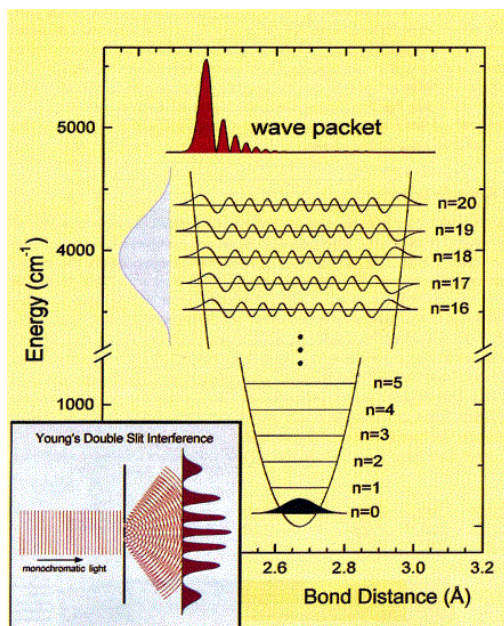
Figure 1.3. Generating vibration wave packet with an ultrashort laser pulse for molecular systems. The inset depicts Young's double slit interference.[9]

1.4 General Mechanism and Dissociation of Radical Cations upon Pump Probe Excitation

In pump-probe measurements of cation dissociation dynamics, the main mechanism of initial excitation from the neutral ground state is the adiabatic ionization to produce the ground state cation, as discussed in Section **1.2.** The weak time-delayed probe pulse is then used to initiate dissociation. Figure 1.4 demonstrates the general mechanism of dissociation of a radical cation upon pump probe excitation. This is the primary ionization mechanism for several compounds such as acetophenone, alkyl aryl ketone derivatives[38] and halogenated methanes.[10,59] Excitation of explosives to neutral excited states also follows similar mechanisms.[12,16,26,31]
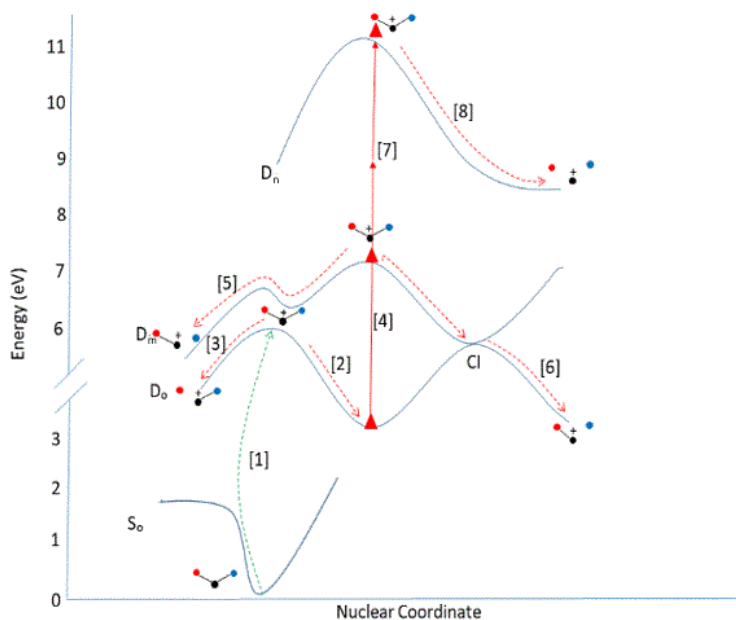
Figure 1.4. A general mechanism of dissociation of radical cation upon pump probe excitation. The red, blue and black balls are just a representation of any molecule.

In the first step of a pump probe experiment [1], the molecule on the neutral ground state is excited to an ionic ground state with the pump pulse (IR) via tunneling ionization. According to the Franck-Condon principle, a vibrational wave packet may be launched vertically upon

ionization when the minima on S_0 and D_0 potential energy surface (PES) do not overlap, while some molecules produce no wave packet when they are excited to D_0 minimum.[12,16,39,44,60] On D_0, the wave packet generated could propagate to the minimum point of the D_0 PES [2] or the vibration in the wave packet can lead directly to bond dissociation [3]. Alternatively, as the wave packet propagates to the minima of D_0, the probe pulse can excite the ion to an electronic excited state whenever the dipole coupling is highest [4].[61] If the wave packet is excited to the maximum of D_m PES, it propagation towards the minimum and can result in excess vibrational energy, causing bond cleavage [5]. On the other side of the PES, the wave packet may encounter a different pathway. A conical intersection (CI) between D_1/D_0 may be available in some molecules to cause bond cleavage as the wave packet rapidly passes through both state and returns to the ground excited state, thereby converting electronic energy into vibrational energy [6].[44,45] Finally, the D_m wave packet could be excited to a higher excited state D_n via two-photon excitation [7], and bond cleavage could be observed as the wave packet makes its way to the bottom of the PES [8]. Since each pathway is capable of making different dissociation products, identifying the yields of each product as a function of the time-delay between pump and probe pulses is critical, which is why a mass spectrometer was employed in the proposed experiments.

CHAPTER 2: Instrumentation and Theoretical Methods

2.1 Light Amplification Stimulated Emission Radiation (LASER)

A solid-state material such as Titanium doped sapphire (Ti:sapphire) is used for laser generation because of its desirable properties. These properties include a broad band width (128 THz) from 700-1100 nm with a 300 nm wavelength range centered at 800 nm, energy storage of about 1 J/cm^2 and a high thermal conductivity and existing passive mode-lock.[62] In the crystal, titanium exhibits a Ti^{3+} ion where 3d orbitals are degenerate under field-free condition. When exposed to an electric field, the orbitals split into the ground and excited states. Absorption of a 500 nm photon causes a transition from the ground to the excited state. The Ti:sapphire crystal exhibits a four level system, a unique property that aids and sustains pulse generation.
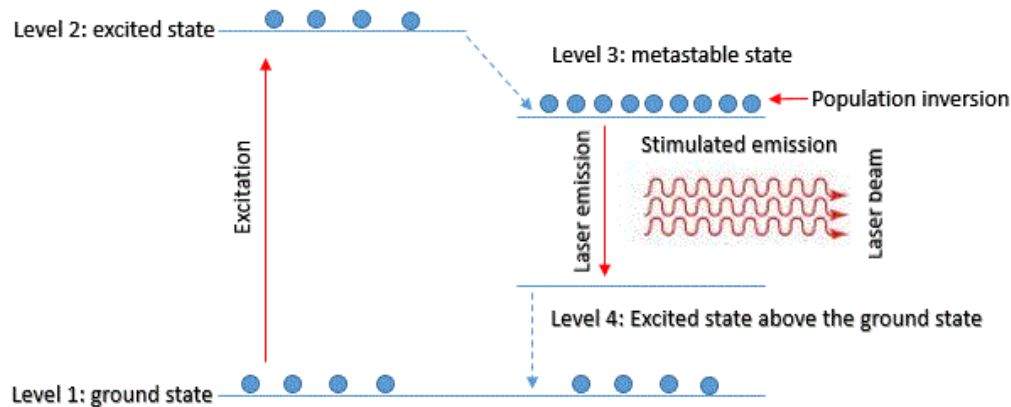
Figure 2.1. Four level laser system showing electrons as blue dots and excitation and laser emission in red arrows.

Figure 2.1 shows an electron transition from the ground state (level 1) via vertical excitation to the excited state (level 2). Electrons quickly relax to the level 3 (metastable state) via a radiationless process, creating a population inversion because of the slow spontaneous relaxation

from level 3 to level 4. At this point the presence of photons stimulate electrons to relax from level

3 to 4, generating an avalanche of emitted photons. This process emits a wide broad band of tunable

wavelength from 700-1100 nm because of multiple vibrational levels in 3 and 4. The fast

radiationless relaxation on level 4 makes electrons available to level 1 to be pumped to start the

process all over again. The laser produced at this point is directed to the oscillator (shown in Figure

2.2) which oscillates the photons between two-fold mirrors with a repetition rate of ~80,000 kHz.

The repetition rate is determined by the length of the cavity (how long it takes one photon to

oscillate back and forth). As the photons oscillates a phase match (mode-lock) is established in the

oscillator, which generates a seed pulse with energy and duration in the range of 10^{-9} J and 10^{-14} s

respectively.
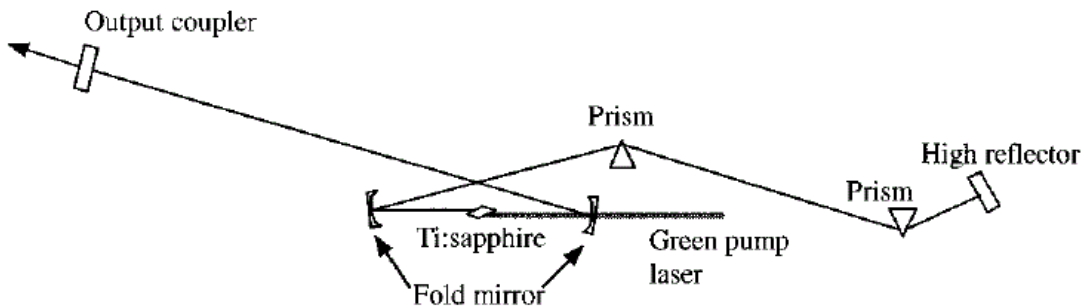
Figure 2.2. Diagram of an oscillator showing a self-modelocked Ti:sapphire laser.[62]

The seed pulse is then sent to stretcher to reduce the peak power by about five order of

magnitude by stretching the pulse from 10^{-14} to 10^{-9} s, in order to avoid damaging the optics in the

subsequent amplifier or to avoid nonlinear distortion to the beam profile. The stretched seed pulse

is then combined with a 528 nm Q-switched Neodymium doped yttrium lithium fluoride (Nd:YLF)

pulsed laser with a 1 kHz repetition rate to pump a second Ti:sapphire in the regenerated amplifier

cavity as shown in Figure 2.3. To overlap a seed pulse with the pump pulse, the seed pulse is injected into the amplifier via the Pockel cell, which flips polarization of the pulse to trap it in the cavity. The pulse is allowed several round trips in the cavity through the Ti:sapphire to build up energy. When the pulse attains its maximum energy, the Pockel cell flips the polarization to the original form ejecting the amplified pulse out of the cavity.
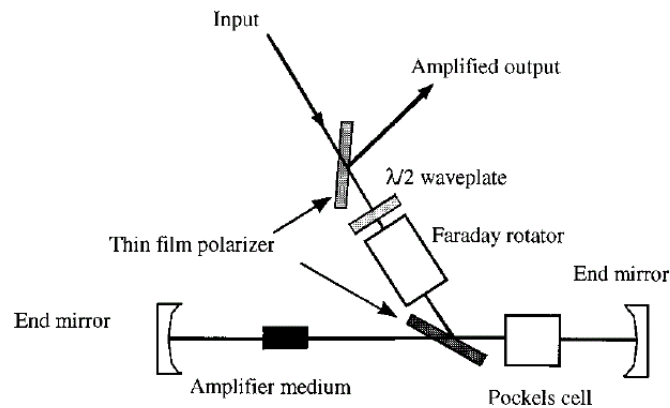
Figure 2.3. Diagram of a regenerated amplifier.[62]

The pulse is then directed to the compressor to reduce the duration to 30 fs. The pulse then comes out as an amplified short pulse. Figure 2.4 shows the schematic of a chirp pulse amplifier.
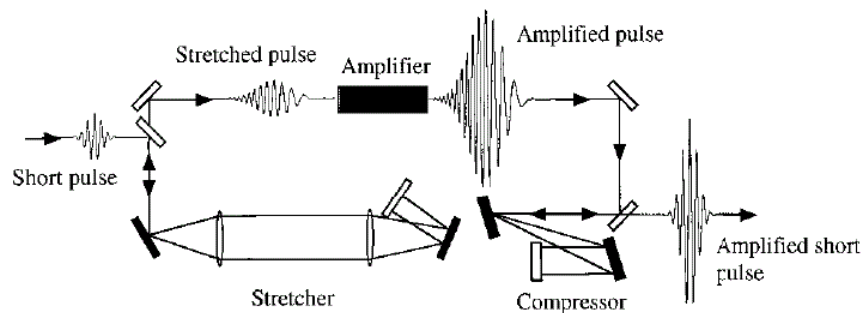
Figure 2.4. Diagram of an amplification system based on the chirped-pulse-amplifier (CPA).[62]

2.2 Optical Parametric Amplifier (OPA)
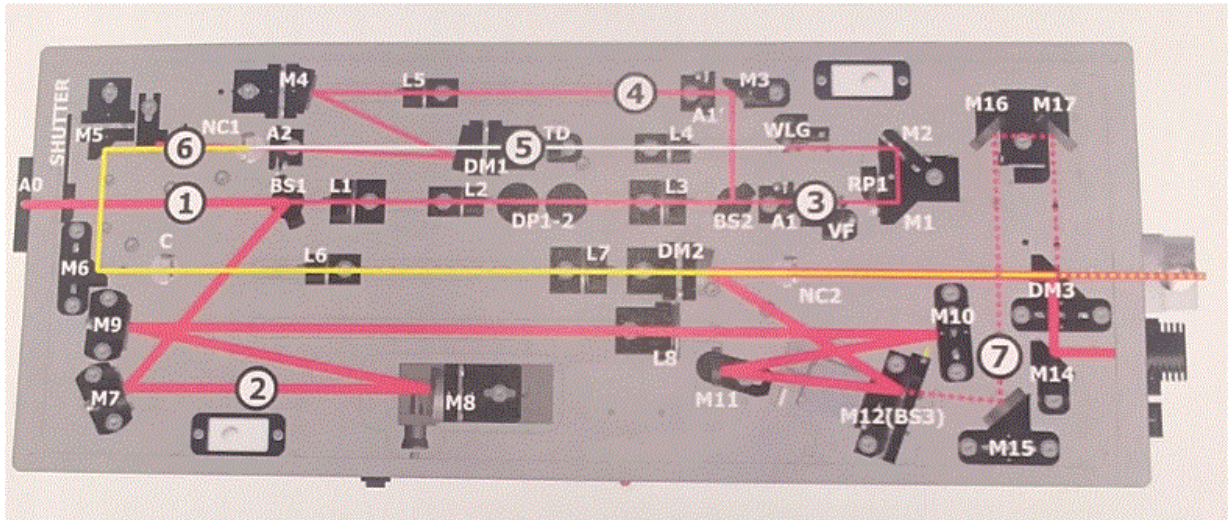
Figure 2.5. A lay out of TOPAS-Prime: 1- input beam, 2-PA2 pump beam, 3-WLG pump beam, 4-PA1 pump beam, 5-White light beam, 6-Signal beam, optional fresh pump stage for sum-frequency generation.[63]

To generate variable wavelength there are two stages:[63] first, the optical parametric generator (OPG) where the white light continuum (WLC) is generated, and second the two stage optical parametric amplifier (OPA), where the signal beam is amplified. In our laboratory, 90% of the compressed pulse generated by the Ti:sapphire laser is sent to the OPA by the way of a beam splitter. Upon entering the aperture, a beam splitter directs a small fraction of about 400 µJ (seed beam) to be used for the first pre-amplification process while the rest about 1.6 mJ is sent via different path to be used as the power amplifier. Another beam splitter splits off 20 µJ of the 400 µJ to produce a white light continuum (WLC) as it passes through a sapphire plate. The remainder of this beam and WLC are directed and focused into a pre-amplifier crystal (BBO), non-collinearly with the white light where the parametric amplification takes place. To achieve a variable

12

wavelength different crystal angles are needed and this is achieved by tuning in the pre-amplification stage, the white light is delayed with respect to the pump pulse for optimal phase matching. Phase matching is achieved when the refractive indices of both beams are the same and the crystal angle is critical to achieving this. Because both the pump beam and the white light propagate non-collinearly, they are easily separated after passing through the crystal. The geometry blocks the pump residue and the signal beam continues to propagate. As the signal propagates it is expanded and collimated by lens telescope and goes through a second amplification stage. The second stage, the power amplification thus optical parametric amplifier (OPA) involves the use of reflected energy (1.6 mJ) where both signal and pump are overlapped in the second nonlinear crystal collinearly producing a collimated signal and idler. A polarizer on the outside filters out the idler, propagating the signal.

2.3 Mass Spectrometer Linear Time of flight (MS-TOF)
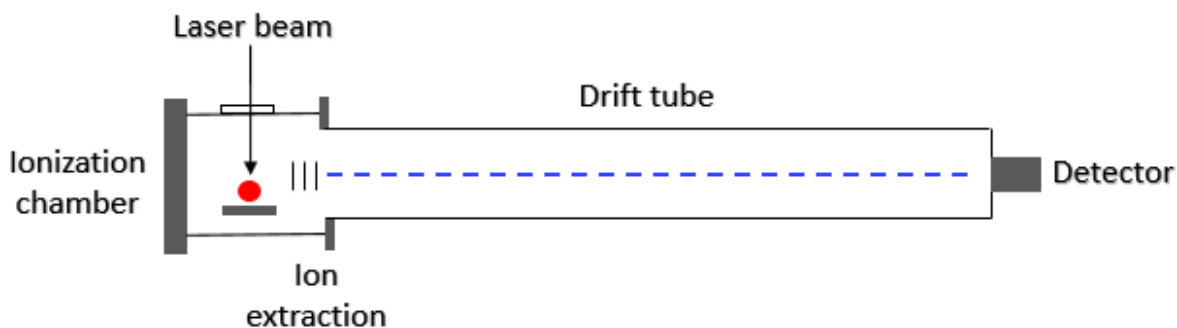
Figure 2.6. General schematics Linear Time of flight Mass spectrometer.

The mass spectrometer is typically divided into ionization source, mass analyzer and the detector. In a typical setup, ions are generated from either hard or soft ionization. Electron impact ionization is regarded as hard ionization while multiphoton ionization (pulsed laser), chemical

ionization, matrix-assisted laser desorption ionization (MALDI) and electro-spray are classified as soft ionization. Pulsed lasers, used as an ionization source in mass spectrometry has many advantages. For example, laser wavelengths are tunable and laser excitation prevents ion accumulators because the laser itself is pulsed (1 ms between each pulse). This aids resolution because ions generated from separate pulse do not overwhelm detectors with limited duty cycle. After the ions are generated the time of flight (TOF) mass analyzers separates ions using specific properties such as the mass to charge ratio (m/z). Ions with the same charge are accelerated with the same kinetic energy into the flight tube, and separation is achieved as ions travel through the flight tube. Separation is based on the velocity of each ion since each ion has different mass, making lighter ions arrive at the detector faster. The final stage involves detections of ions which is done by the micro channel plate (MCP) detector.
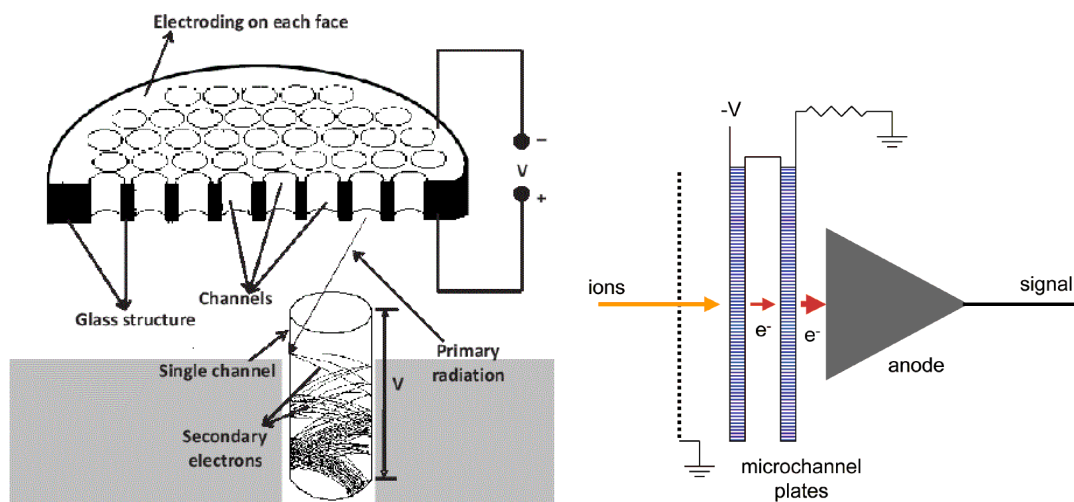
Figure 2.7. Diagram showing a schematic and working principle of microchannel plate detector (MCP).[64]

The microchannel plate is designed to have several separate channels that are capable of producing continuous-dynode electron multiplier when a strong electric field is applied. A single

incident ion enters the channel and emits 2-3 electrons from the channel wall as shown on the left of Figure 2.7. The electrons generated then accelerate down the channel by a positive bias voltage and travel along the parabolic trajectories until they strike the channel surface and produce a cascade of secondary electron emission. The repetition of the process could give up to 10^6 electrons when it exits the plate. This process amplifies the original signal to enhance detection and also gives high gain, high temporal and spatial resolution. The multiplied electrons are collected by anode as they exit the channels at the opposite side (shown on the right of Figure 2.7). Signals are then detected and scanned against the time of arrival to produce mass spectra.

2.4 Theoretical Methods

The theoretical calculations were performed, using Density functional theory (DFT) with the Gaussian 16 suite.[65] All atoms and energies were evaluated using 6-311G* basis set of triple - ζ quality using harmonic calculations to determine minimum energy and frequencies. The convergence threshold for the total energy was recorded to be 10^{-6} eV, while the force energy was set at 10^{-2} eV/Å. The functional BPW91[66,67] from the generalized gradient approximation (GGA) family was used to obtain the initial geometry and the ground state energies for both neutral and cation of nitrobenzene. The ground state potential energy surface (PES) of the neutral and cation were mapped out by calculating the energies as a function of the dihedral angle. The time dependent DFT (TD-DFT) calculations[68] was done to determine the energies of excited states and their oscillator strengths.

CHAPTER 3: Measurement of Ultrafast Vibrational Coherence in Polyatomic Radical

Cation with Strong-Filed Adiabatic Ionization.

Most of the content of this chapter has been adapted with permission from the reference:

Ampadu Boateng, D., Tibbetts, K.M. *J.Vis. Exp*. (138), e58263, doi: 10.9791/58263(2018).

3.1 Experimental Procedure

All commercially acquired instruments and parts including the Ti:sapphire regenerative amplifier (Astrella, Coherent Inc.), optical parametric amplifier (OPA, TOPAS Prime), 1 GHz Oscilloscope (LeCory WaveRunner 610Zi), vacuum pumps (Edwards Vacuum), time of flight tube (TOF), micro channel plate detector and chamber (Jordan TOF Inc.) were installed and operated according to the manufacturer's instructions. All instrumentation is placed on an optical floating table to minimize the effect of vibrations.

3.2 Construction of Time of Flight Mass Spectrometer

A 1 m time of flight tube was mounted on an ultrahigh vacuum chamber of capacity 0.5 cubic feet with a provision to mount an optical window on the 2 ¾" on either side. To save space on the optical table the ion optics and time of flight tube were mounted vertically. The ion optics is made up of the repeller plate (+4180 V), extraction plate (+3910 V) and the ground plate (0 V) as shown in Figure 3.1. The extraction plate has a 0.5 mm slit oriented orthogonal to the laser propagation and ion paths. The slit serves as a filter allowing only ions generated from the central focal volume where the intensity is the highest to pass through the extraction plate. A 1/16" stainless steel tube was inserted into the chamber between the extractor and repeller plates and threaded out of the chamber and connected to a ¼" stainless steel tubing. One or more variable leak valves were attached to the steel ¼" tubing to serve as a sample inlet control for the liquid

molecular sample or gas tank. The 18 mm micro channel plate stack in Z conformation was attached to the end of the flight tube. The two optical windows (1 mm thick, 50 mm in diameter, fused silica) were mounted on the 2 ¾" flange at both ends of the chamber to allow laser beams propagate through between the repeller and extractor plate.
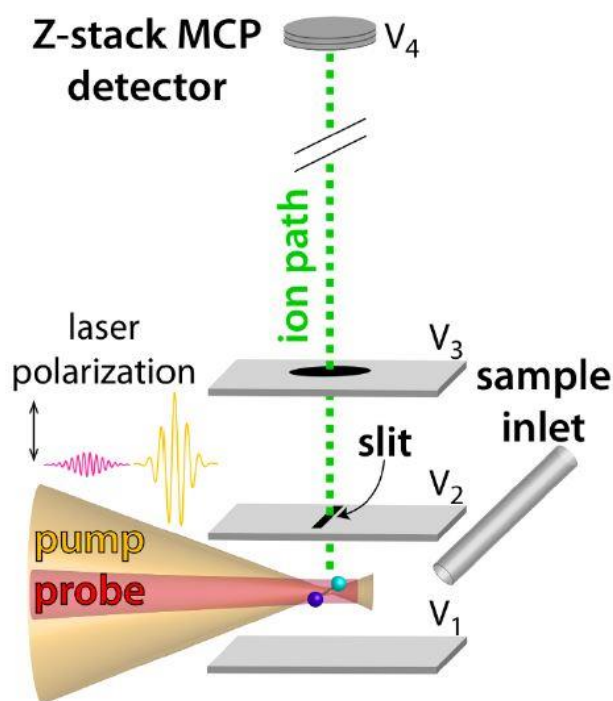
Figure 3.1. Diagram shows the region where both laser pulses and the sample interact. Pump and probe beams are focused between the repeller V_1 and the extractor plates V_2. The ions are accelerated through the ground plate V_3. The polarization of both beams is aligned along the TOF axis and ions detected at microchannel plate detector V_4.

The ion optics and detector were wired to a high voltage supply via current feed-throughs and Bayonet Neill Concelman (BNC) cables. One turbo molecular pump was attached near the ion optics and a second pump to the end of the flight tube near the detector with both pumps attached to an appropriate rotary vane backing pump. Caution was taken when attaching the pump to the end of the vertically mounted time of flight tube to ensure that the TOF system does not lean

forward due to the weight of the pump. This issue however was mitigated by attaching the vacuum chamber to the optical table. The pumps were turn on and left for about 24 hours to attain a pressure 10^{-8} torr. Leaks were checked and nuts were tightened to ensure a firmly sealed system. A 1 GHz digital oscilloscope at sample rate 20 giga samples per second (GS/s) was employed to record mass spectra, which was averaged over 10000 laser shots.

3.4 Construction of Optical Pump and Probe Paths

Two replica 800 nm laser wavelength were generated by a 90:10 (%T:R%) beam splitter placed in the optical path, which were used to construct the pump and the probe beam lines. The laser beam on both sides were checked for adequate delivery with a power meter. The transmitted beam was directed into the OPA and the output was optimized using the procedures outlined in the manual.

3.4.1 Construction of the pump optical path

The OPA software was set to a desirable wavelength (1140 nm to 1600 nm) and beam output was directed to a λ/2 wave plate (WP) and a polarizer (P) for power attenuation. A filter is placed just after the WP and P to filter out all the visible light that propagates along with the IR. The *p*-polarized beam was blocked while the *s*-polarized was directed to a telescope made of two gold spherical mirrors with f = -10 cm and f = 50 cm to expand its diameter by a factor of 5. This results in small beam waist and higher intensity after focusing. With the help of various gold mirrors, the expanded beam is directed to the dichroic mirror (DC).

3.4.2 Construction of the 800 nm probe optical path

Note: The total path length of the pump beam, including the OPA, was taken into consideration when building the probe line.
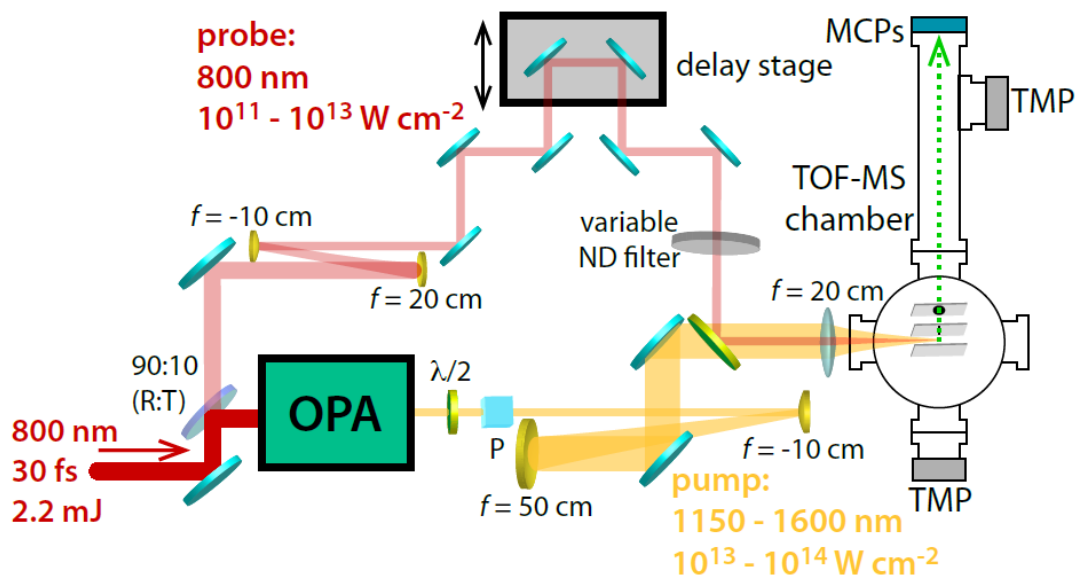
Figure 3.2. Schematic illustration of pump probe setup with 800 nm probe.

As shown in Figure 3.2, a mirror directs the reflected beam to a telescope made of concave mirror (f = 20 cm) and convex mirror (f = -10 cm) to reduce its diameter by a factor of 2. The down-collimated beam is directed to the retro-reflector mounted on a motorized delay stage. The knobs on the flat mirrors prior to the retro-reflector were adjusted to ensure the beam position after the retro-reflector does not change when the stage is moved along its full range. This ensures that the pump-probe spatial overlap will be maintained over the full scan range. A tunable neutral density (ND) filter was placed after the stage to attenuate the power of the probe pulse, while an iris placed just after the ND filter served to adjust the beam diameter. The beam was then directed to the dichroic mirror (DC), which merges both beams.

3.4.3 Construction of the 650 nm optical path

A 50:50 (%R:%T) beam splitter is placed after the OPA output splits a 1300 nm beam into the pump and probe. The pump line and probe lines are constructed as outlined in Figure 3.3.
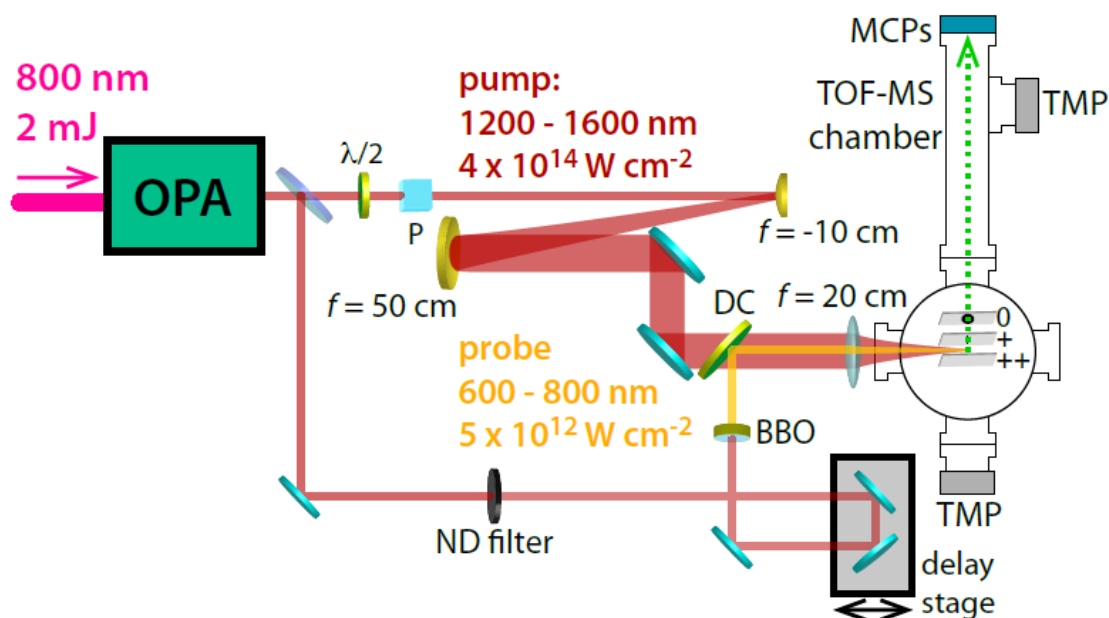
Figure 3.3. Schematic illustration of pump probe setup with 650 nm probe.

The probe beam is directed to a retro-reflector placed on a motorized translation stage (ThorLabs, Inc) by flat mirrors. The knobs on the flat mirrors prior to the retro-reflector was adjusted to ensure the beam position after the retro-reflector does not change when the stage is moved along its full range. This ensures that the pump-probe spatial overlap will be maintained over the full scan range. A tunable neutral density (ND) filter was placed after the stage to attenuate the power of the probe pulse. The frequency of the probe was doubled with a β-barium borate (BBO) crystal and directed to dichroic mirror (DC).

3.4.4 Rough spatial overlap of the pump and probe beams

To determine the spatial overlap of both beams, a 15 mm diameter BBO crystal was mounted after the dichroic mirror to double the wavelength of both beams, thereby making them

visible. It was easiest to use an OPA wavelength of ~1200-1300 nm to make an orange beam that is distinguishable from the blue 400 nm beam. Care was taken to ensure that the most intense region of the pump beam was made to pass through the center of the crystal. The crystal angle was optimized such that both the orange and the blue pulse clearly visible, although this angle may not correspond to the maximum intensity of a given color. The alignments of the pump and probe was adjusted using the mirror mount prior to the dichroic mirror such that both beams propagate collinearly the TOF-MS chamber and out the other side. Since the probe beam is smaller than the pump, the probe was adjusted and centered in the middle of the pump.

In generating a spatial overlap for the 650 nm probe, the BBO crystal was placed before the dichroic mirror because a frequency doubling of 650 nm will not be visible, making it impossible to determine the spatial overlap.

3.4.5 Rough temporal overlap of the pump and probe beam

The temporal overlap was determined by placing a fast photodiode detector placed a few centimeters in front of the window entrance to the TOF-MS in the path of the pump and probe beams. The detector cable was attached to the digital oscilloscope and signals from the pump and probe were located independently, by blocking the path of pump and probe in sequence to determine the position of each beam. The position of the motorized delay stage on the probe line was adjusted such that pump and the probe signals are temporally overlapped. The mount holding the motorized stage was moved if one signal is consistently in front or behind the other in the oscilloscope to shorten or lengthen the path length as needed.

3.4.6 Determination of pump-probe spatial and temporal overlap in the TOF-MS

Note: While Xe gas could be used as a sample to determine spatial and temporal overlap, it is recommended to use target molecules because changes in the mass spectra can be observed over a range of positive time-delay instead of only at zero-delay as with Xe.

Samples were attached to the TOF-MS and pressure adjusted to the range 1-5 x 10^{-7} torr. Both beams were unblocked and aligned collinearly into the TOF-MS chamber. The wave plate was adjusted to give sufficient pump signal while the ND filter was used to adjust the probe to obtain a power that could induce dissociation and not necessary create ions. The spatial position of the probe was adjusted using the knobs on the dichroic mirror mount until either a spike in intensity of all ions is observed (if position of stage is exactly at zero delay) or a significance depletion of the parent ion is observed (if the position corresponds to positive time delay). When no changes in the ion signals is observed after scanning the whole length of the stage, the stage position is likely at negative time-delay (thus probe precedes the pump), in this case the motorized delay stage is placed at a longer probe path and scan again until a change in the mass spectra is observed. The motorized delay stage is then positioned to produce a spike in total ions signal which corresponds to *zero-time delay*.

3.5 Pump-Probe Measurements

3.5.1 Preliminary checks before taking measurements

To starting taking measurements a check on both beams has to be made to ensure that both are propagating collinearly through the window of the chamber. The desired sample is then attached to the TOF-MS chamber and gradually released using the variable valve leaks to achieve the target pressure of 1-5 x 10^{-7} torr. The power supply to the TOF-MS is turned off to avoid damage to the MCP when adjusting due to pressure spike. Samples with very low vapor pressure

were gently heated to achieve the required pressure. The voltage of the TOF-MS was turned on and checked to ensure correct voltages on each ion optic. The data acquisition software was checked to ensure communication with both the motorized stage and the oscilloscope. Both the lens in front of the chamber and the pump-probe alignments was adjusted to optimize ion signal and spatial overlap.

3.5.2 Data acquisition

Acquisition of data started by adjusting the pump and probe energies to obtain desirable ion signal. In the data acquisition software, the scan length and step size were specified usually between 1000-10000 fs and 5-20 fs respectively. The software was run to acquire a mass spectrum at each pump-probe delay, by averaging over 10000 laser shots. To obtain sufficiently high signal-to-noise ratios, 10-20 scans at a desired setting (thus scan length, step size, pump and probe powers) was obtained and averaged. To minimize the effect of laser power drift, scans may be taken in alternating directions of delay stage travel. All data are saved as tab-delimited text files. Raw data for a signal scan of DMMP with scan length 1250 fs and step size of 5 fs is show in Figure 3.4.
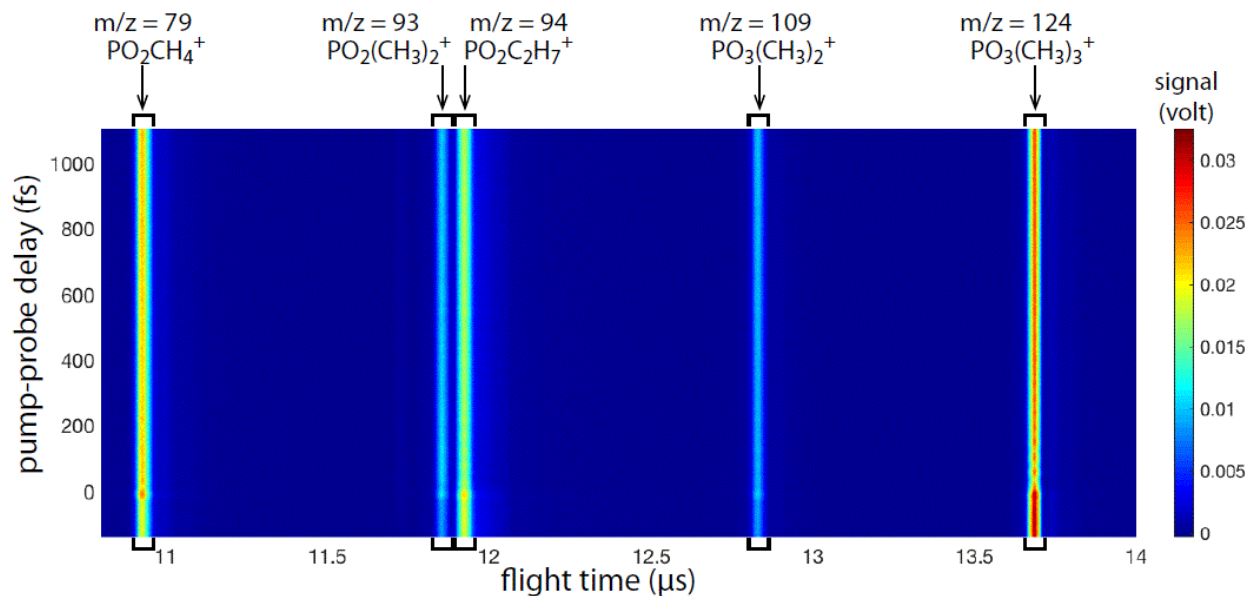
Figure 3.4. Raw pump probe scan showing spectral data recorded with oscilloscope, scanned from -150 fs to +1100 fs. Flight time is labeled on the abscissa and pump probe delay on the ordinate. The DMMP molecular ion and four fragment ion signals are labeled, showing integrated ranges for each ion in brackets.

3.5.3 Data processing

The time-of-flight range for each peak of interest was identified (as illustrated with brackets in Figure 3.4) and integrated in each mass spectrum. The output represents the time-resolved signals of each ion of interest. For example, time resolved dimethyl methylphosphonate (DMMP) parent molecular ion with good and poor pump-probe spatial overlap obtain from one pump-probe scan is shown in Figure 3.5.

24
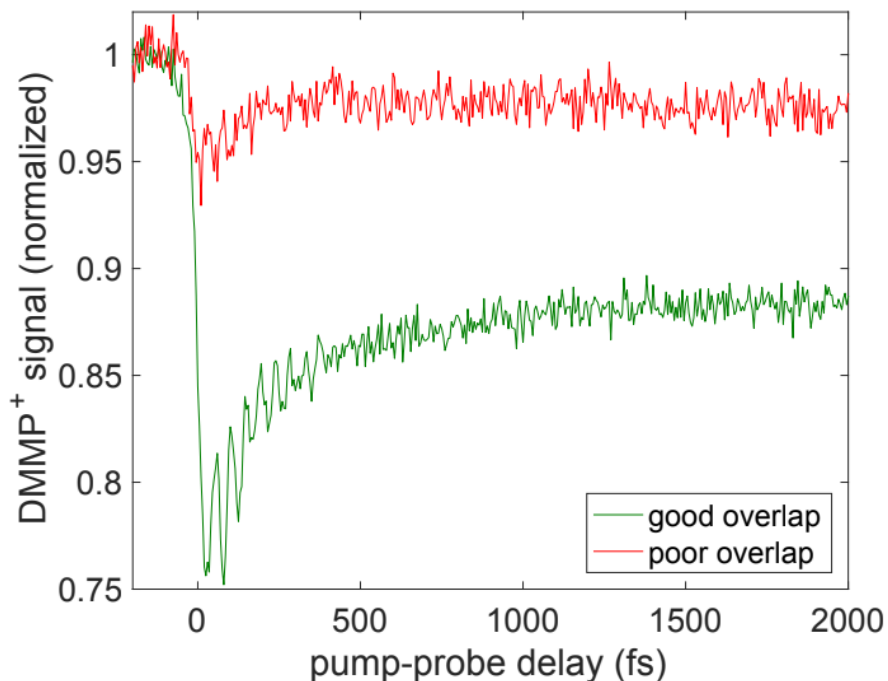
Figure 3.5. Pump probe scan data with good and poor spatial overlap. The integrated signals of DMMP parent molecular ion obtained from signal scan taken with good overlap (good) and poor overlap(red) are plotted as a function of pump probe delay.

3.6 Frequency Resolved Optical Gating (FROG)

For spectroscopic experiments, lasers are needed to be increasingly short to resolve very fast events. This poses a challenge because measuring the parameters of these pulses is very difficult since pulses are shorter than the fastest duration electronics can measure. In view of this, a pulse measurement method called the Frequency Resolved Optical Gating (FROG)[69–72] was developed, which is capable of characterizing a pulse by measuring the intensity and phase. Of the different geometries have been established for FROG, the SHG-FROG is the most sensitive because it is governed by the principles of second order (χ^2) non linearity.

3.6.1 Construction of the Frequency Resolved Optical Gating Second Harmonic Generation (FROG-SHG).
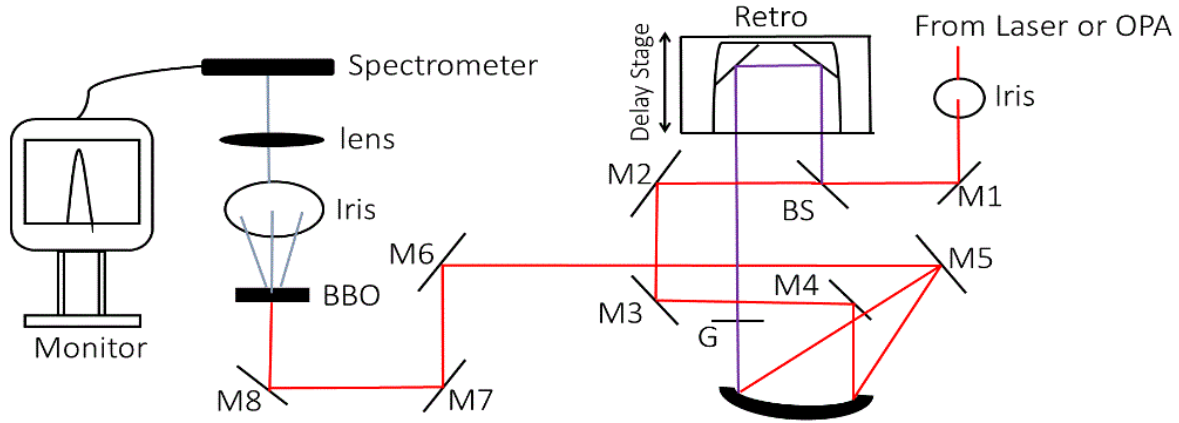
Figure 3.6. The FROG-SHG set up.

To measure pulse duration the FROG set up in Figure 3.6 was used. The pulse to be measured is directed into the FROG where a 50:50 beam splitter generates two identical replicas where the reflected beam is a fixed beam that travels a fixed distance. The other portion is directed into a retro-reflector placed on a motorized stage which is capable of scanning in both directions. This portion is called the delay beam. A clear glass window of thickness 1 mm was placed in the path of the fixed beam to impose the same chip as in the delay beam since it passes through the beam splitter. Both beams are directed to a concave mirror, focused, and finally overlapped in the BBO crystal where the second harmonic generation takes place, illustrated in Figure 3.7. Three spots of light are generated, with the spot of interest called FROG beam located in the middle. In the case of the 1500 nm and the 1300 nm beam a BBO crystal is placed prior to the FROG to generate a visible light for alignment into the FROG. After the beam splitter, the distances travelled by both beams were ensure to be similar to enhance our chances of observing the FROG beam

26

when they overlap both in space and time in the BBO. Occasionally, the angle of the BBO crystal was adjusted for an improved phase matching to have a clear observation of the FROG beam. An iris and a 10 cm lens isolate and focus the FROG beam into a spectrometer connected to a computer where the signal is captured.
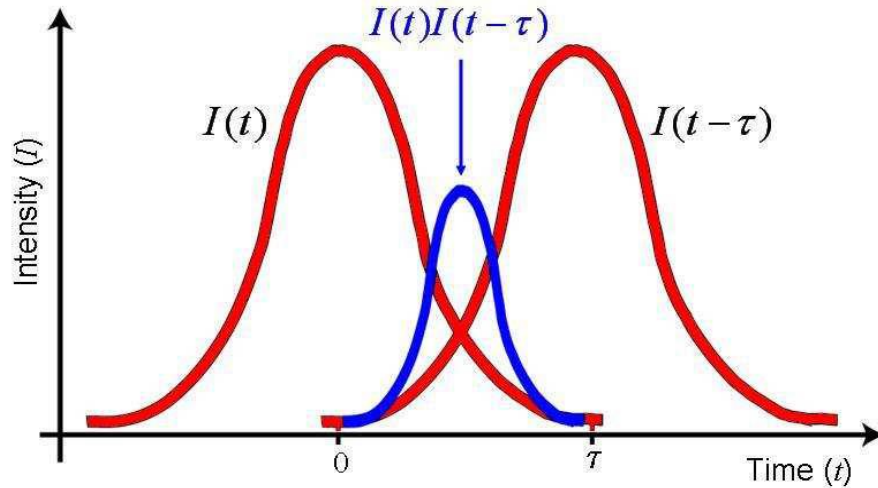
Figure 3.7. The principle of SHG autocorrelation showing the fix pulse I(t), the delayed pulse I(t-τ) all in red and the FROG beam I(t) I(t-τ) in blue.[69]

The SHG FROG signal field depends on the product

$$E_{sig}(t,\tau) = E(t)\,E(t-\tau) \tag{3.1}$$

The signal as indicated above is generated from different delay times input into a spectrophotometer and the intensity yields a FROG trace as shown in Figure 3.8.
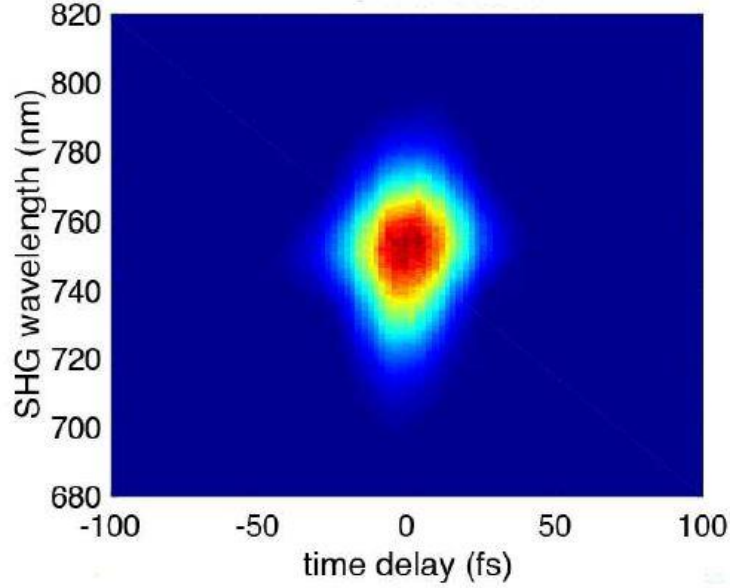
Figure 3.8. The Frog trace centered at zero delay and length scan of 200 fs from -100 fs to 100 fs at 1 fs step with time delay (fs) on the ordinate and SHG wavelength on the abscissa.

Equation 3.2 contains the real-valued function of two variables, frequency and time delay between pulses.

$$I^{SHG}_{FROG} = \left(\int_{-\infty}^{\infty} dt\, E(t)E(t,\tau)\exp(-i\omega t) \right)^2 \tag{3.2}$$

A numerical algorithm[73] is then applied to the FROG trace to retrieve both intensity and phase of the pulse created using an open source MATLAB code.[74] Figure 3.9 shows the retrieved intensity and phase of a 1500 nm pulse measured using our home built SHG-FROG. The pulse duration of wavelength from 1140 nm to 1600 nm ranges from 17 fs to 35 fs and 27 and 25 fs for 800 and 650 nm respectively.
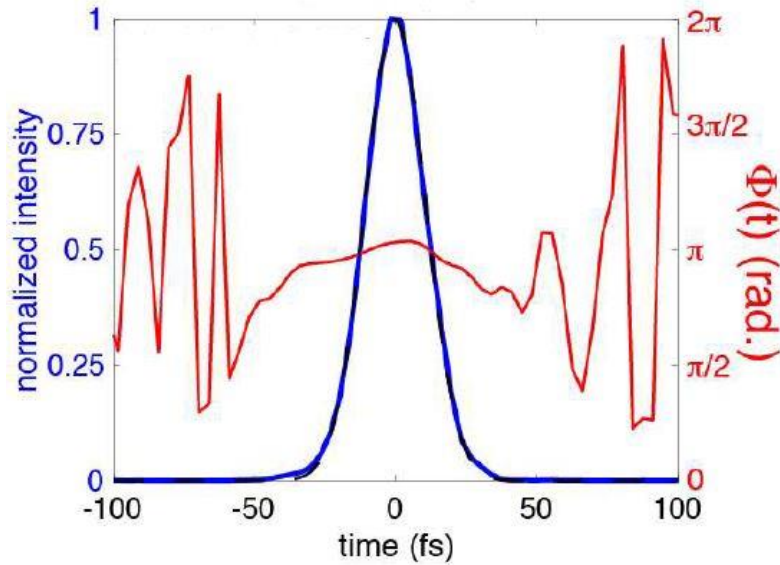
Figure 3.9. The retrieved electric field showing intensity in blue and phase in red, both as a function of time (fs).

3.7 The structure of a focused beam

The structure of a focused beam in our experiment is very important since the Rayleigh range where the beam is focusable, has to be larger than the slit of the extraction plate to allow ions collected from the cylindrical geometry[75] to pass through to mass analyzer. The structure of a focused beam can be seen in Figure 3.10.
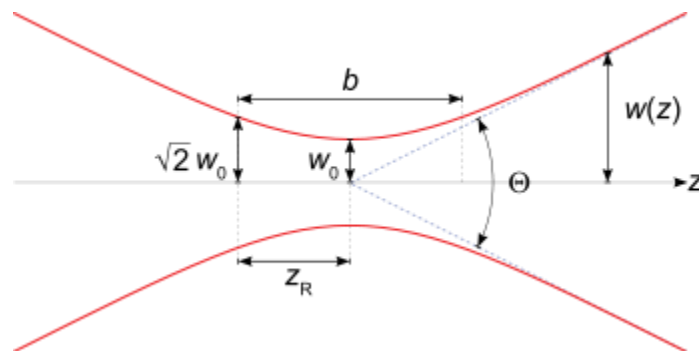
Figure 3.10. Structure of a focused beam.[76,77]

Where w_o is the beam waist and is the measure of the beam size at the point of focus, $\sqrt{2}w_o$ is an appreciable point in the beam where its expandable, z_R is the Rayleigh range where the beam is focusable and its between w_o and $\sqrt{2}w_o$, b is the depth of focus which twice the Rayleigh range. The point where the intensity of the beam drops to $1/e^2$ is called the edge of the beam $w(z)$. As the beam diverges from the focal point it's captured by its divergence Θ which is inversely proportional to the spot size for a given wavelength, i.e. a smaller spot size has a rapid divergence.

3.8 Calibration of Absolute Peak Intensity

3.8.1 Calibration Absolute Peak Intensity of the pump

The experiments performed in the lab make use of different wavelengths from the visible to the near infrared region. It is imperative that the system is calibrated and saturation intensity of each wavelength determined to know the intensity of the pulse at a particular condition. Xenon was used to calibrate our system because it has a low ionization potential (IP), so its saturation intensity is easily achieved with the pulse energies available in the lab. This is important because the amount of energy generated by the laser used in the lab will not be enough to reach saturation levels for atoms such as helium and neon, which have about twice the IP of xenon. The probe beam was block and a lens f = 20 cm was mounted on a translation stage directly before the entrance window to the MS. The wave plate rotation angle was adjusted to maximize the power of the pump beam measure before the lens. The Xe gas tank was attached to the TOF-MS chamber outlet and the leak valve was adjusted controlling gas flow into the chamber such that the pressure guide reads between 5-10 x 10^{-8} torr. The power supply voltage to the TOF-MS detector was off when adjusting the sample pressure to avoid damage to the MCP detector due to pressure spike. Ion signals of Xe^+ (and higher charge states) was checked via a computer connected to the

oscilloscope. Signals were maximized by adjusting the position of the manual translation stage on which the focusing lens is mounted motorized. This ensures that the pump beam focus overlaps with the 0.5 mm slit. The saturation intensity was obtained by adding all ion signals generated by the laser (Xe^+, Xe^{2+}, and Xe^{3+} if present) and plotting them against logarithm of pulse energy (Figure 3.11). The x-axis intercepts denote the energy corresponding to the saturation intensity. The saturation pulse energy was determined to be from 25 µJ to 40 µJ for wavelengths 1160nm-1550nm after averaging data. The saturation intensity of the wavelengths was determined by relating to that of absolute saturation intensity of Xe which has been well established to be 1.12 x 10^{14} Wcm^{-2}.[75] Figure 3.11 shows the saturation energy of 1500 nm wavelength of 34 $\pm$1 µJ.
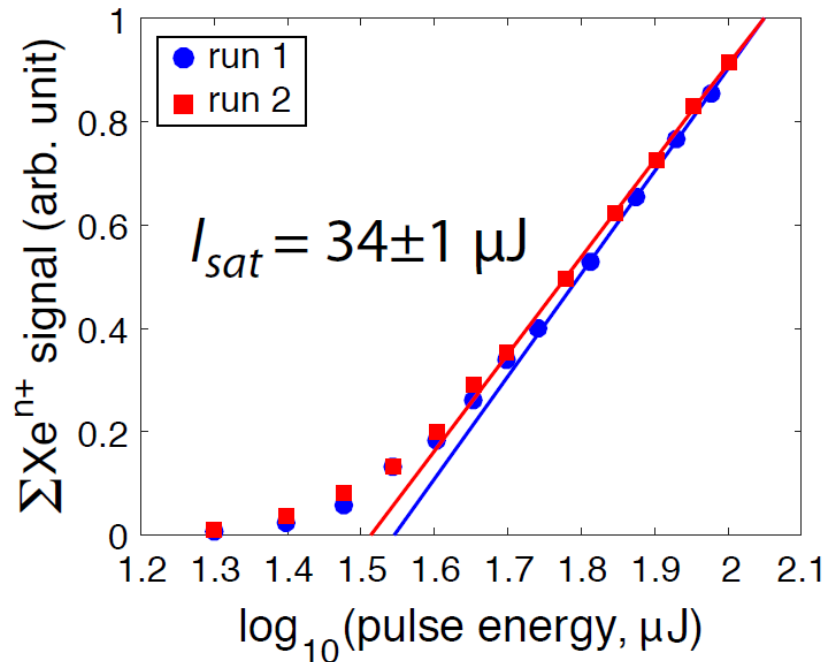
Figure 3.11. The graph showing a semi-log plot of Xe^{n+} signals versus pulse energy. The data points are represented by red squares and the blue circles corresponding to two runs. The linear fit is shown in their corresponding colors.

3.8.2 Calibration of absolute peak intensity of probe pulse

The xenon calibration is not applicable to calibrate the intensity of the probe pulse because the peak intensity generated is below the ionization potential of xenon. Instead the probe intensity was estimated by measuring the spot size at the focal point with a digital CMOS camera, along with the pulse duration energy. The intensity of the probe was determined by blocking the pump and directing the probe beam along a straight path after the dichroic mirror using two flat mirrors. A 20 cm focusing lens was placed in the probe beam path, ensuring that the probe beam passes through its center. The beam energy was minimized using the variable ND filter to attenuate the pulse energy below ~10 nJ. A compact CMOS camera (ThorLabs, Inc., pixel width 5.2μm) was mounted on a manual stage and connected to a computer with suitable data acquisition software. The translation stage was placed in the probe beam path with the camera centered near the focal spot of the beam. The beam was located using the data acquisition software while ND filters were used to minimize saturation of the CMOS detector. Images were recorded over a propagation distance of 13 mm with 0.6 mm intervals. The position of the translation was adjusted to obtain the smallest, most intense laser spot. This location corresponds to the focus of the beam. An image of the focused probe beam taken with the CMOS detector is shown in Figure 3.12. Data from this image can be fit to a Gaussian to retrieve the beam radius ($\delta = 29.3$ μm).
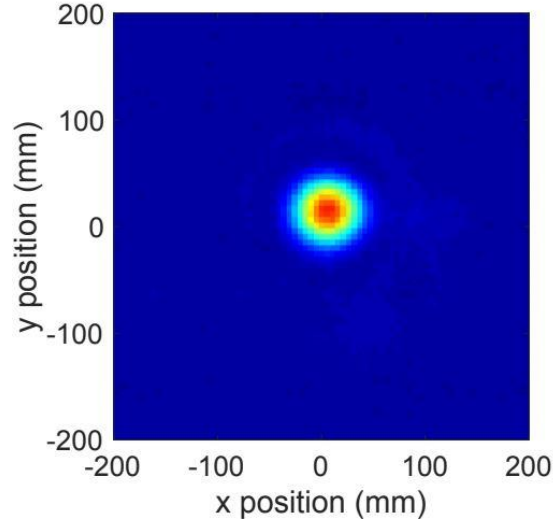
Figure 3.12. The image of a probe focused beam taken using a CMOS detector.

A camera image at the focus was acquired alongside other images corresponding to distance of the translation stage moved in either direction. The data obtained was fit to a two-dimensional Gaussian beam propagation function

$$\omega(z) = \omega_0 \sqrt{1 + \frac{(z-a)^2}{z_R^2}} \qquad (3.3)$$

to obtain fitting parameters $\omega_0 = 29.3 \pm 0.3$ µm, $z_R = 13 \pm 1$ mm and $a = 0.7 \pm 0.4$ mm, as shown in Figure 3.13 where ω_0 is the beam waist, z_R is the Rayleigh range and a is the parameter representing a trivial shift of focus along the propagating axis. With the beam waist of the probe known, the area of the spot size can be estimated and the intensity calculated using the measured pulse energy, which typical is between 10^{10}-10^{12} Wcm^{-2}.
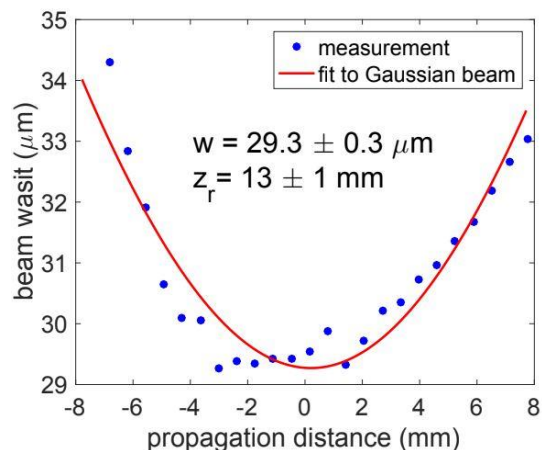
Figure 3.13. Beam waist as a function of propagation distance with measured data in blue circles and fit function in red line.

3.8.3 Cross-Correlation

The cross correlation of both beams was determined for system calibration using the pump probe (both IR and visible beam lines). The cross-correlation on xenon was done to calibrate the system for a maximum overlap in the mass spectrometer and to verify the pulse duration of both pulses. With the gas in the chamber and the beam overlap optimized (as described in section **3.4.6**) the motorized stage was moved to locate *zero-time* delay (thus when the Xe^+ signal is maximized). The motorized stage was scan over the delay range from -200 fs to 200 fs in steps of 5 fs. This scan corresponds to steps of 1.5 µm over a range of 120 µm centered at zero time-delay position. The cross correlation between 1500 nm and 800 nm was recorded to be 26.1 $\pm$ 0.2 fs as shown in Figure 3.14 which shows a good overlap and verifies the duration of both pulses.
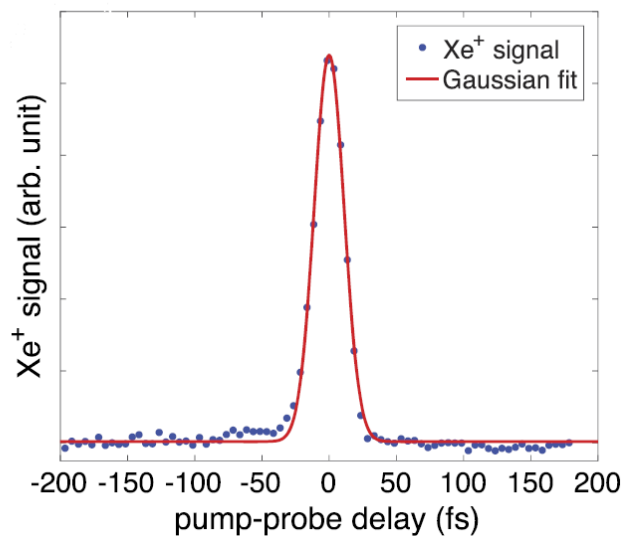
Figure 3.14. Xe measurements showing the Cross-correlation taken with 1500 nm as the pump and 800 nm as the probe. The data points in red and the Gaussian fit line in red.

3.8.4 Knife-edge method

There are many methods used to determine diameter of a beam, however the knife-edge method is the most popular because of its simplicity and the possibility of been used for a wide range of wavelengths. To determine the beam diameter a knife-edge (blade) is placed on a manual stage and positioned on the tail end of the beam parallel to the power meter. The initial power of the beam is recorded and as the blade moves with the help of the manual stage, portions of the power is blocked and recorded alongside the distance moved until the blade completely blocks the laser path. An illustration of the knife edge method is shown in Figure 3.15.
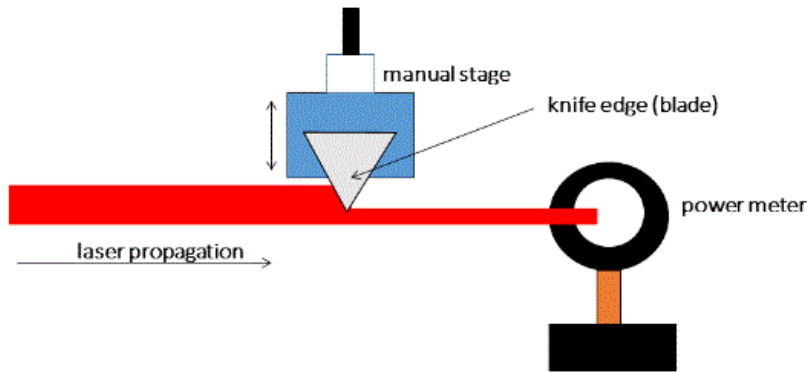
Figure 3.15. Illustration of the knife edge method.

Data is then collected and entered into a lab view program to obtain the beam waist and beam diameter. Typical curves obtain with knife edge measurements are shown in Figure 3.16. This curve represents the enlarged 1300 nm beam with beam waist of 10.95 mm and a beam diameter of 21.91 mm. The method was used to determine the size of all beams prior to focusing.
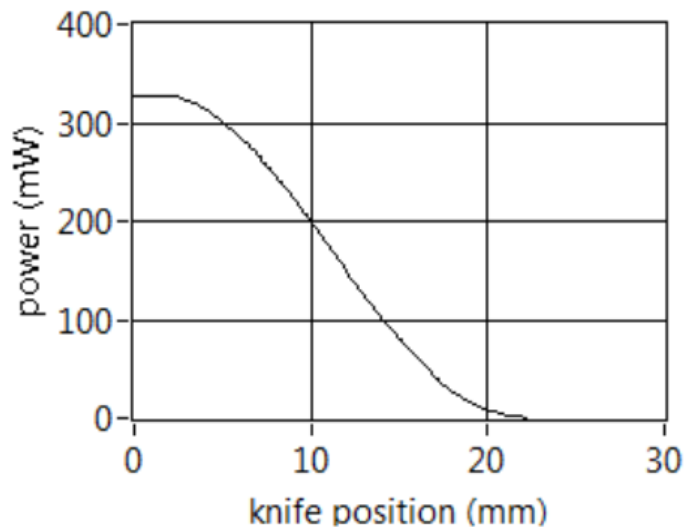
Figure 3.16. Graph obtained from knife edge method showing the data represented in solid curve.

CHAPTER 4: Ultrafast Coherent Vibrational Dynamics in Dimethyl Methylphosphonate Cation.

The content of this chapter has been adapted with permission from the reference:

Ampadu Boateng, D., Gutsev, G.L., Jena, P., and Tibbetts, K.M. Phys. Chem. Phys., **2018**, *20*, 4636.

4.1 Introduction

The development of femtosecond pump–probe techniques by the Zewail group[78,79] to enable the study of coherent vibrational dynamics (i.e., of nuclear ''wavepackets'') on molecular potential energy surfaces have revolutionized understanding of molecular dissociation processes. While early experiments on diatomic molecules such as Na_2[80,81] and Br_2[82] allowed for resolution of 300 fs oscillations in ion and photoelectron kinetic energy yields, recent improvements in femtosecond laser technology producing sub-10 fs pulses have now enabled the direct observation of vibrational wavepackets with sub-40 fs oscillation periods in N_2^+,[83] O_2^+,[83] CO^+,[83] D_2^+,[84,85] H_2^+,[86] and CO_2^+,[87,88] with revivals observable for as long as 30 ps. In contrast, the presence of multiply coupled normal modes in polyatomic molecules results in vibrational wavepacket propagation on a multidimensional potential energy surface (PES), leading to fast dephasing in radical cations within at most several picoseconds of the initial ionization event.[39,44,47,89–94] Furthermore, only low-frequency oscillations have been observed in polyatomic ions for bending modes ($\sim$90–130 cm^{-1})[47,89,90] or even slower torsional modes with oscillation periods of 600–1000 fs.[39,44,91–94] As a result, in many experiments only[79–83] oscillation periods in transient ion yields are visible above the noise level.[39,44,47,89,91–94] These results raise the question as to whether such fast dephasing timescales relative to the wavepacket oscillation frequency inevitably arise in polyatomic molecules, which could limit the potential of controlling dissociation pathways via coherent control schemes. To test the ability of strong field adiabatic ionization to prepare coherent

vibrational states in polyatomic cations, this work considers the molecule dimethyl methylphosphonate (DMMP, $PO_3(CH_3)_3$). The practical importance of DMMP as a flame retardant[95] and as a simulant of organophosphorus chemical warfare agents[96] renders the study of its dissociation dynamics of broad interest, as evident in the plethora of recent theoretical and experimental studies of DMMP dissociation in the gas phase and on heterogeneous catalysts.[97–103] Dissociation pathways in the $DMMP^+$ radical cation have also been widely investigated both theoretically and experimentally.[103–107] This work will demonstrate the preparation of a well-defined coherent state in $DMMP^+$ with an oscillation period of 45 fs, which is significantly faster than previous oscillations observed in coherent states of polyatomic radical cations.[39,44,47,89–94]

4.2 Experimental Methods

Refer to sections **3.4.1** and **3.4.2** for details on schematic experimental methods. The calibration of intensity of pump and probe was done using methods in sections **3.8.1** and **3.8.2** respectively. System optimization was followed according to section **3.4.4 - 3.4.6.**

Pump and probe pulses were prepared from the output of a commercial Ti:sapphire regenerative amplifier (Astrella, Coherent, Inc.). The strong field ionizing pump pulses ($\sim$8 x 10^{13} W cm^{-2}) were either taken directly from the 800 nm output (100 mJ, 31 fs) or an optical parametric amplifier (OPA, TOPAS prime) producing tunable near-IR pulses (1200 -1600 nm, 20-25 mJ, 19-28 fs). The wavepacket dynamics in the resulting radical cation were probed with a weak 800 nm pulse (nonionizing, 20 mJ, $\sim$4 x 10^{12}Wcm^{-2}, 28 fs). All pulse durations were measured with Frequency Resolved Optical Gating (FROG)[72] (Figure 4.1), and are consistent with cross-correlation measurements made on Xe^+ (Figure 3.14). The time delay between pump and probe pulses is scanned in steps of 5 fs with a motorized delay stage (ThorLabs, Inc.). The two beams were

recombined collinearly and focused into a vacuum chamber (base pressure 2 x 10^{-9} Torr) containing an effusive molecular beam of DMMP (Sigma-Aldrich) at a pressure of 5 x 10^{-7} Torr. Time-of-flight mass spectra were collected on a 1 GHz digital oscilloscope (LeCroy WaveRunner 610 Zi) and averaged over 10000 laser shots. The absolute laser intensity was determined by the Xe^+ signal of added xenon gas using the well-established method.[75]

4.2.1 Measurements of Pulse Duration

A home-built Frequency Resolved Optical Gating (FROG) setup was used to measure the spectrograms for each pulse and the time-dependent electric fields were retrieved with an open-source MATLAB code[74] based on the retrieval algorithm in Ref.[73] Figure 4.1 shows the spectrograms (top panels) and retrieved temporal electric fields (bottom panels) for the 800 nm, 1200 nm, and 1500 nm pump pulses, as well as the 800 nm probe pulse. The time-dependent intensity is shown in blue and the temporal phase shown in red. The retrieved full-width-half-maximum (FWHM) pulse durations are indicated in each panel.
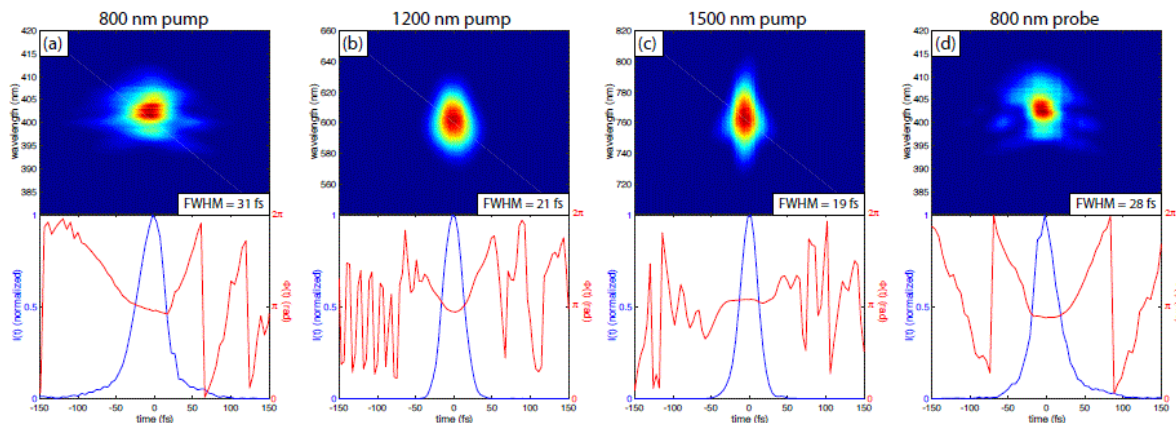
Figure 4.1. Two-dimensional spectrograms recorded with SHG-FROG setup (top panels) and retrieved time-dependent electric fields (bottom panels).

4.2.2 Computational Methods

To interpret the coherent wavepacket dynamics in Figure 4.3, a series of calculations was performed on DMMP and DMMP$^+$. All computations were performed using the 6-311+G* basis set of triple-ζ quality and the Gaussian 09 suite of programs.[65] First, the vibrational spectrum of DMMP$^+$ in its optimized geometry was calculated using density functional theory with both the generalized approximation (DFT-GGA) and hybrid Hartree–Fock DFT methods, BPW91[66,67] and B3LYP,[108,109] respectively, in order to identify the active vibrational mode leading to the observed oscillations.
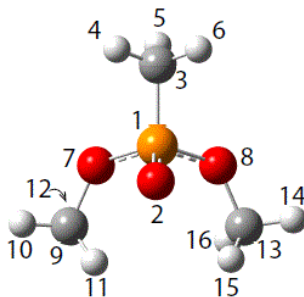
Figure 4.2. DMMP structure with atoms labeled according to the labels in Table A2 in appendix.

4.3 Experimental Results

Figure 4.3 displays the DMMP$^+$ parent molecular ion signal as a function of pump–probe delay for representative pump wavelengths 800 nm (blue), 1200 nm (green) and 1500 nm (red). All transient signals are normalized to unity at negative time delays (i.e., where the probe precedes the pump); the 1200 nm data are shifted on the ordinate axis by +0.1 units for clarity. The dashed vertical lines highlight 6 minima visible in the ion yield with spacing of 45 fs. Such fast-coherent oscillations in the yield of a polyatomic ion are unprecedented in the literature, where reported oscillation periods range from 150–1000 fs.[39,44,47,89–94] Furthermore, while only the 6 highlighted

minima are visible for 800 nm excitation, at least 12 minima are visible when using near-infrared wavelengths. As a result, performing a fast Fourier transform (FFT) of the transients for delays $\tau \geq 50$ fs (inset of Figure 4.3(a)) reveals no features above the noise for the 800 nm pump, while a well-resolved peak around 750 cm^{-1} is visible for the near-infrared wavelengths, consistent with the 45 fs oscillations. We attribute this significantly improved coherent state preparation with near-infrared excitation to the transition from nonadiabatic to adiabatic ionization, which is consistent with the calculated Keldysh parameters and enhanced formation of the parent molecular ion for near-infrared excitation shown in the mass spectra taken at a time delay of -200 fs (Figure 4.4 (b)).
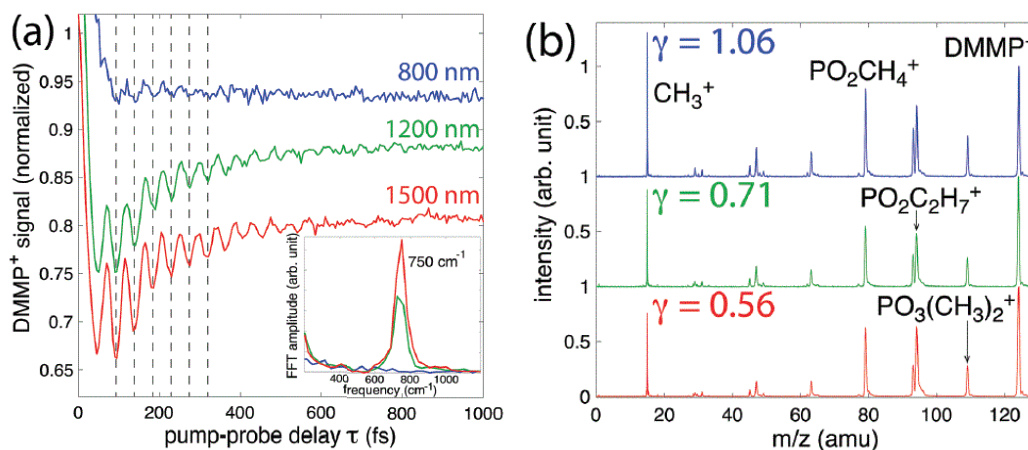
Figure 4.3. (a) Integrated DMMP$^+$ signal as a function of pump–probe delay τ for pump wavelengths 800 nm (blue), 1200 nm (green), and 1500 nm (red). Dashed lines denote minima of the ion yield with a period t = 45 fs. Inset: FFT of transient signals for $\tau > 50$ fs. The FFT resolution limited by sampling rate and number of transform points is 30 cm^{-1} (b) Mass spectra of DMMP at $\tau = -200$ fs, with Keldysh parameters γ. Spectra are normalized to the DMMP ion peak.

It is unlikely that the slightly longer pulse duration of the 800 nm pump wavelength as compared to 1200 and 1500 nm wavelengths limits the coherent state population because Xe^+ cross-correlation measurements show only a small increase from 26 to 32 fs FWHM when comparing the 1500–800 nm and 800–800 nm pump–probe pairs (Figure 4.4 (a,b)).
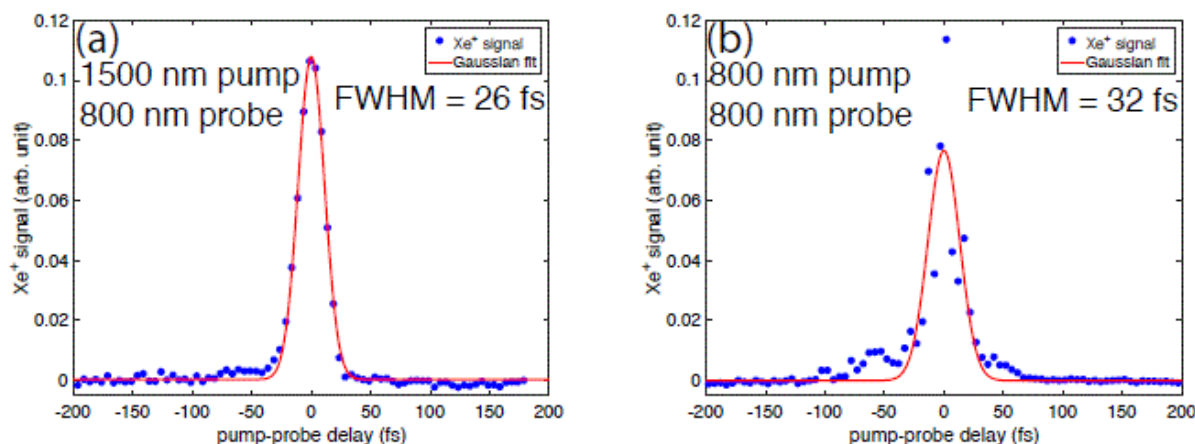
Figure 4.4. Cross-correlation measurements of Xe^+ signal taken with (a) 1500 nm pump - 800 nm probe, and (b) 800 nm pump - 800 nm probe. Gaussian fits to the experimental data and extracted FWHM values are shown.

A 1600 nm pump pulse was also tested to assess the hypothesis that adiabatic ionization is needed to effectively prepare the coherent state in $DMMP^+$ because the pulse duration of the 1600 nm pulse from the OPA increases to 28 fs due to the limited phase matching bandwidth (Figure 4.6 (a)-(b)). Large oscillation amplitudes in the yields of $DMMP^+$ and its dissociation products are observed (Figure 4.5 (c)).
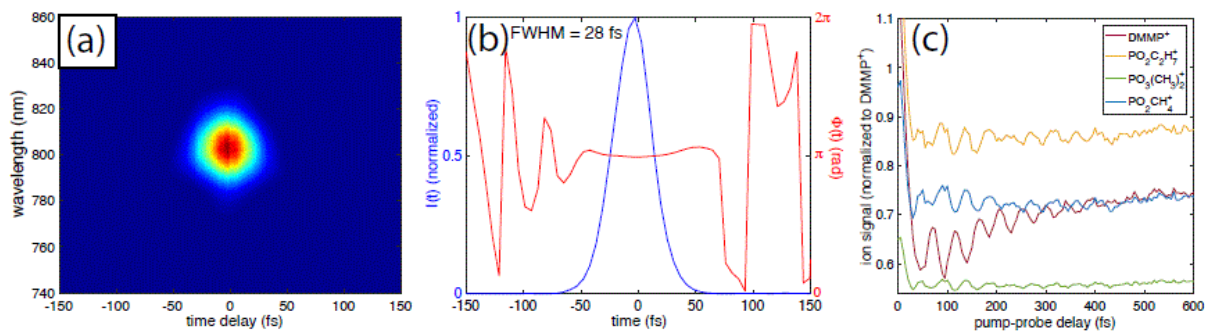
Figure 4.5. (a) FROG spectrogram of 1600 nm pump. (b) Retrieved electric field. (c) Transient ion signals of DMMP$^+$ and dissociation products with 1600 nm pump.

It was also noted that the data shown in Figure 4.3 for the 800 nm pump represents pump and probe pulse intensities producing the largest amplitude oscillations in the DMMP$^+$ yield; changing either the pump or probe intensity reduced the oscillation amplitude, as shown in Figure 4.6.
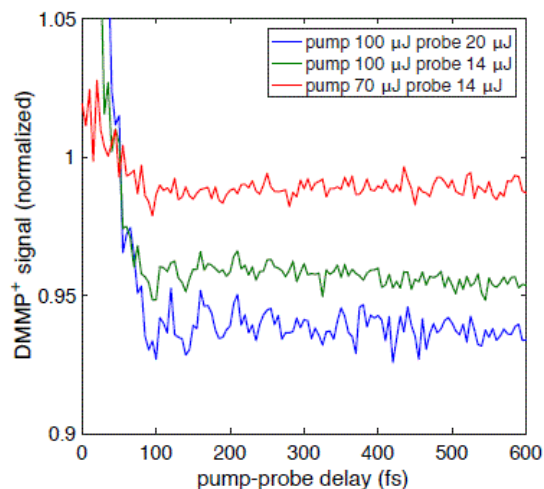
Figure 4.6. Transient ion signals of DMMP$^+$ at various pump and probe energies for 800 nm pump. Signals are normalized to the yield at negative time delays.

To explore the dissociation dynamics of the initially prepared DMMP$^+$ coherent state, we consider the transient ion signals of the three major dissociation products of DMMP that require

the lowest decay energies based on previous theoretical calculations: $PO_2C_2H_7^+$ (m/z = 94, 0.85 eV decay energy), $PO_3(CH_3)_2^+$ (m/z = 109, 1.75 eV), and $PO_2CH_4^+$ (m/z = 79, 1.76 eV).[107] The transient ion signals for the parent cation and these dissociation products were found to fit well with nonlinear least squares methods to the function

$$S(\tau) = ae^{\frac{-\tau}{T}}\left[\sin\left(\frac{2\pi}{t}\tau + \varphi\right) + b\right] + c \tag{4.1}$$

where a denotes the oscillation amplitude, T denotes the wavepacket lifetime, t denotes the oscillation period, and φ denotes the phase. The constant b corresponds to an incoherent contribution to the exponential decay of the ion yield and c corresponds to the final ion yield as $\tau \rightarrow \infty$. Figure 4.8 shows the transient yields of the parent ion DMMP$^+$ (red), $PO_2C_2H_7^+$ (orange), $PO_3(CH_3)_2^+$ (green), and $PO_2CH_4^+$ (blue) for pump wavelengths of 800 nm (top), 1200 nm (middle), and 1500 nm (bottom). All signals are normalized to the yield of the parent ion at negative time delays and shifted on the ordinate axis for clarity. The experimental yields are plotted as dots and the fit functions are plotted as solid lines. The three fragment ion transients for the 800 nm pump displayed no oscillatory behavior that could be resolved within experimental noise, and thus no fit functions are shown for these species in Figure 4.7.
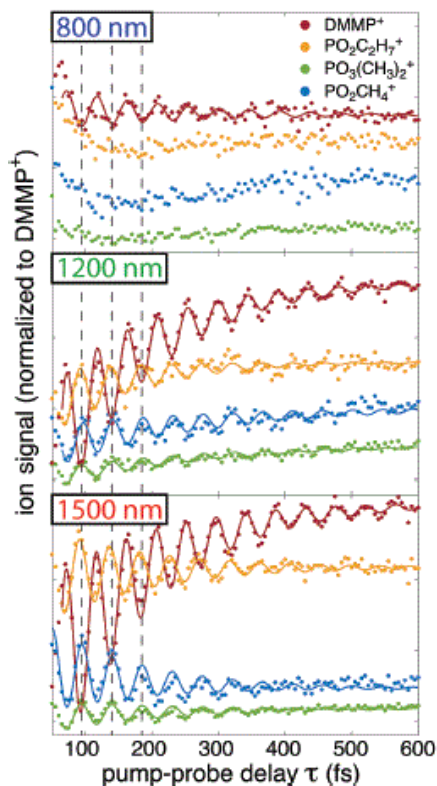
Figure 4.7. Time-dependent signals (dots) of DMMP$^+$ (red), PO$_2$C2H$_7^+$ (orange), PO$_3$(CH$_3$)$_2$ $^+$ (green), and PO$_2$CH$_4$ $^+$ (blue) ions at pump wavelengths of 800 nm (top), 1200 nm (middle), and 1500 nm (bottom), with fits to equation (1) (solid lines).

The extracted coefficients for each transient ion signal and pump wavelength are presented in the Table 4.1.

Table 4.1. Curve fitting coefficients for all transient ions.

Ion	λ(nm)	a	T (fs)	t (fs)	$\emptyset$ (rad)	b	c	R^2
DMMP$^+$	800	0.019±0.008	180±10	45.8±0.8	4.2±0.2	0.3±.2	0.937±0.002	0.51
	1200	0.072±0.007	150±10	45.3±0.3	4.1±0.2	-2.5±.2	0.780±0.002	0.98
	1500	0.100±0.009	150±10	45.0±0.6	4.1±0.1	-1.8±.1	0.805±0.002	0.98
PO$_2$C$_2$H$_7^+$	1200	0.033±0.009	130±30	45.7±0.9	1.4±0.4	-1.3±.3	1.113±0.001	0.81
	1500	0.043±0.009	150±30	45.1±0.4	1.4±0.2	-0.2±.1	1.06±0.001	0.81
PO$_3$(CH$_3$)$_2^+$	1200	0.007±0.002	230±60	45.9±0.9	1.3±0.5	-4±1	0.374±0.002	0.86
	1500	0.014±0.004	170±50	45.5±0.6	1.1±0.3	-0.5±.2	0.329±0.001	0.72
PO$_2$CH$_4^+$	1200	0.018±0.006	230±70	45.0±0.7	0.6±0.4	-1.9±.6	0.931±0.003	0.77
	1500	0.04 ±0.01	140±40	45.2±0.7	0.9±0.3	0.4±.2	0.823±0.001	0.70

The dashed vertical lines in Figure 4.7 denote the first three minima of the DMMP$^+$ ion yield. Inspection of the transient ion signals of the three dissociation products for 1200 nm and 1500 nm pump wavelengths shows that each exhibits a maximum in yield at the same pump–probe delays. This observation is consistent with the phase coefficients φ in equation (1) being approximately π out of phase between the parent and each fragment ion Table 4.1. Similar antiphase behavior between the parent and fragment ion yields has been observed in a number of other molecules and is attributed to excitation by the probe pulse to one or more electronic excited states of the ion. The exact mechanism of dissociation depends on the particular molecule and the electronic manifold of states in its radical cation. For instance, in CH_2IBr, the excited ionic state was found to be dissociative,[47,89,90] while in acetophenone, dissociation was found to occur following relaxation of the excited state ion through a conical intersection, with dissociation occurring on the ionic ground state PES.[39,44] We plan to conduct high level calculations of the relevant ground and excited state PES's in DMMP$^+$ in order to determine whether one of these mechanisms, or an entirely different mechanism, leads to the observed dissociation dynamics.

4.4 Theoretical Results

The vibrational frequencies were computed using an anharmonic approximation. The full sets of computed harmonic and anharmonic vibrational frequencies are presented in the appendix Table A1. The observed oscillation frequency of 750 cm^{-1} most closely matches the mode shown in Figure 4.8 (a) with the calculated anharmonic vibrational frequencies of 754.7 cm^{-1} (BPW91) and 742.2 cm^{-1} (B3LYP). A similar vibrational mode has previously been observed at 818.2 cm^{-1} in recent gas phase IR spectroscopic measurements of neutral DMMP.[110] To gain insight in the dependence of the anharmonic vibrational frequencies on the choice of basis set, we repeated the

computations using significantly larger basis set 6-311+G (3df,3pd). Recomputed anharmonic vibrational frequencies are 773.6 cm^{-1} (BPW91) and 741.5 cm^{-1} (B3LYP), respectively. As can be seen, the B3LYP values are nearly the same whereas the new BPW91 value is larger by 19 cm^{-1}. The recomputed values are again the closest ones to the experimental value of 750 cm^{-1} among all other vibrational frequencies computed by both methods with this larger basis set. In order to confirm the mode assignment, the relaxation pathway from the geometrical structure at which the vertical excitation occurred to the equilibrium cation geometry was computed using the Synchronous Transit-Guided Quasi-Newton method QST2.
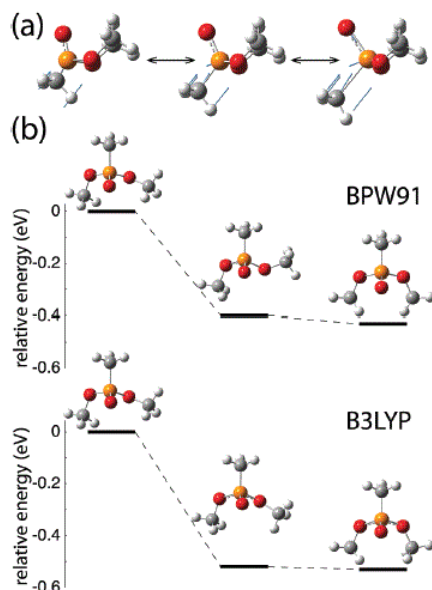
Figure 4.8. (a) Active vibrational mode of coherent motion in DMMP$^+$. (b)Geometrical relaxation pathways of DMMP$^+$ calculated at the BPW91 (top) and B3LYP (bottom) levels.

The pathway shown in Figure 4.8 (b) was found to possess a transition state that is close in total energy to the total energy of the final cation state, by 0.03 eV and 0.01 eV, at the BPW91 and B3LYP levels, respectively. The total energy gain due to the relaxation was found to be 0.43 eV

and 0.53 eV at these two levels, respectively. The computed changes in bond radii and bond angles upon relaxation are given in the appendix Table A2.

The two most significant geometrical changes were as follows: (1) the P-O bond lengthens by 2.8% and 6.6% at the BPW91 and B3LYP levels, respectively, and (2) the $H_3CO–P–OCH_3$ bond angle increases by 10.7% and 14.9% at the BPW91 and B3LYP levels, respectively. In addition, the other O–P–O bond angles change by at least 5% at both levels. Collectively, these coordinates correspond to the dominant motions in the coherently excited normal mode. This matching of the geometric relaxation pathway in $DMMP^+$ with a single normal mode likely contributes to its long-lived coherence over 12 cycles, despite the presence of a number of modes with lower frequencies (appendix Table A1).

4.5 Conclusions

This work has documented coherent vibrational dynamics in the $DMMP^+$ radical cation with a significantly faster oscillation period of 45 fs than previously reported in the literature for polyatomic ions. At least 12 oscillation periods are visible in the $DMMP^+$ transient yield when the laser excitation wavelength is sufficiently long ($\geq$1200 nm) such that an adiabatic ionization mechanism operates. The wavepacket motion is assigned to a bending motion in $DMMP^+$ with an observed frequency of approximately 750 cm^{-1}, which agrees well with DFT calculations reporting this mode at 754.7 cm^{-1} and 742.2 cm^{-1} at the BPW91 and B3LYP levels, respectively. The ion yield of the parent ion $DMMP^+$ is found to oscillate approximately out of phase with the yields of the fragment ions $PO_2C_2H_7^+$, $PO_3(CH_3)_2^+$, and $PO_2CH_4^+$, indicating that the probe pulse induces dissociation through population of one or more electronic excited states of the ion. While additional experiments and calculations of the ground and excited PES's of $DMMP^+$ are needed to fully understand these dynamics, the present results demonstrate the importance of coherent

nuclear dynamics to the dissociation pathways of DMMP$^+$. This observation raises the possibility that dissociation pathways in related chemical warfare agents may be actively controlled via coherent control schemes, which could lead to the development of new technologies for chemical warfare agent detection and destruction.

CHAPTER 5: Dissociation of 3- and 4-nitrotoluene radical cations: Coherently driven C-NO₂ bond homolysis

The content of this chapter has been reproduced from:

5.1 Introduction

Understanding the detonation mechanisms of energetic materials used in military[111] and mining[112] operations has been an active area of research for decades. While extensive studies have unraveled mechanisms of stored energy released in bulk energetic materials,[113–117] initial dissociation mechanisms of isolated energetic molecules still constitute an active area of investigation.[11–14,35] In energetic materials, excited electronic states and molecular ions are thought to drive initial energy release processes based on the observation of tribological luminescence.[118,119] Thus, understanding relaxation and dissociation processes from excited states and ions of isolated energetic molecules is needed to fully understand initial excitation events in energetic materials, which may facilitate longstanding goals such as developing photoactive high explosives that can be initiated by lasers.[120] Because ultrafast events associated with the initial dissociation pathways of energetic molecules typically occur within a few picoseconds of the initial excitation,[121] time-resolved pump-probe methods originally developed by Zewail[78] are needed to investigate their dynamics. Pump-probe studies have revealed the dynamics of fast evolving events in energetic molecules including HMX and RDX,[18] nitramines,[19–21] nitromethane,[23] and furazan.[22] In all of these molecules, the ionized fragment NO^+ was formed from the electronically excited parent molecules within the pulse duration of 180 fs.

In other studies, dissociation of NO_2 from nitromethane was found to occur within 81 fs[122] and the transient parent cations of nitrotoluenes formed from electronically excited neutrals were found to have lifetimes of 50-70 fs.[123] While these studies and others attest to ultrafast time scales leading to decomposition of energetic molecules from their neutral excited states, less is known about the dissociation dynamics of their radical cations. It is thought that the radical cations of energetic molecules dissociate via low-lying electronic states based on photoelectron-photoion coincidence measurements of nitromethane[124] and nitrobenzene,[125] as well as shaped 800 nm femtosecond laser pulse excitation of 4-nitrotoluene.[43] Recent theoretical studies have also identified ground state dissociation pathways in the radical cations of 1-nitropropane[33] and trinitrotoluene (TNT).[34] However, the time scales of these dissociation processes remain unknown. One of the most important families of energetic molecules is the nitrotoluenes, with TNT being the most widely investigated due to its practical uses.[34,42,112,117,126–129] While multiple rearrangement reactions can occur in excited TNT and other nitrotoluenes, the homolysis of one or more NO_2 groups has been found to drive initial detonation processes based on its thermodynamic favorability.[117]

This work will present pump-probe measurements on the radical cations of the isomeric compounds 3-nitrotoluene (3-NT) and 4-nitrotoluene (4-NT), along with nitrobenzene (NB). The high yield of parent molecular ions when using 1500 or 1300 nm pulses for ionization enables observation of coherent nuclear dynamics in the parent radical cations of 3-NT, 4-NT, and NB. The ion yields exhibit distinct oscillatory dynamics, indicating coherent excitation of distinct normal modes. Interpretation of the experimental results is supported by a series of density functional theory (DFT) calculations of the optimized geometries, relaxation pathways, and vibrational frequencies in 3-NT, 4-NT and NB radical cations.

5.2 Experimental Methods

Refer to section **3.4.1**, **3.4.2 and 3.4.3** for details on schematic experimental methods. Details of cross correlation measurements of Xe^+ using 1500 nm and 800 nm probe can be found in section **3.8.3**. System optimization was followed according to section **3.4.4 - 3.4.6.**

The pump and probe pulses are generated from a Ti:sapphire regenerative amplifier (Astrella, Coherent, Inc.) producing 30 fs, 800 nm, 5 mJ pulses. 2.2 mJ of the laser output is split with a 90:10 (r:t) beam splitter, with 1.9 mJ used to pump an optical parametric amplifier (OPA, TOPAS Prime) to produce 1500 nm, 18 fs, 300 μJ pulses that are used as the pump. The pump pulse energy is attenuated with a $\lambda/2$ waveplate and polarizer and expanded using two spherical gold mirrors with $f = $ -10 cm and $f = 50$ cm to increase the beam diameter (measured with the knife-edge method) from 4.5 mm to 22 mm [Section **3.4.1,** yellow beamline]. This beam expansion results in a smaller focal beam waist and thus higher intensity. The remaining 200 µJ of 800 nm acts as the probe pulse and is down-collimated using two spherical gold mirrors with $f = 20$ cm and $f = $ -10 cm to reduce the beam diameter from 11.6 mm to 5.8 mm. The probe beam is then directed to a retro-reflector (PLX, Inc.) placed on a motorized translation stage (ThorLabs, Inc.), attenuated with a variable density filter and passed through an iris to isolate the most intense portion of the beam [Section **3.4.2**, red beamline]. Section **3.4.3** outlines the generation of the 650 nm beam.

Pump and probe beams are recombined on a dichroic mirror and focused with an $f = 20$ cm fused silica biconvex lens. The durations of the pump and probe pulses were measured with a homebuilt Frequency Resolved Optical Gating (FROG)[72]setup to be 18 fs and 25 fs, respectively (Figure 5.1 and 5.2). The focused laser pulses are introduced into an ultrahigh vacuum chamber (base pressure 2 x 10^{-9} Torr) coupled to a linear time-of-flight mass spectrometer (TOF-MS,

Jordan, Inc.) described in our earlier work.[107] The focus of the laser beam is centered between the charged repeller (+4180 V) and extraction (+3910 V) plates, where a 1/16″ diameter stainless steel tube introduces the sample as an effusive molecular beam approximately 1 cm from the laser focus. The extraction plate has a 0.5 mm slit orthogonal to the laser propagation and TOFMS axes, which serves as a filter to allow only ions produced at the central focal volume of the laser beam where the intensity is the highest to enter the flight tube.[75] Samples of 3-NT, 4-NT and NB (Sigma Aldrich, Inc.) are used without further purification and introduced directly into the chamber. Due to the low vapor pressures of the nitrotoluenes, the sample holders are heated with resistive heating tape to produce a pressure of 10^{-7} Torr at the Z-gap microchannel plate (MCP) detector. Mass spectra are recorded with a 1 GHz digital oscilloscope at a sampling rate of 20 giga samples per second (GS/s) (LeCory WaveRunner 610Zi). All mass spectra are averaged over 10000 laser shots.

5.2.1 Beam Diagnosis

The durations of the pump and probe pulses were measured using a home-built Frequency Resolved Optical Gating (FROG) setup[72] to obtain the autocorrelation spectrograms. The time-dependent electric fields were retrieved with an open-source MATLAB code[74] based on the retrieval algorithm in Ref.[73] The spectrograms and retrieved temporal electric fields for each pulse are shown in Figure 5.1 and 5.2 respectively. The duration of the 1500 and 1300 nm pump pulse was 18 and 17 fs and the duration of the 800 and 650 nm probe pulse were both 25 fs.
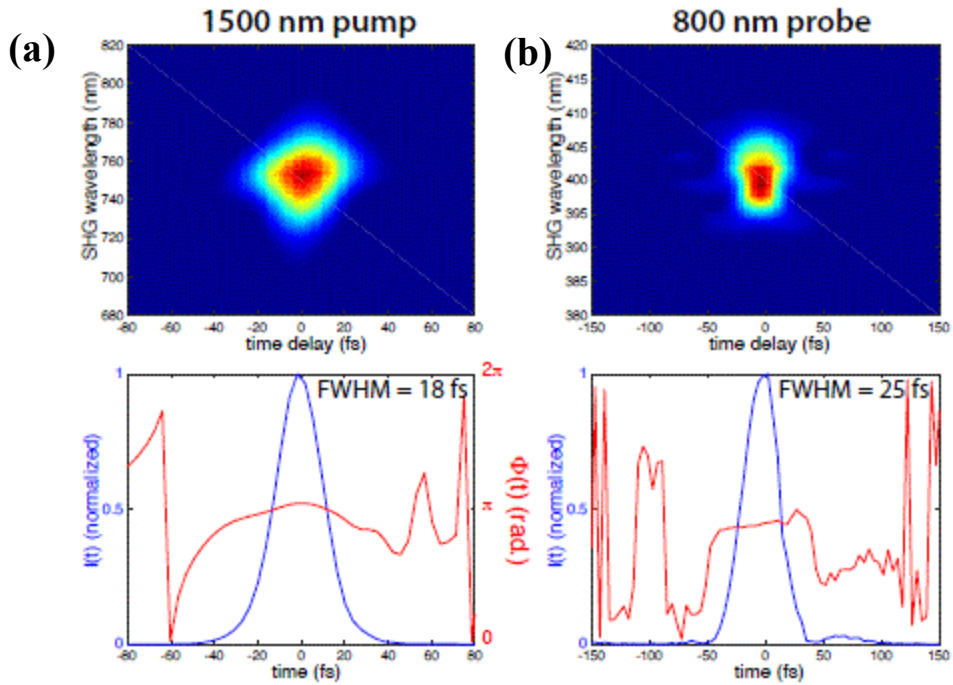
Figure 5.1. Spectrogram (top) and retrieved temporal intensity and phase of 1500 nm pump pulse (a) and 800 nm probe pulse (b).
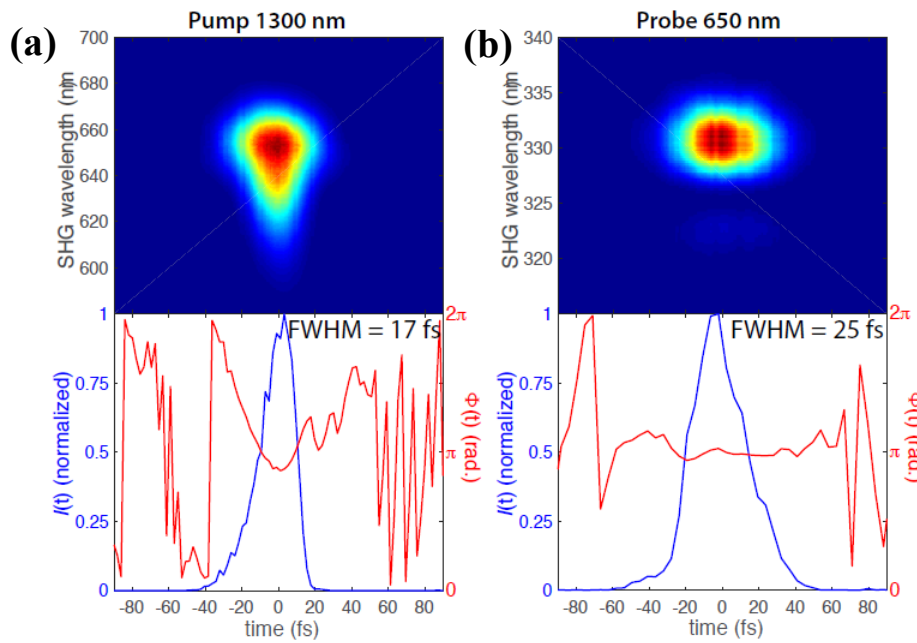
Figure 5.2. Spectrograms (top) and retrieved temporal intensities and phases of the 1500 nm pump pulse (a) and the 800 nm probe pulse (b).

The beam waist and Rayleigh range of the probe pulse were measured with a CMOS camera (ThorLabs, Inc., pixel width 5.2 μm) mounted on a linear translation stage. Images of the beam were recorded over a propagation distance of 13 mm at an interval of 0.6 mm. The beam spot in each image was fit to a Gaussian function in both the x and y directions using a MATLAB code, and the average waist at intensity $1/e^2$ of the maximum recorded. Figure 5.3 (a) shows a representative CMOS image of the beam and Figure 5.3 (b) shows its fit to a Gaussian function in the x direction. The $1/e^2$ width is plotted as a function of beam propagation distance in Figure 5.2 (c). The data were fit to the Gaussian beam propagation function

$$\omega(z) = \omega_0 \sqrt{1 + \frac{(z-a)^2}{z_R^2}} \qquad (5.1)$$

to obtain the fitting parameters $\omega_0 = 29.4 \pm 0.2$ μm, $z_R = 16 \pm 1$ mm, and $a = 0.7 \pm 0.4$ mm. The a parameter represents a trivial shift of the focus along the propagation axis, while the parameters ω_0 and z_R represent the beam waist and Rayleigh range, respectively.
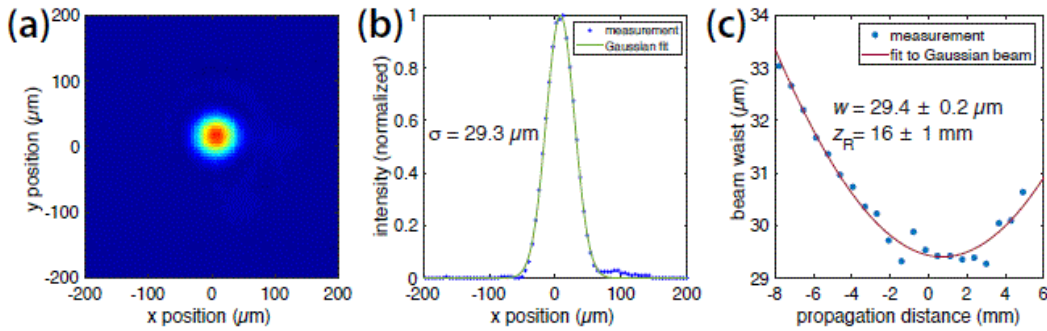
Figure 5.3. Beam parameters of 800 nm showing (a) False color CMOS image of probe beam at the focus, (b) Gaussian fit in x direction to the image in (a), (c) Measured beam radius as a function of propagation distance (circle) and to equation 5.1 (solid line). The beam propagation was in the direction of increasing z value.

Figure 5.4 (a) shows a representative CMOS image of the 650 nm beam. The $1/e^2$ width is plotted as a function of beam propagation distance in Figure 5.4 (b). The data were fit to the Gaussian beam propagation function to obtain the fitting parameters $w_0 = 37.9 \pm 0.3$ μm, $z_R = 9.8 \pm 0.3$ mm, and $a = 0.2 \pm 0.1$ mm. The a parameter represents a trivial shift of the focus along the propagation axis, while the parameters w_0 and z_R represent the beam waist and Rayleigh range, respectively.
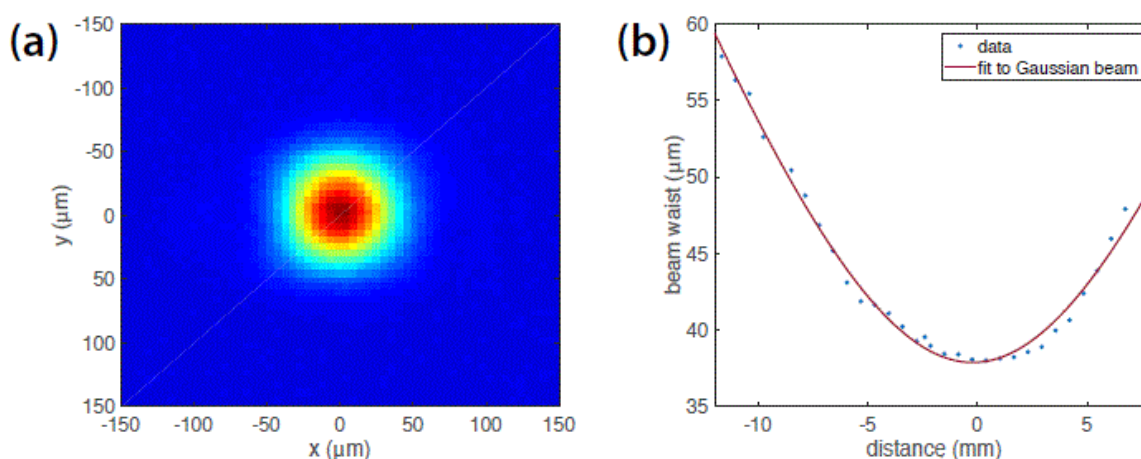
Figure 5.4. Beam parameters of 650 nm showing (a) False color CMOS image of probe beam at the focus. (b) Measured beam radius as a function of propagation distance (circles) and fit to (eq 5.1) (solid line). The beam propagation was in the direction of increasing z value.

5.3 Computational Methods

Our computations are performed using the widely used B3LYP method,[108,130] for 3NT and 4NT and BPW91[66,67] from the generalized gradient approximation (GGA) family for NB as implemented in Gaussian 09 suite of programs.[65] We choose a balanced split-valence Def2-TZVPP $[(11s6p2d1f)/5s3p2d1f]$ and 6-311G* basis of triple-ζ quality for the nitrotoluenes and nitrobenzene respectively. The convergence threshold for total energy was set to 10^{-8} eV and the

force threshold was set to 10^{-3} eV/Å. Each geometric optimization was followed by harmonic frequency computations in order to confirm the stationary character of the state obtained. In order to test the accuracy of our computational approach, we have optimized the anionic states in addition to the neutral and cationic states of both 3-NT and 4-NT. The ground state of the neutral 4-NT molecule was found to be lower in total energy than the ground state of neutral 3- NT by 0.018 eV. This difference comes from only electronic total energies since the zero-point vibrational energies match each other within 0.001 eV. The ionization energies computed as the difference in total energies of the cation and its neutral parent at the equilibrium geometry of the neutral are rather close to each other; namely, 9.60 eV and 9.48 for 4-NT and 3-NT which compare well with the experimental values of 9.54 eV[131] and 9.48 eV,[132] respectively. The ionization energy computed for NB thus 9.28 eV was a little lower compared to 4-NT and 3-NT. Our computed electron affinities of the para- and meta-isomers of 1.04 eV and 1.09 eV practically match the experimental values of 0.932 ± 0.087 eV[133] and 0.99 ± 0.10 eV,[134] respectively, within the experimental uncertainty bars. In view of close agreement of our computed values with experiments, one can expect the B3LYP/Def2-TZVPP approach to be accurate in the same extent when computing other properties of the nitrotoluene isomers.

5.4 Experimental Results

5.4.1 Time-resolved mass spectra and transient ion signals

Figures 5.5 (a) and 5.5 (b) display the mass spectra of 4- NT and 3-NT taken with pump intensity 8 x 10^{13} W cm^{-2} and probe intensity 1 x 10^{13} W cm^{-2} at pump-probe delays τ = -200 fs (purple) and τ = +4000 fs (green). The mass spectra are normalized to the respective parent ion yields at τ = -200 fs (probe precedes pump). In this situation, all ions are generated solely from the pump because the probe intensity is well below the ionization threshold and the parent molecular ion is the most intense peak for both 3-NT and 4-NT. The predominant formation of parent molecular ions is consistent with previous studies on other molecules under adiabatic ionization conditions.[38–40,44–46,48–51,135–137] For both 3-NT and 4-NT at τ = +4000 fs, the parent ion signal is depleted and the $C_7H_7^+$ ion signal is enhanced, indicating that the weak field probe pulse is capable of exciting ions generated by the pump to form $C_7H_7^+$ through the cleavage of the C–NO$_2$ bond. Because the most significant changes in ion yields due to the probe pulse affect the parent ion and $C_7H_7^+$, we will focus on the dynamics of these two ions. Other fragments are visible in the spectra, including $C_7H_7O^+$, formed from the parent ion via nitro-nitrite rearrangement, and $C_5H_5^+$, formed from the dissociation of $C_7H_7^+$.[131] NO_2^+ and NO^+ in both molecules are formed via Coulomb explosion of a multiply charged precursor based on the split peaks marked with a * in the mass spectra.[138]
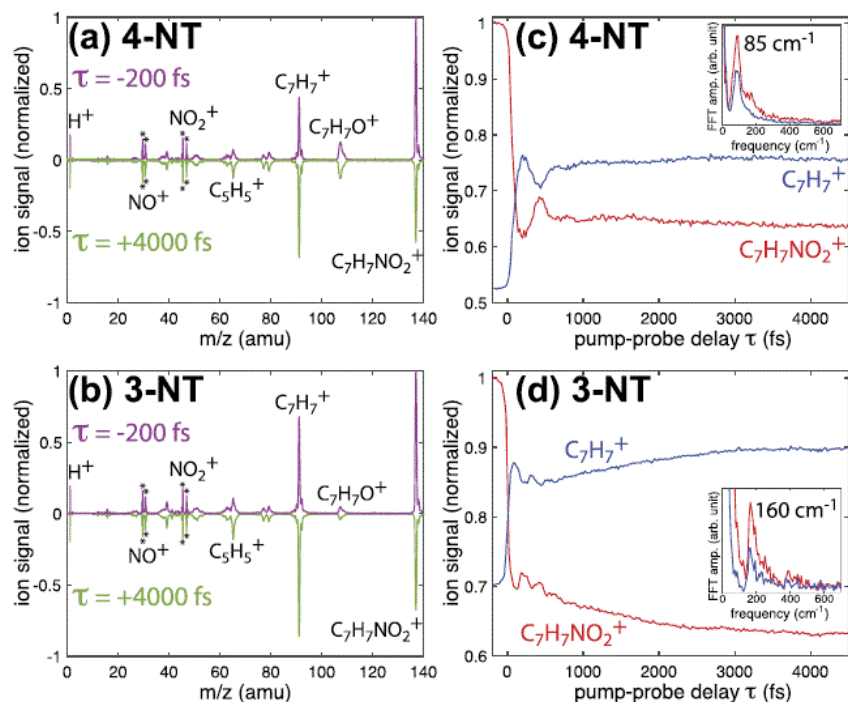
Figure 5.5. Mass spectra of (a) 4-NT and (b) 3-NT taken at pump-probe delays τ = -200 fs in (purple) and τ = +4000 fs (green). Transcient ion yields of parent molecular ion (red) and $C_7H_7^+$ (blue) in (c) 4-NT and (d) 3-NT as a function of pump-probe delay. Inset: FFT of the transient signals showing the oscillation frequencies.

The transient ion signals of the parent ion $C_7H_7NO_2^+$ (red) and $C_7H_7^+$ (blue) as a function of pump-probe delay τ are shown in Figure 5.5 (c) and 5.5 (d) for 4-NT and 3-NT, respectively. Ion signals in each molecule are normalized to the parent ion yield at τ = -200 fs. While there is a significant depletion of the parent and an increase $C_7H_7^+$ at $\tau > 0$ in both molecules, the transient dynamics of these species are quite distinct. Out-of-phase oscillations of the parent and $C_7H_7^+$ ion signals are visible in each molecule, suggesting (1) that coherent vibrational motions are excited upon ionization of both 4-NT and 3-NT and (2) that $C_7H_7^+$ is formed via excitation with the probe pulse to an excited electronic state in the $C_7H_7NO_2^+$ ion.[39,40,44,47,59,91–94,137] Performing a fast Fourier transform (FFT) on the transient signals produced well-resolved peaks at approximately

85 cm^{-1} and 160 cm^{-1} for 4-NT and 3-NT, respectively [insets of Figures 5.5 (c) and 5.5 (d)]. The transient signals remain unchanged at $\tau >$ 1500 fs for 4-NT and $\tau > +4000$ fs for 3-NT, indicating no further dynamics.
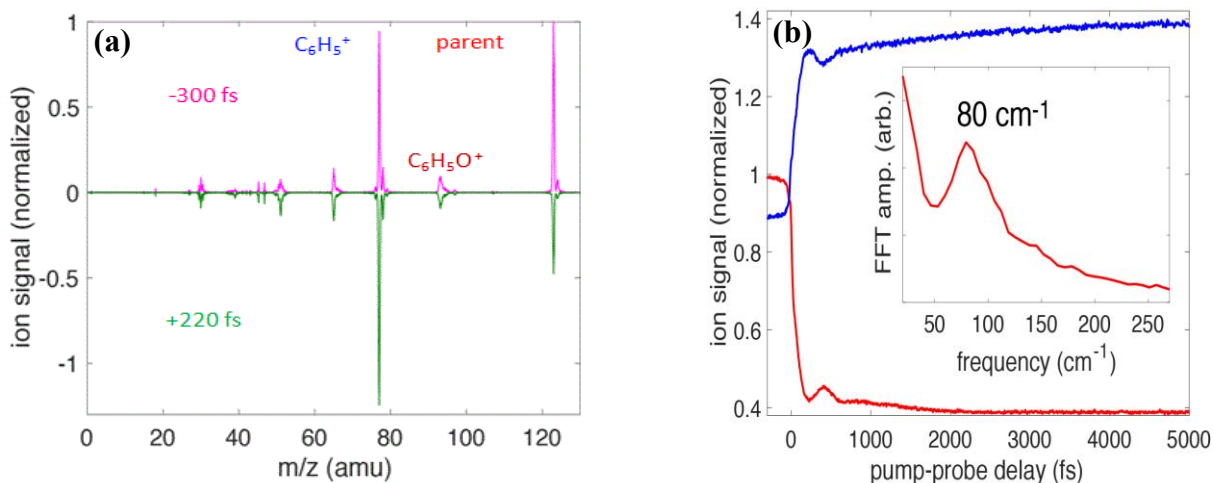
Figure 5.6. (a) Mass spectrum of nitrobenzene from pump probe delay in $\tau =$ -300 fs and +220 fs. (b) Transient ion signals of parent in red and $C_6H_5^+$ in blue with the frequency as the inset.

The mass spectrum of nitrobenzene is shown in Figure 5.6 (a). The ions were generated from 1500 nm pump and 800 nm probe, with intensities 2 x 10^{14} and 5 x 10^{12} W cm^{-2} respectively. Since the probe intensity is below the ionization threshold, all fragments observed are generated by the pump. The upper panel in pink shows fragments in the negative delay ($\tau =$ -300 fs), where the probe precedes the pump. The parent ion is observed to be the base peak, and other fragments such as $C_6H_5^+$ with the cleavage of NO_2 and $C_6H_5O^+$ with the loss of NO is also observed. The lower panel in green shows a different spectrum with the positive delay ($\tau = + 220$ fs) as the pump precedes the probe. The parent ion depleted significantly with a corresponding enhancement of the $C_6H_5^+$ indicating a weak field of the 800 nm probe capable of exciting ions generated by the pump

via the C-NO$_2$ cleavage. From the mass spectrum it can be observed that no relative change was observed in C$_6$H$_5$O$^+$ signal.

Figure 5.6 (b) shows transient ion signals for the parent ion in red and C$_6$H$_5$$^+$ in blue. The ion signal of C$_6$H$_5$$^+$ is normalized to the parent yield at -200 fs delay. The signal as a function of pump probe delay was taken from -500 fs to 5000 fs with 10 fs steps. Depletion in the parent ion and an increase in C$_6$H$_5$$^+$ at $\tau < 0$ can be observed. The oscillation in both transient ion signals are antiphase with respect to each other, which suggests a vibrational wave packet excitation and an excitation by the probe pulse. A Fast Fourier Transformation (FFT) on the parent oscillation reveals a frequency of 80 cm^{-1} (inset Figure 5.6). No further dynamics were observed as the transient ion signals of both ions remained unchanged at $\tau > +2500$.

5.4.2 Analysis of the oscillatory motions for 4-NT and 3-NT

To gain further insight into the oscillatory dynamics observed in 4-NT, 3-NT, the transient ion signals for the parent ion and C$_7$H$_7$$^+$ at $\tau > 40$ fs (i.e., after the pump pulse is over) were fit using nonlinear least square methods to the following equations:

$$S_{4-NT}(\tau) = a \exp\left(-\frac{\tau}{T}\right)\left[\sin\left(\frac{2\pi\tau}{t} + \varphi\right) + b\right] + c \tag{5.2}$$

$$S_{3-NT}(\tau) = a \exp\left(-\frac{\tau}{T1}\right)\left[\sin\left(\frac{2\pi\tau}{t} + \varphi\right) + b\right] + c + d \exp\left(-\frac{\tau}{T2}\right) \tag{5.3}$$

where a denotes the oscillation amplitude, T and T_1 denote the coherent lifetime in 4-NT [eq 5.2] and 3-NT [eq 5.3], respectively, t denotes the oscillation period, and φ denotes the phase. For all molecules, the constant b corresponds to an incoherent contribution to the exponential decay and c corresponds to the final yield as $\tau \to \infty$. The transient signals for 3-NT require a second

exponential decay term with amplitude d indicating lifetime T_2 [eq 5.3] to account for the slow decay until $\tau \sim 5000$ fs.
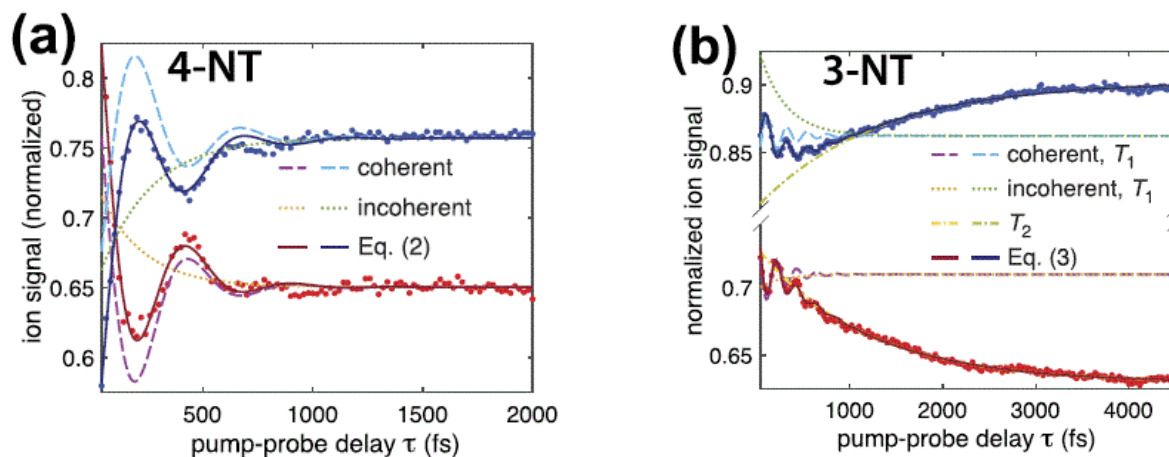
Figure 5.7. Normalized transient ion yields of parent molecular ion (red) and $C_7H_7^+$ (blue) with curve fitting component for 4-NT (a) and 3-NT (b), respectively.

Figure 5.7 shows the fit results for the transient parent and $C_7H_7^+$ ion signals in 4-NT (a) and 3-NT (b) from Figure 5.5. Experimental data points are shown as red (parent) and blue ($C_7H_7^+$) dots, and the fit functions to eq 5.2 and 5.3 for 4-NT and 3-NT as solid lines. The coherent portions of the respective fit functions are shown as magenta and light blue dashed lines for the parent and $C_7H_7^+$ ions, and the incoherent portions shown as orange and green dotted lines, respectively. The second exponential contribution in eq 5.3 for 3-NT is shown as light and dark yellow dash-dot lines for the parent and $C_7H_7^+$ ions in Figure 5.7(b).

To fully characterize the excitation leading to the cleavage of the $C–NO_2$ bond, pump-probe measurements were performed on both molecules at a series of probe intensities from approximately 2 x 10^{12} to 2 x 10^{13} W cm^{-2} and fit to eq 5.2 or 5.3. Figure 5.8 shows the probe intensity series.
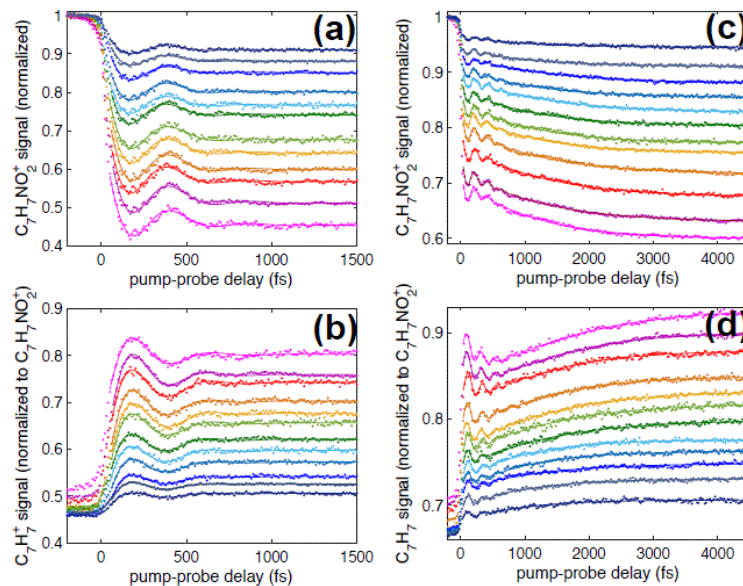
Figure 5.8. Transient ion signals of 4-nitrotoluene (left) and 3-nitrotoluene (right) displaying the measured transient ion signals (normalized to the parent ion yield at negative time delays) for the parent molecular ion (top) and $C_7H_7^+$ (bottom) for 4-nitrotoluene (left) and 3-nitrotoluene (right). The dots denote experimental data and the solid lines denote fits to eq (5.2) and (5.3) for 4-nitrotoluene and 3-nitrotoluene, respectively.

For both molecules, the following fit parameters were found to be independent of the probe intensity: coherent and incoherent lifetimes, oscillation periods, and phase (summarized in Table 5.1; all fit parameters to the data in Figure 5.8, Tables are presented in appendix B1–B4). The consistent dynamical time scales and phase difference of approximately π radians between the parent and $C_7H_7^+$ ions indicate that the same excitation processes occur over this range of probe intensities.

Table 5.1. Dynamical time scales and phase obtained by fitting the transient ion signals to Equation 2 and 3. Errors denote the standard deviation of the fitted coefficient value over the 12 measured probe powers.

Molecule	Species	T(fs)	T_1 (fs)	T_2 (fs)	t (fs)	$\emptyset$
4-NT	Parent	210±10			480±20	2.2±0.1
	$C_7H_7^+$	200±10			460±10	5.2±0.1
3-NT	Parent		220±20	1100±100	216±3	1.4±0.2
	$C_7H_7^+$		220±40	1200±200	220±3	4.5±0.2

The amplitude coefficients corresponding to coherent dynamics [a in eq (5.2) and (5.3)] and slow time decay [d in eq (5.3)] were observed to grow with increasing probe intensity. Figures 5.9 (a) and 5.9 (b) show the magnitude of the amplitude coefficients for the parent molecular ions of 4-NT and 3-NT, respectively, as a function of probe intensity. The analogous coefficients for the $C_7H_7^+$ ions are shown in Figure 5.9 (c) and 5.9 (d).
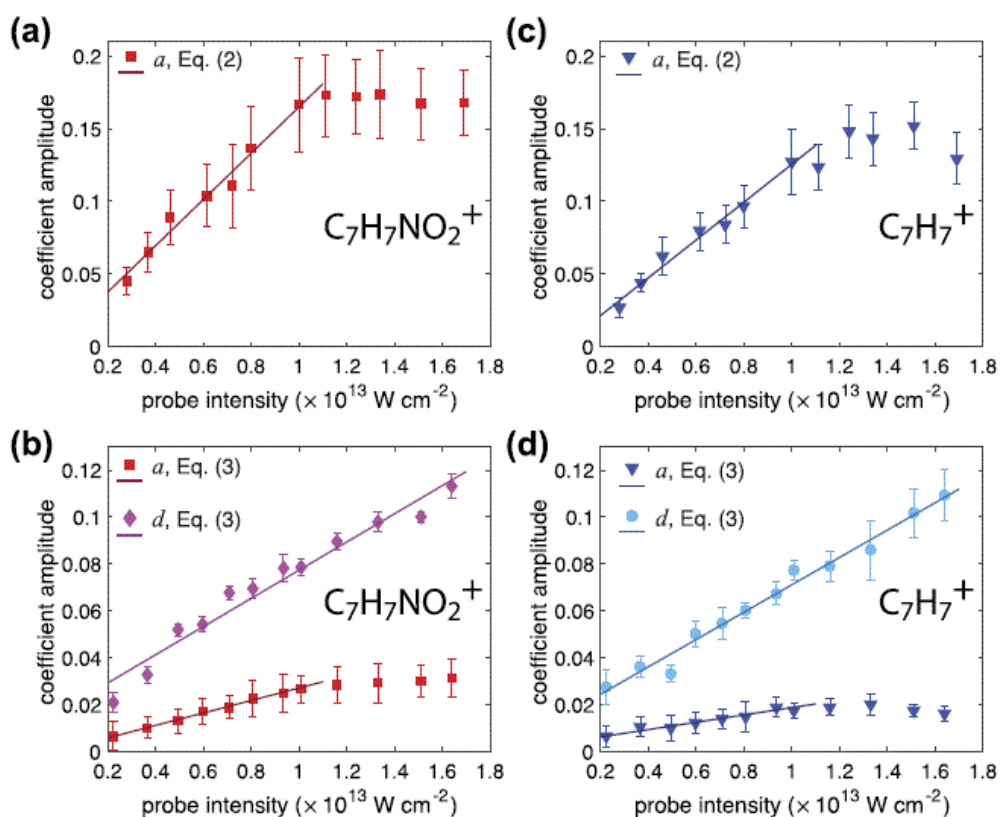
Figure 5.9. Amplitude coefficients for the parent molecular ion as a function of probe intensity in 4-NT (a) and 3-NT (b). Amplitude coefficients for the $C_7H_7^+$ ion as a function of probe intensity in 4- NT (c) and 3-NT (d), respectively. Error bars denote 95% confidence intervals.

For all transients, the amplitude coefficients grow linearly with the probe intensity, as shown by the least squares fit lines. This linear growth indicates a one-photon excitation process, resulting in C–NO$_2$ bond cleavage. A one-photon excitation was also found to lead to methyl loss in acetophenone radical cations.[39] While the a coefficients for each transient ion saturate at probe intensities above $\sim 10^{13}$ W cm^{-2}, the d coefficient in eq (5.3) for 3-NT continues to grow [magenta and light blue data, Figures 5.9 (b) and (d)]. This different behavior in the short- and long-time dynamics of 3-NT suggests that two distinct excitations may contribute to NO$_2$ loss in 3-NT.

The dynamics of homolysis in 4-NT were investigated further by using various combinations of pump and probe wavelengths as shown in Figure 5.10. The pump wavelengths were taken from the range of 1300 nm (light yellow) to 1600 nm (deep red) with the probe 650 nm (green) and 800 nm (deep blue). All the transient ion signals were normalized to the parent at unity.
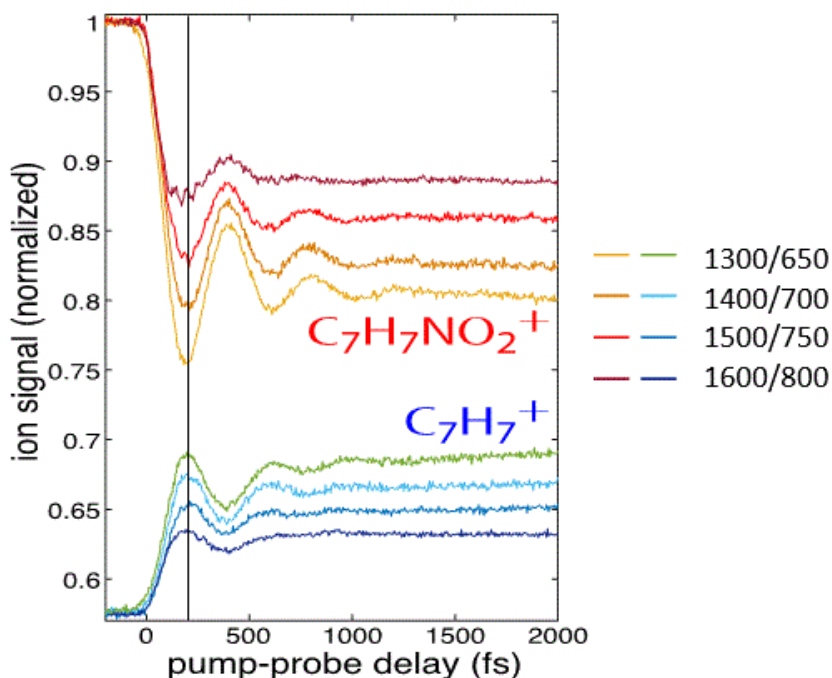
Figure 5.10. Homolysis of 4-NT using various wavelengths of pump and probe.

It can be observed that the amplitude of the oscillation in both the parent ion and $C_7H_7^+$ decreased with pump/probe wavelength combination from 1300/650 nm to 1600/800 nm as shown with the black solid line. Even though different pump wavelengths were used, the dynamics of the parent ions did not change as was established in our recent publication.[40] Therefore, the probe wavelength must be responsible for the dynamics observed. At $\tau = 200$ fs an enhancement in oscillation of 1300/650 nm wavelength combination can be observed, which indicates strong coupling to the excited state responsible for $C_7H_7^+$ ion formation. This means that the photon energy of 650 nm (1.9 eV) is more capable of accessing the excited state responsible for the homolysis in 4-NT compared to the other wavelengths.

5.4.3 Analysis of the oscillatory motions for Nitrobenzene
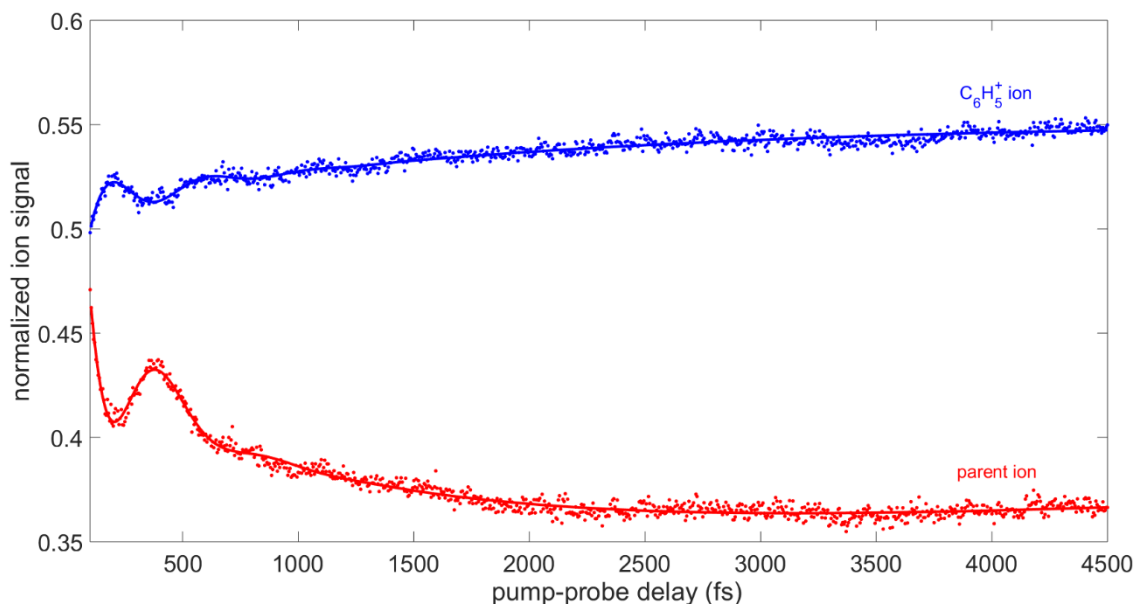
Figure 5.11. Transient ion signal of NB showing the parent ion and the $C_6H_5^+$. Experimental data for the parent ion and $C_6H_5^+$ is shown with red and blue dots respectively with its respective fitting in solid line.

The transient ion signals fitted to eq 5.4 for the parent and $C_6H_5^+$ of NB are shown in Figure 5.11.

$$S_{NB}(\tau) = a \exp\left(\frac{\tau}{T_1}\right)\left[\sin\left(\frac{2\pi\tau}{t} + \varphi\right)\right] + b + c \exp\left(-\frac{\tau}{T_2}\right) \tag{5.4}$$

In eq 5.4, a denotes the oscillation amplitude, T_1 denotes the coherent lifetime in NB, t denotes the oscillation period, and φ denotes the phase, b corresponds to the final yield as $\tau \to \infty$. The transient signals for NB require a second exponential decay term with amplitude c and a longtime decay constant T_2 [eq 5.4] to account for the slow decay until $\tau \sim 5000$ fs.

The data points are shown in red (parent) and blue ($C_6H_5^+$) dots with the fit function in solid lines. The results obtained (Table 5.2) indicate that the oscillation period of both ions is different, with the parent and $C_6H_5^+$ having 440 fs and 355 fs respectively. The difference in the phase of both oscillations is 2.3 radians, meaning similar fragments could have also been made during the ionization process. This means a probe excitation is needed to induce the formation of $C_6H_5^+$. Both ions exhibit similar coherent decay lifetime constants with 159 and 118 fs for parent and $C_6H_5^+$ respectively, even though the parent ion has a slightly longer decay compared to that of the $C_6H_5^+$. Because of the slow decay, a third term is needed to fit the function, $C_6H_5^+$, which is indicated by a long-time scale of 1739 fs.

Table 5. 2. Dynamical time scales and phase obtained by fitting the transient ion signals of NB to equation 5.4.

Molecule	Species	T_1(fs)	T_2 (fs)	t (fs)	$\emptyset$
NB	Parent	159±50	580±200	440±20	0.0±0.1
	$C_6H_5^+$	118±50	1739±100	355±10	2.3±0.1

4.4.3 Theoretical Results
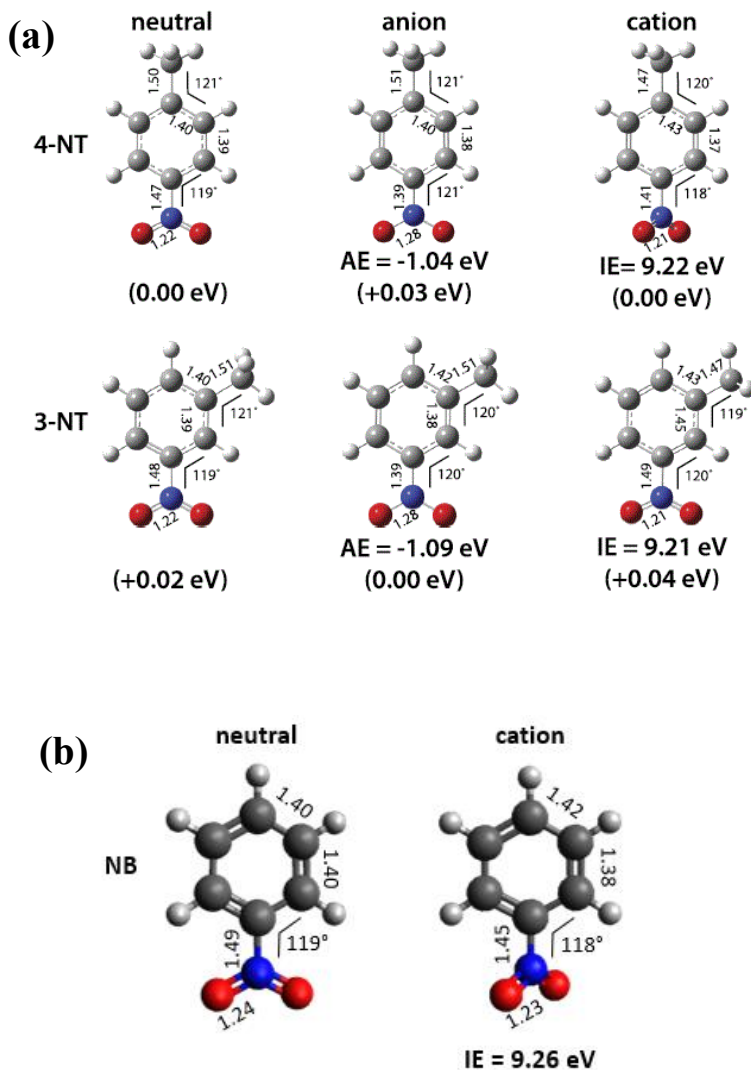
Figure 5.12. (a) Optimized geometrical structures of neutral and singly charged isomers of nitrotoluene. (b) Optimized geometric structure of neutral and cation of nitrobenzene. Bond lengths are in Å and angles in degrees. EA: adiabatic electron affinity; IE: adiabatic ionization energy. Numbers in parentheses denote relative energies between isomers in each charge state.

Our optimized structures of neutral and charged 3-NT and 4-NT isomers are displayed in Figure 5.12. Structural experimental data have been obtained for 4-NT crystals,[139] and the measured bond distances agree with our computed values for neutral 4-NT to within ~0.02 Å. As

can be seen in the Figure 5.12, the differences in total energy between the two NT isomers are quite small independent of charge, and the largest difference of 0.04 eV belongs to the cation pair. Attachment of an extra electron leads to a significant change in the geometry of the NO_2 group in both 3-NT and 4-NT anions compared to the geometries of their neutral parents as evident in the shortened C–N bonds and lengthened N–O bonds (Tables B5 and B6 in the appendix). Electron attachment also makes 3-NT lower in total energy than 4-NT by 0.03 eV. According to the results of Mulliken analysis, there are 0.6 extra electrons localized over the NO_2 group in both $C_7H_7NO_2^-$ anions (Tables B7 and B8 in appendix).

Electron detachment changes the bond lengths in the C6 rings of both isomers (Figure 5.12) and the ring carries about 0.75 e excessive charge in the 4-NT cation and nearly 0.9 e in the 3- NT cation (Tables B7 and B8 in appendix). Since electron detachment from the neutral 3-NT does not lead to a change in the geometrical topology, there is no energy barrier for a transition from the neutral geometry to the optimal cation geometry. However, this is not the case for the neutral 4-NT, where electron detachment results in the NO_2 plane rotating by 52.5° relative to the plane of the phenyl ring. In order to find the pathway from the neutral geometry to the cation geometry, we applied the QST2 approach and found that the pathway proceeds via two transition states as shown in Figure 5.13.
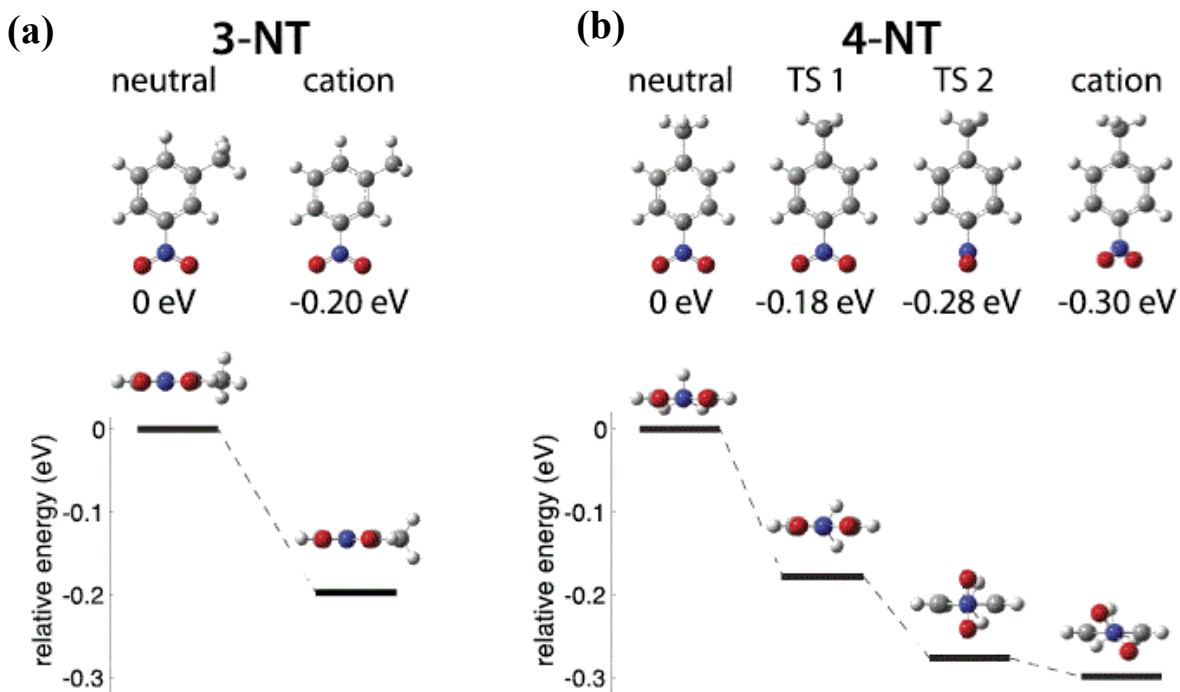
Figure 5.13. The relaxation pathways and energies for the transitions from the neutral geometry to the cation geometries in 3-NT (a) and 4-NT (right).

Because the observed oscillations in the 4-NT and 3-NT ion yields arise from coherent vibrational motions in the parent radical cations,[39,40,44,47,59,91–94,137] it is of interest to determine the vibrational modes in both molecules. The frequencies and intensities of the vibrational modes in both the neutral molecules and their cations were calculated via normal mode analysis. In order to improve comparison with experiments, we have computed third-order anharmonic corrections to the harmonic frequencies of the neutral and cationic 4-NT and 3-NT isomers, whereas the intensities were taken from the harmonic frequency computations. To benchmark the calculated frequencies and intensities, the predicted infrared spectra for the neutral molecules were compared to experimental spectra obtained from NIST[140] (Figure 5.14).
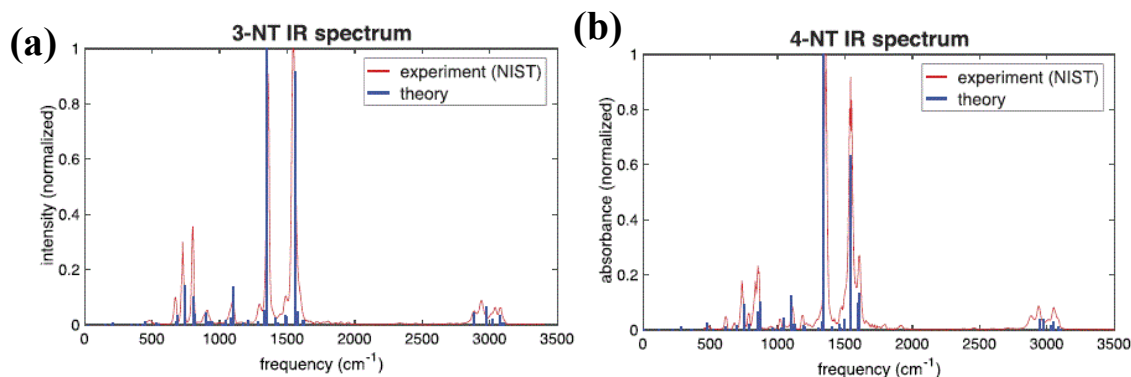
Figure 5.14. Experimental and computed IR spectra for 3-NT (a) and 4-NT (b).

The calculated anharmonic frequencies match the experimental peaks to within 15 cm^{-1} over the frequency range ~1000–1600 cm^{-1} and within 25 cm^{-1} at lower frequencies, indicating the effectiveness of the method and suggesting that the computed cation frequencies should be reasonably accurate. However, adding anharmonic corrections can lead to imaginary (negative) anharmonic frequencies, which is observed for the lowest frequency mode corresponding to the nearly free rotation of the CH$_3$ group. Full tabulated results of the harmonic and anharmonic vibrational frequencies in the neutral molecules and cations are presented in Tables B9 and B10 in the appendix.

5.4. Discussion

5.4.1 Assignment of coherently excited normal modes for 4-NT, 3-NT and Nitrobenzene

Comparison of the computed relaxation pathways and vibrational frequencies to the observed coherent oscillations in 4-NT, 3-NT and NB radical cations allows for the determination of the coherent nuclear motions excited upon ionization. Based on the experimental observation of oscillations at 85 cm^{-1} (based on FFT analysis) or 460-480 fs (69-73 cm^{-1}, based on curve-fitting) in 4-NT and 80 cm^{-1} or 475-490 fs (68-70 cm^{-1}) in NB and the optimal minimum value at

52.5° (Figure 5.15) and 53.5° (Figure 5.16) respectively, the rotation in the C–C–N–O torsional angle upon electron detachment is most likely that the NO_2 torsional mode is excited. The observed frequency is in reasonable agreement with the computed oscillation frequencies in this mode of 59.8 cm^{-1} in the neutral and 46.1 cm^{-1} in the ion. To confirm that the NO_2 torsional mode is responsible for the observed coherent oscillations, the potential energy curves along the NO_2 dihedral angle were computed as a function of the NO_2 dihedral angle with steps of 5° and 10°. Figure 5.15 and 5.16 shows the potential energy curves along the NO_2 dihedral angle from 3-NT (red), 4-NT (blue) and NB respectively.
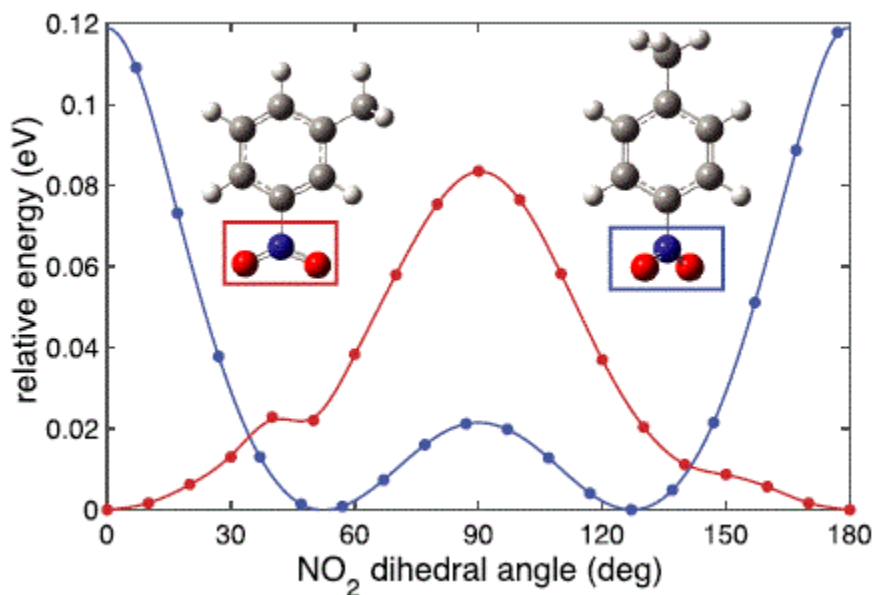
Figure 5.15. Potential energy curves along the C–C–N–O dihedral angle for 4-NT (blue) and 3-NT (red).
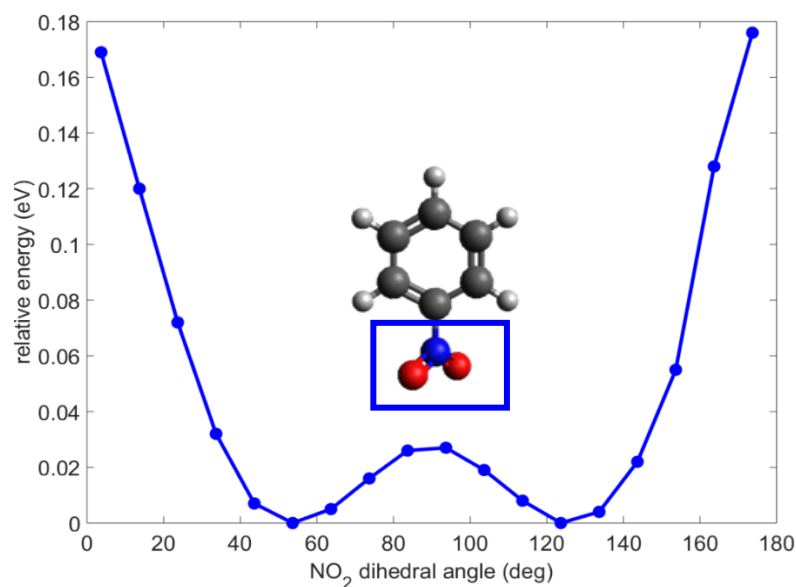
Figure 5.16. Potential energy curves along the C–C–N–O dihedral angle for NB.

As expected, the potential energy decreases by 0.12 eV in 4-NT and 0.18 eV in NB as the NO$_2$ group rotates away from 0° to its optimal value at 52.5° and 53.5 respectively. The global maximum at 0° and local minimum at 90° correspond to TS 1 and TS 2, respectively, of the relaxation pathway in Figure 5.13, which is suspected to also be exhibited by NB (based on its similar PES in Figure 5.16). It is of interest to note that the shape of the 4-NT and NB potential energy curve along the NO$_2$ dihedral angle possesses a remarkable similarity to that of the analogous curve along the COCH$_3$ dihedral angle in acetophenone, which has a local minimum at 90° and global maxima at 0° and 180°.[39,44]

In contrast to the 4-NT and NB cases, the potential energy in the 3-NT radical cation increases as the NO$_2$ group is rotated away from 0° (red curve, Figure 5.15), indicating that the NO$_2$ torsional mode cannot account for the observed oscillations in 3-NT. This result is consistent

with the 160 cm^{-1} oscillations observed in the 3-NT ion yields because the NO$_2$ torsional mode would be expected at 29 cm^{-1} in the neutral and 40 cm^{-1} in the cation according to our computational results (Table B10 in the appendix). Instead, we consider a group of three normal modes with computed frequencies in the range of 158-207 cm^{-1} in the neutral and 143-202 cm^{-1} in the cation (Table B10 in appendix) to account for the 160 cm^{-1} oscillations. These modes correspond to the low frequency bending motions shown in Figure 5.16. Because modes **A** and **B** correspond to out-of-plane bending motions in the benzene ring, neither is likely to be excited in our experiments because the benzene ring does not change from its planar geometry upon ionization (Figures 5.12 and 5.13). Thus, we suggest that mode **C** corresponding to the in-plane bending motion of the NO$_2$ and CH$_3$ moieties gives rise to the observed oscillations.

This mode assignment is supported by the changes in bond lengths and angles involving the benzene ring, NO$_2$, and CH$_3$ groups in 3-NT when going from the neutral to cation geometry (Figure 5.12). The coherent excitation of a torsional motion in ionized 4-NT may be expected because coherent torsional mode excitation has been observed in a number of molecules including acetophenone and its derivatives,[39,44,93,94] 1,3-dibromopropane,[92] and azobenzene.[91,137] The lack of torsional mode excitation in 3-NT upon ionization also resembles the case of 3-methylacetophenone, where no coherent oscillations were observed.[94] The authors attributed the lack of oscillations in 3-methylacetophenone to the increase in the potential energy upon rotation of the acetyl group away from the planar geometry, which is similar to the potential energy curve in 3-NT (Figure 5.15). Unlike the latter results, we do see coherent oscillations in the 3-NT ion yields from excitation of the in-plane bending mode **C** shown in Figure 5.17. We attribute this ability to resolve such small-amplitude oscillations to the use of a 1500 nm pump wavelength that ensures adiabatic ionization and predominant population of the ground state molecular ion.[40,44,50,51]
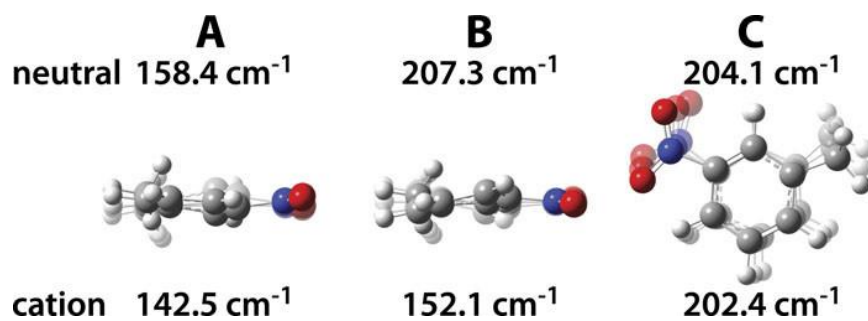
Figure 5.17. Low frequency bending motions in 3-NT.

5.4.4.2 Dynamical time scales in 3-NT, 4-NT and NB

The oscillations in 3-NT, 4-NT and NB decay with similar time constants of 220 fs, 200 fs, and 159 fs respectively. This short coherence lifetime stands in contrast to the longer coherent lifetimes of torsional wave packets in acetophenone (560-600 fs)[39,44] and azobenzene (880-1000 fs).[137] Unlike the latter molecules, which are not known to undergo rearrangement reactions, the nitro group can undergo the nitro-nitrite rearrangement (NNR) reaction (NO2 → ONO). This rearrangement would change the topology of the molecule and thus be expected to destroy the initially excited coherent nuclear motion. The observation of $C_7H_7O^+$ arising from NO loss following NNR in our mass spectra (Figure 5.5) indicates that NNR takes place in the 4-NT, 3-NT and NB radical cations, so this rearrangement may be expected to cause the faster decoherence as compared to other aromatic molecules. However, the $C_7H_7O^+$ transient dynamics (Figure 5.18) suggest that NNR does not drive the fast decoherence in either 4-NT or 3-NT. If the NNR reaction were the primary cause of decoherence, an exponentially increasing yield of $C_7H_7O^+$ with a similar time constant of ~200 fs as the wavepacket decay time constant would be expected. Instead, the

$C_7H_7O^+$ transients in NB and 4-NT (which both have similar dynamics) has completely different

dynamics from 3-NT from the respective parent molecular ions and $C_7H_7^+$ fragments.
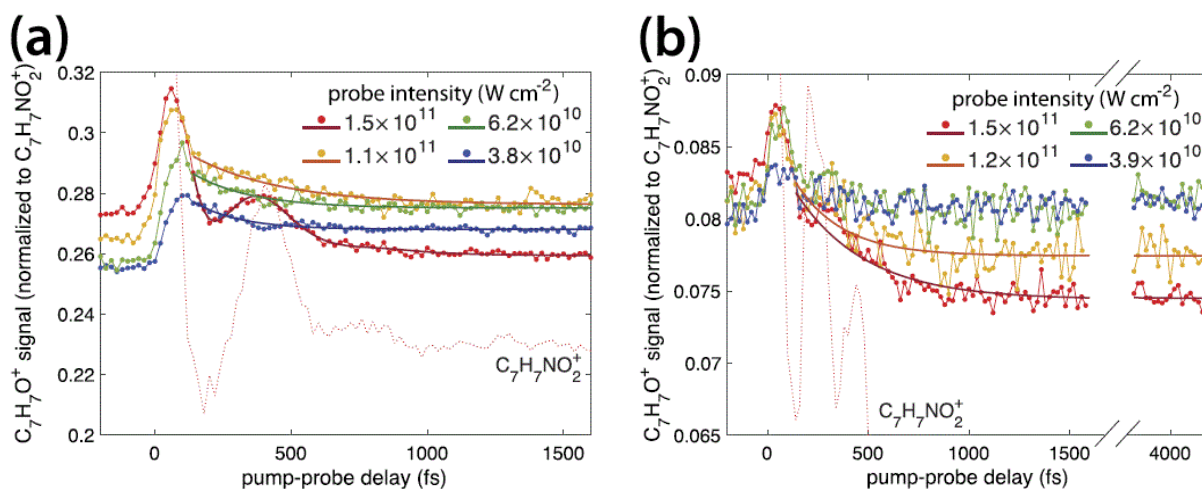
Figure 5.18. Transient ion signals of $C_7H_7O^+$ in (a) 4-NT and (b) 3-NT at selected probe intensities (dots), indicated by different colors in the figure. Fit functions to Eq. (3) or a decaying exponential are shown as solid lines. The signals in 3-NT at intensities below 10^{13} W cm^{-2} were too noisy for curve fitting. The transient signal of the parent molecular ion is shown as the dotted line.

While parent and $C_7H_7^+$ dynamics are the same at all probe intensities in a given isomer (Figure 5.8), the $C_7H_7O^+$ dynamics in all molecule isomers are sensitive to the probe intensity. At intensities above 6 x 10^{12} W cm^{-2}, NB, 4-NT and 3- NT produce a spike in $C_7H_7O^+$ yield approximately 60-80 fs after the ionization event, followed by exponential decay of the signal with time constants ranging from 170 to 350 fs (solid lines in Figure 5.17 fit coefficients given in Tables 5.3 and 5.3).

The $C_7H_7O^+$ transient in 4-NT was fit to eq 5.2 at probe intensity of 1.5 x 10^{13} W/cm^2:

Table 5.3. Fitting parameters for $C_7H_7O^+$ in 4-NT to eq 5.2.

I (W/cm2)	a	T_1(fs)	t (fs)	b	c	$\emptyset$
1.5 x 10^{13}	0.007$\pm$0.006	210$\pm$0.04	220$\pm$0.03	-0.3$\pm$0.8	0.945	1.2$\pm$0.1

For 4-NT at lower probe powers intensity and higher probe intensity for 3-NT, the transient ions were fit to an exponential decay which are represented in Table 5.4.

$$S(\tau) = a \exp\left(\frac{\tau}{T}\right) + c \tag{5.5}$$

Table 5.4. Fitting parameters for $C_7H_7O^+$ to eq 5.5.

Molecule	I (W/cm^2)	a	T (fs)	c
3-NT	1.5 x 10^{13}	0.011$\pm$0.002	350$\pm$40	0.0744$\pm$0.0001
3-NT	1.2 x 10^{13}	0.009$\pm$0.004	240$\pm$90	0.0769$\pm$0.0002
4-NT	1.1 x 10^{13}	0.024$\pm$0.004	330$\pm$80	0.276$\pm$0.002
4-NT	6.2 x 10^{12}	0.022$\pm$0.006	220$\pm$50	0.275$\pm$0.001
4-NT	3.8 x 10^{12}	0.021$\pm$0.005	170$\pm$30	0.268$\pm$0.001

These results suggest that excitation of 4-NT and 3-NT radical cations at short time delays can facilitate the NNR reaction and that the excitation probability quickly decreases at longer time-delays. In 4-NT and NB, the $C_7H_7O^+$ transient exhibits similar oscillatory dynamics in phase with the parent molecular ion at a high probe intensity of 1.5 x 10^{13} W cm^{-2}, as seen in the fit function of eq 5.2 and 5.4 (solid red line) respectively, indicating that the NNR reaction can also take place on the ground electronic state of the 4-NT cation. However, the lack of these dynamics at lower probe intensities when using 800 nm suggests that spontaneous rearrangement on the ground state is not the primary NNR pathway in 4-NT.
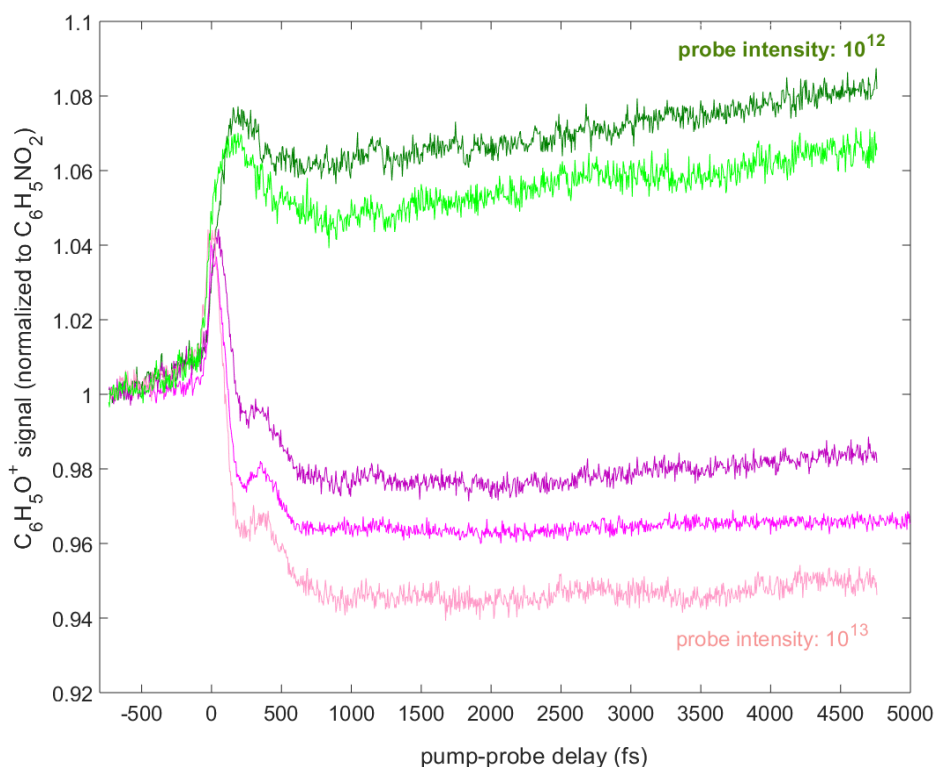
Figure 5.19. Normalized transient ion signal of $C_6H_5O^+$ with various intensities using 800 nm.

The dynamics exhibited by NB with various intensities strikes a similar resemblance to 4-NT with 800 nm as probe. In Figure 5.19 it was observed that at higher intensities (purple) the NNR formation is facilitated at short times and decreases rapidly with time. The dynamics when compared to the parent ion are in-phase. At lower intensities, the NNR is greatly enhanced and its dynamics are similar to $C_6H_5^+$.

The 650 nm wavelength emphasizes the distinct dynamics at high and low probe intensities in 4-NT. Figure 5.20 shows the transient oscillations for a series of probe intensities. At higher intensities (red line, 8 x 10^{12} Wcm^{-2}) the transient ion signal is in-phase with the parent ion (red dots), suggesting a spontaneous formation on the ground state with no probe excitation.
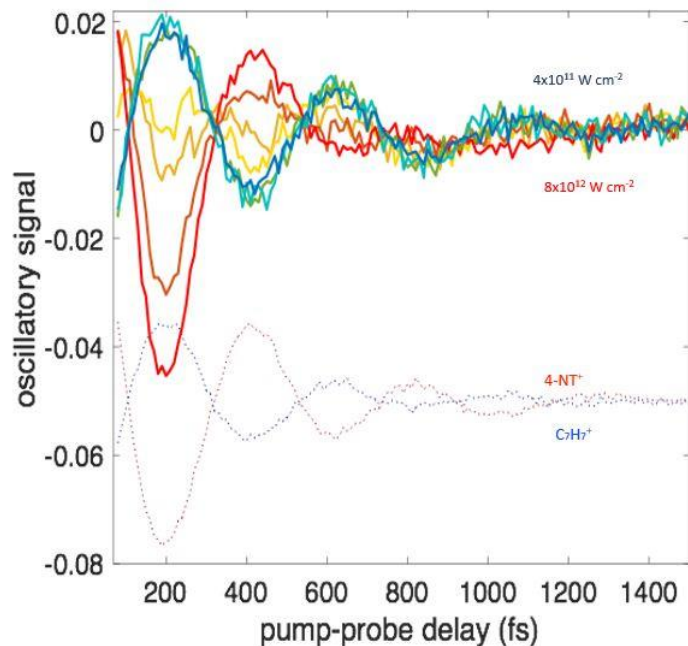
Figure 5.20. Transient ion signals of $C_7H_7O^+$ for 4-NT at various 650 nm probe intensities indicated by different colors. Parent (red) and $C_7H_7^+$(blue) ion signals are indicated on the graph with dots.

At lower intensities (green line, 4 x 10^{11} Wcm^{-2}) the transient ion signal is out-of-phase with the parent and in phase with the $C_7H_7^+$ (blue dots), indicating that NNR occurs after probe excitation. The phenomena are still under study, however two transitions states were found with the Def2-TZVPP [(11s6p2d1f)/5s3p2d1f] basis set and the B3LYP method of theory, which suggests two different reaction pathways may be responsible as indicated in Figure 5.21.
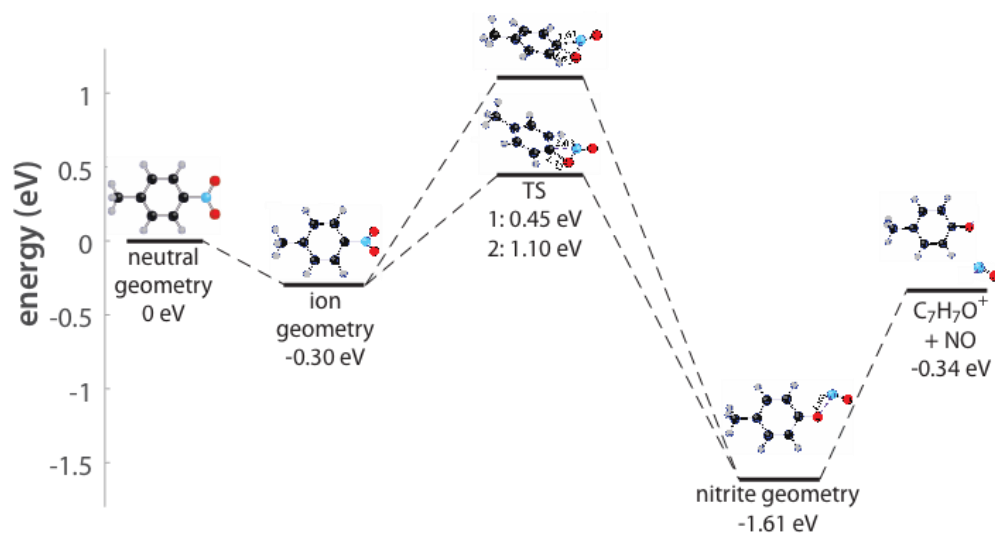
Figure 5.21. Energy level diagram depicting formation of NNR in PNT.

The complex dynamics of the $C_7H_7O^+$ ion in NB, 4-NT and 3-NT suggest that multiple pathways involving NNR exist in the respective radical cations separately from the coherent excitation pathways leading to $C–NO_2$ bond cleavage. Furthermore, the incoherent 1.1 ps decay of the parent ion yield and increase of the $C_7H_7^+$ yield in 3-NT suggests that an additional dynamical relaxation process facilitates the excitation, leading to $C–NO_2$ bond cleavage in 3-NT radical cations, while the analogous process is absent in 4-NT. The observation that the amplitude coefficient associated with the slow decay in 3-NT continues to grow at high probe powers where the amplitude coefficient associated with the coherent excitation is saturated suggests that two different excitation processes, possibly involving distinct excited states, may form $C_7H_7^+$ in 3-NT. Determination of all pathways leading to both NNR and $C–NO_2$ cleavage will require high-level quantum chemical calculations of both the ground and excited state potential energy surfaces along the relevant reaction coordinates. We plan to perform these and other calculations in order to gain a greater understanding of the excitation and dissociation mechanisms involved.

5.5 Conclusion

The ultrafast dynamics of nitrobenzene, 3- and 4-nitrotoluene radical cations were investigated with femtosecond pump-probe measurements and high-level DFT calculations. Oscillations in the parent and $C_7H_7^+$ ion yields with pump-probe delay arising from coherent vibrational excitations were present in all molecules, with similar coherent lifetimes of approximately 200 fs. The distinct oscillation periods of 159 fs, 470 fs and 216 fs in NB, 4-NT and 3-NT, respectively, were attributed to the excitation of the NO_2 torsional mode in NB and 4-NT, and an in-plane bending mode involving the NO_2 and CH_3 moieties in 3-NT. These normal mode assignments were supported by a series of DFT calculations at the B3LYP/Def2-TZVPP and BPW911/6-311G* levels of the ionization potentials, relaxation pathways, and normal mode frequencies for 3- and 4-nitrotoluene and nitrobenzene respectively. Loss of NO_2 from the parent ions 3-NT, 4-NT and NB to form $C_7H_7^+$ was found to arise from a one-photon excitation of the initially formed ground state molecular ion based on the linear growth of the fitted amplitude coefficients with the probe pulse intensity. These results show that coherent nuclear dynamics contribute to C–NO_2 homolysis in both nitrotoluene radical cations and open up the potential for further investigation of coherent control schemes to manipulate dissociation pathways in nitroaromatic and other energetic molecules.

CHAPTER 6: Probing Coherent Vibrations of Organic Phosphonate Radical Cations with Femtosecond Time-Resolved Mass Spectrometry

The content of this chapter has been adapted with permission from the reference:

6.1 Introduction

Organic phosphates and phosphonates comprise important cellular components including the DNA backbone, lipid membranes, and post-translationally modified proteins. The phosphate group in DNA is a primary target of radiation-induced damage, where one-electron oxidation of the phosphate results in formation of sugar radicals that induce lesions such as single- and double-strand breaks.[4] Due to the importance of understanding the dynamics and chemical mechanisms leading to DNA damage upon one-electron oxidation of the sugar-phosphate backbone, many experimental techniques have been applied for this purpose. For instance, experiments conducted at cryogenic temperatures have identified the structures of sugar radicals formed by one-electron phosphate oxidation in γ-irradiated DNA.[141] Picosecond time-resolved electronic spectroscopy of nucleotides irradiated with 5 ps electron pulses has determined lifetimes of phosphate radicals and timescales of backbone-to-base hole transfer.[142,143] Mass spectrometry is also widely used to characterize the products of radiation-induced DNA damage including modified sugars and bases.[144] While these studies provide significant insight into how one-electron oxidation of the sugar-phosphate backbone leads to DNA damage, little is known about how vibrational excitations in oxidized phosphates may influence reaction mechanisms leading to DNA damage.

Femtosecond time-resolved mass spectrometry (FTRMS) is uniquely suited to resolve vibrational excitations in molecular radical cations such as one-electron oxidized organic

phosphates. FTRMS of radical cations is a pump–probe technique that involves: (1) ionization of the target molecule with an intense fs laser "pump" pulse to produce the molecular cation, which is followed by (2) excitation of the cation with a weaker "probe" pulse that induces dissociation. The resulting fragment ions are then detected in a time-of-flight mass spectrometer. The exceptionally short duration and broad bandwidth of the ionizing pump pulse results in the simultaneous population of multiple excited vibrational states with accessible Franck–Condon factors in the cation, which creates a coherent superposition, or vibrational "wave packet".[9] Tracking the subsequent ultrafast dynamics of the wave packet with probe excitation has revealed how coherent vibrational excitation leads to bond dissociation in a number of polyatomic radical cations.[39,44,47,89–94,137,145,146] While FTRMS measurements are inherently in the gas phase, the fundamental insights into molecular dissociation dynamics of molecules independent of solvent effects provide a baseline for comparison to solution-phase studies, as noted in recent reviews of DNA electronic excited-state dynamics measurements with FTRMS.[147,148]

Recently, we reported on coherent vibrational dynamics in the radical cation of dimethyl methylphosphonate (DMMP), a model of the DNA sugar-phosphate backbone.[40] In this work, we compare the vibrational dynamics in DMMP to the related molecules diethyl methylphosphonate (DEMP), diisopropyl methylphosphonate (DIMP) and trimethyl phosphate (TMP) (Scheme 6.1). These molecules were under investigation model not only the DNA sugar-phosphate backbone, but also an important class of phosphonate natural products that have antibacterial and other interesting properties.[149] Although the present study considered neutral molecules instead of the anions present under biological conditions, formation of radical cations in our experiments can be considered in analogy to the formation of neutral radicals via one-electron oxidation in biological systems. The similarities and differences in the coherent

vibrational dynamics across this molecular series reveal important information about how small changes in molecular structure can influence the ionization-induced vibrational dynamics and subsequent bond-dissociation reactions. These results not only provide insight into the potential contributions of vibrational excitation to ionization-induced reactions of biologically relevant organophosphorus compounds, but also raise the possibility of distinguishing between similar molecules with mass spectrometry through the unique vibrational signatures reflected in their fragment ions.
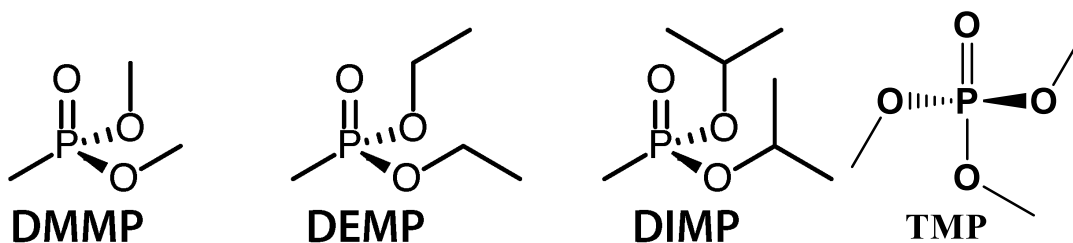
Scheme 6.1. Structures of molecules investigated in this work.

6.2 Experimental Procedure

6.2.1 Materials

DMMP (97%) and DEMP (97%) were purchased from Sigma-Aldrich (St. Louis, MO, USA), DIMP (95%) was purchased from Alfa Aesar (Tewksbury, MA, USA) and TMP (97%) purchased from Strem Chemicals (Newbury port, MA). All samples were used as received. A small toluene impurity in the DIMP sample was observable in the mass spectrum upon initial introduction, but disappeared after a few days; all DIMP data were recorded after the toluene disappearance.

6.2.2 Experimental Methods

Refer to section **3.4.1** and **3.4.2** for details on schematic experimental methods. The calibration of intensity of pump and probe was done using methods in section **3.8.1** and **3.8.2** respectively. System optimization was followed according to section **3.4.4 - 3.4.6.**

The output of a commercial Ti:sapphire regenerated amplifier (Astrella, Coherent, Inc., Santa Clara, CA, USA) producing 30 fs, 800 nm, 2.2 mJ pulses was split with a 10:90 (r:t) beam splitter. The 90% portion was directed into an optical parametric amplifier (OPA, TOPAS Prime) to produce 1500 nm, 200 µJ, 18 fs pulses used as the pump. The smaller portion of the beam used as the probe pulse was directed onto a retro-reflector placed on a motorized stage to adjust the delay between pump and probe pulses. With a home-built frequency resolved optical gating (FROG) apparatus[70] the duration of the pump and probe pulses were measured to be 18 fs and 25 fs, respectively. The pump and probe beams are recombined on a dichroic mirror and focused with a 20 cm fused silica biconvex lens to into the extraction region of a custom-built time-of-flight (TOF) mass spectrometer. The focal intensities of the pump and probe pulses were estimated as 1.5×10^{14} and 1.5×10^{13} W cm^{-2}, respectively, based on previously established methods described in Ref.[150]. The molecular sample was introduced into the ultrahigh vacuum chamber (base pressure 2×10^{-9} Torr) through the effusive source of a 1/16" OD stainless steel tube with outlet 1 cm away from the laser focus. The resulting sample pressure was kept at approximately 2×10^{-7} Torr as measured near the microchannel plate detector. Mass spectra at each pump–probe delay was collected by a 1 GHz digital oscilloscope (LeCroyWaveRunner, Chestnut Ridge, NY, USA) and averaged over 1000 laser shorts. The pump–probe delay was scanned in steps of 5 fs over the approximate range from -500 fs to +5000 fs, and 40 scans were averaged to produce the reported experimental data.

6.2.3 Theoretical Methods

Our density functional theory (DFT) calculations to interpret the coherent vibrational dynamics of the DMMP, DIMP, and DEMP cations were conducted using Gaussian 16 suite of programs.[65] All computations were performed using Gaussian 6-311+G* (5s4p1d) basis set[151] and generalized for all atoms. Neutral geometries were optimized beginning from geometries obtained from the PubChem database.[152] Chemcraft software[153] was used to specify Cs symmetry for the starting geometry of each cation optimization based on the previous finding of nearly Cs symmetry for DMMP$^+$.[40,107] The optimized geometries and vibrational spectra of each neutral and cation were evaluated using the generalized approximation (DFT-GGA) and hybrid Hartree–Fock method B3LYP.[108] These methods produced energies of DMMP and DMMP$^{\bullet+}$ within 0.01 eV of previous literature.[40,107] The same methods were applied to compute optimized geometries and vibrational frequencies of DIMP, DIMP$^{\bullet+}$, DEMP, and DEMP$^{\bullet+}$. The vertical ionization potentials and relaxation energies for all species were evaluated with the same methods.

6.3 Results

This section presents FTRMS results on DMMP, DEMP, DIMP and TMP indicating that coherent vibrational motion is excited upon electron removal to form the respective radical cations. All measurements were taken with 1500 nm, 18 fs, 1.5 x 10^{14} W cm^{-2} ionizing pump pulses and 800 nm, 25 fs, 1.5 x 10^{13} W cm^{-2} probe pulses. The coherently excited vibrational mode(s) in each molecule were assigned using DFT calculations of each radical cation (Section 6.3) except for TMP were calculations are still on going.

6.3.1 Femtosecond Time-Resolved Mass Spectrometry (FTRMS)

Figure 6.1 (a) (top) shows the mass spectra of DMMP (red), DEMP (magenta), DIMP (violet) and TMP (blue) taken with only the 1500 nm pump pulse, while 6.1 (b) shows mass spectrum taken with a probe difference. DMMP, DEMP and TMP show a prominent parent molecular ion signal, while only a small amount of parent ion is present in DIMP. Each molecule produced a series of fragment ions, some of which (e.g., m/z = 79, marked with a #) were observed in all four molecules. Significant changes in the fragmentation pattern of each molecule were observed when the 800 nm probe pulse arrived at a delay of $\tau = 100$ fs after the ionizing pump pulse. In particular, the yield of each parent ion and large fragment ions marked with a $*$ decreased, while the yield of smaller fragment ions increased. By measuring mass spectra of each molecule while scanning the pump–probe delay, the transient yields of the parent and dominant fragment ions as a function of delay τ could be extracted.
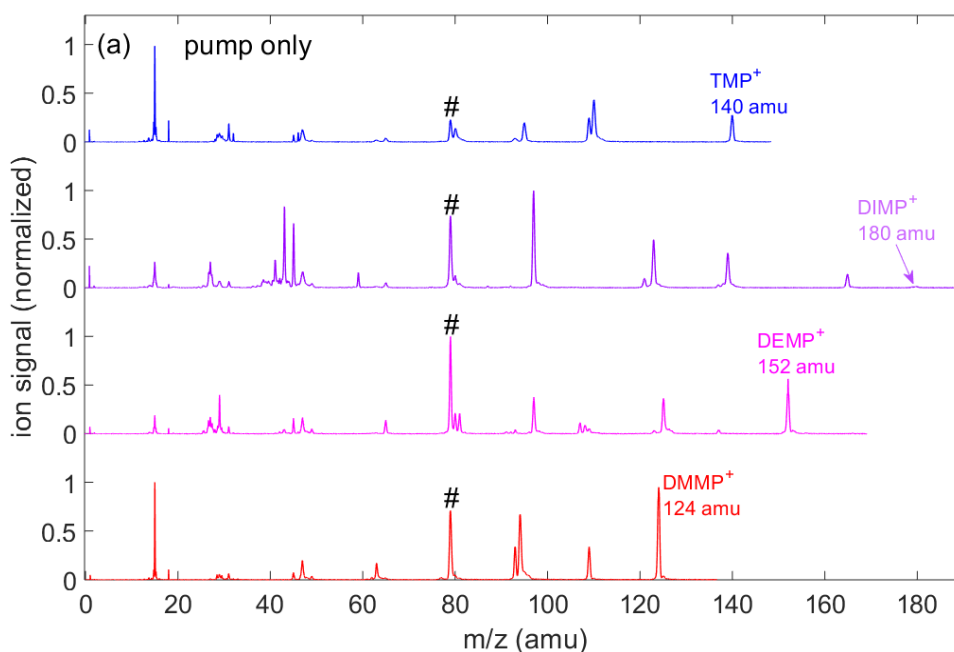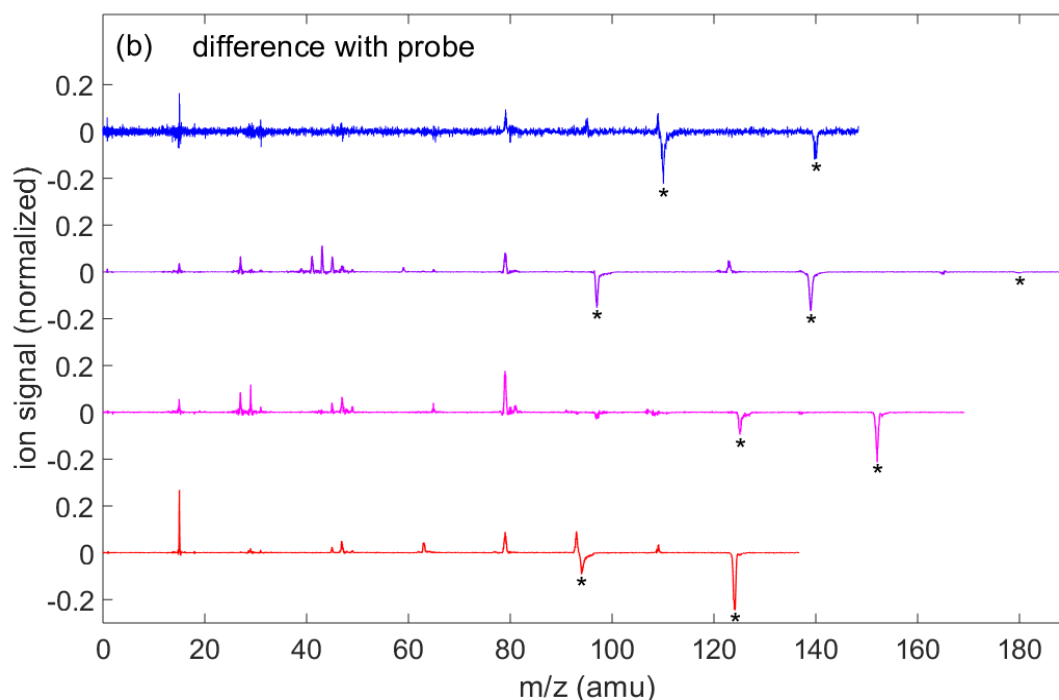
Figure 6.1. (a) Mass spectra for DMMP (red), DEMP (magenta), DIMP (violet) and TMP (blue) taken with only pump pulse; and **(b)** difference between pump-only mass spectra and mass spectra taken with probe pulse at delay of $\tau = 100$ fs.

Figure 6.2 shows the transient yields of the DMMP, DEMP, DIMP and TMP parent molecular ions as a function of pump–probe delay. The yields were obtained from the integrated intensity over the corresponding mass spectral peaks (m/z = 124 for DMMP, m/z = 152 for DEMP, m/z = 180 for DIMP and m/z = 140 for TMP). All signals were normalized to unity at negative delays, and the signals of DEMP and DIMP were shifted on the ordinate axis for clarity. While the most salient feature of each transient ion signal is its slow decay dynamics over the 5000 fs measurement window, embedded in these signals are ultrafast oscillations in the yield signals. These oscillations in the raw ion signals were present over the first ~700 fs after ionization, as seen in the magnified inset labeled "raw." Oscillating ion yields with pump–probe delay signify

vibrational wave packet dynamics in radical cations, and the frequency of these oscillations specifies the vibrational mode that is coherently excited during ionization.[39,47,89–94,135,137,145,146]

To isolate the oscillations in the transient ion signals for further analysis, the slow decay dynamics may be fit to a multi exponential decay function,

$$S(\tau) = a \exp\left(\frac{-\tau}{T_1}\right) + b \exp\left(\frac{-\tau}{T_2}\right) + c \exp\left(\frac{-\tau}{T_3}\right) + d \qquad (6.1)$$

where T_1, T_2, and T_3 denote dynamical timescales, and the constants $a - c$ denote corresponding relative amplitudes. The constant d corresponds to the asymptotic ion signal as the delay $\tau \to \infty$. The dynamical timescales may correspond to processes including geometric relaxation, excited state lifetimes, and intramolecular rearrangement reactions. Assignment of these timescales was not the goal of the present work; instead we focused on the residual oscillatory signals remaining after subtraction of the dynamics described by eq 6.1. The nonlinear least squares fit of each transient signal in Figure 6.2 to eq 6.1 are shown as the dark solid lines. The residual oscillatory ion signals that remain after subtraction of eq 6.1 make the oscillations clearer, as shown in the inset labeled "residual." In the following sections on DMMP, DEMP, DIMP, and TMP, the oscillatory parent transient signals are compared with those of fragment ions in each molecule that exhibits oscillations.
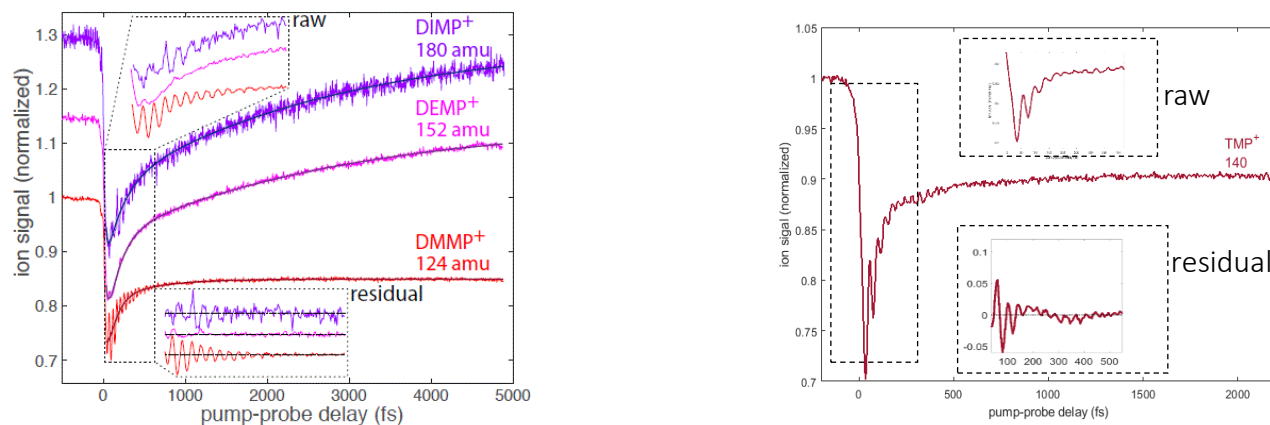
Figure 6.2. Transient ion signals of the parent molecular ions of DMMP (red), DEMP (magenta), and DIMP (violet) as a function of pump–probe delay. The region between 30 and 700 fs is magnified in the insets to show the oscillations. The dark solid lines denote fits to eq 6.1.

6.3.2 DMMP
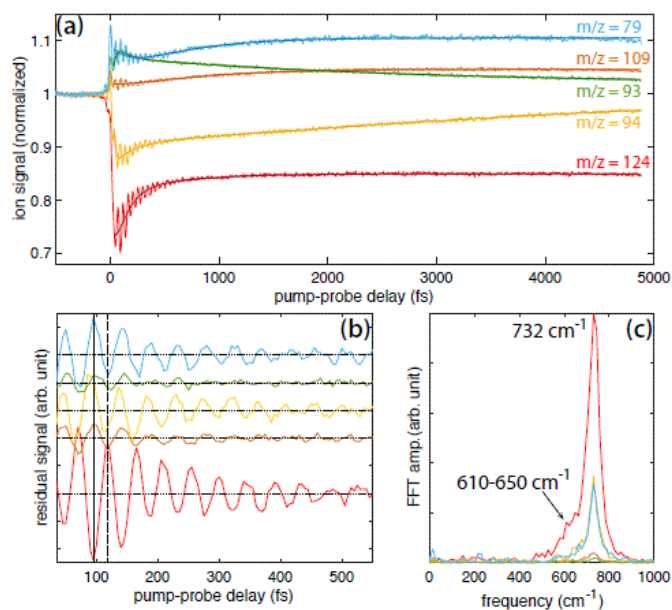
Figure 6.3. (**a**) Transient signals of DMMP$^{\bullet+}$ (m/z = 124, red), PO$_3$(CH$_3$)$_3$$^+$ (m/z = 109, orange), PO$_2$C$_2$H$_7$ $^+$ (m/z = 94, gold), PO$_2$(CH$_3$)$_2$ $^+$ (m/z = 93, green), and PO$_2$CH$_4$ $^+$ (m/z = 79, blue). The dark solid lines denote fits to eq 6.1. (**b**) Residual ion signals after exponential dynamics are subtracted. Dotted horizontal lines denote zero residual for each signal. Solid and dashed vertical

lines denote the first minimum and maximum of the parent ion yield, respectively. (**c**) FFT of residual ion signals in (**b**).

Figure 6.3 (a) shows the transient ion signals of DMMP that exhibit oscillations: parent molecular ion DMMP$^{\bullet+}$ (m/z = 124, red), $PO_3(CH_3)_2^+$ (m/z = 109, orange), $PO_2C_2H_7^+$ (m/z = 94, gold), $PO_2(CH_3)_2^+$ (m/z = 93, green), and $PO_2CH_4^+$ (m/z = 79, blue). All ion signals were normalized to the parent ion yield at negative delay and shifted on the ordinate axis to unity at negative delay to illustrate the relative change in each signal upon interaction with the probe pulse. At positive delays, the depletion of the DMMP$^{\bullet+}$ and $PO_2C_2H_7^+$ signals and enhancement of the $PO_3(CH_3)_2^+$, $PO_3(CH_3)_2^+$, and $PO_2CH_4^+$ signals indicate that the probe pulse induced formation of the latter enhanced species via excitation of the depleted DMMP$^{\bullet+}$. [39,47,89–94,135,137,145,146] The dark solid lines denote fits to eq 6.1, and fitting coefficients for each signal are provided in Table 6.1.

Table 6. 1. Fit coefficients for ions associated with DMMP.

Ion	m/z	A	T_1 (fs)	b	T_2 (fs)	c	T_3 (fs)	d
DMMP$^+$	124	0.15±0.009	37±34	-0.18±0.8	112±54	-0.042±0.019	541±0.002	0.849±0.001
$PO_3(CH_3)_2^+$	109	-	-	0.029±0.027	299±143	-0.056±0.029	629±0.002	0.412±0.001
$PO_2C_2H_7^+$	94	0.66±0.21	16±12	-0.05±0.008	152±28	-0.14±0.02	7900±0.001	0.963±0.002
$PO_3(CH_3)_2^+$	93	0.17±0.02	30±8	0.054±0.030	91±23	0.051±0.002	2820±0.002	0.400±0.002
$PO_2CH_4^+$	79	-	-	0.079±0.022	190±47	-0.092±0.025	538±69	1.051±0.001

The residual ion signals upon subtraction of eq 6.1 are shown in Figure 6.3 (b). The first maximum and minimum of the parent signal are indicated by the dashed and solid lines, respectively. All fragment ion signals oscillate approximately antiphase with the parent signal; they exhibit a maximum at the solid line and a minimum at the dashed line. The antiphase oscillations indicate that these dissociation products are formed upon probe pulse excitation when the vibrational wave packet passes through a geometry with strong dipole coupling to one or more excited states that

are accessible by the probe photon energy. [39,47,89–94,135,137,145,146] The oscillation period therefore determines the vibrational frequency of the coherently excited normal mode, which can be obtained by Fast Fourier Transform (FFT) of the time-dependent residual ion signals. FFT was performed over the sampling window of 35–2500 fs with 5 fs resolution, yielding a frequency resolution of 14 cm^{-1}. The FFT frequency spectra (Figure 6.3 c) exhibit a strong peak at 732$\pm$28 cm^{-1} (error estimated by the peak full width at half maximum). This peak is slightly down-shifted from the 750 cm^{-1} frequency reported in Ref.,[40] although the observed frequencies agree to within the estimated error. The DMMP$^{\bullet+}$ spectrum also contains a distinct shoulder in the range of 610–650 cm^{-1} that was not visible in the previous investigation, likely because the slow exponential dynamics were not subtracted off prior to implementing the FFT or because the longer sampling window in the present work results in better frequency resolution. This shoulder peak may be attributed to an additional vibrational excitation not previously reported, as discussed below in 6.3.1. The lower intensity of the shoulder peak suggests that its associated mode has a lower probability of being excited than the mode associated with the main peak.

The dissociation products analyzed in Figure 6.3 have been observed in numerous mass spectrometry studies of DMMP. [103,105–107,149,154–157] Their assigned structures based on these studies and our recently reported theoretical calculations[107] are given in Scheme 6.2. While the m/z = 109 and 93 structures result from direct cleavage of a methyl and methoxy group, respectively, the m/z = 94 and 79 structures involve hydrogen atom migration to the phosphate oxygen atom. This hydrogen migration has been likened to keto-enol isomerization[106] (Scheme 6.3) and has a transition state barrier of 0.42 eV from the relaxed ion geometry, with only an additional 0.03 eV required to lose CH_2O and form $PO_2C_2H_7^+$ according to our recent calculations.[107] The present

FTRMS results indicate that this dissociation pathway can be induced by probe excitation of the

parent cation.

Scheme 6.2. Fragments ions of DMMP.

Scheme 6.3. H-atom shift in DMMP$^+$.

6.3.3 DEMP

Figure 6.4. (**a**) Transient signals of ions from DEMP: DEMP$^{\bullet+}$ (m/z = 152, magenta), PO$_3$C$_3$H$_{10}^+$ (m/z = 125, orange), PO$_3$CH$_6^+$ (m/z = 97, green), and PO$_2$CH$_4^+$ (m/z = 79, blue). The dark solid lines denote fits to eq 6.1. (**b**) Residual ion signals after exponential dynamics are subtracted. (**c**) FFT of residual DEMP$^{\bullet+}$ signal in (**b**).

Figure 6.4(a) shows the transient ion signals of DEMP: DEMP$^{\bullet+}$ (m/z = 152, magenta), PO$_3$C$_3$H$_{10}^+$ (m/z = 125, orange), PO$_3$CH$_6^+$ (m/z = 97, green), and PO$_2$CH$_4^+$ (m/z = 79, blue). The signals are normalized to yields at negative time delay as in Figure 6.4 (a). The fit coefficients to eq 1 (solid lines in Figure 6.4a) are given in the Table 6.2 below, and the residual ion signals are plotted in Figure 6.4 (b).

Table 6.2. Fit coefficient for ions associated with DEMP

Ion	m/z	A	T_1 (fs)	b	T_2 (fs)	c	T_3 (fs)	d
DEMP$^+$	152	0.31±0.05	30±5	-0.224±0.023	168±9	-0.229±0.002	3020±120	0.993±0.004
PO$_3$C$_3$H$_{10}$$^+$	125	0.15±0.05	28±12	-0.067±0.025	122±33	-0.194±0.002	1390±30	0.885±0.001
PO$_3$CH$_6$$^+$	97	-	-	-0.22±0.12	850±190	0.15±0.13	1900±900	0.894±0.007
PO$_2$CH$_4$$^+$	79	-0.51±0.11	26±3	-	-	0.285±0.003	1150±30	2.430±0.001
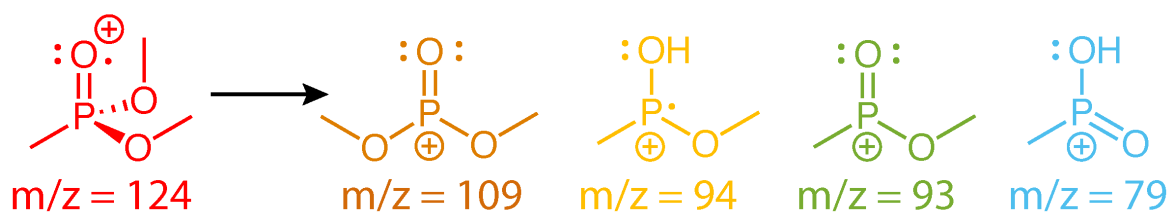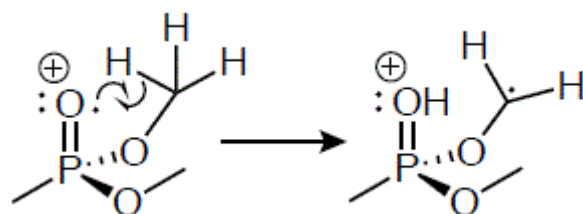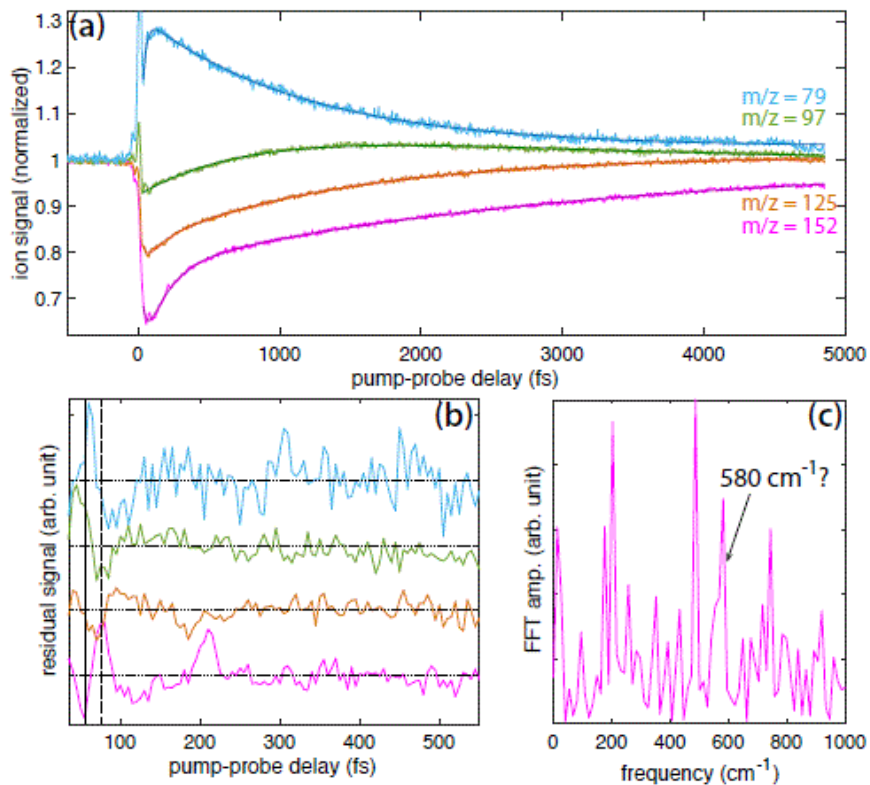
Unlike in DMMP, the DEMP ion signals exhibit at most one or two visible oscillations, primarily before 100 fs delay, although the parent signal exhibits a revival at 210 fs delay. It is also worth noting that the first minimum (solid line) and maximum (dashed line) of the parent ion signal do not correspond to maxima or minima of the dissociation products, although the PO$_3$CH$_6$$^+$ yield exhibits a minimum at the delay indicated by the dashed line. We hypothesize that this lack of a well-defined phase relationship between the parent and fragment ion oscillations causes extremely rapid disappearance of the oscillations. This situation could arise if the maximum probability of producing each fragment ion occurs at a different position of the vibrational wave packet. The resulting destructive interference between different excitation pathways would preclude clear observation of the wave packet motion in the ion signals. In any case, the lack of well-resolved oscillations precludes effective FFT analysis of the oscillatory dynamics, with no signal clearly visible above the noise (Figure 6.4(c)), although the broad width of the feature around 580 cm^{-1} suggests a possible weak signal. The structures of DEMP$^{•+}$ and fragment ions taken from the literature [156,157] are shown in Scheme 6.4.

Scheme 6.4. Fragment ions of DEMP$^{•+}$.

Scheme 6.5. McLafferty rearrangement mechanism in DEMP.

These fragments have been reported to form along a sequential dissociation pathway beginning from the parent ion: $m/z = 152 \rightarrow 125 \rightarrow 97 \rightarrow 79$.[157] The first two steps involve McLafferty type rearrangements,[158] as shown in Scheme 6.5. Two hydrogen atoms migrate in the first step, resulting in simultaneous loss of $C_2H_3^{\cdot}$ (27 amu) to form the $PO_3C_3H_{10}^{+}$ ion. A single hydrogen atom migration in the second step results in subsequent loss of C_2H_4 (28 amu) to form the PO_3CH_6 ion, which can subsequently lose H_2O to form $PO_2CH_4^{+}$.[156,157] This complex sequence of dissociative rearrangement reactions in DEMP$^{\cdot+}$ may be expected to destroy any initially prepared vibrational coherence if the hydrogen migrations are sufficiently fast, which would explain the lack of well-defined oscillations in the ion yields shown in Figure 6.4. However, our results on DIMP do not support this assertion, as discussed below. Therefore, we attribute the lack of long-lived coherence to the phase offsets of each product ion visible in Figure 6.4 (b), which will require further investigation of the relevant excited states to explain.

6.3.4 DIMP

Figure 6.5. (**a**) Transient signals of ions from DIMP: DIMP$^{\bullet+}$ (m/z = 180, violet, magnified by a factor of 10), PO$_3$C$_4$H$_{12}$$^+$ (m/z = 139, orange), PO$_3$C$_3$H$_8$$^+$ (m/z = 123, gold), PO$_3$CH$_6$$^+$ (m/z = 97, green), and PO$_2$CH$_4$$^+$ (m/z = 79, blue). The dark solid lines denote fits to eq 1. (**b**) Residual ion signals after exponential dynamics subtracted. (**c**) FFT of residual PO$_3$C$_4$H$_{12}$$^+$, PO$_3C_3H_8$$^+$, and PO$_3CH_6$$^+$ ion signals in (**b**).
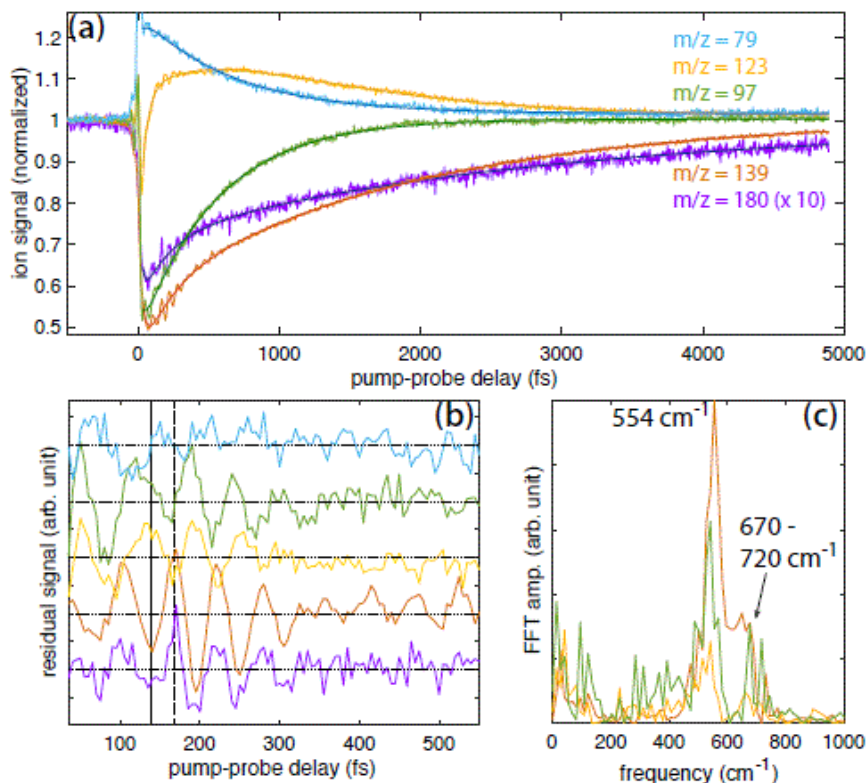
Figure 6.5(a) shows transient ion signals of DIMP: DIMP$^{\bullet+}$ (m/z = 180, violet), PO$_3$C$_4$H$_{12}$$^+$ (m/z = 139, orange), PO$_3$C$_3$H$_8$$^+$ (m/z = 123, gold), PO$_3$CH$_6$$^+$ (m/z = 97, green), and PO$_2$CH$_4$$^+$ (m/z = 79, blue). Signals are normalized as in Figures 6.4 (a) and 6.5 (a), with the exception that the DIMP$^{\bullet+}$ signal is magnified by a factor of 10 due to its small yield in the mass spectrum (cf., Figure

6.1). The coefficients extracted from fitting the ion signals to eq 1 (dark lines in Figure 6.5 (a)) are presented in Table 6.3.

Table 6.3. Fit coefficient for ions associated with DIMP.

Ion	m/z	a	T_1 (fs)	b	T_2 (fs)	c	T_3 (fs)	d
$DIMP^+$(x10)	180	0.21 ± 0.19	27 ± 22	-0.16 ± 0.03	202 ± 45	-0.27 ± 0.01	2740 ± 290	0.987 ± 0.012
$PO_3C_4H_{12}^+$	139	0.80 ± 0.13	30 ± 6	-0.35 ± 0.03	203 ± 21	-0.86 ± 0.01	1880 ± 60	2.185 ± 0.004
$PO_3C_3H_8^+$	123	-0.88 ± 0.05	43 ± 4	-0.84 ± 0.51	570 ± 120	-0.95 ± 0.53	990 ± 160	2.804 ± 0.003
$PO_3CH_6^+$	97	0.05 ± 0.03	27 ± 11	-0.20 ± 0.01	548 ± 5	-	-	1.001 ± 0.001
$PO_2CH_4^+$	79	-0.02 ± 0.01	48 ± 24	0.11 ± 0.01	659 ± 12	-	-	1.007 ± 0.001

The residual ion signals in Figure 6.5 (b) show more well-resolved oscillations than DEMP, with the oscillations in $PO_3C_4H_{12}^+$ resolved at delays longer than 500 fs. The solid and dashed lines indicating a minimum and maximum of the $DIMP^{\bullet+}$ yield, respectively, show that this $PO_3C_4H_{12}^+$ fragment exhibits perfectly in-phase oscillations with the parent ion. In-phase oscillations of parent and fragment ions in polyatomic molecules have not previously been observed in FTRMS experiments[39,47,89–94,135,137,145,146] and suggest that dissociation of $DIMP^{\bullet+}$ to form $PO_3C_4H_{12}^+$ occurs spontaneously without probe excitation. The oscillations of the smaller dissociation product $PO_3C_3H_8^+$ are approximately antiphase with $DIMP^{\bullet+}$ and $PO_3C_4H_{12}^+$, suggesting it can be formed upon probe excitation of the parent ion. Meanwhile, the oscillations of $PO_3CH_6^+$ and $PO_3CH_4^+$ are somewhat phase-shifted from the larger transients but approximately antiphase with each other. These complex phase relationships may point to the presence of two different wave packets, as suggested in FTRMS experiments on acetophenone,[39] although further investigation will be needed to test this hypothesis. FFT of the ion signals over the 30–2500 fs window yields a prominent peak at approximately 554 ± 28 cm^{-1} and a weaker peak in the range of 670–720 cm^{-1}. The structures of DIMP fragment ions are shown in Scheme 6.6.
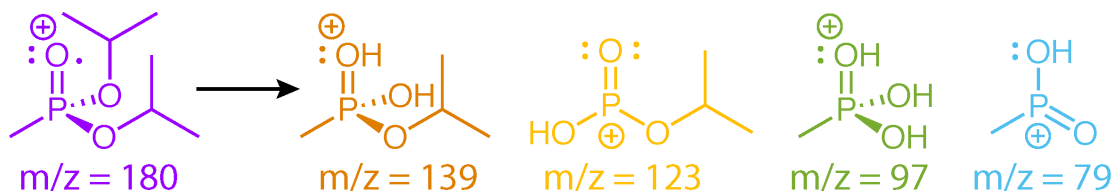
Scheme 6.6. Fragments ions for DIMP

Previous mass spectral studies of DIMP indicate that it undergoes a sequential dissociation pathway analogous to DEMP: m/z = 180 → 139 → 97 → 79 via two McLafferty type rearrangements (Scheme 6.5).[156,157] The m/z = 123 product is formed through the sequence m/z = 180 → 165 → 123, which involves the direct cleavage of the methyl group followed by C_3H_6 loss via a McLafferty rearrangement.[157] While these dissociative rearrangement reactions resemble those in DEMP, the preservation of ion yield oscillations over ~500 fs in DIMP suggests that these reactions either do not destroy the initial vibrational coherence or occur on a slower timescale than the coherence lifetime.

6.3.5 TMP

Figure 6.6 shows the transient ion signals of $TMP^{\bullet+}$ (m/z =140, red), $PO_3C_2H_7^+$ (m/z = 110, orange), $PO_3C_2H_6^+$ (m/z = 109, blue), $PO_3CH_4^+$ (m/z = 95, yellow), and HPO_3^+ (m/z = 79, green). All ion signals were normalized to the parent ion at negative delay. At positive delay, a depletion in the parent ion and $PO_3C_2H_7^+$ is observed with an enhancement in $PO_3C_2H_6^+$, $PO_3CH_4^+$, HPO_3^+ indicating a probe induced formation of the latter ions. The residual ion signal, upon subtracting eq 6.1, is shown on panel (b). The first minimum and maximum are shown by the solid and dash lines respectively. All transient ion signals oscillate approximately antiphase with the parent ion and exhibit maximum and minimum on the solid and dash lines respectively. The formation of these ions indicate they can be formed from probe excitation of the parent ion. Looking at the solid

line for the parent ion (minimum) and the other transient ions (maximum), it is observed to phase-shift from the parent ion, which may be an indication of the activity of different wave packets. The FFT of the ion in panel (c) over the 30-2500 fs window yields two prominent peaks at approximately 759 ± 20 cm^{-1} and 878 ± 25 cm^{-1}.
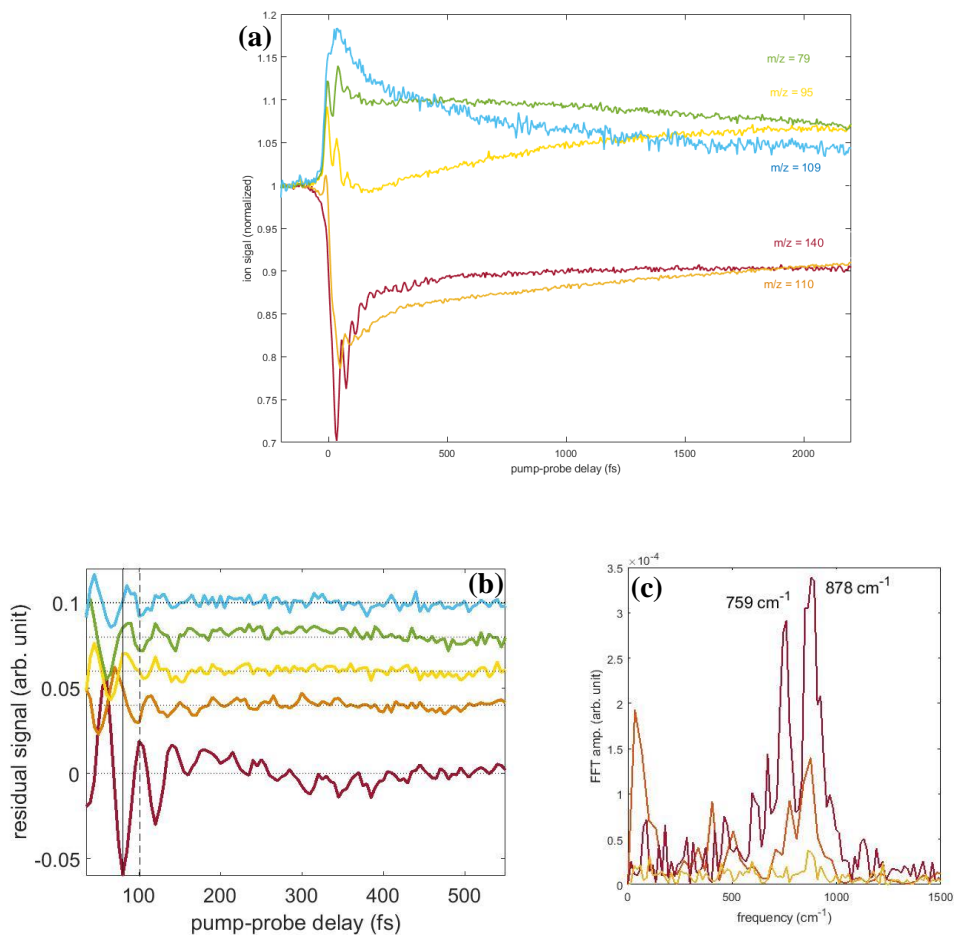
Figure 6.6. (**a**) Transient signals of ions from DIMP: TMP$^{\bullet+}$ (m/z = 140), PO$_3$C$_2$H$_7$ $^+$ (m/z = 110, orange), PO$_3$C$_2$H$_6$ $^+$ (m/z = 109, blue), PO$_3$CH$_4$ $^+$ (m/z = 95, yellow), and PO$_4$ $^+$ (m/z = 79, green). (**b**) Residual ion signals after exponential dynamics subtracted. (**c**) FFT of residual TMP$^{\bullet+}$, PO$_3$C$_2$H$_7$ $^+$, and PO$_3$CH$_4$ $^+$ ion signals on the left.

The structure and the fragmented ions of TMP$^{\bullet+}$ are shown in scheme 6.7 and 6.8. The radical cation TMP$^{\bullet+}$ exhibits a sequential fragmentation via two dissociation pathways. The first pathway involves fragments from hydrogen transfer with a loss of CH_2O and a sequential loss of $CH_3^{\bullet}$ m/z $= 140 \rightarrow 110 \rightarrow 95 \rightarrow 80$, while the second pathway involves a direct cleavage of OCH_3 and two subsequent losses of $CH_3^{\bullet}$ in a sequence m/z $= 140 \rightarrow 109 \rightarrow 94 \rightarrow 79$. During the first process, one hydrogen atom migrates to the oxygen bonded to the phosphorus resulting in an enol (scheme 6.7) and a subsequent loss of CH_2O (30 amu) to form $PO_3C_2H_7^+$ ion. Sequential $CH_3^{\bullet}$ moiety (15 amu) is lost from $PO_3C_2H_7^+$ ion to form $PO_3CH_4^+$ and HPO_3^+ respectively. In the second pathway, a direct CH_3O moiety (31 amu) is lost from the parent ion to form $PO_3C_2H_6^+$, followed by two successive losses of $CH_3^{\bullet}$ (15 amu) to form $PO_3CH_3^+$ and PO_3^+ respectively.
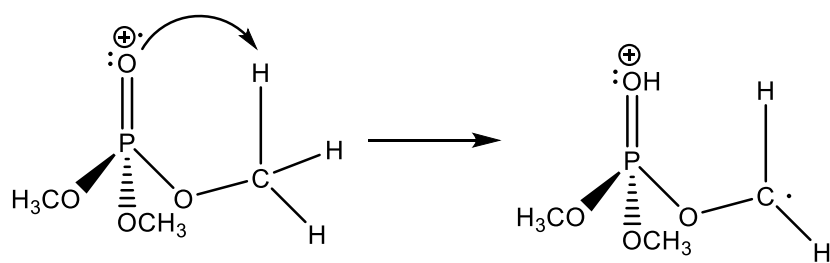
Scheme 6.7. Hydrogen shift in TMP.

m/z $= 140$ m/z $= 110$ m/z $= 109$
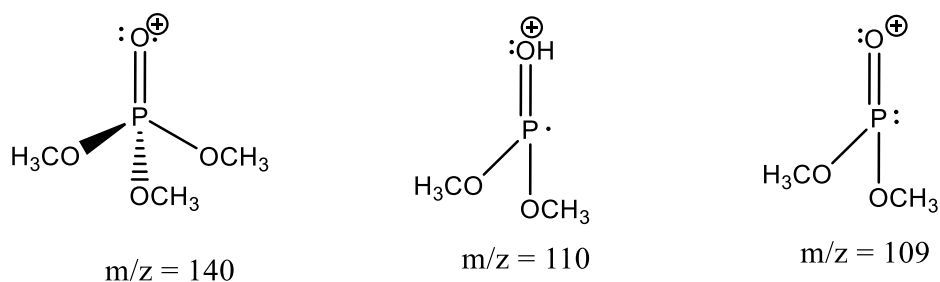
Scheme 6.8. Fragment ions in TMP

Table 6.4. Fit coefficient for ions associated with TMP.

Ion	m/z	a	T_1 (fs)	b	T_2 (fs)	c	d
TMP^+	140	0.91$\pm$0.19	60$\pm$8	0.08$\pm$0.03	400$\pm$100	-0.05$\pm$0.01	0.96$\pm$0.01
$PO_3C_2H_6^+$	109	0.09$\pm$0.13	45$\pm$30	0.02$\pm$0.03	3000$\pm$2000	-0.04$\pm$0.01	0.44$\pm$0.04
$PO_3CH_4^+$	95	0.15$\pm$0.05	43$\pm$4	0.07$\pm$0.51	-	-0.17$\pm$0.53	0.70$\pm$0.03
HPO_3^+	79	0.87$\pm$0.03	27$\pm$11	0.4$\pm$0.01	-	0.10$\pm$0.02	0.15$\pm$0.01

6.4 Assignments of Coherently Excited Vibrational Modes

Coherent vibrational excitation in radical cations arises due to the mismatch between the molecular geometries of the neutral and radical cation. For instance, many substituted benzenes exhibit planar or near-planar geometry as neutrals but non-planar geometry as radical cations, which induces coherent excitation of the torsional vibration of the substituent with respect to the benzene ring. [39,91–94,135,137,145,146,146] Our recent results on DMMP indicated that the lengthening of the P—O bond and changing angles of the methoxy substituents induces excitation of the O–P–O bending mode that includes P—O and P–C stretching.[40] To predict whether similar geometrical changes occur in DEMP and DIMP, the neutral and cation geometries were computed at the B3LYP/6-311+G* level. The computed geometries of DMMP agree with previous results[40,107,110] and serve to benchmark the method for DEMP and DIMP. Figure 6.7 depicts the neutral and cation geometries of DMMP, DEMP, and DIMP with the P=O, P–O, P–C, and C-O bond lengths and O–P–O angle labeled. The geometric coordinates of all atoms in the structures are given in the appendix (Tables C1–C3). The associated vertical ionization potentials (IP$_{vert}$) and cation relaxation energies (E$_{relax}$) for each molecule are listed in Table 6.5. We note that the location of the unpaired electron in the relaxed cations remained on the oxygen atom initially double-bonded to the phosphorus atom; the known radical migrations in these molecules are associated with hydrogen atom transfers shown in Schemes 6.3 and 6.5.[103,105–107,154–158]

Table 6. 5. Computed ionization and relaxation energies.

Molecule	Neutral E (Hatree)	Relaxed Cation E (Hatree)	IP $_{vert}$ (eV)	Erelax (eV)
DMMP	-686.8138	-686.4663	10.31	0.66
DEMP	-765.4112	-7656.0739	9.82	0.64
DIMP	-884.0129	-843.6786	9.55	0.58

Ionization induces a number of analogous geometrical changes across the methylphosphonate series, as observed in Figure 6.7. First, the P=O bond lengthens by 6.8% and the P–C bond shortens by 1.7% in each molecule. Second, the O–P–O angle increases from 102–106° in the neutrals to 117° in the cations. Third, P–O single bonds shorten by 1.9–4.3% in each molecule, but DMMP$^{+\bullet}$ exhibits identical P–O bond lengths, while one of the P–O bonds becomes slightly shorter than the other in both DEMP$^{+\bullet}$ and DIMP$^{+\bullet}$. Finally, both C–O bonds lengthen by approximately 3% in each cation. These geometric changes are expected to induce coherent excitation along one or more associated vibrational modes in each molecule.
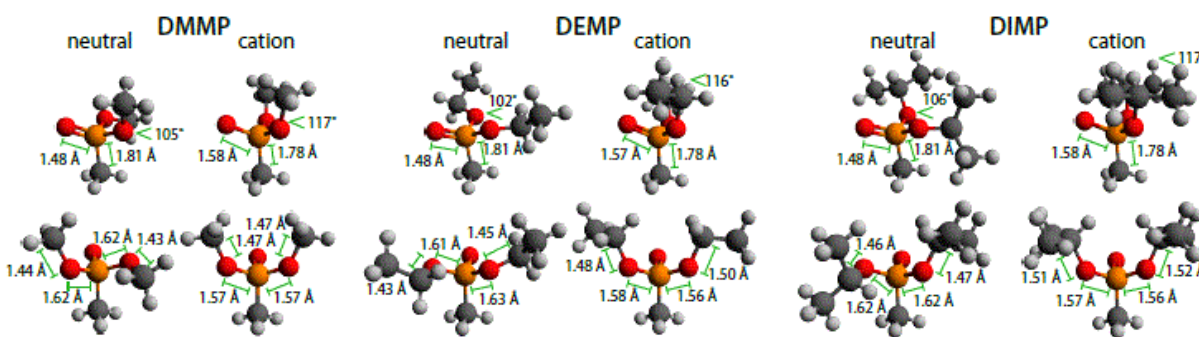
Figure 6.7. Neutral and cation geometries of DMMP, DEMP, and DIMP with selected bond lengths and angles labeled.

To identify potential coherently excited vibrations, the normal modes for both the neutral and cation geometries of DMMP, DEMP, and DIMP were computed and compared to experimental IR and Raman measurements[159–162] (Appendix, Tables C4–C7 and main work Figures 6.8–6.9).
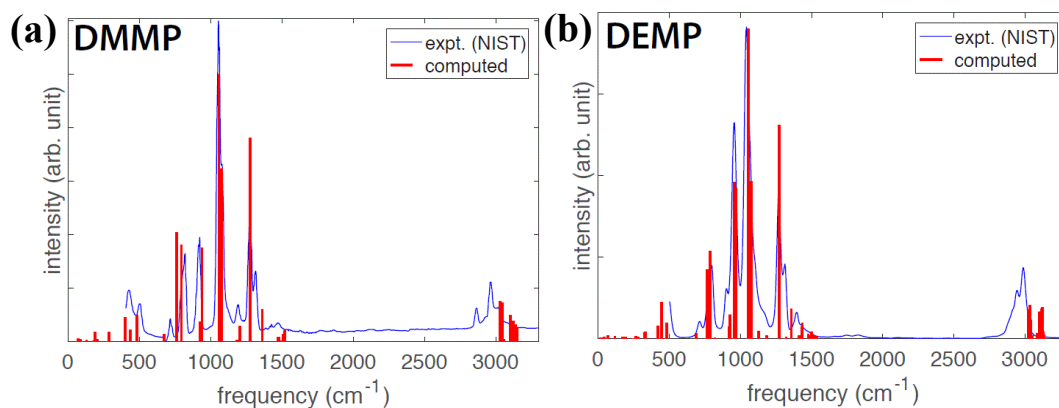
Figure 6.8. Experimental[162] and computed vibrational spectra of DMMP (a) and DEMP (b).
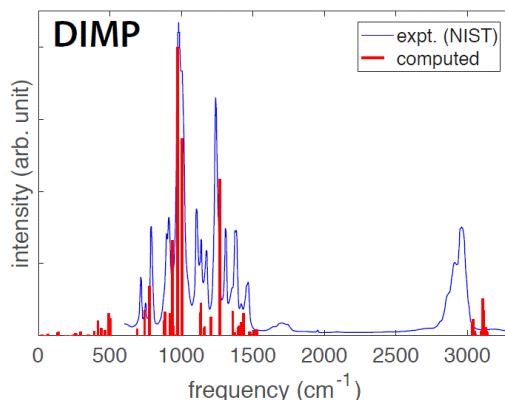
Figure 6.9. Experimental[162] and computed vibrational spectra of DIMP.

The rough agreement of the computed spectra of the DMMP, DEMP, and DIMP neutrals with experimental measurements is similar to recent computational studies of the IR spectra of these molecules.[110,163] Based on these computed normal modes, the ionization-induced geometrical changes, and experimentally observed oscillation frequencies, we focused on a cluster of three

normal modes labeled **A**, **B**, and **C** with computed frequencies for the neutrals and cations given in Table 6.6 and illustrations of the motions given in Figure 6.10. Modes **A** and **B** have been defined as symmetric and asymmetric O–P–O bending modes, respectively, and Mode **C** as the P–C stretch,[164] although additional motions are clear in Figure 6.6.

Table 6.6. Computed vibrational energies of DMMP, DEMP, and DIMP in cm^{-1}. Experimental values given in parentheses. a: Ref.[161]; b: Ref.[159]; c: Ref.[160]

Mode	DMMP Neutral	Cation	DEMP Neutral	Cation	DIMP Neutral	Cation
A	672 (712[a])	659	689 (715[b])	656	690 (719[c])	651
B	759 (786[a])	761	765 (771[b])	711	742 (748[c])	665
C	794 (818[a])	767	788 (806[b])	756	778 (791[c])	750

The 732 ± 28 cm^{-1} coherent oscillations in DMMP[•+] were previously assigned to Mode **C**.[40] This mode was computed at 752 cm^{-1} using an anharmonic correction,[40] and our current computations with no anharmonic correction predict this mode at 767 cm^{-1}, in agreement with the previous uncorrected results in Ref.[40] (Appendix, Table C4). The additional shoulder peak at 610–650 cm^{-1} visible in Figure 6.3 (c) can be attributed to Mode **A**, the symmetric O–P–O bend. While Modes **B** and **C** have almost identical frequencies, excitation of Mode **C** is more likely because it involves symmetric motions of the two methoxy substituents, which have nearly identical geometric parameters in the DMMP[•+] (Figure 6.7). As a result, it is unlikely that the asymmetrical motions of Mode **B** would be excited by ionization.

In DEMP, the lack of sufficient resolution of oscillations precludes the assignment of any coherently excited normal modes, although the potential weak feature around 580 cm^{-1} in Figure 4 (c) could arise from excitation of Mode **A**. In DIMP, the strong feature at 554 ± 28 cm^{-1} observed in Figure 6.5 (c) is most likely due to Mode **A**, even though the calculated frequency exceeds the

experimental frequency by around 100 cm^{-1} because the geometrical changes in P–O and C–O bond lengths in Figure 6.7 are consistent with the motions of mode **A** in Figure 6.10. The weak peak in the range of 670–720 cm^{-1} is most likely attributable to mode **C**; a similar overestimation of this frequency in the calculations is observed. As with DMMP, excitation of Mode **B** in DIMP$^{\bullet+}$ is unlikely due to its asymmetric motion and the symmetric geometrical changes upon ionization.
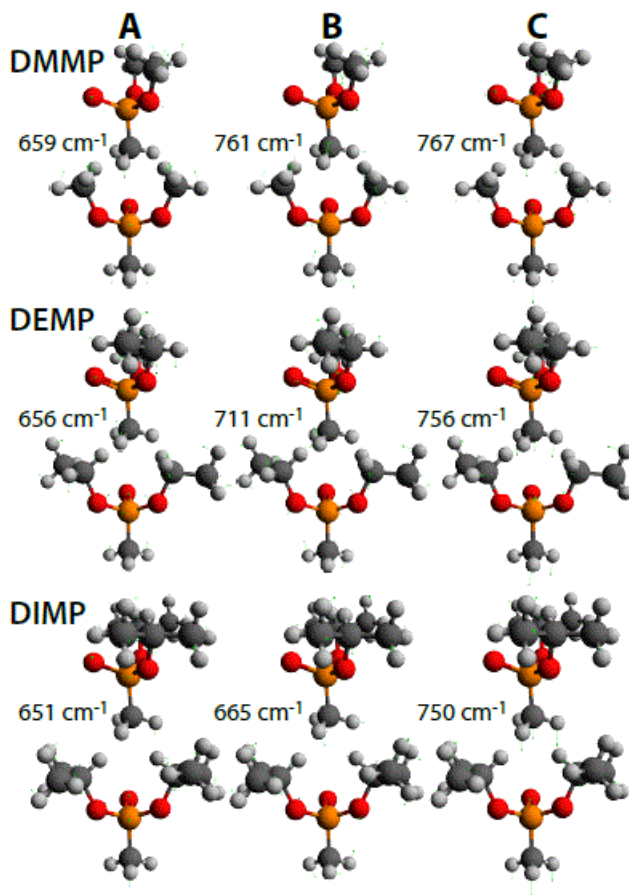
Figure 6.10. Potential coherently excited vibrational modes in DMMP, DEMP, and DIMP.

6.4.1 Assignments of modes for TMP

The DFT calculation is currently on going for TMP, however from the experimental results obtained from the FFT suggest the presence of a bimodal frequency at 759 and 878 cm^{-1}. Since no theoretical calculation is done yet, we assigned these vibrational frequencies based on

literature.[164,165] A symmetric and asymmetric stretching of the O-P bonds from literature was assigned to frequencies 750 and 850 cm^{-1} respectively as shown in Figure 6.11.
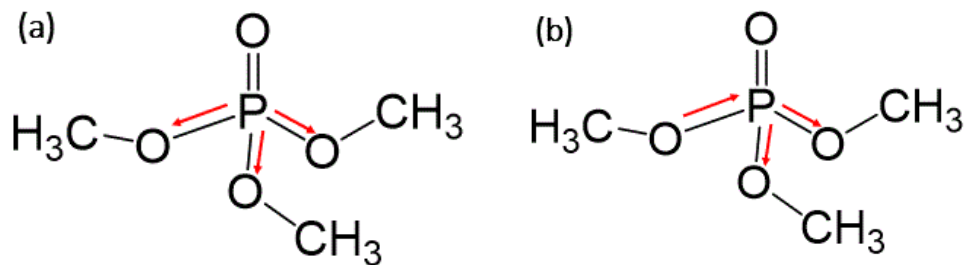
Figure 6.11. Potential coherently excited vibrational modes in TMP showing symmetric (a) and asymmetric (b) modes.

6.5 Discussion

The FTRMS measurements presented here demonstrate how the coherent vibrational motions of polyatomic radical cations may be investigated with only mass spectrometric detection. With the assistance of DFT calculations, the coherent excitation of the same two vibrational modes in DMMP$^{•+}$, DIMP$^{•+}$ and TMP$^{•+}$ could be identified. While no definitive mode assignments could be made in DEMP$^{•+}$ due to the relative lack of visible coherent dynamics, the excitation of one of the same modes is suggested in the data. These results add to the growing body of FTRMS studies of coherent vibrational dynamics in polyatomic radical cations. [39,47,89–94,135,137,145,146] The observed coherent dynamics in these studies are assumed to arise from vibrational motion on the electronic ground state of the cation, which requires its selective population during the ionization process. Strong-field excitation at the 1500 nm wavelength used in this work is known to produce greater cationic ground state population than the Ti:sapphire wavelength of 800 nm due to a well-established adiabatic electron tunneling ionization mechanism.[40,44,50]

Moreover, the strong electric fields required for non-resonant femtosecond laser ionization typically remove an electron before significant neutral excited state population can occur.[94] However, strong-field tunneling ionization still populates ionic excited states in the organic phosphonates, as evident in the large yields of small fragment ions in Figure 6.1. This limitation of FTRMS may ultimately be overcome upon the development of facile methods of producing femtosecond pulses in the VUV spectral range, which would allow for single-photon ionization. This result that ionization induces coherent excitation of the same vibrational modes across the methylphosphonate series points to a generic vibrational excitation mechanism in ionized organic phosphonates. Additionally, the similar cation relaxation and dissociation dynamics of each molecule reflected in the observed exponential decay signals suggests common mechanistic pathways across the series. These results, combined with the well-known shared intramolecular rearrangement and dissociation pathways of organic phosphonates with the related phosphates [104,154,156–158], raise the possibility that analogous vibrational excitation and dissociation mechanisms operate across a broad class of biologically relevant organophophorous compounds. Further investigation of these dynamical pathways may lead to enhanced understanding of the mechanisms leading to radiation-induced DNA damage. For instance, these pathways may explain the observed rapid formation of sugar-centered radicals in one-electron oxidized DNA.[141] The presence of common vibrational excitations and dissociation dynamics in the radical cations of methylphosphonates also mirrors shared vibrational excitations in classes of organic radical cations including alkyl phenyl ketones,[93,94] nitrotoluenes,[145,146] and halogenated methanes.[47] In addition to the common vibrational excitation and dissociation pathways observed across the methyl phosphonate and phosphate, the distinct oscillation periods and dynamics observed in each molecule suggest that FTRMS may enable discrimination among possible source molecules in a

complex mixture that give rise to mass spectral peaks with the same m/z value. As an illustration, the residual oscillatory dynamics of the peaks at m/z = 97 and m/z = 79 (Figure 6.12) are highly dependent on the source molecule. Both the oscillation period and duration of observable oscillations are different in DMMP, DEMP, and DIMP.
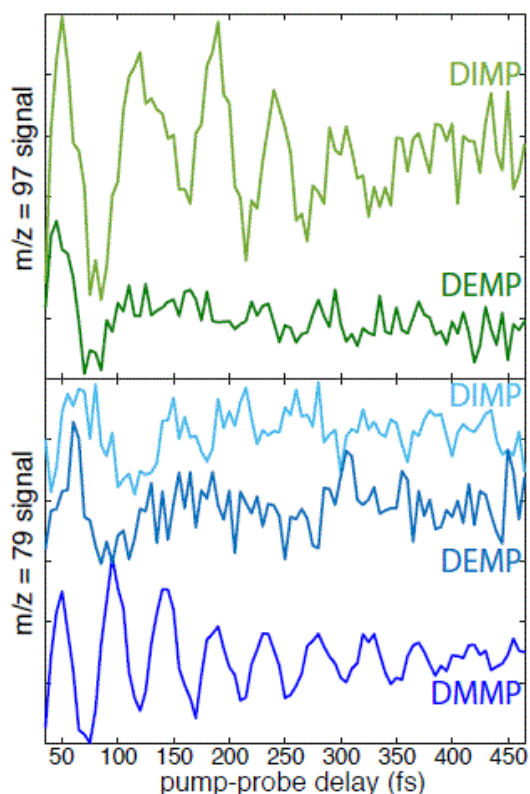
Figure 6.12. Oscillatory components of m/z = 97 (**top**) and m/z = 79 (**bottom**) signals in DMMP, DEMP, and DIMP.

Despite the noisy signals in the present data that preclude resolution in a mixture, significant improvements in signal resolution could, in principle, enable the deconvolution of multiple oscillatory signals by FFT or other methods. In particular, further refinement of the FTRMS technique single-photon VUV ionization and tunable probe excitation wavelengths may provide the necessary signal resolution. This potential ability of FTRMS to obtain vibrational information

from mass spectrometry measurements could significantly enhance the capabilities of modern analytical mass spectrometry techniques such as femtosecond laser desorption-post ionization, which has been used to image biological materials including microbial biofilms and mammalian tissue.[166–170] In particular, replacing the commonly used VUV ionization laser with a pump–probe pulse pair could provide a coherent vibrational "fingerprint" of constituent molecules detected in the mass spectrometer. This combination of FTRMS with desorption techniques therefore has the potential to yield new detection and discrimination capabilities for analysis of biological samples.

6.6 Conclusions

Femtosecond time-resolved mass spectrometry was used to record coherent vibrational dynamics in radical cations of the methylphosphonate and phosphate of molecules DMMP, DEMP, DIMP and TMP. The time-domain measurements recorded oscillations in ion yields as a function of pump–probe delay extending to ∼500 fs after ionization with a period of 45 fs in DMMP, 55 fs in DIMP and 40 fs in TMP. FFT analysis of the oscillatory ion signals yielded a strong 732 ± 28 cm^{-1} peak and weak 610–650 cm^{-1} feature in DMMP and strong and weak peaks at 554 ± 28 cm^{-1} and 670–720 cm^{-1}, respectively, in DIMP. DEMP exhibited less well-defined oscillations in ion yields and no definitive frequency retrievable with FFT, although a weak feature around 580 cm^{-1} barely visible above the noise was observed. TMP yielded two frequencies of 759 ± 28cm^{-1} and 878 ± 28cm^{-1}. DFT calculations of the cation vibrational modes in the cations enabled assignment of the low- and high-frequency features in DMMP and DIMP to the symmetric O–P–O bend and P–C stretch modes, respectively, and possible assignment of the weak DEMP oscillations to the O–P–O bend. Assignment of vibrational modes of TMP was based on literature enabling both frequencies to be assigned to symmetric and asymmetric stretching of O-P-O bond. These results demonstrate the ability of FTRMS measurements to directly extract information

about vibrational excitations in polyatomic cations that are models for biologically relevant organophosphorus compounds using only mass spectrometric detection and can inform future development of the FTRMS technique for bioanalytical applications.

CHAPTER 7: Conserved Vibrational Coherence in the Ultrafast Rearrangement of 2-Nitrotoluene Radical Cation.

The content of this chapter has been adapted with permission from the reference:

7.1 Introduction

The photolabile 2-nitrobenzyl functional group has a number of applications including as a protecting group in organic synthesis,[171] as a precursor in the synthesis of DNA microarrays,[172] and in caged compounds for biomolecule encapsulation.[173] In addition to these applications, the 2-nitrobenzyl group is found in the military explosive 2,4,6-trinitrotoluene (TNT),[111] which has been the subject of numerous experimental[42,126,127,129] and theoretical[34,117,128,174] investigations into its dissociation pathways. The nitrotoluene (NT) isomers 2-, 3-, and 4-NT are often used as model compounds for TNT, and their photodissociation pathways have been studied for decades using mass spectrometric detection of cationic photoproducts.[43,129,131,145,175–181] These studies have demonstrated clear differences in reaction pathways of 2-NT as compared to 3- and 4-NT due to the proximity of the CH_3 and NO_2 groups on the 2-nitrotoluyl moiety.

Upon ionization, all three NT isomers undergo direct homolysis of the weak $C-NO_2$ bond (Scheme 7.1), producing the $C_7H_7^+$ ion with m/z = 91 in mass spectrometry experiments.[43,129,131,145,177–181]
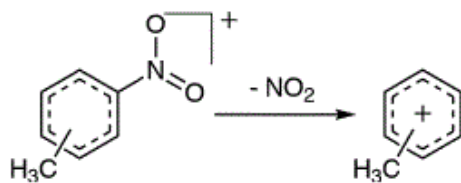
Scheme 7.1. C-NO$_2$ Homolysis in NTs.

The C−NO$_2$ cleavage is also the primary initiator of detonation in TNT.[117] The 3- and 4-NT cations also undergo nitro−nitrite rearrangement (NNR, Scheme 7.2), leading to the loss of NO and the formation of C$_7$H$_7$O$^+$ ions with m/z = 107. [129,131,145,175–180] The m/z = 107 ion is formed at significantly reduced yields in 2-NT,[129,179,180] indicating that NNR is not energetically favorable for this isomer.
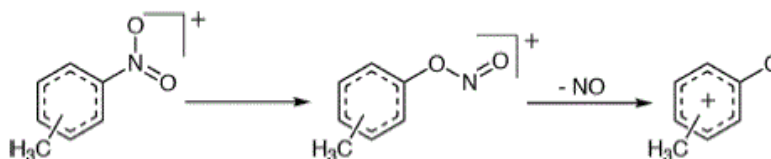
Scheme 7.2. NNR in 3- and 4-NT.

Instead of NNR, the 2-NT cation undergoes a unique process called *aci*-rearrangement wherein the aliphatic hydrogen migrates to the nitro group, which results in the formation of an *aci*-nitro tautomer in a process called H atom attack (Scheme 7.3). The *aci*-nitro tautomer loses OH, forming C$_7$H$_6$NO$^+$ ions with m/z = 120, which can subsequently lose CO to produce C$_6$H$_6$N$^+$ with m/z = 92. [129,145,175,176,178–181] The *aci*-rearrangement reaction in neutral 2-NT was first reported in 1962[182] and was determined to be the initial step in the sequential dissociation of 2-NT cation to form m/z = 120 and 92 ions in 1965.[175] More recently, theoretical studies have proposed

mechanisms for this sequential dissociation pathway in neutral 2-NT[183–185] and 2-NT cation[181] in the gas phase.
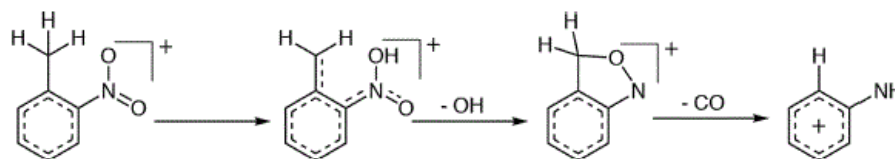
Scheme 7.3. *Aci*-rearrangement and Sequential Dissociation in 2-NT.

However, the reaction dynamics and their time scales are still only partially understood. The ultrafast dynamics of the *aci*-rearrangement in neutral 2-NT and other 2-nitrobenzyl compounds have been studied in the solution phase using time-resolved pump−probe experiments with femtosecond laser pulses.[186,187] Upon excitation of 2-NT to the $\pi\pi^*$ (S_2) state, *aci*-rearrangement occurs following relaxation to the $n\pi^*$ (S_1) state on a time scale of 10 ps or after intersystem crossing to the triplet manifold on a time scale of 1300 ps.[186] While these experiments provide key insights into the *aci*-rearrangement dynamics in neutrals, the solution-phase time scales may be affected by solvent interactions, and subsequent molecular dissociation pathways have not been explored.[186,187] Additionally, no *aci*-rearrangement or subsequent dissociation time scales have been reported in the 2-NT cation. As a result, knowledge of both the *aci*-rearrangement and subsequent dissociation mechanisms may be gained through femtosecond pump−probe measurements on the isolated 2-NT cation.

Pump−probe experiments have provided extensive insight into the dissociation dynamics of isolated organic cations including halogenated methanes,[47,59,89,188] alkyl aryl ketones[39,44,93,94] azobenzene,[91,137] dimethyl methylphosphonate,[40] and 3- and 4-NT.[145] In these molecules, ionization with a strong-field femtosecond pump pulse results in the formation of a coherent superposition of vibrational states, or "wave packet", in the ground electronic state of the cation.

Wave packet excitation to a dissociative ionic excited state by the time-delayed probe pulse results in oscillations in the parent and fragment ion yields as a function of probe delay with period corresponding to the coherently excited vibrational mode.[39,40,44,47,59,89,91,93,94,137,145,188] Our recent pump−probe study of 3- and 4-NT cations[145] determined that wave packets are formed along an in-plane bending mode in (216 fs period, 160 cm^{-1}) 3-NT cation and the C−NO$_2$ torsional mode (470 fs period, 70 cm^{-1}) in 4-NT cation. Coherent excitation with the probe pulse was found to drive the C−NO$_2$ homolysis pathway in Scheme 7.1. To answer outstanding questions about the dynamical time scales involved in H atom attack and subsequent dissociation pathways in 2-NT, this work reports the first femtosecond pump−probe measurements on the isolated 2-NT cation.

Interpretation of the experimental dissociation dynamics is supported by a series of density functional theory (DFT) calculations of the energies, relaxation pathways, and vibrational frequencies of the 2-NT cation and its *aci*-nitro tautomer, along with molecular dynamics simulations to estimate the time scale of H atom attack. We will show that coherent torsional wave packet motion is conserved following H atom attack, with the *aci*-nitro tautomer of 2-NT cation producing distinct dynamics in the −OH loss product at m/z = 120 as compared to other ions. These results open up the possibility of coherent control over the reactions of photolabile 2-nitrobenzyl protecting groups.

7.2 Methods

Refer to section **3.4.1** and **3.4.3** for details on experimental methods. The calibration of intensity of pump and probe was done using methods in section **3.8.1** and **3.8.2** respectively. System optimization was followed according to section **3.4.4 - 3.4.6.**

A commercial Ti:sapphire regenerative amplifier (Astrella, Coherent, Inc.) producing 30 fs, 800 nm, 2.2 mJ pulses is used to pump an optical parametric amplifier (OPA, TOPAS Prime) to produce 1200−1600 nm, 20 fs, 300 μJ pulses. Figure 3.3 shows a schematic diagram of the beam paths. A 50:50 (r:t) beam splitter placed after the OPA output splits the beam into pump and probe lines. The pump beam passes through a λ/2 wave plate and Wollaston polarizer for attenuation and is then expanded by a telescope made of spherical mirrors with f = −10 and 50 cm to increase the beam diameter (measured with the knife-edge method) from 4.5 to 22.0 mm. The expanded beam has maximum energy ranging from 50 to 150 μJ depending on the wavelength and can reach focal peak intensities exceeding 4×10^{14} W cm^{-2}.[107] The probe beam is directed to a retroreflector placed on a motorized translation stage (ThorLabs, Inc.), attenuated with a variable neutral density filter, and frequency-doubled with a β-barium borate (BBO) crystal. The maximum probe energy is 10 μJ at 650 nm. With a home-built frequency-resolved optical gating (FROG) setup,[72] the durations of the pump and probe were measured to be 18 and 25 fs, respectively (Figure 7.1). Pump and probe beams are recombined on a dichroic mirror and focused with an f = 20 cm fused silica biconvex lens into an ultrahigh vacuum chamber (base pressure 2×10^{-9} Torr) coupled to a custom-built linear time-of-flight mass spectrometer (TOFMS) described previously.[107,150] Pump−probe measurements on 2-NT were taken with a pump wavelength of 1300 nm at intensities of 1×10^{14} and 2×10^{14} W cm^{-2}, as determined by the yield of Xe^{n+} ions using the method of Hankin.[75] The 650 nm probe intensity was determined through measurement of the energy using a pyroelectric power meter (PM-USB, Coherent, Inc.) and the beam waist using a CMOS camera (DCC1645M, ThorLabs, Inc.). The beam waist and Rayleigh range were 38 μm and 10 mm, respectively (Figure 7.2), producing estimated peak intensities ranging from 9×10^{11} to 5×10^{12} W cm^{-2} at pulse energies of 1−6 μJ. The pump− probe delay was scanned from −500 fs (probe before pump) to

+8000 fs in steps of 20 fs. The 2-NT sample (99%, Sigma-Aldrich) was used without further purification and introduced into the TOFMS at a pressure of 1.2×10^{-7} Torr measured near the microchannel plate (MCP) detector. Mass spectra of 2-NT taken at each pump−probe delay and averaged over 1000 laser shots were recorded with a 1 GHz digital oscilloscope (LeCroy WaveRunner 610Zi). The reported transient ion signals were obtained from averaging 40 pump−probe scans taken over 3 days.

7.2.1 Experimental

7.2.1.1 Pulse Characterization

This was done in accordance with methods in sections **3.6** and **3.8.2**

The durations of the pump and probe pulses were measured using a home-built Frequency Resolved Optical Gating (FROG) setup[72] to obtain the autocorrelation spectrograms. The time-dependent electric fields were retrieved with an open-source MATLAB code[74] based on the retrieval algorithm in Ref.[73] The spectrograms and retrieved temporal electric fields for each pulse are shown in Figure 7.1.
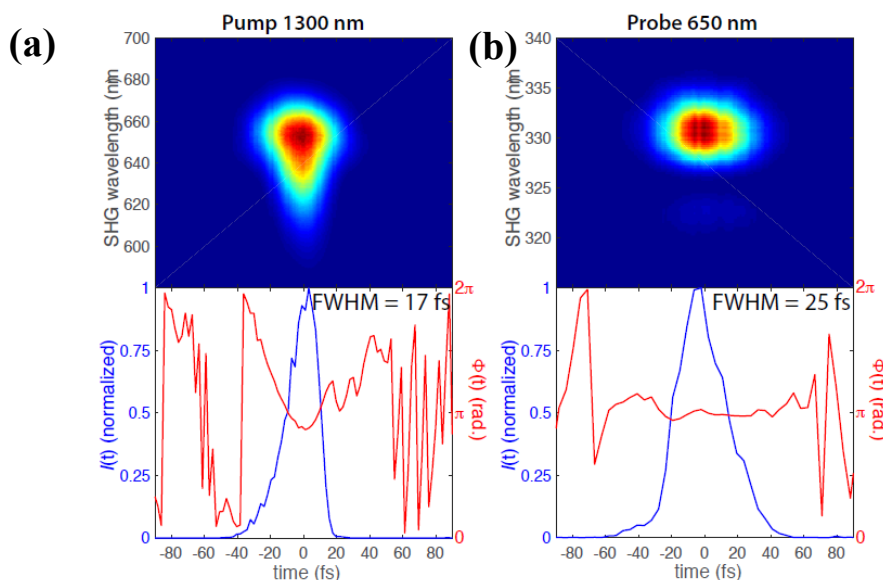
Figure 7.1. Spectrograms (top) and retrieved temporal intensities and phases of the 1500

nm pump pulse (a) and the 800 nm probe pulse (b).

The FWHM durations of the pump and probe pulses were 18 fs and 25 fs, respectively. The beam waist and Rayleigh range of the probe pulse were measured with a CMOS camera (ThorLabs, Inc., pixel width 5.2 µm) mounted on a linear translation stage. Images of the beam were recorded over a propagation distance of 20 mm at an interval of 0.6 mm. The beam parameters for the probe 650 nm is presented in Figure 7.2.
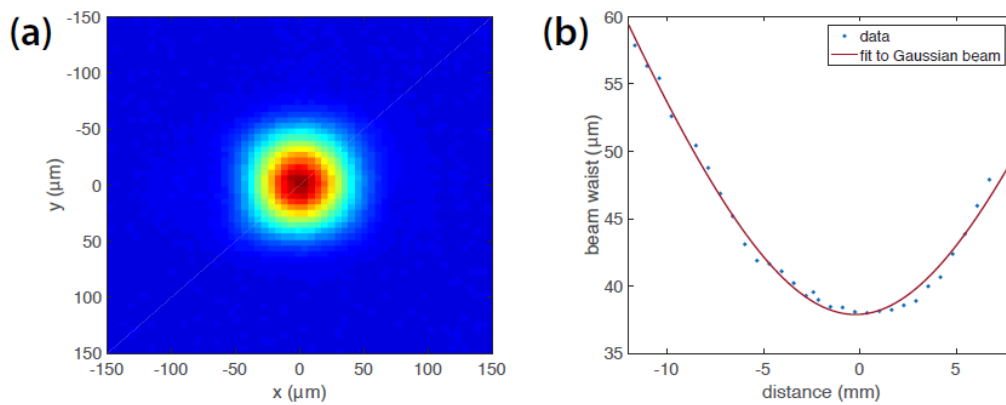
Figure 7.2. (a) False color CMOS image of probe beam at the focus. (b) Measured beam radius as a function of propagation distance (circles) and fit to eq 7.1 (solid line). The beam propagation was in the direction of increasing z value.

The beam waist and Rayleigh range of the probe pulse were measured with a CMOS camera (ThorLabs, Inc., pixel width 5.2 μm) mounted on a linear translation stage. Images of the beam were recorded over a propagation distance of 13 mm at an interval of 0.6 mm. The beam spot in each image was fit to a Gaussian function in both the x and y directions using a MATLAB code, and the average waist at intensity $1/e^2$ of the maximum recorded. Figure 7.2 (a) shows a representative CMOS image of the probe beam at the focus. (b) shows its fit to a Gaussian function in the z direction. The data were fit to the Gaussian beam propagation function

$$\omega(z) = \omega_0 \sqrt{1 + \frac{(z-a)^2}{z_R^2}} \qquad (7.1)$$

obtain the fitting parameters $\omega_0 = 37.9\pm0.3$ μm, $z_R = 9.8\pm0.3$ mm, and $a = 0.2\pm0.1$ mm. The a

parameter represents a trivial shift of the focus along the propagation axis, while the parameters

ω_0 and z_R represent the beam waist and Rayleigh range, respectively.

7.2.2 Theory

Our DFT calculations were conducted using the Gaussian 16 suite of programs.[65] The 6-311+G* (5s4p1d) basis set[151] was initially used for all atoms, and subsequent calculations with the larger CBSB7 basis set[189] were performed to evaluate the energies. The total energy threshold was 10^{-8} au, while the convergence threshold was set to 10^{-3} eV/Å. We used the BPW91[190] functional for preliminary geometry and ground-state energy calculations, which is in the generalized gradient approximation (GGA) family. After these preliminary calculations, neutral and cation geometries were optimized with the hybrid functionals B3LYP,[108,109] CAMB3LYP,[191] and ωB97XD,[192] along with the Møller−Plesset perturbation theory method truncated at second order (MP2).[193] The calculated neutral and cation energies, along with comparison to the literature at the CBS-QB3 level and VUV photoionization experiments,[181] are given in Table 7.1.

Table 7.1. Calculated Energies of 2-NT and Comparison to Literature.

Molecule	Neutral (Hartree)	Cation (Hartree)	IP $_{vert}$ (eV)
BPW91	-476.011304	-475.677837	9.074
B3LYP	-476.046909	-475.703077	9.356
CAM-B3LYP	-475.814173	-475.465865	9.478
BP7XD	-475.878995	-475.531522	9.455
MP2	-474.688852	-474.329081	9.790
CBS-QB3[a]	-475.311340	-474.959199	9.582
Exp[a]			9.43
[a]Reference[181]			

It is notable that the dispersion-corrected meta-GGA exchange functionals ωB97XD and CAM-B3LYP predict vertical ionization potentials (IPs) that agree to within 0.05 eV with the recently reported experimental value of 9.43 eV.[181] Figure 7.3 shows 2-NT at its neutral geometry with all labeled atoms. In the appendix Table D1 shows the optimized geometries for 2-NT neutral and cation and D2 shows the optimized geometry for *aci*-nitro tautomer structures INT1r and INT2. The harmonic vibrational frequencies obtained from these calculations are tabulated in the appendix on Tables D3−D5.
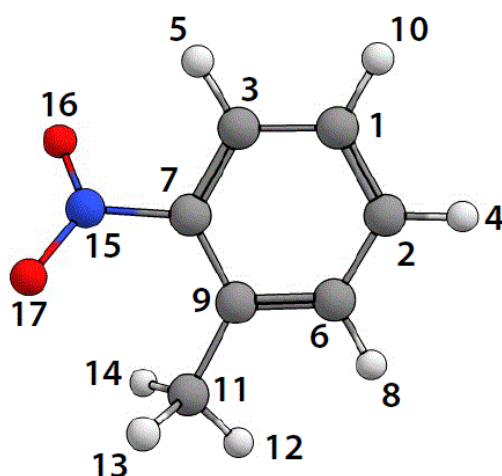
Figure 7.3. Structure with atomic labels of 2-NT

To determine the excited-state energies of the 2-NT neutral and cation, we performed time-dependent DFT (TDDFT) calculations[68] to obtain the simulated optical spectrum of each species. We calculated the first 100 singlet−singlet (for neutral 2-NT) and doublet−doublet (for 2-NT cation) transitions with four different functionals: BPW91, B3LYP, CAM-B3LYP, and ωB97XD. Tabulated results for the 12 lowest neutral 2-NT energies and 23 lowest cation energies, along

with oscillator strengths, are given in the appendix, Tables D6 and D7. The simulated spectra for neutral 2-NT superimposed on the experimental spectrum obtained from NIST[162] are shown in Figure 7.4 (a) As with the predicted IP$_{vert}$ values, the predicted excited-state energies computed with the ωB97XD and CAM-B3LYP functionals agree very well with one another and capture the strong absorption feature centered around 4.9 eV in the experimental spectrum. The excitation energies and oscillator strengths for the 2-NT cation shown in Figure 7.4 (b) suggest that the lowest-lying accessible excited state lies at approximately 1.8−1.9 eV and that the next state lies at approximately 3.2−3.4 eV. On the basis of these results, the probe wavelength was set at 650 nm (1.9 eV) for the experiments. The experimental probe spectrum is shown as the orange shaded region in Figure 7.4 (b). This probe spectrum and the associated 1300 nm pump wavelength were used for all experimental measurements presented below.
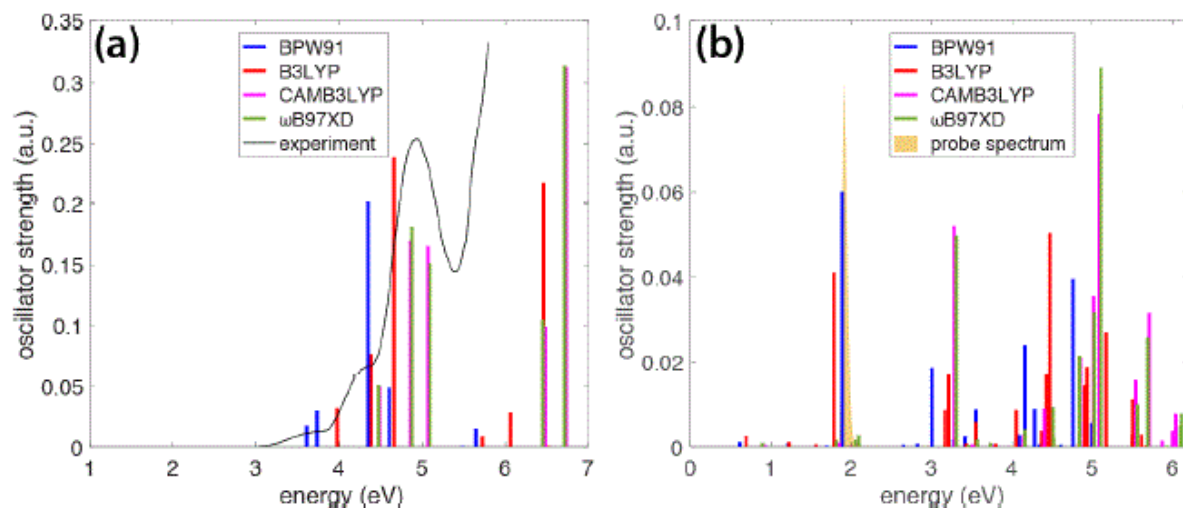
Figure 7.4. (a) TDDFT spectra for neutral 2-NT. Experimental spectrum obtained from NIST.[162] (b) TDDFT spectra for 2-NT cation. The probe spectrum is shown as the orange shaded region. Spectra were computed using the BPW91 (blue), B3LYP (red), CAMB3LYP (magenta), and ωB97XD (green) functionals with the 6-311+G* basis.

The transition states of the hydrogen transfer in *aci*-rearrangement were prepared via displacements of the hydrogen atoms. The transition states of rotations and bond breaking were scanned for using a Modredundant scan in Gaussian 16. The geometries found at the energetic cusps were then optimized using the Berny Algorithm. Using vibrational frequency calculations, these states were confirmed to correlate to first-order saddle points because each transition state had one imaginary frequency with the imaginary mode vectors. To confirm the validity of the transition states found, synchronous transit-guided quasi-Newton (STQN)[194] calculations were performed with and without initial guesses (QST3 and QST2, respectively). To ensure that no transition state was missed, we used the transition state already found as the starting or ending point for the QST calculations. The proposed pathways were then justified using full internal reaction coordinate (IRC)[195] pathways. Energies for the reaction pathways using the ωB97XD/CBSB7 combination of exchange functional and basis sets are reported. Finally, 100 ab initio molecular dynamics runs using the ADMP method[196] with 0.1 fs time steps and 280 fs duration were performed to determine the time required for the *aci*-rearrangement. In ADMP calculations, the forces between atoms are calculated via DFT (in our computations using the BPW91 functional) while the velocities are propagated classically. These simulations were initiated from the transition state for the H atom attack and included all post-ionization relaxation energy (differences in vertical and adiabatic energies of 0.1951 eV) in the imaginary mode.

7.3 Results and Discussion

The experiments and calculations presented here demonstrate the surprising result that vibrational coherence in 2-NT cation is preserved after it undergoes spontaneous H atom attack to form the *aci*-nitro tautomer. This finding is the first (to the best of our knowledge) report of preserved vibrational coherence following an intramolecular rearrangement reaction in a radical

cation and builds on recent reports of preserved vibrational coherence in the radical cations of azobenzene[137] and N-methyl morpholine[197,198] following internal conversion. The determination of vibrational coherence preservation rests on the experimental and theoretical results presented in this section, which paint a complex picture of both coherent and incoherent excitation pathways leading to the dissociation of the 2-NT cation. This section is organized as follows: First, we present the pump−probe mass spectrometry results (section 7.3.1), followed by a detailed analysis of the observed oscillatory ion yield dynamics (section 7.3.2). Next, we present the computed reaction pathways leading to the formation of $C_7H_7^+$, $C_7H_6NO^+$, and $C_6H_6N^+$ (section 7.3.3). We then discuss the experimental and theoretical evidence for coherent vibrational motions of the *aci-nitro* tautomer (section 7.3.4). Finally, we present a full picture of the coherent and incoherent dissociation pathways in 2-NT$^+$ (section 7.3.5).

7.3.1 Pump−Probe Measurements.
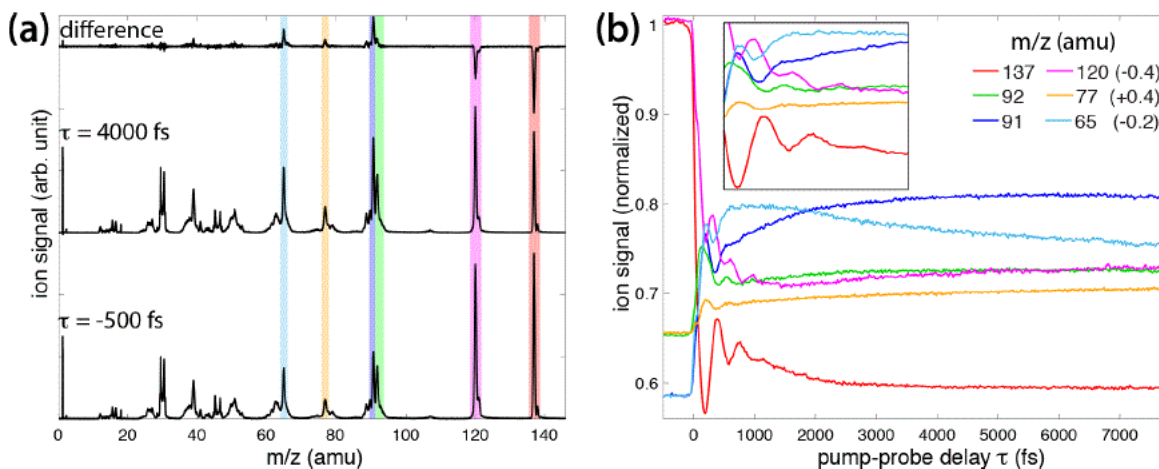
Figure 7.5. (a) Mass spectra of 2-NT taken at $\tau = -500$ and 4000 fs, along with their difference. (b) Transient ion signals as a function of the pump−probe delay. The inset magnifies the region from 50 to 1500 fs.

Figure 7.5 (a) shows the mass spectra of 2-NT taken with 1300 nm, 18 fs, 2×10^{14} W cm^{-2} pump pulses and 650 nm, 25 fs, 5×10^{12} W cm^{-2} probe pulses at pump−probe delays of $\tau = -500$ (bottom) and +4000 fs (middle), as well as their difference (top). At negative delay, the largest peaks in the mass spectrum are the parent 2-NT cation at m/z = 137 (highlighted in red) and the OH loss product $C_7H_6NO^+$ at m/z = 120 (magenta). Because the probe is nonionizing, the ion signal is exclusively due to the 1300 nm pump pulse. The large yield of parent 2-NT$^+$ as compared to previously reported mass spectra taken with femtosecond lasers[129,179,180] is consistent with the expected adiabatic ionization process at 1300 nm excitation.[39,40,44,50,51,137,145] At positive delay, a decrease in the m/z = 137 and 120 peaks accompanied by an increase in the peaks corresponding to the smaller ions at m/z = 92 (green), 91 (blue), 77 (orange), and 65 (cyan) is observed. On the basis of previous reports, [129,145,175,176,178–181] these m/z values are assigned as to the following ions: $C_6H_6N^+$ (92), $C_7H_7^+$ (91), $C_6H_5^+$ (77), and $C_5H_5^+$ (65). The increase in these fragment ion yields at the expense of the parent ion indicates that they are formed via excitation of the parent 2-NT$^+$ by the 650 nm probe pulse.[39,40,44,47,59,89,91,93,94,137,145,188] Figure 7.5 (b) shows the transient ion signals highlighted in panel (a) as a function of pump−probe delay τ, with all signals normalized to the signal of the parent 2-NT$^+$ at negative time delay. The m/z = 120, 77, and 65 signals have been shifted on the ordinate axis by −0.4, +0.4, and −0.2 units, respectively, for clarity. The inset in Figure 7.5 (b) magnifies the region from 50 to 1500 fs, showing the oscillating ion signals that indicate coherent vibrational dynamics. At short delay times, the oscillations in the m/z = 137 and 120 ions are roughly out-of-phase with the oscillations of the smaller fragment ions, consistent with coherent excitation by the probe pulse. [39,40,44,47,59,89,91,93,94,137,145,188] The same transient dynamics with smaller-amplitude features were observed for lower pump and probe intensities shown in Figure 7.6.
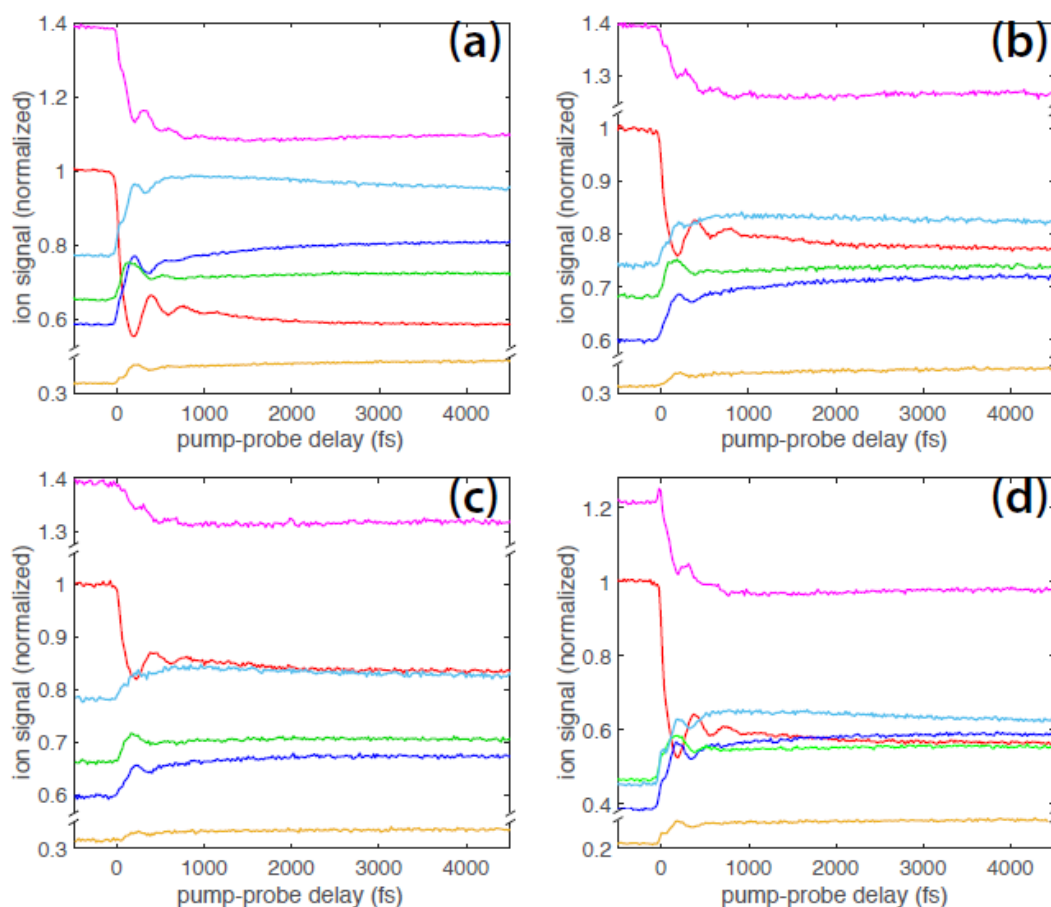
Figure 7.6. Transient ion signals of 2-NT taken at (a) 2×10^{14} W cm^{-2} pump, 5×10^{12} W cm^{-2} probe; (b) 2×10^{14} W cm^{-2} pump, 2×10^{12} W cm^{-2} probe; (c) 2×10^{14} W cm^{-2} pump, 8×10^{11} W cm^{-2} probe; (d) 1×10^{14} W cm^{-2} pump, 5×10^{12} W cm^{-2} probe.

7.3.2 Analysis of Oscillatory Dynamics.

The ~380 fs oscillation period in the 2-NT ion signals is of similar magnitude to oscillation periods in the related molecules 4-NT (470 fs),[145] acetophenone (650 fs),[39,44,199] and 4-methylacetophenone (730 fs).[94] In the latter molecules, the oscillations were attributed to the torsional motion of the nitro or acetyl substituent with respect to the benzene ring due to the relaxation of the cation from the planar neutral geometry to the nonplanar optimized geometry.[39,44,94,145,199] Our ωB97XD/CBSB7 calculations indicate that the C$-$NO$_2$ torsional angle

of 26.0° in neutral 2-NT shifts to 35.5° at the optimized cation geometry (Figure 7.7), suggesting that the torsional vibrational mode can be excited upon ionization.
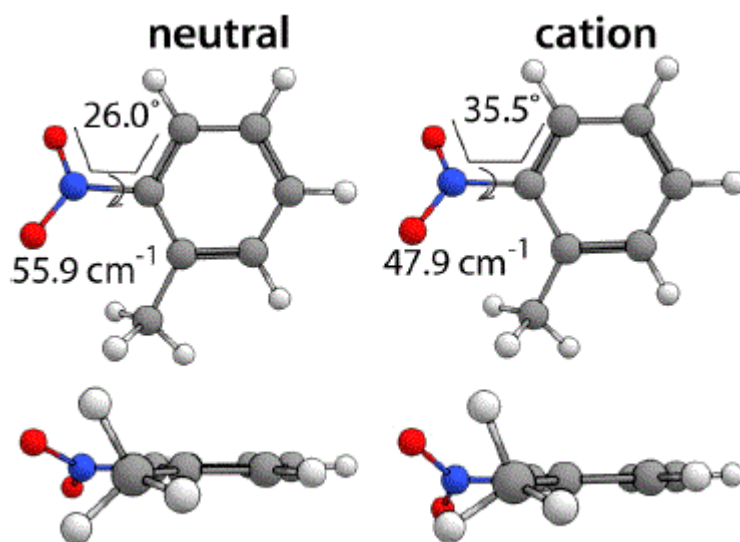
Figure 7.7. Neutral and ion geometries of 2-NT shown in two orientations with torsional angles and frequencies labeled.

The torsional angle for neutral 2-NT is in reasonable agreement with previous theoretical results at the PBE0/6-31+G level reporting an angle of 19.4°[184] and within the magnitude of the estimated equilibrium torsional angle of $35 \pm 15°$ relative to the planar geometry obtained by gas-phase electron diffraction measurements.[200] The calculated vibrational frequency of the torsional mode (shown in Figure 7.7) ranged from 45.0 to 65.7 cm^{-1} in neutral 2-NT and 31.9 to 57.1 cm^{-1} in 2-NT$^+$, depending on the method (Appendix, Tables D4 and D5). The slower predicted oscillation periods of 580−1200 fs as compared to the observed 380 fs (88 cm^{-1}) can be explained by the inherent uncertainty of ∼30−100 cm^{-1} in the computed values; a similar underestimation of the torsional frequency was found for the 4-NT cation in our previous work.[145] We also note that the out-of-plane ring-bending mode calculated at 89.7−105.8 cm^{-1} in 2-NT$^+$ is unlikely to contribute to the observed oscillations because the ring geometry remains planar upon ionization

of 2-NT to 2-NT$^+$ (Figure 7.7). On the basis of these observations, we assign the coherent dynamics to the torsional mode. The coherent dynamics may be analyzed in more detail by fitting the signals $S(\tau)$ for the parent 2-NT$^+$ (C$_7$H$_7$NO$_2{}^+$) and the dissociation products highlighted in Figure 7.6 to the equation

$$S(\tau) = ae^{-\tau/T1}\cos\left(\frac{2\pi}{t}\tau + \emptyset\right) + be^{-\tau/T2} + ce^{-\tau/T3} + d \qquad (7.1)$$

where a, b, and c are amplitude coefficients, t is the oscillation period, T_1 is the coherence lifetime, T_2 is a second incoherent lifetime, T_3 is a third incoherent lifetime, and d is the final ion yield as $\tau \rightarrow \infty$. Each transient signal was fit to eq 7.2 using nonlinear least-squares curve fitting in MATLAB.
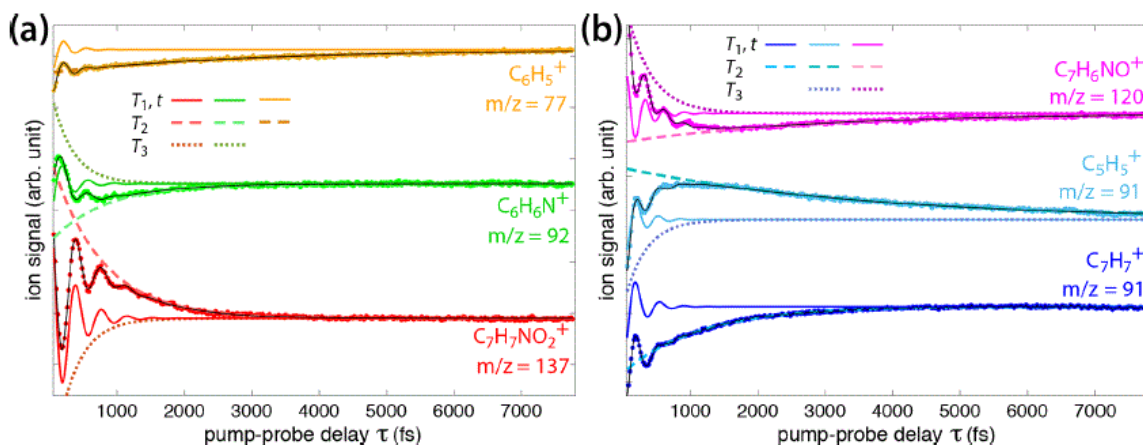
Figure 7.8. Transient signals (dots) of (a) C$_7$H$_7$NO$_2{}^+$ (red), C$_6$H$_6$N$^+$ (green), C$_6$H$_5{}^+$(orange) and (b) C$_7$H$_7{}^+$ (blue), C$_5$H$_5{}^+$(cyan), C$_7$H$_6$NO+(magenta). All transients are shown with fits to eq 7.2 (black lines) and individual components (thick solid, dashed, and dotted lines).

Figure 7.8 shows the transient ion signals at $\tau > 40$ fs (dots) fit to eq 7.2: C$_7$H$_7$NO$_2{}^+$ (red), C$_6$H$_6$N$^+$ (green), and C$_6$H$_5{}^+$ (orange) in Figure 7.8 (a); C$_7$H$_7{}^+$ (blue), C$_5$H$_5{}^+$ (cyan), and C$_7$H$_6$NO$^+$ (magenta) in Figure 7.8 (b). For each transient signal, the fit components corresponding to the coherent T_1 decay (thick solid lines), T_2 decay (dashed lines), and T_3 decay (dotted lines) are shown

in addition to the full fit function (black lines). The $C_7H_7NO_2^+$, $C_5H_5^+$, $C_7H_6NO^+$, and $C_6H_6N^+$ transients required the additional T_3 decay, while the $C_7H_7^+$ and $C_6H_5^+$ transients required only two decay time constants. The coefficients extracted from curve fitting to each transient in Figure 7.8 (a, b) are given in Tables 7.2 and 7.3, respectively.

Table 7.2. Coefficients Extract from Fitting Transient Ion Signal in Figure 7.8 (a) to Equation 7.2.

eq 7.1	$C_7H_7NO_2^+$	$C_6H_6N^+$	$C_6H_5^+$
a	0.124±0.003	0.037±0.004	0.025±0.003
T_1 (fs)	288±7	244±36	188±19
t (fs)	382±2	386±13	338±13
$\emptyset$ (rad)	-0.17±0.03	3.12±0.16	2.23±0.14
b	0.149±0.029	-0.066±0.031	-0.0225±0.0005
T_2 (fs)	760±40	720±120	2930±150
c	-0.15±0.02	0.10±0.03	-
T_3 (fs)	317±31	322±63	-
d	0.594±0.001	0.725±0.001	0.296±0.001

Table 7.3. Coefficients Extract from Fitting Transient Ion Signal in Figure 7.8 (b) to Equation 7.2.

eq 7.1	$C_7H_6NO^+$	$C_6H_6N^+$	$C_7H_7^+$
a	0.072±0.004	0.065±0.006	0.087±0.005
T_1 (fs)	260±17	212±20	210±11
t (fs)	291±3	330±10	361±5
$\emptyset$ (rad)	-0.95±0.08	2.45±0.17	2.91±0.15
b	0.040±0.002	0.076±0.002	-0.096±0.0001
T_2 (fs)	2890±480	3580±280	1100±20
c	0.174±0.003	-0.127±0.004	-
T_3 (fs)	359±14	316±19	-
d	1.131±0.001	0.937±0.001	0.809±0.001

All transient signals have coherent lifetimes (T_1) between approximately 200 and 300 fs, similar to the lifetimes found in 3-NT and 4-NT.[145] In Table 7.2, the oscillation periods (t) are nearly

identical for the parent $C_7H_7NO_2^+$ (382 fs) and $C_6H_6N^+$ transients (386 fs), and their phases are roughly π radians out-of-phase. In contrast, Table 7.3 shows a significantly shorter period of 290 fs for $C_7H_6NO^+$, and its phase is offset from that of the $C_7H_7NO_2^+$ transient by $\pi/4$ radians. The remaining excited-state products $C_6H_5^+$, $C_5H_5^+$, and $C_7H_7^+$ exhibit oscillation periods and phases in between these two extremes. Also, of note are the similar T_3 values in $C_7H_7NO_2^+$, $C_7H_6NO^+$, $C_6H_6N^+$, and $C_5H_5^+$, indicating an incoherent excitation process linking these four transients.
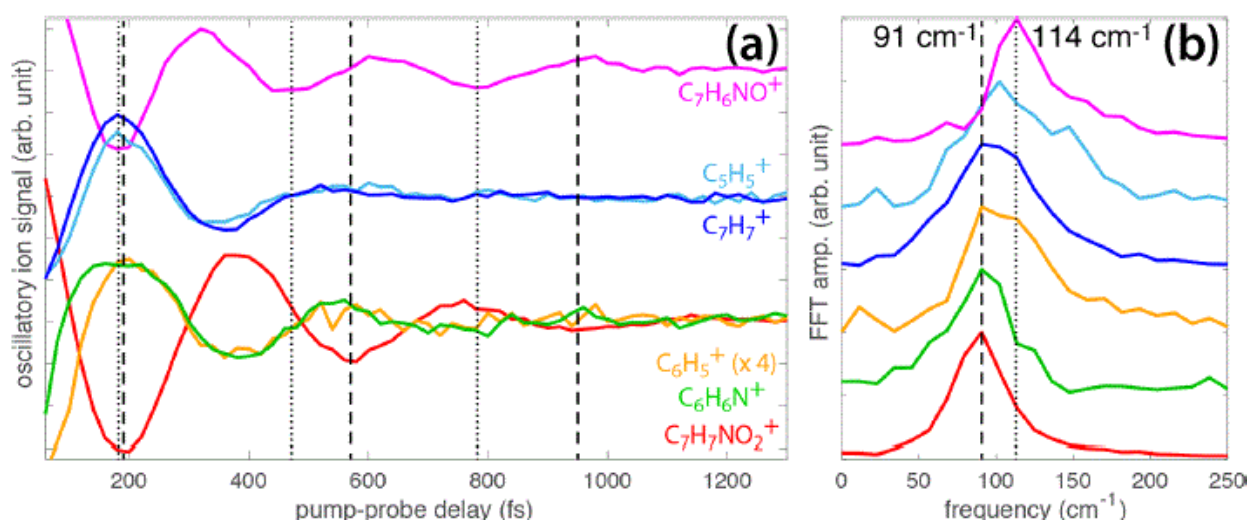
Figure 7.9. (a) Oscillatory components of the transient ion signals of $C_7H_7NO_2^+$ (red), $C_6H_6N^+$ (green), $C_7H_7^+$ (blue), and $C_7H_6NO^+$ (magenta). Dashed and dotted lines denote minima in $C_7H_7NO_2^+$ and $C_7H_6NO^+$, respectively. (b) FFT of signals in (a).

To assess the potential significance of the distinct oscillation periods across the transient ions extracted from curve-fitting, the T_2 and T_3 components of eq 7.2 were subtracted off from each transient ion signal and the residuals plotted in Figure 7.9 (a). The dashed lines at 190, 570, and 950 fs indicate minima in the yield of $C_7H_7NO_2^+$ (red), showing a constant period of 380 fs. Both the $C_6H_6N^+$ (green) and $C_6H_5^+$ (orange) transients exhibit almost perfectly antiphase

oscillations with the parent ion, indicating their formation from its coherent excitation. The $C_7H_7^+$ transient (blue) oscillations are also almost antiphase with the $C_7H_7NO_2^+$, although the first $C_7H_7^+$ minimum at 370 fs is approximately 10 fs ahead of the first $C_7H_7NO_2^+$ maximum at 380 fs. The dotted lines at 180, 470, and 780 fs indicate minima in the $C_7H_6NO^+$ yield, indicating that the oscillation period increases from 290 fs between the first and second minima to 310 fs between the second and third minima. These distinct oscillatory dynamics indicate that a different structure gives rise to the $C_7H_6NO^+$ oscillations as compared to the parent $C_7H_7NO_2^+$ oscillations. The $C_5H_5^+$ signal (cyan) exhibits oscillations that are not perfectly out-of-phase with either the $C_7H_7NO_2^+$ or $C_7H_6NO^+$ transients: its first minimum at 340 fs is 40 fs ahead of the $C_7H_7NO_2^+$ maximum and 20 fs behind the first $C_7H_6NO^+$ maximum at 320 fs. These results suggest that $C_5H_5^+$ can be formed by excitation of both the $C_7H_7NO_2^+$ and $C_7H_6NO^+$ precursor structures.

Fast Fourier transform (FFT) of the oscillatory signals from 60 to 3000 fs in Figure 7.9 (a) are shown in Figure 7.9 (b). The well resolved peak in the $C_7H_7NO_2^+$ signal (red) at 91 cm^{-1} (367 fs period) indicated by the dashed line agrees with the 383 fs oscillation period obtained from fitting to eq 7.2. The $C_6H_6N^+$ (green), $C_6H_5^+$ (orange), and $C_7H_7^+$ (blue) signals also show this peak, although the peaks are somewhat broadened in $C_6H_5^+$ and $C_7H_7^+$. In contrast, the $C_7H_6NO^+$ peak (magenta) is clearly up-shifted to 114 cm^{-1} (293 fs period), indicated by the dotted line, with a long tail extending to the higher frequencies. The asymmetrical peak is consistent with the slowing oscillation period observed in Figure 7.9 (a). The distinctly higher frequency for $C_7H_6NO^+$ provides further evidence that the structure that gives rise to these oscillations is distinct from the parent 2NT$^+$. The $C_5H_5^+$ (cyan) peak is also up-shifted from the $C_7H_7NO_2^+$, frequency, providing further evidence that it can be formed from both the parent 2NT$^+$ and the $C_7H_6NO^+$ precursor structure. In order to rationalize the observation of two distinct coherently excited structures in our

pump−probe data, we present results of computed reaction pathways in 2-NT$^+$ in section 7.3.3 and then propose that the oscillations in the C$_7$H$_6$NO$^+$ yield may be attributed to coherent motion and relaxation of the *aci*-nitro tautomer of 2-NT$^+$ in section 7.3.4.

7.3.3 Computed Reaction Pathways in 2-NT$^+$

We now consider the reaction pathways that lead to the formation of the 2-NT$^+$ fragmentation products C$_7$H$_7^+$, C$_7$H$_6$NO$^+$, and C$_6$H$_6$N$^+$. All computational results were performed with the ωB97XD/CBSB7 method.

7.3.3.1 Direct C-NO2 Bond Homolysis: Formation of C$_7$H$_7^+$.

The similar oscillation periods and offset phases of the C$_7$H$_7$NO$_2^+$ and C$_7$H$_7^+$ transients (Tables 7.2 and 7.3 and Figure 7.9) suggest that coherent excitation of the parent molecular ion results in C−NO$_2$ homolysis to form C$_7$H$_7^+$, as was observed in 3-NT and 4-NT.[145] Computation of this dissociation pathway revealed no transition state and formation of C$_7$H$_7^+$ in the singlet and triplet states at 10.98 and 11.69 eV, respectively (Figure 7.10).
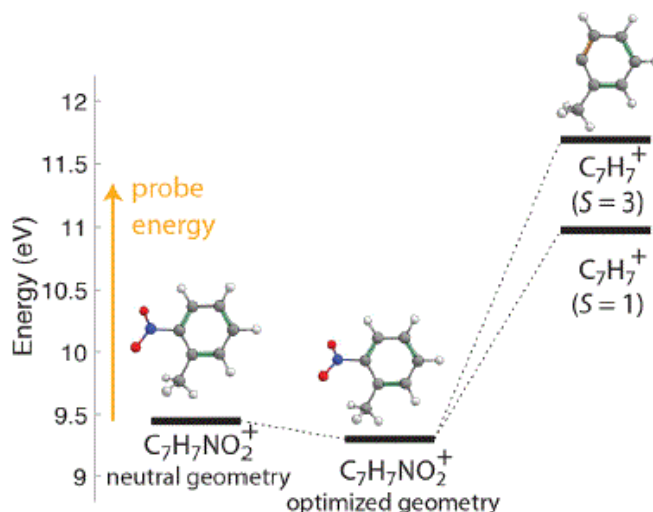
Figure 7.10. Mechanism of NO$_2$ loss from 2-NT$^+$ showing the energy required to form C$_7$H$_7^+$ in both singlet (S = 1) and triplet (S = 3) states. The probe photon energy is shown to scale (orange arrow).

The singlet dissociation energy is in good agreement with recent VUV photoionization experiments giving an appearance energy for $C_7H_7^+$ at 11.01 ± 0.03 eV and calculations at the CBS-QB3 level indicating dissociation at 11.17 eV.[181] The 1.9 eV probe pulse (orange arrow, Figure 7.10) can easily exceed the dissociation barrier to singlet $C_7H_7^+$ formation but does not exceed the barrier for triplet formation, suggesting that the observed $C_7H_7^+$ is formed exclusively in the singlet state.

7.3.3.2. H Atom Attack and OH Loss: Formation of $C_7H_6NO^+$.

The high yield of $C_7H_6NO^+$ in our mass spectra at negative time delay (i.e., in the absence of the probe pulse) indicates that the parent $2NT^+$ can spontaneously undergo *aci*-rearrangement via H atom attack and lose OH on the $\sim\mu s$ flight time in the TOF-MS, consistent with previous mass spectrometry studies.[129,175,176,178–181] According to our computations of the *aci*-rearrangement reaction pathway (Figure 7.11), the reaction has an activation barrier of 0.76 eV from the vertical IP of 9.45 eV.
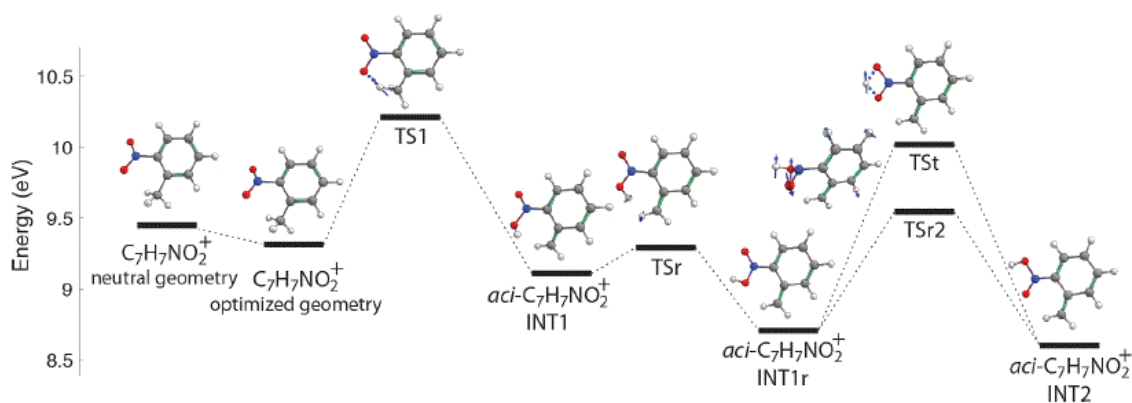
Figure 7.11. Mechanism of *aci*-rearrangement in $2NT^+$ computed at the ωB97XD/CBSB7 level.

This energy is lower than the pump photon energy (0.95 eV at 1300 nm), which suggests that absorption of an additional pump photon during the ionization process can provide the

necessary energy to initiate the H atom attack. Once TS1 is reached and the hydrogen transfers to the nitro oxygen (INT1 in Figure 7.11), a series of rotations (TSr, Int1r, and TSr2 in Figure 7.11) result in the most stable *aci*-nitro tautomer INT2 at 8.62 eV. This mechanism generally agrees with the recently reported pathway computed at the CBS-QB3 level with the 6-311G basis,[181] with three notable exceptions. First, the 10.22 eV energy of the transition state TS1 is 0.2 eV higher than the CBS-QB3 value. Second, the final transition state TSr2 was not reported in the CBS-QB3 results but rather the transition state TSt, which was reported to be the highest-energy transition state in the pathway at 10.16 eV (compared to 10.01 eV in our calculations). Third, the *aci*-nitro tautomer INT2 was reported to be 0.38 eV higher at 9.00 eV. These discrepancies are likely due to the use of a composite method to compute energies with DFT-optimized geometries in ref [181], in contrast to the use of a consistent DFT method to optimize both the geometries and energies in the present calculations. Furthermore, all transition states in our computations were verified with IRC pathway calculations. The corresponding structures (Appendix, Figure D1) clearly show the displacement vectors in each transition state. To estimate the time needed for H atom transfer to the nitro oxygen, ADMP trajectories were computed beginning from TS1 with the excess energy of 0.195 eV from cation relaxation. The zero point vibrational energy (ZPVE) was also included and partitioned among the nonimaginary vibrational modes using microcanonical sampling. Hydrogen transfer was measured using the bond radii R(11−14) (C−H) and R(14−17) (O−H) (Figure 7.12).
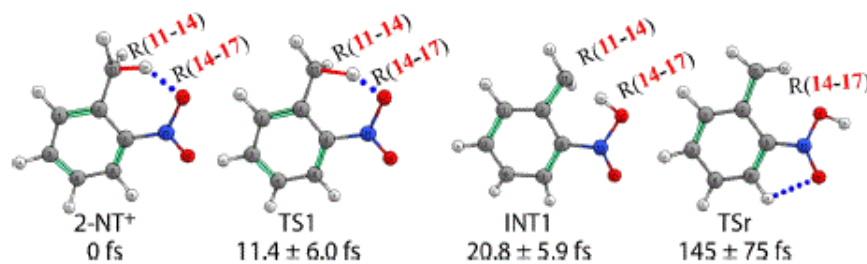
Figure 7.12. Structures involved in the H atom transfer to the nitro oxygen, along with average times required to reach them.

The average times required to reach TS1 and INT1 from the optimized 2-NT$^+$ geometry

obtained by these calculations (Figure 7.12) indicate that the INT1 *aci*-nitro tautomer structure can

be accessed as soon as 20.8 ± 5.9 fs. The average trajectories for the forward (from TS1 to INT1)

and reverse (from TS1 to 2NT$^+$) hydrogen motions leading to the computed reaction time are given

in Figure 7.13.
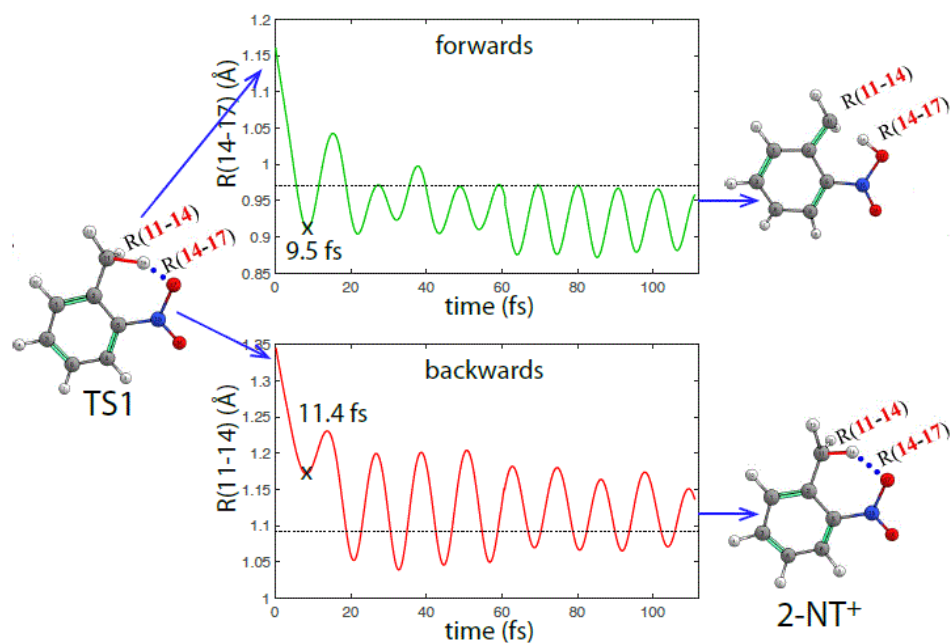
Figure 7.13. Average forward and backward ADMP trajectories showing extracted times for

each H-atom transfer. The black dotted lines denote the equilibrium bond lengths.

Continued simulation of the forward reaction out to 500 fs found that the average time required to

access the next transition state TSr is 145 ± 75 fs. Because the ADMP trajectories were initiated

from TS1, the computed 21 fs time scale likely represents a lower limit on the reaction time. A

more reasonable time scale is on the order of ∼60 fs, which was observed for intramolecular H

atom attack reactions in excited-state methyl salicylate[201] and 2-(2'-hydroxyphenyl)

benzothiazole.[202] The excited-state dynamics leading to such rapid H atom attack in the latter works also suggest that the reaction in 2-NT cation may occur on an excited-state PES, although future computational studies will be needed to test this hypothesis. Nevertheless, the calculations suggest that some population of *aci*-nitro tautomer as structure INT1 is likely present by the time the coherent oscillations are observable beginning at ∼100 fs (cf., Figure 7.9), while the structure's relaxation to the stable structure INT2 is expected to proceed over the next several hundred femtoseconds. As will be discussed in section 7.3.4, both the H atom transfer and relaxation time scales are consistent with the observed oscillations in the $C_7H_6NO^+$ transient arising from coherent torsional motion of the *aci*-nitro tautomer. We next consider pathways to OH loss and formation of $C_7H_6NO^+$ beginning from INT2 (Figure 7.14 and Appendix, Figure D2). The most favorable pathway leads to $C_7H_6NO^+$ in the singlet state and involves first cyclization (TS2 and INT3) followed by OH cleavage to produce $C_7H_6NO^+$ (P2, S = 1, Figure 7.14).
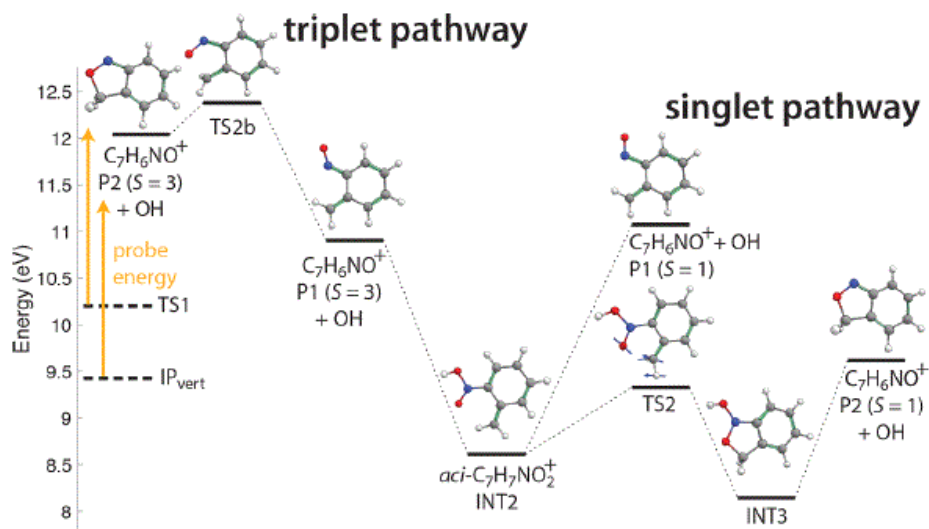
Figure 7.14. Mechanism of dissociation from the *aci*-nitro tautomer to $C_7H_6NO^+$ products formed in the singlet and triplet states.

Because the energy of P2 (9.63 eV, in good agreement with the 9.65 eV reported with CBS-QB3 calculations[181]) is lower than the TS1 energy required to initiate *aci*-rearrangement, this pathway requires no additional input energy, and we can assume that any spontaneously formed *aci*-nitro tautomer will lose OH before reaching the ion detector in our experiments. This result explains the high yield of $C_7H_6NO^+$ at negative time delays in our experiments, which we assign to the $S = 1$ P2 product.

In addition to the spontaneous P2 formation pathway, Figure 7.14 also indicates three higher-energy pathways leading to different $C_7H_6NO^+$ structures that become accessible upon absorption of one probe photon (orange arrows) from either the vertical IP (i.e., by the parent molecular ion 2-NT$^+$) or the *aci*-nitro tautomer with initial energy equal to that of TS1. Direct OH loss from INT2 can form either singlet ($S = 1$) or triplet ($S = 3$) $C_7H_6NO^+$ as structure P1 with energies of 11.07 and 10.90 eV, respectively. The $S = 3$ product can then cyclize with an additional 1.32 eV energy through TS2b to produce the cyclic P2 in the triplet state. These dissociation pathways, which are only accessible upon probe excitation, explain the presence of the T_3 time scale in the transient ion signals of the parent 2-NT$^+$ and $C_7H_6NO^+$, where the opposite signs of the corresponding amplitude coefficients (c in Tables 7.2 and 7.3) indicate that direct excitation of the parent ion can induce OH loss. As a result, the T_3 contribution to the $C_7H_6NO^+$ signal in our experiments is expected to arise from both the singlet state P1 and triplet state P1/P2 dissociation pathways.

7.3.3.3. CO Loss from $C_7H_6NO^+$: Formation of $C_6H_6N^+$.

Finally, we turn to the CO loss pathway from $C_7H_6NO^+$ to form $C_6H_6N^+$. Previous theoretical studies examined CO loss from only the singlet $C_7H_6NO^+$ product (P2, Figure 7.14), which indicated a large 2.61 eV dissociation barrier.[181] We computed the CO loss pathways

beginning from the P2 structures in both the singlet and triplet states (Figure 7.15 (a, b) respectively, and Appendix, Figures D3 and D4).
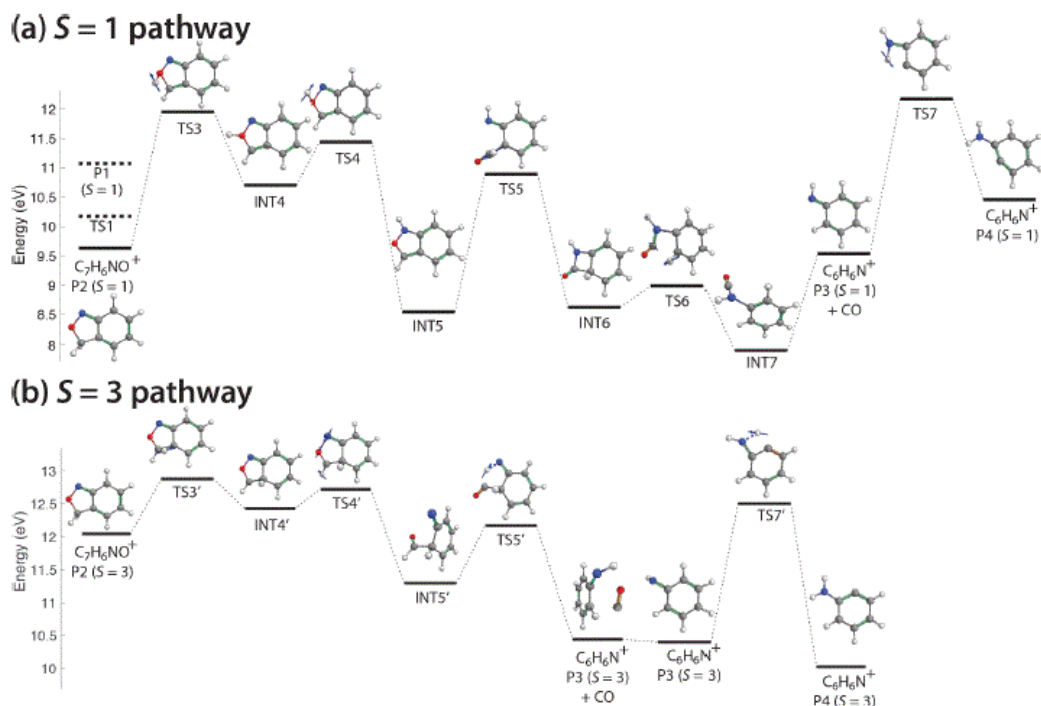
Figure 7.15. Mechanism of CO loss from $C_7H_6NO^+$ products P2 formed in (a) singlet and (b) triplet states.

In rough agreement with ref [181], the singlet $C_7H_6NO^+$ requires 2.32 eV to lose the CO moiety. These results indicate that the $C_7H_6NO^+$ formed via the lowest-energy singlet pathway in Figure 7.15 does not have enough energy to lose CO, even when taking into consideration the TS1 energy, as the energy barrier to reach TS3 is still 1.73 eV. In contrast, the singlet P1 that becomes accessible following absorption of a probe photon (dashed line, Figure 7.15 (a)) only requires an extra 0.88 eV to induce a series of hydrogen atom migrations and internal rotations that leads to CO loss and production of the $C_6H_6N^+$ product P3 (Figure 7.15 (a)). From the triplet P2, an additional energy input of 0.84 eV initiates a more direct CO loss pathway to form P3 in the triplet state (Figure 7.15 (b)). We note that an additional higher-energy triplet dissociation pathway

analogous to the singlet pathway in Figure 7.15 (a) was also identified, as shown in the Appendix, Figures D5 and D6. Collectively, these computed dissociation pathways suggest that the $C_7H_6NO^+$ formed in either the singlet or triplet state upon absorption of a probe photon can lose CO with little additional energy input. Therefore, both the observed T_3 relaxation time scale and oscillations in the $C_6H_6N^+$ fragment can be attributed to excitation of the parent ion by the probe pulse.

7.3.4 Preservation of Vibrational Coherence

The distinct oscillatory dynamics observed in the $C_7H_6NO^+$ ion as compared to other ions (Figure 7.9) suggests that its precursor is a distinct structure from the parent 2-NT$^+$. Coupled to the ADMP results in Figure 7.12 and previous pump−probe results on intramolecular H atom attack in excited-state neutrals,[201,202] we propose that these oscillations arise from coherent vibrational dynamics in the *aci*-nitro tautomer of 2-NT$^+$. The *aci*-nitro tautomer as structure INT1 is predicted to form as early as ∼20 fs based on the ADMP results and at least by ∼60 fs based on earlier experiments.[201,202] Therefore, INT1 is expected to be present for the dynamics recorded after 60 fs in Figure 7.9. The subsequent relaxation of INT1 to the more stable INT1r and INT2 structures is predicted to occur over the next several hundred fs. These *aci*-nitro tautomer structures are predicted to have higher frequency torsional vibrations (86.9 cm^{-1} for INT1, 61.0 cm^{-1} for INT1r, and 79.8 cm^{-1} for INT2, Figure 7.16) than the 2-NT cation at 47.9 cm^{-1}.
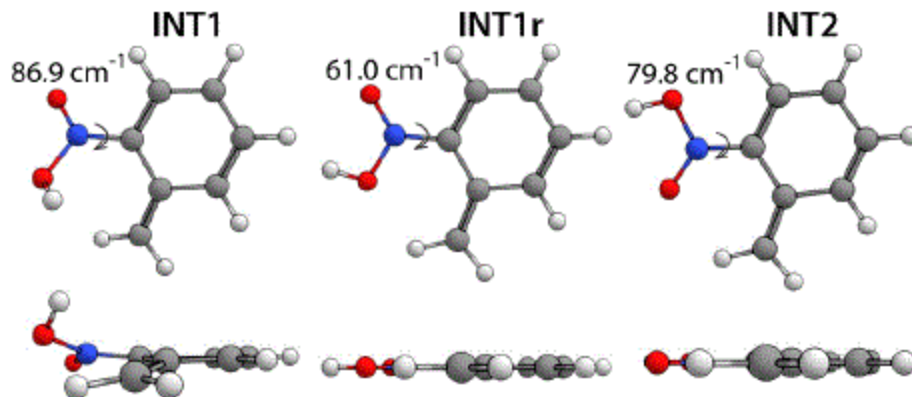
Figure 7.16. *Aci* structures.

These results suggest that the faster 114 cm^{-1} oscillations observed in the C$_7$H$_6$NO$^+$ transient as compared to the 91 cm^{-1} oscillations of the parent 2-NT$^+$ (Figure 7.9) may be attributed to the coherent torsional motion of the *aci*-nitro tautomer. Additional insight into the dynamics of conversion from the initial INT1 *aci*-nitro tautomer to the INT1r and INT2 structures can be gained through analysis of the slowing oscillations of the C$_7$H$_6$NO$^+$ transient with increasing pump−probe delay, as noted in Figure 7.9. The oscillatory component of the C$_7$H$_6$NO$^+$ signal from Figure 7.9 was fit to an exponentially decaying cosine function

$$S(\tau) = ae^{-\frac{\tau}{T}} \cos\left(2\pi f \tau + \emptyset\right) \tag{7.2}$$

with frequency $f = 115$ cm^{-1} and phase $\phi = -0.97$ rad, as well as an exponentially decaying linearly chirped cosine function

$$S(\tau) = ae^{-\tau/T} \cos\left(2\pi\left[f_0\tau + \frac{1}{2}k\tau^2\right] + \emptyset_0\right) \tag{7.3}$$

with initial frequency $f_0 = 127$ cm^{-1}, chirp rate $k = 0.972$ ps^{-2}, and initial phase $\phi_0 = -1.22$ rad. The experimental C$_7$H$_6$NO$^+$ oscillatory signals fit to both equations 7.2 (red) and 7.3 (blue) is shown in Figure 7.17. The dotted lines corresponding to the ion yield minima at 180, 470, and 780

fs match to within $\pm$ 2 fs of the minima in eq 7.3, while the second and third minima of eq 7.2 are 6 fs behind and 34 fs ahead of the experimental minima, respectively. The instantaneous frequency $f(\tau)$ according to eq 7.3 decreases from 121 cm^{-1} at 180 fs to 101 cm^{-1} at 780 fs.
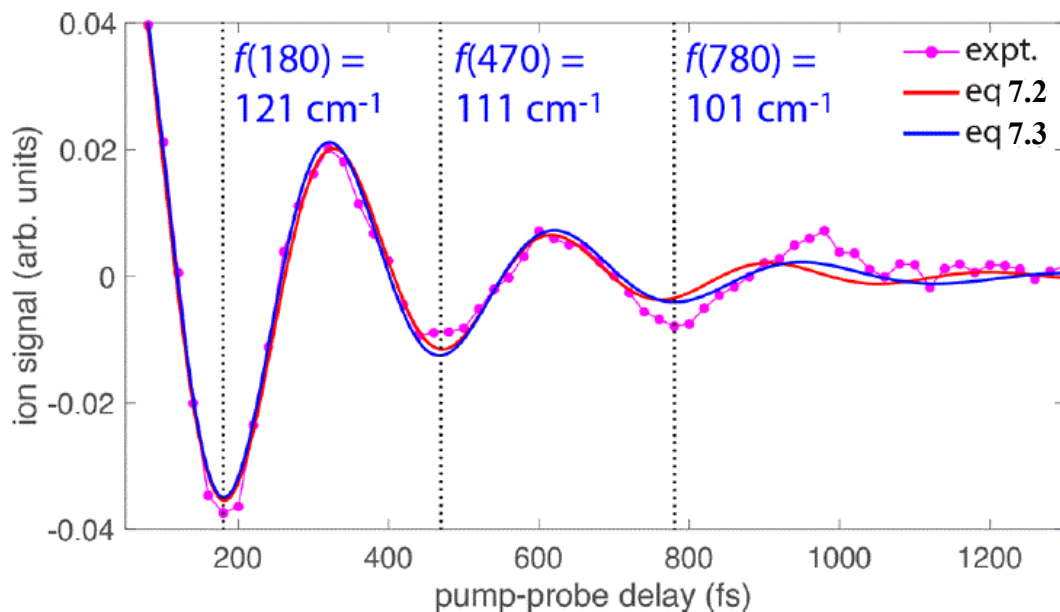
Figure 7.17. Oscillatory $C_7H_6NO^+$ ion signal (magenta dots) fit to eq 7.2 (red) and 7.3 (blue). Dotted lines indicate minima in the experimental ion yield.

This 17% decrease in the instantaneous frequency is in between the ~30% frequency decrease between INT1 and INT1r and the 8% decrease between INT1 and INT2 seen in Figure 7.16. Although the expected errors in computed frequencies preclude a direct comparison between the experimental and computed frequencies, the observed frequency decrease suggests that some mixture of INT1, INT1r, and INT2 structures is present by 780 fs after ionization. The collective experimental and computational results discussed above provide substantial evidence that the observed slowing oscillations in the $C_7H_6NO^+$ product can be assigned to the coherent torsional motion of the *aci*-nitro tautomer and its conversion from the initially formed INT1 to more stable structures. This finding indicates that the initially prepared vibrational coherence in the parent 2-

NT$^+$ ion is preserved following the H atom attack that forms the *aci*-nitro tautomer. To the best of our knowledge, this result is the first report of conserved vibrational coherence upon intramolecular rearrangement in a radical cation. These results build on a previous study showing conserved vibrational coherence following H atom transfer in neutral excited 2-(2′-hydroxyphenyl)-benzothiazole.[202] Additional recent studies have reported conserved vibrational coherence following internal conversion in excited cyclohexadiene,[203] benzonitriles,[204,205] Rydberg states of N-methyl morpholine,[197,198] and azobenzene radical cation.[137] CO loss from excited-state metal hexacarbonyls has also been reported to result in coherent vibrational motion of the remaining metal pentacarbonyl.[206–208] In 2-NT cation, we attribute this coherence conservation to the exceptionally fast H atom attack within ∼20−60 fs, which maintains the localized vibrational excitation along the torsional coordinate before intramolecular vibrational energy redistribution (IVR) can occur.

7.3.5. Summary of 2-NT$^+$ Rearrangement and Dissociation Dynamics.

The experimental and theoretical results presented in the previous sections are combined to form our current understanding of 2-NT$^+$ rearrangement and dissociation dynamics, presented in Figure 7.18. The black structure denotes the *aci*-nitro tautomer intermediate, while the colored structures correspond to the products indicated in Figures 7.5, 7.8, and 7.9. The colored arrows denote excitation by the pump (dark red) or probe (orange), the solid black arrows denote reaction pathways computed in section 7.3.3, and the dotted arrows denote additional proposed pathways toward observed dissociation products. The reaction pathways labeled **I** through **IV** are summarized below.
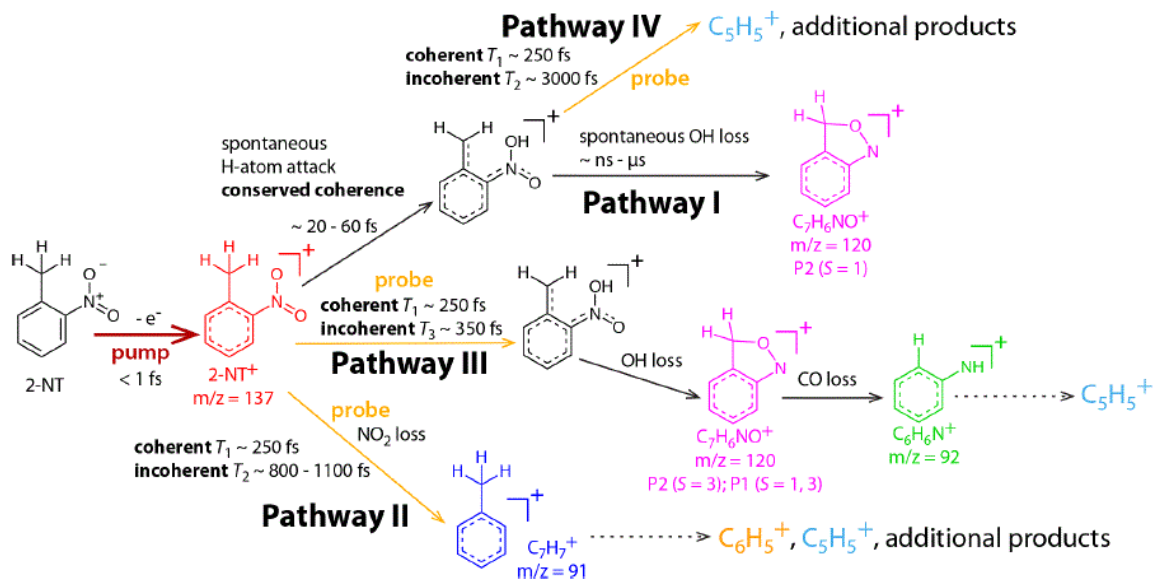
Figure 7.18. Tentative dissociation pathway scheme.

First, the pump pulse ionizes 2-NT to produce 2-NT$^+$. In the absence of probe pulse excitation, a significant fraction of the ions produced undergo no further dissociation, producing the large peak at m/z = 137 seen in Figure 7.5 (a) at negative time delay and denoted as the red parent ion in Figure 7.18. Much of the remaining parent ion population has sufficient energy to overcome the *aci*-rearrangement energy barrier of 0.76 eV (Figure 7.11), which produces the *aci*-nitro tautomer as structure INT1 (Figure 7.11) as early as ~20 fs according to our ADMP simulations (Figure 7.12). The calculated reaction pathway shown in Figure 7.13 indicates that the *aci*-nitro tautomer is expected to spontaneously lose OH to form $C_7H_6NO^+$ at m/z = 120 (magenta) via pathway I in Figure 7.18. This pathway produces exclusively $C_7H_6NO^+$ structure P2 with S = 1 (Figure 7.13). The high yield of m/z = 120 at negative time delays (Figure 7.5) is consistent with pathway I requiring no probe excitation.

We next consider the pathways induced by excitation of the parent 2-NT$^+$ (red in Figure 7.18) structure with the probe pulse. Probe excitation can induce direct NO$_2$ loss from the parent

ion to produce $C_7H_7^+$ (m/z = 91, blue, pathway II). This direct dissociation pathway occurs following coherent probe excitation on the T_1 time scale of ∼250 fs based on the observed oscillations, as well as the incoherent T_2 time scale of 800−1100 fs (Tables 7.2 and 7.3). The $C_7H_7^+$ may further dissociate to form $C_6H_5^+$, $C_5H_5^+$, and other smaller products. In particular, the nearly perfect antiphase oscillations of $C_6H_5^+$ with the parent ion suggest that the coherent pathway II can form this product. The additional sequential dissociation pathway III involves first *aci*-rearrangement induced by probe excitation, followed by OH loss to form $C_7H_6NO^+$ (magenta) as structure P1 with S = 1,3 and/or P2 with S = 3 (Figure 7.13).

A portion of this excited $C_7H_6NO^+$ undergoes subsequent CO loss to form $C_6H_6N^+$ (green). These species arise from an incoherent excitation pathway on the T_3 time scale of ∼350 fs and could be formed as either singlet or triplet products (Figures 7.13 and 7.14). It is worth noting that the $C_6H_6N^+$ product also exhibits antiphase oscillations with the same frequency as the parent ion, suggesting that coherent excitation on the T_1 time scale can also initiate dissociation via pathway III. However, the lack of corresponding oscillations at the same frequency and phase in the $C_7H_6NO^+$ product suggests that the coherently excited parent ion undergoes the full sequential dissociation shown in pathway III to form $C_6H_6N^+$. Finally, the presence of the T_3 time scale in the $C_5H_5^+$ ion suggests that the $C_6H_6N^+$ can undergo further dissociation to form this product. Finally, we consider the interaction of the spontaneously formed *aci*-nitro tautomer with the probe pulse (pathway IV). The coherent dynamics of this species discussed in section 7.3.4 indicate that one or more dissociation products can be formed upon its coherent excitation. On the basis of the observed $C_5H_5^+$ oscillations being close to antiphase with the $C_7H_6NO^+$ (Figure 7.9), it is likely that $C_5H_5^+$ is a significant product of *aci*-nitro tautomer excitation. Additionally, the observation that the oscillations in the m/z = 91 product (assigned to $C_7H_7^+$) are somewhat shifted from

antiphase with the parent ion suggests that an additional product with this m/z value, i.e., $C_6H_5N^+$, may be formed by excitation of the *aci*-nitro tautomer. The presence of small amounts of m/z = 89 and 90 (likely $C_6H_3N^+$ and $C_6H_4N^+$) observable in Figure 7.5 suggests that such dissociation pathways involving the loss of one or more H atoms are possible.

7.4. Conclusions

Coherent vibrational dynamics in 2-NT radical cation were probed using strong-field adiabatic ionization with near infrared pulses and cation excitation with visible pulses. Observed oscillations in ion yields with pump−probe delay were attributed to the coherent excitation of the C−NO$_2$ torsional motion in the parent 2-NT cation. This vibrational coherence was found to be preserved upon spontaneous H atom attack to form the *aci*-nitro tautomer based on the faster oscillations in the $C_7H_6NO^+$ ion formed by −OH loss from the *aci*-nitro tautomer structure. A series of DFT calculations both supported the assertion of preserved coherence in the *aci*-nitro tautomer and determined the H atom attack mechanism involving three *aci*-nitro tautomer structures. The subsequent −OH and −CO loss pathways from the *aci*-nitro tautomer determined through DFT calculations found that these dissociation reactions could produce both singlet and triplet $C_7H_6NO^+$ products. Collectively, these results provide a detailed picture of the coherent and incoherent excitation pathways in 2-NT radical cation that lead to the formation of multiple dissociation products. Future high-level calculations of ground- and excited-state potential energy surfaces in 2-NT cation and the *aci*-nitro tautomer, along with additional time-resolved measurements with different probe wavelengths, could provide further insight into the specific excited states accessed by the coherent excitation pathways observed in this work. Building on the present results, such additional studies could help develop efficient coherent control schemes for 2-NT and other nitroaromatic energetic molecules.

8.0 CONCLUSIONS

Understanding ultrafast dissociation mechanisms of isolated radical cations of nitroaromatic and organophosphorus compounds not only provides insight into the photodissociation reaction of energetic molecules and chemical warfare agents, but also provides a base line comparison to condensed-phase processes such as radiations induced DNA damage. These experiments in the gas phase isolate relevant dynamics from interference of solvent effect to allow for an effective study of dynamics. Femtosecond time-resolved mass spectrometry (FTRMS) with the pump-probe technique was applied to two sets of model compounds, organophosphorus and nitroaromatic compounds. The pump-probe technique in these experiments made use of a short intense near infrared pump pulse and a weak visible probe pulse, which enabled measurements of coherent vibrational dynamics in parent radical cation to be recorded in the time domain. The observation of these vibrational dynamics is a result of nuclear wave packets that are generated upon a vertical electronic excitation in accordance with the Frank Condon principle upon encountering an ionizing laser pulse. This results in the simultaneous population of multiple eigen states with the superposition of the wavefunction, generating a constructive and destructive interference in time across the potential energy well. The oscillatory dynamics are a result of the coherent vibrational motion on the potential energy surface when monitored with a weak probe pulse. The oscillatory dynamics could be observed in various fragments and obtained as a function of pump probe delay extending over a range from -500 (i.e., probe before pump) to up to 8000 fs. These oscillatory dynamics were converted to the frequency domain to access their vibrational frequencies. To understand and interpret the observed vibrational frequencies, DFT calculations using various methods and basis sets were employed. Amongst previously studied polyatomic molecules, the organophosphates and nitroaromatic compounds have been observed to have very

fast oscillations. In previous experiments, low-frequency oscillation observed in polyatomic ions was a bending mode (~90-130 cm^{-1})[47,89,90] and even slower torsional modes exhibited oscillations 600-1000 fs.[39,44,91–94] With these molecules only 2-6 visible oscillation periods above the noise level were observed.[39,44,47,89,91–94] In contrast, some of the molecules studied in this research had between 7-12 visible oscillation periods and faster oscillations with bending and stretching modes 550-750 cm^{-1}.

The time dependent yields of DMMP, DIMP, DEMP and TMP parent molecular ions exhibited ultrafast oscillations with the period depending on the parent molecule. In DMMP, a well resolved peak of 45 fs (732 ± 28 cm^{-1}) was observed with a weak feature at 610-650 cm^{-1}, while DIMP exhibits bimodal oscillation with frequencies of 554 ± 28 and 670-720 cm^{-1}. Oscillations for DEMP were barely visible due to rapid decay. The high- and low- frequency oscillations in DMMP and DIMP were assigned to coherent excitation of P-C and O-P-O bend stretching respectively based on DFT calculations. Bimodal oscillations at 770 and 880 cm^{-1} in TMP were also observed and are tentatively assigned to the symmetric and asymmetric P-O stretching modes.

The oscillation frequencies observed in three derivatives PNT (85 cm^{-1}), ONT (91 cm^{-1}), and NB (80 cm^{-1}) were assigned to the torsional motion of the NO_2 group with respect to the benzene ring based on DFT calculations. In literature, torsional motion of slower frequencies can also be observed in other substituted benzene such as acetophenone (55 cm^{-1}), [39,44] and azobenzene (33 cm^{-1}).[137] The finding from this research and literature puts into contest of more evidence of torsional motion as a general featured exhibited by most substituted benzenes. The frequency observed in MNT (160 cm^{-1}) was roughly twice as fast compared to the others. After further investigation this frequency was assigned to a symmetric bending mode of the CH_3 and NO_2

moiety. The close proximity of the hydrogen and oxygen atom in ONT induces a unique reaction called the H attack. This process generates an *aci*-nitro tautomer which yields a unique oscillation frequency much faster than the torsional motion (91 cm^{-1}) exhibited by the parent ion. The oscillation frequency generated by *aci*-nitro tautomer is said to also exhibit the torsional motion (114 cm^{-1}). The oscillation frequency of 114 cm^{-1} observed in the fragment with m/z =120 which preserves the torsional motion was also supported by series of DFT calculations.

The results obtained from this research demonstrate that femtosecond time-resolved mass spectrometry (FTRMS) with near-infrared excitation limits fragmentation of the parent ion, which enables these molecular cations to be isolated and studied for their dissociation dynamics on the femtosecond time-scale. Coupled with high level quantum calculations, the potential energy surfaces (PES) of the cations of these molecules can be mapped out, and vibrational frequencies and dissociation dynamics can be obtained, laying down the foundation to understand the fundamental reactions of the molecules. In principle, FTRMS can be used as an analytical tool to discriminate between molecules based on their unique vibrational frequencies and dynamics. For example, since organophosphorus (nerve agents) and nitroaromatic (explosives) compounds have unique dynamics, FTRMS can detect them from other similar compounds.

Understanding coherent control in organophosphorus compounds could lay a foundation for developing sensors and catalysts that can detect and drive the decomposition of chemical warfare agents. The reaction pathways of organophosphorus compounds in the gas phase can be used as a baseline to understand reactions of ionized DNA in the condensed phase and also predict the hydrogen atom transfer scales in ionized DNA. The coherent control in nitroaromatics could inform the development of photolabile explosives. The results obtained indicate that explosives could be selectively initiated upon interacting with a laser, which could help to design energetic

materials for military purposes. Furthermore, information gathered from this research could help build a portable device used as advance alert system to help save lives of US troops on the battlefield and also to combat terrorism. A soldier could simply press a button on a portable device to fire a laser and detects an explosive hidden in an abandoned car 50 meters away as he beckons his vehicle away to safety. With this technology, security agencies can do a quick and accurate sweep of traces of explosives in public places and also detect explosives hidden on terrorists by aiming a laser, which confirms and alerts security agencies. In addition, this technology can be used by investigators to search for traces of explosives after a terror attack.[209,210]

List of References

(1) Snow, T. P.; Bierbaum, V. M. Ion Chemistry in the Interstellar Medium. *Annu. Rev. Anal. Chem.* **2008**, *1* (1), 229–259. https://doi.org/10.1146/annurev.anchem.1.031207.112907.

(2) Kuklja, M. M.; Tsyshevsky, R. V.; Sharia, O. Effect of Polar Surfaces on Decomposition of Molecular Materials. *J. Am. Chem. Soc.* **2014**, *136* (38), 13289–13302. https://doi.org/10.1021/ja506297e.

(3) Prier, C. K.; Rankic, D. A.; MacMillan, D. W. C. Visible Light Photoredox Catalysis with Transition Metal Complexes: Applications in Organic Synthesis. *Chem. Rev.* **2013**, *113* (7), 5322–5363. https://doi.org/10.1021/cr300503r.

(4) Sevilla, M. D.; Becker, D.; Kumar, A.; Adhikary, A. Gamma and Ion-Beam Irradiation of DNA: Free Radical Mechanisms, Electron Effects, and Radiation Chemical Track Structure. *Radiat. Phys. Chem.* **2016**, *128*, 60–74. https://doi.org/10.1016/j.radphyschem.2016.04.022.

(5) Gibson, Q. H. [6] Rapid Mixing: Stopped Flow. In *Methods in Enzymology*; Fast Reactions; Academic Press, 1969; Vol. 16, pp 187–228. https://doi.org/10.1016/S0076-6879(69)16009-7.

(6) Porter, G.-N.; Norrish, R. G. W. Flash Photolysis and Spectroscopy. A New Method for the Study of Free Radical Reactions. *Proc. R. Soc. Lond. Ser. Math. Phys. Sci.* **1950**, *200* (1061), 284–300. https://doi.org/10.1098/rspa.1950.0018.

(7) Wall, K.F.; Sanchez, A. Titanium Sapphire Lasers. *Linc. Lab. J.* **1990**, *3*, 447–462.

(8) Zewail, A. H. Laser Selective Chemistry—Is It Possible? *Phys. Today* **1980**, *33* (11), 27–33. https://doi.org/10.1063/1.2913821.

(9) Zewail, A. H. Femtochemistry: Atomic-Scale Dynamics of the Chemical Bond. *J. Phys. Chem. A* **2000**, *104* (24), 5660–5694. https://doi.org/10.1021/jp001460h.

(10) Dantus, M.; Rosker, M. J.; Zewail, A. H. Femtosecond Real-time Probing of Reactions. II. The Dissociation Reaction of ICN. 14.

(11) Zeng, Z.; Bernstein, E. R. Photoelectron Spectroscopy and Density Functional Theory Studies of N-Rich Energetic Materials. *J. Chem. Phys.* **2016**, *145* (16), 164302. https://doi.org/10.1063/1.4964944.

(12) Yuan, B.; Yu, Z.; Bernstein, E. R. Initial Mechanisms for the Decomposition of Electronically Excited Energetic Salts: TKX-50 and MAD-X1. *J. Phys. Chem. A* **2015**, *119* (12), 2965–2981. https://doi.org/10.1021/jp510995z.

(13) Yuan, B.; Bernstein, E. R. Initial Mechanisms for the Unimolecular Decomposition of Electronically Excited Bisfuroxan Based Energetic Materials. *J. Chem. Phys.* **2017**, *146* (1), 014301. https://doi.org/10.1063/1.4972259.

(14) Yuan, B.; Bernstein, E. R. Initial Mechanisms for the Unimolecular Decomposition of Electronically Excited Nitrogen-Rich Energetic Materials with Tetrazole Rings: 1-DTE, 5-DTE, BTA, and BTH. *J. Chem. Phys.* **2016**, *144* (23), 234302. https://doi.org/10.1063/1.4953552.

(15) Greenfield, M. T.; McGrane, S. D.; Bolme, C. A.; Bjorgaard, J. A.; Nelson, T. R.; Tretiak, S.; Scharff, R. J. Photoactive High Explosives: Linear and Nonlinear Photochemistry of Petrin Tetrazine Chloride. *J. Phys. Chem. A* **2015**, *119* (20), 4846–4855. https://doi.org/10.1021/acs.jpca.5b02092.

(16) Soto, J.; Arenas, J. F.; Otero, J. C.; Peláez, D. Effect of an S1/S0 Conical Intersection on the Chemistry of Nitramide in Its Ground State. A Comparative CASPT2 Study of the Nitro-Nitrite Isomerization Reactions in Nitramide and Nitromethane. *J. Phys. Chem. A* **2006**, *110* (26), 8221–8226. https://doi.org/10.1021/jp0617219.

(17) Im, H.-S.; Bernstein, E. R. On the Initial Steps in the Decomposition of Energetic Materials from Excited Electronic States. *J. Chem. Phys.* **2000**, *113* (18), 7911–7918. https://doi.org/10.1063/1.1315609.

(18)   Greenfield, M.; Guo, Y. Q.; Bernstein, E. R. Ultrafast Photodissociation Dynamics of HMX and RDX from Their Excited Electronic States via Femtosecond Laser Pump–Probe Techniques. *Chem. Phys. Lett.* **2006**, *430* (4–6), 277–281. https://doi.org/10.1016/j.cplett.2006.09.025.

(19)   Guo, Y. Q.; Greenfield, M.; Bernstein, E. R. Decomposition of Nitramine Energetic Materials in Excited Electronic States: RDX and HMX. *J. Chem. Phys.* **2005**, *122* (24), 244310. https://doi.org/10.1063/1.1929741.

(20)   Guo, Y. Q.; Greenfield, M.; Bhattacharya, A.; Bernstein, E. R. On the Excited Electronic State Dissociation of Nitramine Energetic Materials and Model Systems. *J. Chem. Phys.* **2007**, *127* (15), 154301. https://doi.org/10.1063/1.2787587.

(21)   Guo, Y.; Bhattacharya, A.; Bernstein, E. R. Ultrafast S_1 to S_0 Internal Conversion Dynamics for Dimethylnitramine through a Conical Intersection. *J. Phys. Chem. A* **2011**, *115* (34), 9349–9353. https://doi.org/10.1021/jp109150u.

(22)   Guo, Y. Q.; Bhattacharya, A.; Bernstein, E. R. Excited Electronic State Decomposition of Furazan Based Energetic Materials: 3,3′-Diamino-4,4′-Azoxyfurazan and Its Model Systems, Diaminofurazan and Furazan. *J. Chem. Phys.* **2008**, *128* (3), 034303. https://doi.org/10.1063/1.2822283.

(23)   Guo, Y. Q.; Bhattacharya, A.; Bernstein, E. R. Photodissociation Dynamics of Nitromethane at 226 and 271 Nm at Both Nanosecond and Femtosecond Time Scales. *J. Phys. Chem. A* **2009**, *113* (1), 85–96. https://doi.org/10.1021/jp806230p.

(24)   Bhattacharya, A.; Bernstein, E. R. Nonadiabatic Decomposition of Gas-Phase RDX through Conical Intersections: An ONIOM-CASSCF Study. *J. Phys. Chem. A* **2011**, *115* (17), 4135–4147. https://doi.org/10.1021/jp109152p.

(25)   Guo, Y.; Bhattacharya, A.; Bernstein, E. R. Decomposition of Excited Electronic State S-Tetrazine and Its Energetic Derivatives. *J. Chem. Phys.* **2011**, *134* (2), 024318. https://doi.org/10.1063/1.3523649.

(26)   Bhattacharya, A.; Guo, Y. Q.; Bernstein, E. R. Experimental and Theoretical Exploration of the Initial Steps in the Decomposition of a Model Nitramine Energetic Material: Dimethylnitramine. *J. Phys. Chem. A* **2009**, *113* (5), 811–823. https://doi.org/10.1021/jp807247t.

(27)   Bhattacharya, A.; Guo, Y.; Bernstein, E. R. A Comparison of the Decomposition of Electronically Excited Nitro-Containing Molecules with Energetic Moieties C–NO2, N–NO2, and O–NO2. *J. Chem. Phys.* **2012**, *136* (2), 024321. https://doi.org/10.1063/1.3668139.

(28)   Yu, Z.; Bernstein, E. R. Decomposition of Pentaerythritol Tetranitrate [C(CH2ONO2)4] Following Electronic Excitation. *J. Chem. Phys.* **2011**, *135* (15), 154305. https://doi.org/10.1063/1.3652893.

(29)   Yu, Z.; Bernstein, E. R. Experimental and Theoretical Studies of the Decomposition of New Imidazole Based Energetic Materials: Model Systems. *J. Chem. Phys.* **2012**, *137* (11), 114303. https://doi.org/10.1063/1.4752654.

(30)   Yu, Z.; Bernstein, E. R. On the Decomposition Mechanisms of New Imidazole-Based Energetic Materials. *J. Phys. Chem. A* **2013**, *117* (8), 1756–1764. https://doi.org/10.1021/jp312527u.

(31)   Zhuang, X.; Wang, J.; Lan, Z. Photoinduced Nonadiabatic Decay and Dissociation Dynamics of Dimethylnitramine. *J. Phys. Chem. A* **2013**, *117* (23), 4785–4793. https://doi.org/10.1021/jp402180p.

(32)   Kimmel, A. V.; Sushko, P. V.; Shluger, A. L.; Kuklja, M. M. Effect of Charged and Excited States on the Decomposition of 1,1-Diamino-2,2-Dinitroethylene Molecules. *J. Chem. Phys.* **2007**, *126* (23), 234711. https://doi.org/10.1063/1.2741530.

(33)   Tsyshevsky, R. V.; Garifzianova, G. G.; Shamov, A. G.; Khrapkovskii, G. M. Fragmentation Reactions in the 1-Nitropropane Radical Cation Induced by γ-Hydrogen Shift: Ab Initio Study. *Int. J. Mass Spectrom.* **2014**, *369*, 36–43. https://doi.org/10.1016/j.ijms.2014.06.002.

(34)   Nguyen Van, B.; Nikolaeva, E. V.; Shamov, A. G.; Khrapkovskii, G. M.; Tsyshevsky, R. V. Exploration of Decomposition Pathways of 2,4,6-Trinitrotoluene (TNT) Radical Ions by Means of Density Functional Theory. *Int. J. Mass Spectrom.* **2015**, *392*, 7–15. https://doi.org/10.1016/j.ijms.2015.08.016.

(35) Jeilani, Y. A.; Duncan, K. A.; Newallo, D. S.; Thompson, A. N.; Bose, N. K. Tandem Mass Spectrometry and Density Functional Theory of RDX Fragmentation Pathways: Role of Ion–Molecule Complexes in Loss of NO3 and Lack of Molecular Ion Peak. *Rapid Commun. Mass Spectrom.* **2015**, *29* (9), 802–810. https://doi.org/10.1002/rcm.7167.

(36) Florián, J.; Gao, L.; Zhukhovskyy, V.; MacMillan, D. K.; Chiarelli, M. P. Nitramine Anion Fragmentation: A Mass Spectrometric and Ab Initio Study. *J. Am. Soc. Mass Spectrom.* **2007**, *18* (5), 835–841. https://doi.org/10.1016/j.jasms.2007.01.009.

(37) Postler, J.; Goulart, M. M.; Matias, C.; Mauracher, A.; da Silva, F. F.; Scheier, P.; Limão-Vieira, P.; Denifl, S. Dissociative Electron Attachment to the Nitroamine HMX (Octahydro-1,3,5,7-Tetranitro-1,3,5,7-Tetrazocine). *J. Am. Soc. Mass Spectrom.* **2013**, *24* (5), 744–752. https://doi.org/10.1007/s13361-013-0588-y.

(38) Bohinski, T.; Moore Tibbetts, K.; Tarazkar, M.; Romanov, D.; Matsika, S.; Levis, R. J. Measurement of an Electronic Resonance in a Ground-State, Gas-Phase Acetophenone Cation via Strong-Field Mass Spectrometry. *J. Phys. Chem. Lett.* **2013**, *4* (10), 1587–1591. https://doi.org/10.1021/jz400516h.

(39) Tibbetts, K. M.; Tarazkar, M.; Bohinski, T.; Romanov, D. A.; Matsika, S.; Levis, R. J. Controlling the Dissociation Dynamics of Acetophenone Radical Cation through Excitation of Ground and Excited State Wavepackets. *J. Phys. B At. Mol. Opt. Phys.* **2015**, *48* (16), 164002. https://doi.org/10.1088/0953-4075/48/16/164002.

(40) Boateng, D. A.; L. Gutsev, G.; Jena, P.; Moore Tibbetts, K. Ultrafast Coherent Vibrational Dynamics in Dimethyl Methylphosphonate Radical Cation. *Phys. Chem. Chem. Phys.* **2018**, *20* (7), 4636–4640. https://doi.org/10.1039/C7CP07261A.

(41) Tasker, A. D.; Robson, L.; Ledingham, K. W. D.; McCanny, T.; Hankin, S. M.; McKenna, P.; Kosmidis, C.; Jaroszynski, D. A.; Jones, D. R. A High Mass Resolution Study of the Interaction of Aromatic and Nitro-Aromatic Molecules with Intense Laser Fields. *J. Phys. Chem. A* **2002**, *106* (16), 4005–4013. https://doi.org/10.1021/jp013830n.

(42) Mullen, C.; Coggiola, M. J.; Oser, H. Femtosecond Laser Photoionization Time-of-Flight Mass Spectrometry of Nitro-Aromatic Explosives and Explosives Related Compounds. *J. Am. Soc. Mass Spectrom.* **2009**, *20* (3), 419–429. https://doi.org/10.1016/j.jasms.2008.10.022.

(43) Lozovoy, V. V.; Zhu, X.; Gunaratne, T. C.; Harris, D. A.; Shane, J. C.; Dantus, M. Control of Molecular Fragmentation Using Shaped Femtosecond Pulses. *J. Phys. Chem. A* **2008**, *112* (17), 3789–3812. https://doi.org/10.1021/jp071691p.

(44) Bohinski, T.; Moore Tibbetts, K.; Tarazkar, M.; Romanov, D. A.; Matsika, S.; Levis, R. J. Strong Field Adiabatic Ionization Prepares a Launch State for Coherent Control. *J. Phys. Chem. Lett.* **2014**, *5* (24), 4305–4309. https://doi.org/10.1021/jz502313f.

(45) Bohinski, T.; Moore Tibbetts, K.; Tarazkar, M.; Romanov, D.; Matsika, S.; Levis, R. Measurement of Ionic Resonances in Alkyl Phenyl Ketone Cations via Infrared Strong Field Mass Spectrometry. *J. Phys. Chem. A* **2013**, *117* (47), 12374–12381. https://doi.org/10.1021/jp4089047.

(46) Yatsuhashi, T.; Nakashima, N. Effects of Polarization of 1.4 Mm Femtosecond Laser Pulses on the Formation and Fragmentation of Naphthalene Molecular Ions Compared at the Same Effective Ionization Intensity. *J. Phys. Chem. A* **2005**, *109* (42), 9414–9418. https://doi.org/10.1021/jp053868q.

(47) Pearson, B. J.; Nichols, S. R.; Weinacht, T. Molecular Fragmentation Driven by Ultrafast Dynamic Ionic Resonances. *J. Chem. Phys.* **2007**, *127* (13), 131101. https://doi.org/10.1063/1.2790419.

(48) Murakami, M.; Mizoguchi, R.; Shimada, Y.; Yatsuhashi, T.; Nakashima, N. Ionization and Fragmentation of Anthracene with an Intense Femtosecond Laser Pulse at 1.4μm. *Chem. Phys. Lett.* **2005**, *403* (4–6), 238–241. https://doi.org/10.1016/j.cplett.2005.01.008.

(49) Tanaka, M.; Kawaji, M.; Yatsuhashi, T.; Nakashima, N. Ionization and Fragmentation of Alkylphenols by 0.8−1.5 Mm Femtosecond Laser Pulses. *J. Phys. Chem. A* **2009**, *113* (44), 12056–12062. https://doi.org/10.1021/jp902557v.

(50) Lezius, M.; Blanchet, V.; Ivanov, M. Yu.; Stolow, A. Polyatomic Molecules in Strong Laser Fields: Nonadiabatic Multielectron Dynamics. *J. Chem. Phys.* **2002**, *117* (4), 1575–1588. https://doi.org/10.1063/1.1487823.

(51) Lezius, M.; Blanchet, V.; Rayner, D. M.; Villeneuve, D. M.; Stolow, A.; Ivanov, M. Yu. Nonadiabatic Multielectron Dynamics in Strong Field Molecular Ionization. *Phys. Rev. Lett.* **2001**, *86* (1), 51–54. https://doi.org/10.1103/PhysRevLett.86.51.

(52) Nishida, J.; Yan, C.; Fayer, M. D. Orientational Dynamics of a Functionalized Alkyl Planar Monolayer Probed by Polarization-Selective Angle-Resolved Infrared Pump–Probe Spectroscopy. *J. Am. Chem. Soc.* **2016**, *138* (42), 14057–14065. https://doi.org/10.1021/jacs.6b08672.

(53) Keldysh, L. V. Ionization in the Field of a Strong Electromagnetic Wave. **1965**, *20* (5).

(54) Rosker, M. J.; Dantus, M.; Zewail, A. H. Femtosecond Clocking of the Chemical Bond. *Science* **1988**, *241* (4870), 1200–1202. https://doi.org/10.1126/science.241.4870.1200.

(55) Tibbetts, K. Coherent Vibrational and Dissociation Dynamics of Polyatomic Radical Cations. *Chem. - Eur. J.* **2019**, *25*, 8431–8439. https://doi.org/10.1002/chem.201900363.

(56) Rosker, M. J.; Dantus, M.; Zewail, A. H. Femtosecond Real-time Probing of Reactions. I. The Technique. *J Chem Phys* **1988**, *89* (10), 16.

(57) Zewail, A. H. Femtochemistry: Recent Progress in Studies of Dynamics and Control of Reactions and Their Transition States. *J. Phys. Chem.* **1996**, *100* (31), 12701–12724. https://doi.org/10.1021/jp960658s.

(58) Warren, W. S.; Rabitz, H.; Dahleh, M. Coherent Control of Quantum Dynamics: The Dream Is Alive. *Science* **1993**, *259* (5101), 1581–1589. https://doi.org/10.1126/science.259.5101.1581.

(59) González-Vázquez, J.; González, L.; Nichols, S. R.; Weinacht, T. C.; Rozgonyi, T. Exploring Wavepacket Dynamics behind Strong-Field Momentum-Dependent Photodissociation in CH2BrI+. *Phys. Chem. Chem. Phys.* **2010**, *12* (42), 14203. https://doi.org/10.1039/c0cp00303d.

(60) Levine, B. G.; Martínez, T. J. Isomerization Through Conical Intersections. *Annu. Rev. Phys. Chem.* **2007**, *58* (1), 613–634. https://doi.org/10.1146/annurev.physchem.57.032905.104612.

(61) Geißler, D.; Pearson, B. J.; Weinacht, T. Wave Packet Driven Dissociation and Concerted Elimination in CH2I2. *J. Chem. Phys.* **2007**, *127* (20), 204305. https://doi.org/10.1063/1.2805186.

(62) Backus, S.; Durfee, C. G.; Murnane, M. M.; Kapteyn, H. C. High Power Ultrafast Lasers. *Rev. Sci. Instrum.* **1998**, *69* (3), 1207–1223. https://doi.org/10.1063/1.1148795.

(63) Light Conversion. *Traveling-Wave Optical Parametric Amplifier of White Light Continuum (TOPAS Prime): User's Manual.*; Vilnius Lithuania, 2015.

(64) www.iuac.res.in/atmol/~safvan/mridulathesis/node21.html. Accessed on 7th December 2019.

(65) Frish, M; Trucks, G; Schlegel, H; Scuseria, G; Robb, M. Gaussian 09, Revision B.01. **2016**.

(66) Becke, A. D. Density-Functional Exchange-Energy Approximation with Correct Asymptotic Behavior. *Phys. Rev. A* **1988**, *38* (6), 3098–3100. https://doi.org/10.1103/PhysRevA.38.3098.

(67) Perdew, J. P.; Wang, Y. Accurate and Simple Analytic Representation of the Electron-Gas Correlation Energy. *Phys. Rev. B* **1992**, *45* (23), 13244–13249. https://doi.org/10.1103/PhysRevB.45.13244.

(68) Bauernschmitt, R.; Ahlrichs, R. Treatment of Electronic Excitations within the Adiabatic Approximation of Time Dependent Density Functional Theory. *Chem. Phys. Lett.* **1996**, *256* (4), 454–464. https://doi.org/10.1016/0009-2614(96)00440-X.

(69) Trebino, R.; Zeek, E. The Autocorrelation, the Spectrum, and Phase Retrieval. In *Frequency-Resolved Optical Gating: The Measurement of Ultrashort Laser Pulses*; Trebino, R., Ed.; Springer US: Boston, MA, 2000; pp 61–99. https://doi.org/10.1007/978-1-4615-1181-6_4.

(70) Trebino, R.; Kane, D. J. Using Phase Retrieval to Measure the Intensity and Phase of Ultrashort Pulses: Frequency-Resolved Optical Gating. *J. Opt. Soc. Am. A* **1993**, *10* (5), 1101. https://doi.org/10.1364/JOSAA.10.001101.

(71) DeLong, K. W.; Trebino, R.; Hunter, J.; White, W. E. Frequency-Resolved Optical Gating with the Use of Second-Harmonic Generation. *J. Opt. Soc. Am. B* **1994**, *11* (11), 2206. https://doi.org/10.1364/JOSAB.11.002206.

(72) Kane, D. J.; Trebino, R. Characterization of Arbitrary Femtosecond Pulses Using Frequency-Resolved Optical Gating. *IEEE J. Quantum Electron.* **1993**, *29* (2), 571–579. https://doi.org/10.1109/3.199311.

(73) Kane, D. J. Recent Progress toward Real-Time Measurement of Ultrashort Laser Pulses. *IEEE J. Quantum Electron.* **1999**, *35* (4), 421–431. https://doi.org/10.1109/3.753647.

(74) Byrnes. S; Wyatt, A. Frequency Resolved Optical Gating, MATLAB File Exchange, Last Accessed 26 November 2019.

(75) Hankin, S. M.; Villeneuve, D. M.; Corkum, P. B.; Rayner, D. M. Intense-Field Laser Ionization Rates in Atoms and Molecules. *Phys. Rev. A* **2001**, *64* (1), 013405. https://doi.org/10.1103/PhysRevA.64.013405.

(76) Damask, J. N. *Polarization Optics in Telecommunications*; Springer Science & Business Media, 2004.

(77) Siegman, A.E. *Lasers*; University Science books, 1986.

(78) Zewail, A. H. Laser Femtochemistry. *Science* **1988**, *242* (4886), 1645–1653. https://doi.org/10.1126/science.242.4886.1645.

(79) Mokhtari, A.; Cong, P.; Herek, J. L.; Zewail, A. H. Direct Femtosecond Mapping of Trajectories in a Chemical Reaction. *Nature* **1990**, *348*, 225.

(80) Baumert, T.; Engel, V.; Röttgermann, C.; Strunz, W. T.; Gerber, G. Femtosecond Pump—Probe Study of the Spreading and Recurrence of a Vibrational Wave Packet in Na2. *Chem. Phys. Lett.* **1992**, *191* (6), 639–644. https://doi.org/10.1016/0009-2614(92)85602-7.

(81) Assion, A.; Geisler, M.; Helbing, J.; Seyfried, V.; Baumert, T. Femtosecond Pump-Probe Photoelectron Spectroscopy: Mapping of Vibrational Wave-Packet Motion. 4.

(82) Vrakking, M. J. J.; Villeneuve, D. M.; Stolow, A. Observation of Fractional Revivals of a Molecular Wave Packet. *Phys. Rev. A* **1996**, *54* (1), R37–R40. https://doi.org/10.1103/PhysRevA.54.R37.

(83) De, S.; Magrakvelidze, M.; Bocharova, I. A.; Ray, D.; Cao, W.; Znakovskaya, I.; Li, H.; Wang, Z.; Laurent, G.; Thumm, U.; et al. Following Dynamic Nuclear Wave Packets in N 2 , O 2 , and CO with Few-Cycle Infrared Pulses. *Phys. Rev. A* **2011**, *84* (4). https://doi.org/10.1103/PhysRevA.84.043410.

(84) Bryan, W. A.; McKenna, J.; English, E. M. L.; Wood, J.; Calvert, C. R.; Torres, R.; Murphy, D. S.; Turcu, I. C. E.; Collier, J. L.; McCann, J. F.; et al. Isolated Vibrational Wavepackets in D 2 + : Defining Superposition Conditions and Wavepacket Distinguishability. *Phys. Rev. A* **2007**, *76* (5). https://doi.org/10.1103/PhysRevA.76.053402.

(85) Calvert, C. R.; Bryan, W. A.; Newell, W. R.; Williams, I. D. Time-Resolved Studies of Ultrafast Wavepacket Dynamics in Hydrogen Molecules. *Phys. Rep.* **2010**, *491* (1), 1–28. https://doi.org/10.1016/j.physrep.2009.12.004.

(86) Kelkensberg, F.; Lefebvre, C.; Siu, W.; Ghafur, O.; Nguyen-Dang, T. T.; Atabek, O.; Keller, A.; Serov, V.; Johnsson, P.; Swoboda, M.; et al. Molecular Dissociative Ionization and Wave-Packet Dynamics Studied Using Two-Color XUV and IR Pump-Probe Spectroscopy. *Phys. Rev. Lett.* **2009**, *103* (12). https://doi.org/10.1103/PhysRevLett.103.123005.

(87) Erattupuzha, S.; Larimian, S.; Baltuška, A.; Xie, X.; Kitzler, M. Two-Pulse Control over Double Ionization Pathways in CO ₂. *J. Chem. Phys.* **2016**, *144* (2), 024306. https://doi.org/10.1063/1.4939638.

(88) Rudenko, A.; Makhija, V.; Vajdi, A.; Ergler, T.; Schürholz, M.; Kushawaha, R. K.; Ullrich, J.; Moshammer, R.; Kumarappan, V. Strong-Field-Induced Wave Packet Dynamics in Carbon Dioxide Molecule. *Faraday Discuss.* **2016**, *194*, 463–478. https://doi.org/10.1039/C6FD00152A.

(89) Nichols, S. R.; Weinacht, T. C.; Rozgonyi, T.; Pearson, B. J. Strong-Field Phase-Dependent Molecular Dissociation. *Phys. Rev. A* **2009**, *79* (4). https://doi.org/10.1103/PhysRevA.79.043407.

(90) Geißler, D.; Rozgonyi, T.; González-Vázquez, J.; González, L.; Nichols, S.; Weinacht, T. Creation of Multihole Molecular Wave Packets via Strong-Field Ionization. *Phys. Rev. A* **2010**, *82* (1). https://doi.org/10.1103/PhysRevA.82.011402.

(91)   Ho, J.-W. (何智偉); Chen, W.-K. (陳偉侃); Cheng, P.-Y. (鄭博元). Femtosecond Pump-Probe Photoionization-Photofragmentation Spectroscopy: Photoionization-Induced Twisting and Coherent Vibrational Motion of Azobenzene Cation. *J. Chem. Phys.* **2009**, *131* (13), 134308. https://doi.org/10.1063/1.3236813.

(92)   Brogaard, R. Y.; Møller, K. B.; Sølling, T. I. Real-Time Probing of Structural Dynamics by Interaction between Chromophores. *J. Phys. Chem. A* **2011**, *115* (44), 12120–12125. https://doi.org/10.1021/jp2072588.

(93)   Zhu, X.; Lozovoy, V. V.; Shah, J. D.; Dantus, M. Photodissociation Dynamics of Acetophenone and Its Derivatives with Intense Nonresonant Femtosecond Pulses. *J. Phys. Chem. A* **2011**, *115* (8), 1305–1312. https://doi.org/10.1021/jp1029486.

(94)   Konar, A.; Shu, Y.; Lozovoy, V. V.; Jackson, J. E.; Levine, B. G.; Dantus, M. Polyatomic Molecules under Intense Femtosecond Laser Irradiation. *J. Phys. Chem. A* **2014**, *118* (49), 11433–11450. https://doi.org/10.1021/jp505498t.

(95)   Xiang, H. F.; Xu, H. Y.; Wang, Z. Z.; Chen, C. H. Dimethyl Methylphosphonate (DMMP) as an Efficient Flame Retardant Additive for the Lithium-Ion Battery Electrolytes. *J. Power Sources* **2007**, *173* (1), 562–564. https://doi.org/10.1016/j.jpowsour.2007.05.001.

(96)   Jang, Y. J.; Kim, K.; Tsay, O. G.; Atwood, D. A.; Churchill, D. G. Update 1 of: Destruction and Detection of Chemical Warfare Agents. *Chem. Rev.* **2015**, *115* (24), PR1–PR76. https://doi.org/10.1021/acs.chemrev.5b00402.

(97)   Mitchell, M. B.; Sheinker, V. N.; Cox, W. W.; Gatimu, E. N.; Tesfamichael, A. B. The Room Temperature Decomposition Mechanism of Dimethyl Methylphosphonate (DMMP) on Alumina-Supported Cerium Oxide − Participation of Nano-Sized Cerium Oxide Domains. *J. Phys. Chem. B* **2004**, *108* (5), 1634–1645. https://doi.org/10.1021/jp035590c.

(98)   Panayotov, D. A.; Morris, J. R. Catalytic Degradation of a Chemical Warfare Agent Simulant: Reaction Mechanisms on TiO $_2$ -Supported Au Nanoparticles. *J. Phys. Chem. C* **2008**, *112* (19), 7496–7502. https://doi.org/10.1021/jp7118668.

(99)   Yang, L.; Shroll, R. M.; Zhang, J.; Lourderaj, U.; Hase, W. L. Theoretical Investigation of Mechanisms for the Gas-Phase Unimolecular Decomposition of DMMP. *J. Phys. Chem. A* **2009**, *113* (49), 13762–13771. https://doi.org/10.1021/jp904232n.

(100)   Chen, D. A.; Ratliff, J. S.; Hu, X.; Gordon, W. O.; Senanayake, S. D.; Mullins, D. R. Dimethyl Methylphosphonate Decomposition on Fully Oxidized and Partially Reduced Ceria Thin Films. *Surf. Sci.* **2010**, *604* (5–6), 574–587. https://doi.org/10.1016/j.susc.2009.12.028.

(101)   Head, A. R.; Tsyshevsky, R.; Trotochaud, L.; Eichhorn, B.; Kuklja, M. M.; Bluhm, H. Electron Spectroscopy and Computational Studies of Dimethyl Methylphosphonate. *J. Phys. Chem. A* **2016**, *120* (12), 1985–1991. https://doi.org/10.1021/acs.jpca.6b01098.

(102)   Ash, T.; Debnath, T.; Ghosh, A.; Das, A. K. Mechanistic Insight into the Molecular TiO $_2$ -Mediated Gas Phase Detoxication of DMMP: A Theoretical Approach. *Chem. Res. Toxicol.* **2017**, *30* (5), 1177–1187. https://doi.org/10.1021/acs.chemrestox.7b00019.

(103)   Liang, S.; Hemberger, P.; Neisius, N. M.; Bodi, A.; Grützmacher, H.; Levalois-Grützmacher, J.; Gaan, S. Elucidating the Thermal Decomposition of Dimethyl Methylphosphonate by Vacuum Ultraviolet (VUV) Photoionization: Pathways to the PO Radical, a Key Species in Flame-Retardant Mechanisms. *Chem. – Eur. J.* **2015**, *21* (3), 1073–1080. https://doi.org/10.1002/chem.201404271.

(104)   Bafus, D. A.; Gallegos, E. J.; Kiser, R. W. An Electron Impact Investigation of Some Alkyl Phosphate Esters. *J. Phys. Chem.* **1966**, *70* (8), 2614–2619. https://doi.org/10.1021/j100880a029.

(105)   Holtzclaw, J. R.; Wyatt, J. R. Keto-to-Enol Isomerization in the Molecular Ion of Dimethylmethylphosphonate. *Org. Mass Spectrom.* **1988**, *23* (4), 261–266. https://doi.org/10.1002/oms.1210230408.

(106)   Holtzclaw, J. R.; Wyatt, J. R.; Campana, J. E. Structure and Fragmentation of Dimethyl Methylphosphonate and Trimethyl Phosphite. *Org. Mass Spectrom.* **1985**, *20* (2), 90–97. https://doi.org/10.1002/oms.1210200205.

(107)   Gutsev, G. L.; Ampadu Boateng, D.; Jena, P.; Tibbetts, K. M. A Theoretical and Mass Spectrometry Study of Dimethyl Methylphosphonate: New Isomers and Cation Decay Channels in an Intense Femtosecond Laser Field. *J. Phys. Chem. A* **2017**, *121* (44), 8414–8424. https://doi.org/10.1021/acs.jpca.7b08889.

(108)   Becke, A. D. Density-functional Thermochemistry. III. The Role of Exact Exchange. *J. Chem. Phys.* **1993**, *98* (7), 5648–5652. https://doi.org/10.1063/1.464913.

(109)   Lee, C.; Yang, W.; Parr, R. G. Development of the Colle-Salvetti Correlation-Energy Formula into a Functional of the Electron Density. *Phys. Rev. B* **1988**, *37* (2), 785–789. https://doi.org/10.1103/PhysRevB.37.785.

(110)   Cuisset, A.; Mouret, G.; Pirali, O.; Roy, P.; Cazier, F.; Nouali, H.; Demaison, J. Gas-Phase Vibrational Spectroscopy and Ab Initio Study of Organophosphorous Compounds: Discrimination between Species and Conformers. *J. Phys. Chem. B* **2008**, *112* (39), 12516–12525. https://doi.org/10.1021/jp804665h.

(111)   Sikder, A. K.; Sikder, N. A Review of Advanced High Performance, Insensitive and Thermally Stable Energetic Materials Emerging for Military and Space Applications. *J. Hazard. Mater.* **2004**, *112* (1–2), 1–15. https://doi.org/10.1016/j.jhazmat.2004.04.003.

(112)   Wharton, R. K.; Formby, S. A.; Merrifield, R. Airblast TNT Equivalence for a Range of Commercial Blasting Explosives. *J. Hazard. Mater.* **2000**, *79* (1–2), 31–39. https://doi.org/10.1016/S0304-3894(00)00168-0.

(113)   Field, J. E.; Swallowe, G. M.; Heavens, S. N. Ignition Mechanisms of Explosives during Mechanical Deformation. *Proc. R. Soc. Math. Phys. Eng. Sci.* **1982**, *382* (1782), 231–244. https://doi.org/10.1098/rspa.1982.0099.

(114)   Tarver, C. M.; Kury, J. W.; Breithaupt, R. D. Detonation Waves in Triaminotrinitrobenzene. *J. Appl. Phys.* **1997**, *82* (8), 3771–3782. https://doi.org/10.1063/1.365739.

(115)   Dremin, A.N. Combustion Explosive and Shock Waves. **2000**, *36*, 704.

(116)   Ramaswamy, A. L. Microscopic Initiation Mechanisms in Energetic Material Crystals. *J. Energ. Mater.* **2001**, *19* (2–3), 195–217. https://doi.org/10.1080/07370650108216126.

(117)   Cohen, R.; Zeiri, Y.; Wurzberg, E.; Kosloff, R. Mechanism of Thermal Unimolecular Decomposition of TNT (2,4,6-Trinitrotoluene): A DFT Study. *J. Phys. Chem. A* **2007**, *111* (43), 11074–11083. https://doi.org/10.1021/jp072121s.

(118)   Zink, J. I.; Kaska, W. C. Triboluminescence of Hexaphenylcarbodiphosphorane. Emission from a Molecular Excited State Populated by Mechanical Stress. *J. Am. Chem. Soc.* **1973**, 3.

(119)   Lin, S. H.; Wutz, D.; Ho, Z. Z.; Eyring, H. Mechanisms of Triboluminescence. *Proc. Natl. Acad. Sci.* **1980**, *77* (3), 1245–1247. https://doi.org/10.1073/pnas.77.3.1245.

(120)   Bowden, M. D.; Cheeseman, M.; Knowles, S. L.; Drake, R. C. Laser Initiation of Energetic Materials: A Historical Overview. In *Optical Technologies for Arming, Safing, Fuzing, and Firing III*; International Society for Optics and Photonics, 2007; Vol. 6662, p 666208. https://doi.org/10.1117/12.734225.

(121)   Dlott, D.D. Energetic Materials: Theoretical and Computational Chemistry. **2003**, 125–191.

(122)   Nelson, T.; Bjorgaard, J.; Greenfield, M.; Bolme, C.; Brown, K.; McGrane, S.; Scharff, R. J.; Tretiak, S. Ultrafast Photodissociation Dynamics of Nitromethane. *J. Phys. Chem. A* **2016**, *120* (4), 519–526. https://doi.org/10.1021/acs.jpca.5b09776.

(123)   Wang, B.; Liu, B.; Wang, Y.; Wang, L. Dynamics of Highly Excited Nitroaromatics. *J. Phys. Chem. A* **2010**, *114* (50), 12972–12978. https://doi.org/10.1021/jp104727p.

(124)   Ogden, I. K.; Shaw, N.; Danby, C. J.; Powis, I. COMPETING DISSOCIATION CHANNELS OF NITROMETHANE AND METHYL NITRITE IONS AND THE ROLE OF ELECTRONIC AND INTERNAL MODES OF EXCITATION. **1983**, 13.

(125)   Panczel, M.; Baer, T. A Photoelectron Photoion Coincidence (PEPICO) Study of Fragmentation Rates and Kinetic Energy Release Distributions in Nitrobenzene. *Int. J. Mass Spectrom. Ion Process.* **1984**, *58*, 43–61. https://doi.org/10.1016/0168-1176(84)80019-1.

(126)   Sulzer, P.; Rondino, F.; Ptasinska, S.; Illenberger, E.; Märk, T. D.; Scheier, P. Probing Trinitrotoluene (TNT) by Low-Energy Electrons: Strong Fragmentation Following Attachment of Electrons near 0eV. *Int. J. Mass Spectrom.* **2008**, *272* (2–3), 149–153. https://doi.org/10.1016/j.ijms.2008.02.007.

(127)   McEnnis, C.; Dikmelik, Y.; Spicer, J. B. Femtosecond Laser-Induced Fragmentation and Cluster Formation Studies of Solid Phase Trinitrotoluene Using Time-of-Flight Mass Spectrometry. *Appl. Surf. Sci.* **2007**, *254* (2), 557–562. https://doi.org/10.1016/j.apsusc.2007.06.053.

(128)   Furman, D.; Kosloff, R.; Zeiri, Y. Mechanism of Intact Adsorbed Molecules Ejection Using High Intensity Laser Pulses. *J. Phys. Chem. C* **2016**, *120* (20), 11306–11312. https://doi.org/10.1021/acs.jpcc.6b03711.

(129)   Weickhardt, C.; Tönnies, K. Short Pulse Laser Mass Spectrometry of Nitrotoluenes: Ionization and Fragmentation Behavior. *Rapid Commun. Mass Spectrom.* **2002**, *16* (5), 442–446. https://doi.org/10.1002/rcm.567.

(130)   Stephens, P. J.; Devlin, F. J.; Chabalowski, C. F.; Frisch, M. J. Ab Initio Calculation of Vibrational Absorption and Circular Dichroism Spectra Using Density Functional Force Fields. *J. Phys. Chem.* **1994**, *98* (45), 11623–11627. https://doi.org/10.1021/j100096a001.

(131)   Zhang, Q.; Fang, W.; Xie, Y.; Cao, M.; Zhao, Y.; Shan, X.; Liu, F.; Wang, Z.; Sheng, L. Photoionization and Dissociation Study of P-Nitrotoluene: Experimental and Theoretical Insights. *J. Mol. Struct.* **2012**, *1020*, 105–111. https://doi.org/10.1016/j.molstruc.2012.03.059.

(132)   Kobayashi, T.; Nagakura, S. Photoelectron Spectra of Substituted Benzenes. *Bull. Chem. Soc. Jpn.* **1974**, *47* (10), 2563–2572. https://doi.org/10.1246/bcsj.47.2563.

(133)   Huh, C.; Kang, C. H.; Lee, H. W.; Nakamura, H.; Mishima, M.; Tsuno, Y.; Yamataka, H. Thermodynamic Stabilities and Resonance Demand of Aromatic Radical Anions in the Gas Phase. *Bull. Chem. Soc. Jpn.* **1999**, *72* (5), 1083–1091. https://doi.org/10.1246/bcsj.72.1083.

(134)   Chowdhury, S.; Heinis, T.; Grimsrud, E. P.; Kebarle, P. Entropy Changes and Electron Affinities from Gas-Phase Electron-Transfer Equilibria: A- + B = A + B-. *J. Phys. Chem.* **1986**, *90* (12), 2747–2752. https://doi.org/10.1021/j100403a037.

(135)   Bohinski, T.; Moore Tibbetts, K.; Munkerup, K.; Tarazkar, M.; Romanov, D. A.; Matsika, S.; Levis, R. J. Radical Cation Spectroscopy of Substituted Alkyl Phenyl Ketones via Tunnel Ionization. *Chem. Phys.* **2014**, *442*, 81–85. https://doi.org/10.1016/j.chemphys.2014.05.019.

(136)   Tibbetts, K. M.; Bohinski, T.; Munkerup, K.; Tarazkar, M.; Levis, R. Controlling Dissociation of Alkyl Phenyl Ketone Radical Cations in the Strong-Field Regime through Hydroxyl Substitution Position. *J. Phys. Chem. A* **2014**, *118* (37), 8170–8176. https://doi.org/10.1021/jp500874r.

(137)   Munkerup, K.; Romanov, D.; Bohinski, T.; Stephansen, A. B.; Levis, R. J.; Sølling, T. I. Conserving Coherence and Storing Energy during Internal Conversion: Photoinduced Dynamics of *Cis* - and *Trans*- Azobenzene Radical Cations. *J. Phys. Chem. A* **2017**, *121* (45), 8642–8651. https://doi.org/10.1021/acs.jpca.7b09185.

(138)   Nibarger, J. P.; Menon, S. V.; Gibson, G. N. Comprehensive Analysis of Strong-Field Ionization and Dissociation of Diatomic Nitrogen. *Phys. Rev. A* **2001**, *63* (5). https://doi.org/10.1103/PhysRevA.63.053406.

(139)   Barve, J. V.; Pant, L. M. The Structure of P-Nitrotoluene. *Acta Crystallogr. B* **1971**, *27* (6), 1158–1162. https://doi.org/10.1107/S0567740871003686.

(140)   See http://webbook.nist.gov/chemistry/for. NIST/EPA Gas-Phase Infrared Database, Last Checked 26 November 2019.

(141)   Adhikary, A.; Becker, D.; Palmer, B. J.; Heizer, A. N.; Sevilla, M. D. Direct Formation of the C5′-Radical in the Sugar–Phosphate Backbone of DNA by High-Energy Radiation. *J. Phys. Chem. B* **2012**, *116* (20), 5900–5906. https://doi.org/10.1021/jp3023919.

(142)   Ma, J.; Marignier, J.-L.; Pernot, P.; Houée-Levin, C.; Kumar, A.; D. Sevilla, M.; Adhikary, A.; Mostafavi, M. Direct Observation of the Oxidation of DNA Bases by Phosphate Radicals Formed under Radiation: A Model of the Backbone-to-Base Hole Transfer. *Phys. Chem. Chem. Phys.* **2018**, *20* (21), 14927–14937. https://doi.org/10.1039/C8CP00352A.

(143)   Ma, J.; Denisov, S. A.; Marignier, J.-L.; Pernot, P.; Adhikary, A.; Seki, S.; Mostafavi, M. Ultrafast Electron Attachment and Hole Transfer Following Ionizing Radiation of Aqueous Uridine Monophosphate. *J. Phys. Chem. Lett.* **2018**, *9* (17), 5105–5109. https://doi.org/10.1021/acs.jpclett.8b02170.

(144)   Cadet, J.; Douki, T.; Ravanat, J.-L. Measurement of Oxidatively Generated Base Damage in Cellular DNA. *Mutat. Res. Mol. Mech. Mutagen.* **2011**, *711* (1), 3–12. https://doi.org/10.1016/j.mrfmmm.2011.02.004.

(145)   Ampadu Boateng, D.; Gutsev, G. L.; Jena, P.; Tibbetts, K. M. Dissociation Dynamics of 3- and 4-Nitrotoluene Radical Cations: Coherently Driven C–NO$_2$ Bond Homolysis. *J. Chem. Phys.* **2018**, *148* (13), 134305. https://doi.org/10.1063/1.5024892.

(146)   Ampadu Boateng, D.; Word, M. D.; Gutsev, L. G.; Jena, P.; Tibbetts, K. M. Conserved Vibrational Coherence in the Ultrafast Rearrangement of 2-Nitrotoluene Radical Cation. *J. Phys. Chem. A* **2019**. https://doi.org/10.1021/acs.jpca.8b11723.

(147)   Roberts, G. M.; Marroux, H. J. B.; Grubb, M. P.; Ashfold, M. N. R.; Orr-Ewing, A. J. On the Participation of Photoinduced N–H Bond Fission in Aqueous Adenine at 266 and 220 Nm: A Combined Ultrafast Transient Electronic and Vibrational Absorption Spectroscopy Study. *J. Phys. Chem. A* **2014**, *118* (47), 11211–11225. https://doi.org/10.1021/jp508501w.

(148)   Stavros, V. G.; Verlet, J. R. R. Gas-Phase Femtosecond Particle Spectroscopy: A Bottom-Up Approach to Nucleotide Dynamics. *Annu. Rev. Phys. Chem.* **2016**, *67* (1), 211–232. https://doi.org/10.1146/annurev-physchem-040215-112428.

(149)   Horsman, G. P.; Zechel, D. L. Phosphonate Biochemistry. *Chem. Rev.* **2017**, *117* (8), 5704–5783. https://doi.org/10.1021/acs.chemrev.6b00536.

(150)   Ampadu Boateng, D.; Tibbetts, K. M. Measurement of Ultrafast Vibrational Coherences in Polyatomic Radical Cations with Strong-Field Adiabatic Ionization. *J. Vis. Exp.* **2018**, No. 138. https://doi.org/10.3791/58263.

(151)   Krishnan, R.; Binkley, J. S.; Seeger, R.; Pople, J. A. Self-consistent Molecular Orbital Methods. XX. A Basis Set for Correlated Wave Functions. *J. Chem. Phys.* **1980**, *72* (1), 650–654. https://doi.org/10.1063/1.438955.

(152)   Bolton, E. E.; Wang, Y.; Thiessen, P. A.; Bryant, S. H. Chapter 12 - PubChem: Integrated Platform of Small Molecules and Biological Activities. In *Annual Reports in Computational Chemistry*; Wheeler, R. A., Spellmeyer, D. C., Eds.; Elsevier, 2008; Vol. 4, pp 217–241. https://doi.org/10.1016/S1574-1400(08)00012-1.

(153)   Zhurko, G.A. Chemcraft: Graphical Program for Visualization of Quantum Chemistry Computations. Available Online: Http://Chemcraftprog.Com/. **2019**.

(154)   Sass, S.; Fisher, T. L. Chemical Ionization and Electron Impact Mass Spectrometry of Some Organophosphonate Compounds. *Org. Mass Spectrom.* **1979**, *14* (5), 257–264. https://doi.org/10.1002/oms.1210140506.

(155)   Zeller, L.; Farrell, J.; Kenttamaa, H. I.; Vainiotalo, P. Long-Lived Radical Cations of Simple Organophosphates Isomerize Spontaneously to Distonic Structures in the Gas Phase. *J. Am. Chem. Soc.* **1992**, *114* (4), 1205–1214. https://doi.org/10.1021/ja00030a013.

(156)   Bell, A. J.; Despeyroux, D.; Murrell, J.; Watts, P. Fragmentation and Reactions of Organophosphate Ions Produced by Electrospray Ionization. *Int. J. Mass Spectrom. Ion Process.* **1997**, *165–166*, 533–550. https://doi.org/10.1016/S0168-1176(97)00202-4.

(157)   S. Groenewold, G.; R. Scott, J.; D. Lee, E.; A. Lammert, S. Rapid Analysis of Organophosphonate Compounds Recovered from Vinyl Floor Tile Using Vacuum Extraction Coupled with a Fast-Duty Cycle GC/MS. *Anal. Methods* **2013**, *5* (9), 2227–2236. https://doi.org/10.1039/C3AY26280D.

(158)   McLafferty, F. W. Mass Spectrometric Analysis. Molecular Rearrangements. *Anal. Chem.* **1959**, *31* (1), 82–87. https://doi.org/10.1021/ac60145a015.

(159)   Meyrick, C.I; Thompson, W.H. Vibrational Spectra of Alkyl Esters Phosphorus Oxy-Acids. *J Chem Soc* **1950**, 225–229.

(160)   Maarsen, J. W.; Smit, M. C.; Matze, J. The Raman and Infra-Red Spectra of Some Compounds (IH7C3O)2PXO. *Recl. Trav. Chim. Pays-Bas* **1957**, *76* (9), 713–723. https://doi.org/10.1002/recl.19570760906.

(161)   Veken, B. J. V. D.; Herman, M. A. Vibrational Spectra of Ch3po(Och3)2 and Isotopically Substituted Derivatives. *Phosphorus Sulfur Relat. Elem.* **1981**, *10* (3), 357–367. https://doi.org/10.1080/03086648108077388.

(162)   NIST Standard Reference Database 96. Last accessed 26 November 2019. Http://Webbook.Nist.Gov/Chemistry/.

(163)   Mott, A. J.; Rez, P. Calculated Infrared Spectra of Nerve Agents and Simulants. *Spectrochim. Acta. A. Mol. Biomol. Spectrosc.* **2012**, *91*, 256–260. https://doi.org/10.1016/j.saa.2012.02.010.

(164)   Hameka, H. F.; Carrieri, A. H.; Jensen, J. O. Calculations of the Structure and the Vibrational Infrared Frequencies of Some Methylphosphonates. *Phosphorus Sulfur Silicon Relat. Elem.* **1992**, *66* (1–4), 1–11. https://doi.org/10.1080/10426509208038325.

(165)   Mortimer, F. S. Vibrational Assignment and Rotational Isomerism in Some Simple Organic Phosphates. *Spectrochim. Acta* **1957**, *9* (4), 270–281. https://doi.org/10.1016/0371-1951(57)80142-8.

(166)   Cui, Y.; Bhardwaj, C.; Milasinovic, S.; Carlson, R. P.; Gordon, R. J.; Hanley, L. Molecular Imaging and Depth Profiling of Biomaterials Interfaces by Femtosecond Laser Desorption Postionization Mass Spectrometry. *ACS Appl. Mater. Interfaces* **2013**, *5* (19), 9269–9275. https://doi.org/10.1021/am4020633.

(167)   Cui, Y.; Veryovkin, I. V.; Majeski, M. W.; Cavazos, D. R.; Hanley, L. High Lateral Resolution vs Molecular Preservation in Near-IR Fs-Laser Desorption Postionization Mass Spectrometry. *Anal. Chem.* **2015**, *87* (1), 367–371. https://doi.org/10.1021/ac5041154.

(168)   Lu, Q.; Hu, Y.; Chen, J.; Jin, S. Laser Desorption Postionization Mass Spectrometry Imaging of Folic Acid Molecules in Tumor Tissue. *Anal. Chem.* **2017**, *89* (16), 8238–8243. https://doi.org/10.1021/acs.analchem.7b00140.

(169)   Chen, J.; Hu, Y.; Lu, Q.; Wang, P.; Zhan, H. Molecular Imaging of Small Molecule Drugs in Animal Tissues Using Laser Desorption Postionization Mass Spectrometry. *Analyst* **2017**, *142* (7), 1119–1124. https://doi.org/10.1039/C6AN02721K.

(170)   Walker, A. V.; Gelb, L. D.; Barry, G. E.; Subanajouy, P.; Poudel, A.; Hara, M.; Veryovkin, I. V.; Bell, G. I.; Hanley, L. Femtosecond Laser Desorption Ionization Mass Spectrometry Imaging and Multivariate Analysis of Lipids in Pancreatic Tissue. *Biointerphases* **2018**, *13* (3), 03B416. https://doi.org/10.1116/1.5016301.

(171)   Rajasekharan Pillai, V. N. Photoremoveable Protecting Groups in Organic Synthesis. **1980**, *1980*, 1–26.

(172)   Gao, X.; Gulari, E.; Zhou, X. In Situ Synthesis of Oligonucleotide Microarrays. *Biopolymers* **2004**, *73* (5), 579–596. https://doi.org/10.1002/bip.20005.

(173)   Ellis-Davies, G. C. R. Caged Compounds: Photorelease Technology for Control of Cellular Chemistry and Physiology. *Nat. Methods* **2007**, *4* (8), 619–628. https://doi.org/10.1038/nmeth1072.

(174)   Wang, B.; Wright, D.; Cliffel, D.; Haglund, R.; Pantelides, S. T. Ionization-Enhanced Decomposition of 2,4,6-Trinitrotoluene (TNT) Molecules. *J. Phys. Chem. A* **2011**, *115* (28), 8142–8146. https://doi.org/10.1021/jp2022852.

(175)   Beynon, J. H.; Saunders, R. A.; Topham, A.; Williams, A. E. 1187. The Dissociation of O - Nitrotoluene under Electron Impact. *J. Chem. Soc. Resumed* **1965**, 6403. https://doi.org/10.1039/jr9650006403.

(176)   Shao, J.-D.; Baer, T. The Dissociation Dynamics of Energy Selected O-Nitrotoluene Ions. *Int. J. Mass Spectrom. Ion Process.* **1988**, *86*, 357–367. https://doi.org/10.1016/0168-1176(88)80078-8.

(177)   Choe, J. C.; Kim, M. S. Photodissociation Kinetics of the P-Nitrotoluene Molecular Ion on a Nanosecond Time Scale. *J. Phys. Chem.* **1991**, *95* (1), 50–56. https://doi.org/10.1021/j100154a014.

(178)   Simeonsson, J. B.; Lemire, G. W.; Sausa, R. C. Trace Detection of Nitrocompounds by ArF Laser Photofragmentation/Ionization Spectrometry. *Appl. Spectrosc.* **1993**, *47* (11), 1907–1912. https://doi.org/10.1366/0003702934066190.

(179)   Kosmidis, C.; Marshall, A.; Clark, A.; Deas, R. M.; Ledingham, K. W. D.; Singhal, R. P.; Harris, F. M. Multiphoton Ionization and Dissociation of Nitrotoluene Isomers by UV Laser Light. *Rapid Commun. Mass Spectrom.* **1994**, *8* (8), 607–614. https://doi.org/10.1002/rcm.1290080808.

(180)   Kosmidis, C.; Ledingham, K. W. D.; Kilic, H. S.; McCanny, T.; Singhal, R. P.; Langley, A. J.; Shaikh, W. On the Fragmentation of Nitrobenzene and Nitrotoluenes Induced by a Femtosecond Laser at 375 Nm. *J. Phys. Chem. A* **1997**, *101* (12), 2264–2270. https://doi.org/10.1021/jp963187i.

(181)   Cao, M.; Li, Y.; Chu, G.; Chen, J.; Shan, X.; Liu, F.; Wang, Z.; Sheng, L. VUV Photoionization and Dissociation of O-Nitrotoluene: Experimental and Theoretical Insights. *J. Electron Spectrosc. Relat. Phenom.* **2013**, *191*, 41–47. https://doi.org/10.1016/j.elspec.2013.09.006.

(182)   Wettermark, G. Photochromism of o -Nitrotoluenes. *Nature* **1962**, *194* (4829), 677–677. https://doi.org/10.1038/194677a0.

(183)   Chen, S. C.; Xu, S. C.; Diau, E.; Lin, M. C. A Computational Study on the Kinetics and Mechanism for the Unimolecular Decomposition of O-Nitrotoluene. *J. Phys. Chem. A* **2006**, *110* (33), 10130–10134. https://doi.org/10.1021/jp0623591.

(184)   Fayet, G.; Joubert, L.; Rotureau, P.; Adamo, C. A Theoretical Study of the Decomposition Mechanisms in Substituted O-Nitrotoluenes. *J. Phys. Chem. A* **2009**, *113* (48), 13621–13627. https://doi.org/10.1021/jp905979w.

(185)   Gudem, M.; Hazra, A. Intersystem Crossing Drives Photoisomerization in O-Nitrotoluene, a Model for Photolabile Caged Compounds. *J. Phys. Chem. A* **2018**, *122* (21), 4845–4853. https://doi.org/10.1021/acs.jpca.8b03439.

(186)   Schmierer, T.; Laimgruber, S.; Haiser, K.; Kiewisch, K.; Neugebauer, J.; Gilch, P. Femtosecond Spectroscopy on the Photochemistry of Ortho-Nitrotoluene. *Phys. Chem. Chem. Phys.* **2010**, *12* (48), 15653–15664. https://doi.org/10.1039/C004025H.

(187)   Fröbel, S.; Gilch, P. Femtochemistry of Selected Di-Substituted Benzenes. *J. Photochem. Photobiol. Chem.* **2016**, *318*, 150–159. https://doi.org/10.1016/j.jphotochem.2015.05.036.

(188)   Geißler, D.; Marquetand, P.; González-Vázquez, J.; González, L.; Rozgonyi, T.; Weinacht, T. Control of Nuclear Dynamics with Strong Ultrashort Laser Pulses. *J. Phys. Chem. A* **2012**, *116* (46), 11434–11440. https://doi.org/10.1021/jp306686n.

(189)   Montgomery, J. A.; Frisch, M. J.; Ochterski, J. W.; Petersson, G. A. A Complete Basis Set Model Chemistry. VI. Use of Density Functional Geometries and Frequencies. *J. Chem. Phys.* **1999**, *110* (6), 2822–2827. https://doi.org/10.1063/1.477924.

(190)   Burke, K.; Predew, J.; Wang, Y.; Dobson, J.F.; Vignale, G.; Das, M.P. *Electronic Density Functional Theory: Recent Progress and New Directions*; Springer US: New York, 1998.

(191)   Yanai, T.; Tew, D. P.; Handy, N. C. A New Hybrid Exchange–Correlation Functional Using the Coulomb-Attenuating Method (CAM-B3LYP). *Chem. Phys. Lett.* **2004**, *393* (1), 51–57. https://doi.org/10.1016/j.cplett.2004.06.011.

(192)   Chai, J.-D.; Head-Gordon, M. Long-Range Corrected Hybrid Density Functionals with Damped Atom–Atom Dispersion Corrections. *Phys. Chem. Chem. Phys.* **2008**, *10* (44), 6615–6620. https://doi.org/10.1039/B810189B.

(193)   Head-Gordon, M.; Pople, J. A.; Frisch, M. J. MP2 Energy Evaluation by Direct Methods. *Chem. Phys. Lett.* **1988**, *153* (6), 503–506. https://doi.org/10.1016/0009-2614(88)85250-3.

(194)   Montgomery, J. A.; Frisch, M. J.; Ochterski, J. W.; Petersson, G. A. A Complete Basis Set Model Chemistry. VII. Use of the Minimum Population Localization Method. *J. Chem. Phys.* **2000**, *112* (15), 6532–6542. https://doi.org/10.1063/1.481224.

(195)   Fukui, K. The Path of Chemical Reactions - the IRC Approach. *Acc. Chem. Res.* **1981**, *14* (12), 363–368. https://doi.org/10.1021/ar00072a001.

(196)   Schlegel, H. B.; Iyengar, S. S.; Li, X.; Millam, J. M.; Voth, G. A.; Scuseria, G. E.; Frisch, M. J. Ab Initio Molecular Dynamics: Propagating the Density Matrix with Gaussian Orbitals. III.

Comparison with Born–Oppenheimer Dynamics. *J. Chem. Phys.* **2002**, *117* (19), 8694–8704. https://doi.org/10.1063/1.1514582.

(197)   J. Waters, M. D.; B. Skov, A.; B. Larsen, M. A.; M. Clausen, C.; M. Weber, P.; I. Sølling, T. Symmetry Controlled Excited State Dynamics. *Phys. Chem. Chem. Phys.* **2019**, *21* (5), 2283–2294. https://doi.org/10.1039/C8CP05950K.

(198)   Zhang, Y.; Jónsson, H.; M. Weber, P. Coherence in Nonradiative Transitions: Internal Conversion in Rydberg-Excited N -Methyl and N -Ethyl Morpholine. *Phys. Chem. Chem. Phys.* **2017**, *19* (38), 26403–26411. https://doi.org/10.1039/C7CP05244H.

(199)   Zhu, X.; Lozovoy, V. V.; Shah, J. D.; Dantus, M. Photodissociation Dynamics of Acetophenone and Its Derivatives with Intense Nonresonant Femtosecond Pulses. *J. Phys. Chem. A* **2011**, *115* (8), 1305–1312. https://doi.org/10.1021/jp1029486.

(200)   Shishkov, I. F.; Vilkov, L. V.; Kovács, A.; Hargittai, I. Molecular Geometry of 2-Nitrotoluene from Gas Phase Electron Diffraction and Quantum Chemical Study. *J. Mol. Struct.* **1998**, *445* (1), 259–268. https://doi.org/10.1016/S0022-2860(97)00429-8.

(201)   Herek, J. L.; Pedersen, S.; Bañares, L.; Zewail, A. H. Femtosecond Real-time Probing of Reactions. IX. Hydrogen-atom Transfer. *J. Chem. Phys.* **1992**, *97* (12), 9046–9061. https://doi.org/10.1063/1.463331.

(202)   Lochbrunner, S.; Wurzer, A. J.; Riedle, E. Ultrafast Excited-State Proton Transfer and Subsequent Coherent Skeletal Motion of 2-(2′-Hydroxyphenyl)Benzothiazole. *J. Chem. Phys.* **2000**, *112* (24), 10699–10702. https://doi.org/10.1063/1.481711.

(203)   Kosma, K.; Trushin, S. A.; Fuß, W.; Schmid, W. E. Cyclohexadiene Ring Opening Observed with 13 Fs Resolution: Coherent Oscillations Confirm the Reaction Path. *Phys Chem Chem Phys* **2009**, *11* (1), 172–181. https://doi.org/10.1039/B814201G.

(204)   Yatsuhashi, T.; Trushin, S. A.; Fuß, W.; Rettig, W.; Schmid, W. E.; Zilberg, S. Ultrafast Charge Transfer and Coherent Oscillations in 4-Piperidino-Benzonitrile. *Chem. Phys.* **2004**, *296* (1), 1–12. https://doi.org/10.1016/j.chemphys.2003.09.011.

(205)   Fuß, W.; Schmid, W. E.; Kuttan Pushpa, K.; Trushin, S. A.; Yatsuhashi, T. Ultrafast Relaxation and Coherent Oscillations in Aminobenzonitriles in the Gas Phase Probed by Intense-Field Ionization. *Phys Chem Chem Phys* **2007**, *9* (10), 1151–1169. https://doi.org/10.1039/B611877A.

(206)   Trushin, S. A.; Fuß, W.; Schmid, W. E. Conical Intersections, Pseudorotation and Coherent Oscillations in Ultrafast Photodissociation of Group-6 Metal Hexacarbonyls. *Chem. Phys.* **2000**, *259* (2), 313–330. https://doi.org/10.1016/S0301-0104(00)00198-1.

(207)   Trushin, S. A.; Kosma, K.; Fuß, W.; Schmid, W. E. Wavelength-Independent Ultrafast Dynamics and Coherent Oscillation of a Metal–Carbon Stretch Vibration in Photodissociation of Cr(CO)6 in the Region of 270–345nm. *Chem. Phys.* **2008**, *347* (1), 309–323. https://doi.org/10.1016/j.chemphys.2007.09.057.

(208)   Kosma, K.; A. Trushin, S.; Fuß, W.; E. Schmid, W.; R. Schneider, B. M. Photodissociation of Group-6 Hexacarbonyls: Observation of Coherent Oscillations in an Antisymmetric (Pseudorotation) Vibration in Mo(CO)5 and W(CO)5. *Phys. Chem. Chem. Phys.* **2010**, *12* (40), 13197–13214. https://doi.org/10.1039/C0CP00731E.

(209)   Hahn, D. W.; Omenetto, N. Laser-Induced Breakdown Spectroscopy (LIBS), Part II: Review of Instrumental and Methodological Approaches to Material Analysis and Applications to Different Fields. *Appl. Spectrosc.* **2012**, *66* (4), 347–419. https://doi.org/10.1366/11-06574.

(210)   Bol'shakov, A. A.; Yoo, J. H.; Liu, C.; Plumer, J. R.; Russo, R. E. Laser-Induced Breakdown Spectroscopy in Industrial and Security Applications. *Appl. Opt.* **2010**, *49* (13), C132–C142. https://doi.org/10.1364/AO.49.00C132.

Appendix A

Chapter 4: Ultrafast coherent vibrational dynamics in dimethyl methylphosphonate radical cation.

Table A1: Calculated normal modes of DMMP⁺.

BPW91 mode	ν_{harm} (cm^{-1})	ν_{anharm} (cm^{-1})	I_{harm} km/mol	I_{anharm} km/mol	**B3LYP**	ν_{harm} (cm^{-1})	ν_{anharm} (cm^{-1})	I_{harm} km/mol	I_{anharm} km/mol
1	40.91	61.33	1.69	1.58		19.27	-467.96	0.001	221.11
2	80.87	43.91	1.70	1.16		69.54	-119.57	0.23	3.69
3	97.04	63.32	1.23	0.58		84.03	74.78	2.96	2.19
4	120.73	94.20	1.48	2.73		99.72	83.09	2.46	4.50
5	151.96	121.67	2.03	6.14		133.60	160.11	4.54	9.09
6	161.71	147.04	6.31	27.54		154.69	135.60	0.77	11.28
7	166.71	152.59	14.69	13.58		166.52	159.89	15.15	16.07
8	232.45	230.90	7.77	13.63		204.71	218.16	10.28	4.58
9	236.88	217.98	4.38	11.21		253.09	245.36	3.46	2.54
10	270.05	257.44	1.63	34.61		271.82	268.02	8.01	6.20
11	270.43	260.17	4.85	5.21		346.10	331.31	10.01	3.79
12	456.72	444.07	33.44	34.79		471.50	462.55	26.80	25.72
13	610.71	583.28	4.86	2.59		659.12	641.83	24.98	23.41
14	686.55	649.17	0.41	0.85		760.83	715.42	0.64	0.92
15	772.79	754.66	17.55	15.98		766.97	742.20	4.70	8.98
16	863.04	827.65	6.71	49.04		864.02	834.09	13.13	6.70
17	863.82	832.65	9.71	97.59		934.66	910.52	15.19	8.37
18	913.70	898.08	22.36	16.42		952.94	935.45	34.93	28.81
19	946.88	916.91	5.08	11.09		1044.26	1005.66	180.21	88.76
20	1036.50	1009.49	249.38	65.55		1065.54	1026.02	371.47	310.84
21	1105.33	1075.83	14.25	0.97		1165.06	1136.55	2.74	1.53
22	1112.65	1079.99	2.44	4.54		1168.16	1137.93	0.20	0.72
23	1138.09	1112.54	3.31	20.37		1193.50	1156.89	31.98	6.54
24	1138.17	1114.13	7.49	6.20		1193.89	1159.18	17.05	6.04
25	1325.94	1293.71	32.06	26.55		1375.94	1345.20	32.59	28.91
26	1400.74	1353.62	7.30	11.82		1454.26	1417.39	17.40	18.97
27	1403.29	1359.26	2.28	55.20		1454.42	1417.39	10.49	11.43
28	1409.46	1365.70	24.75	35.02		1476.73	1440.99	3.58	1145.53
29	1411.58	1371.51	32.34	22.24		1478.22	1442.73	4.47	5.19
30	1414.79	1376.17	12.53	6.19		1481.76	1433.39	13.10	198.80
31	1415.36	1375.39	9.75	12.14		1491.56	1443.71	0.64	6.07
32	1443.52	1402.71	106.92	90.26		1502.53	1450.00	7.20	6.83
33	1460.52	1411.80	72.77	51.57		1507.95	1455.68	59.09	28.08
34	2978.86	2854.75	74.53	354.81		3059.30	2942.92	16.93	19.38
35	2981.99	2850.16	21.29	671.12		3078.34	2980.18	0.53	5.50
36	3002.87	2880.43	16.53	18.41		3079.80	2976.54	7.36	4.70
37	3073.87	2899.24	5.61	27.73		3149.72	3005.34	6.74	5.21
38	3074.81	2909.01	6.22	19.48		3150.15	3005.92	5.39	4.33
39	3096.35	2947.64	6.79	5.58		3176.98	3036.45	2.61	2.40
40	3099.79	2952.78	6.10	4.72		3177.53	3034.16	2.66	3.88
41	3113.58	2937.77	17.65	26.30		3201.86	3056.59	1.45	1.31
42	3114.85	2941.32	13.77	20.43		3202.33	3057.00	0.65	0.26

Table A2: Coordinate differences

	BPW91			B3LYP		
coordinate	neutral	cation	% diff.	neutral	cation	% diff.
R(1,2)	1.497	1.540	2.811	1.484	1.582	6.555
R(1,3)	1.813	1.783	1.622	1.804	1.775	1.591
R(1,7)	1.646	1.614	1.950	1.627	1.565	3.836
R(1,8)	1.630	1.615	0.932	1.611	1.570	2.551
R(3,4)	1.097	1.097	0.073	1.090	1.091	0.110
R(3,5)	1.098	1.097	0.073	1.091	1.091	0.046
R(3,6)	1.098	1.098	0.027	1.091	1.092	0.018
R(7,9)	1.445	1.457	0.851	1.438	1.471	2.274
R(8,13)	1.446	1.457	0.754	1.438	1.469	2.148
R(9,10)	1.097	1.095	0.246	1.090	1.088	0.183
R(9,11)	1.096	1.100	0.347	1.089	1.088	0.046
R(9,12)	1.101	1.096	0.427	1.093	1.085	0.741
R(13,14)	1.099	1.100	0.091	1.092	1.088	0.339
R(13,15)	1.099	1.095	0.346	1.091	1.088	0.312
R(13,16)	1.095	1.096	0.064	1.088	1.086	0.211
A(2,1,3)	116.55	119.49	2.527	116.46	116.31	0.132
A(2,1,7)	113.69	108.27	4.766	113.29	106.83	5.697
A(2,1,8)	117.33	108.11	7.858	116.85	103.78	11.189
A(3,1,7)	106.01	104.50	1.431	106.09	106.80	0.666
A(3,1,8)	100.04	104.49	4.442	100.71	106.90	6.143
A(7,1,8)	101.16	111.98	10.701	101.57	116.65	14.851
A(1,3,4)	110.75	110.51	0.215	110.71	109.84	0.791
A(1,3,5)	109.25	108.64	0.551	109.31	109.01	0.271
A(1,3,6)	108.83	108.63	0.183	109.02	109.02	0.003
A(4,3,5)	109.66	109.80	0.129	109.56	109.74	0.163
A(4,3,6)	109.58	109.79	0.193	109.52	109.53	0.005
A(5,3,6)	108.74	109.44	0.638	108.69	109.69	0.922
A(1,7,9)	120.04	129.32	7.732	121.29	131.30	8.249
A(1,8,13)	119.42	129.34	8.307	120.70	131.79	9.192
A(7,9,10)	110.97	111.81	0.757	110.81	110.24	0.508
A(7,9,11)	106.27	106.32	0.757	106.41	17.60	1.112
A(7,9,12)	110.38	106.12	3.860	110.30	105.20	4.624
A(10,9,11)	110.20	111.46	1.646	110.28	111.85	1.429
A(10,9,12)	109.66	111.46	1.646	109.64	110.90	1.150
A(11,9,12)	109.31	109.18	0.118	109.35	110.78	1.312
A(8,13,14)	110.36	106.25	3.721	110.25	106.35	3.536
A(8,13,15)	110.73	111.85	1.006	110.57	110.84	0.247
A(8,13,16)	105.97	106.16	0.174	106.20	105.90	0.283
A(14,13,16)	110.13	111.68	1.407	110.12	111.69	0.990
A(14,13,16)	109.69	109.14	0.499	109.70	110.79	0.990
A(15,13,16)	109.87	111.47	1.455	109.93	111.02	0.928

Appendix B

Chapter 5: Dissociation dynamics of 3- and 4-nitrotoluene radical cations: Coherently driven C-NO$_2$ bond homolysis.

Table B1: Fitting parameters for parent molecular ion of 4-NT to eq 5.2

I (W/cm^2)	a	T (ps)	t (ps)	ϕ (rad)	b	c
2.8×10^{10}	0.04 ± 0.01	0.22 ± 0.03	0.45 ± 0.03	2.2 ± 0.2	0.52 ± 0.07	0.910 ± 0.001
3.7×10^{10}	0.07 ± 0.01	0.20 ± 0.02	0.46 ± 0.03	2.2 ± 0.2	0.59 ± 0.07	0.881 ± 0.001
4.6×10^{10}	0.09 ± 0.01	0.19 ± 0.03	0.48 ± 0.03	2.2 ± 0.2	0.45 ± 0.07	0.851 ± 0.001
6.2×10^{10}	0.10 ± 0.02	0.21 ± 0.03	0.48 ± 0.02	2.3 ± 0.1	0.52 ± 0.06	0.801 ± 0.001
7.2×10^{10}	0.11 ± 0.02	0.20 ± 0.03	0.48 ± 0.03	2.3 ± 0.2	0.54 ± 0.07	0.766 ± 0.001
8.0×10^{10}	0.14 ± 0.02	0.19 ± 0.03	0.49 ± 0.03	2.4 ± 0.2	0.58 ± 0.07	0.741 ± 0.001
1.0×10^{11}	0.17 ± 0.02	0.20 ± 0.02	0.51 ± 0.04	2.4 ± 0.2	0.66 ± 0.07	0.676 ± 0.001
1.1×10^{11}	0.17 ± 0.03	0.20 ± 0.02	0.49 ± 0.02	2.3 ± 0.1	0.61 ± 0.06	0.642 ± 0.001
1.2×10^{11}	0.17 ± 0.03	0.21 ± 0.02	0.48 ± 0.02	2.2 ± 0.1	0.60 ± 0.05	0.598 ± 0.001
1.3×10^{11}	0.17 ± 0.03	0.20 ± 0.02	0.48 ± 0.02	2.3 ± 0.1	0.57 ± 0.07	0.567 ± 0.001
1.5×10^{11}	0.17 ± 0.02	0.22 ± 0.02	0.48 ± 0.02	2.2 ± 0.1	0.67 ± 0.05	0.511 ± 0.001
1.7×10^{11}	0.17 ± 0.02	0.21 ± 0.02	0.48 ± 0.02	2.1 ± 0.1	0.59 ± 0.07	0.453 ± 0.001

Table B2: Fitting parameters for $C_7H_7^+$ from 4-NT to equation 5.2

I (W/cm^2)	a	T (ps)	t (ps)	ϕ (rad)	b	c
2.8×10^{10}	0.03 ± 0.01	0.24 ± 0.03	0.46 ± 0.04	5.3 ± 0.2	-0.90 ± 0.09	0.506 ± 0.001
3.7×10^{10}	0.04 ± 0.01	0.20 ± 0.02	0.45 ± 0.02	5.2 ± 0.2	-0.77 ± 0.05	0.526 ± 0.001
4.6×10^{10}	0.06 ± 0.01	0.20 ± 0.02	0.47 ± 0.03	5.3 ± 0.2	-0.87 ± 0.06	0.542 ± 0.001
6.2×10^{10}	0.08 ± 0.01	0.20 ± 0.02	0.47 ± 0.02	5.4 ± 0.2	-0.83 ± 0.07	0.573 ± 0.001
7.2×10^{10}	0.08 ± 0.01	0.22 ± 0.03	0.47 ± 0.02	5.4 ± 0.2	-0.78 ± 0.06	0.598 ± 0.001
8.0×10^{10}	0.10 ± 0.01	0.21 ± 0.02	0.46 ± 0.02	5.3 ± 0.1	-0.73 ± 0.06	0.622 ± 0.001
1.0×10^{11}	0.13 ± 0.02	0.20 ± 0.02	0.47 ± 0.03	5.3 ± 0.2	-0.62 ± 0.07	0.657 ± 0.001
1.1×10^{11}	0.12 ± 0.02	0.21 ± 0.02	0.46 ± 0.02	5.2 ± 0.1	-0.58 ± 0.05	0.677 ± 0.001
1.2×10^{11}	0.15 ± 0.02	0.20 ± 0.02	0.46 ± 0.02	5.2 ± 0.1	-0.58 ± 0.07	0.703 ± 0.001
1.3×10^{11}	0.14 ± 0.02	0.21 ± 0.02	0.46 ± 0.02	5.3 ± 0.1	-0.53 ± 0.05	0.743 ± 0.001
1.5×10^{11}	0.15 ± 0.02	0.19 ± 0.02	0.45 ± 0.02	5.3 ± 0.1	-0.22 ± 0.05	0.760 ± 0.001
1.7×10^{11}	0.13 ± 0.02	0.20 ± 0.02	0.47 ± 0.02	5.0 ± 0.2	-0.28 ± 0.07	0.803 ± 0.001

Table B3: Fitting parameters for parent molecular ion of 3-NT to eq 5.3

I (W/cm^2)	a	T_1 (ps)	t (ps)	ϕ (rad)	b	c	d	T_2 (ps)
2.2×10^{10}	0.007±0.006	0.21±0.04	0.22±0.03	1.2±0.7	-0.3±0.8	0.945±0.001	0.021±0.004	0.9±0.2
3.7×10^{10}	0.010±0.005	0.26±0.09	0.21±0.01	1.7±0.4	-0.2±0.6	0.910±0.001	0.033±0.002	1.1±0.2
4.9×10^{10}	0.013±0.005	0.21±0.08	0.21±0.01	1.2±0.4	-0.8±0.5	0.879±0.001	0.052±0.002	1.3±0.1
6.0×10^{10}	0.017±0.005	0.25±0.07	0.22±0.01	1.7±0.4	-0.1±0.4	0.854±0.001	0.054±0.003	1.2±0.1
7.1×10^{10}	0.019±0.006	0.26±0.04	0.22±0.01	1.4±0.2	-0.4±0.4	0.827±0.001	0.068±0.003	1.3±0.1
8.1×10^{10}	0.023±0.007	0.21±0.06	0.21±0.01	1.4±0.2	-0.4±0.4	0.803±0.001	0.070±0.004	1.1±0.1
9.3×10^{10}	0.025±0.008	0.24±0.07	0.22±0.01	1.3±0.3	-0.4±0.4	0.772±0.001	0.078±0.005	1.1±0.1
1.0×10^{11}	0.027±0.005	0.22±0.04	0.21±0.01	1.7±0.2	-0.4±0.3	0.753±0.001	0.079±0.004	1.1±0.1
1.2×10^{11}	0.029±0.008	0.22±0.06	0.21±0.01	1.4±0.2	-0.2±0.4	0.716±0.001	0.089±0.004	1.2±0.1
1.3×10^{11}	0.029±0.008	0.22±0.05	0.22±0.01	1.2±0.2	-0.4±0.3	0.675±0.001	0.098±0.004	1.2±0.1
1.5×10^{11}	0.030±0.007	0.22±0.05	0.21±0.01	1.5±0.2	-0.4±0.3	0.630±0.001	0.100±0.002	1.2±0.1
1.6×10^{11}	0.031±0.008	0.20±0.04	0.22±0.01	1.5±0.2	-0.8±0.5	0.599±0.001	0.113±0.005	1.1±0.1

Table B4: Fitting parameters for $C_7H_7^+$ from 3-NT to eq 5.3

I (W/cm^2)	a	T_1 (ps)	t (ps)	ϕ (rad)	b	c	d	T_2 (ps)
2.2×10^{10}	0.006 ± 0.005	0.24 ± 0.09	0.23 ± 0.03	4.7 ± 0.7	2 ± 1	0.706 ± 0.001	-0.027 ± 0.008	0.9 ± 0.2
3.7×10^{10}	0.010 ± 0.005	0.23 ± 0.09	0.22 ± 0.02	4.5 ± 0.4	0.9 ± 0.8	0.731 ± 0.001	-0.036 ± 0.005	0.9 ± 0.2
4.9×10^{10}	0.010 ± 0.005	0.23 ± 0.09	0.22 ± 0.02	4.3 ± 0.5	0.6 ± 0.8	0.749 ± 0.001	-0.033 ± 0.004	1.1 ± 0.2
6.0×10^{10}	0.012 ± 0.004	0.21 ± 0.09	0.22 ± 0.02	4.4 ± 0.4	2 ± 1	0.762 ± 0.001	-0.050 ± 0.005	0.9 ± 0.2
7.1×10^{10}	0.014 ± 0.004	0.22 ± 0.06	0.22 ± 0.01	4.2 ± 0.3	2 ± 1	0.756 ± 0.001	-0.055 ± 0.007	0.9 ± 0.2
8.1×10^{10}	0.015 ± 0.006	0.19 ± 0.06	0.22 ± 0.02	4.4 ± 0.4	1.3 ± 0.8	0.799 ± 0.001	-0.060 ± 0.005	1.3 ± 0.1
9.3×10^{10}	0.019 ± 0.005	0.25 ± 0.08	0.22 ± 0.01	4.4 ± 0.3	1.2 ± 0.6	0.818 ± 0.001	-0.067 ± 0.005	1.3 ± 0.1
1.0×10^{11}	0.017 ± 0.004	0.24 ± 0.04	0.22 ± 0.01	4.8 ± 0.3	2.0 ± 0.6	0.833 ± 0.001	-0.077 ± 0.005	1.3 ± 0.1
1.2×10^{11}	0.019 ± 0.004	0.26 ± 0.05	0.22 ± 0.01	4.6 ± 0.2	2.3 ± 0.7	0.850 ± 0.001	-0.079 ± 0.007	1.1 ± 0.1
1.3×10^{11}	0.020 ± 0.005	0.29 ± 0.06	0.22 ± 0.01	4.2 ± 0.3	3 ± 1	0.880 ± 0.001	-0.086 ± 0.008	1.1 ± 0.1
1.5×10^{11}	0.018 ± 0.003	0.31 ± 0.04	0.22 ± 0.01	4.7 ± 0.2	4 ± 1	0.902 ± 0.001	-0.10 ± 0.009	1.2 ± 0.1
1.6×10^{11}	0.016 ± 0.004	0.32 ± 0.06	0.22 ± 0.01	4.8 ± 0.3	6 ± 1	0.929 ± 0.001	-0.11 ± 0.009	1.4 ± 0.2

Additional Theoretical Results

Figure B1 shows 4-NT and 3-NT at their neutral geometries with all atoms labeled according to the subsequent tables. Table B5 and B6 shows the optimized geometries of the neutrals, anions, and cations of 4-NT and 3-NT, respectively. Table B7 and B8 show the Milliken charges on each atom in 4-NT and 3-NT respectively. Tables B9 and B10 shows the harmonic and anharmoic vibrational frequencies for 4-NT and 3-NT respectively.
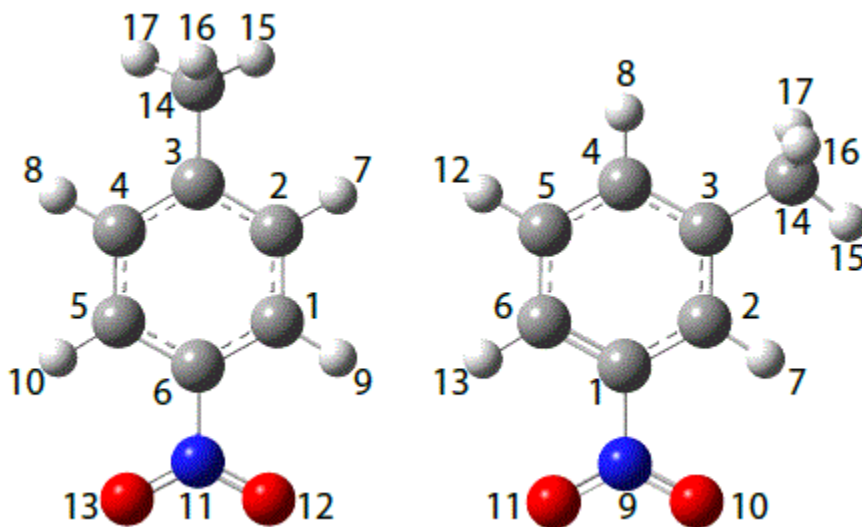
Figure B1. Structures with atomic labels of 4-nitrotoluene (left) and 3-nitrotoluene (right)

Table B5: Geometric coordinates for 4-NT.

atom		neutral x (Å)	y (Å)	z (Å)	anion x (Å)	y (Å)	z (Å)	cation x (Å)	y (Å)	z (Å)
1	C	0.041925	1.211232	-0.001089	0.044620	1.214515	-0.003792	0.035048	1.240375	0.082888
2	C	-1.344135	1.200265	-0.005698	-1.337034	1.197630	-0.010023	-1.330517	1.233027	0.073043
3	C	-2.060051	0.000000	-0.005278	-2.071308	0.000000	-0.011113	-2.054958	0.003384	-0.027507
4	C	-1.344135	-1.200265	-0.005698	-1.337034	-1.197630	-0.010023	-1.330887	-1.228593	-0.110414
5	C	0.041925	-1.211232	-0.001089	0.044620	-1.214515	-0.003792	0.034613	-1.239149	-0.095882
6	C	0.718977	0.000000	0.002393	0.770728	0.000000	0.003452	0.704105	-0.000242	0.000237
7	H	-1.879673	2.140928	-0.012507	-1.871734	2.143292	-0.018013	-1.880752	2.162002	0.133604
8	H	-1.879673	-2.140928	-0.012507	-1.871734	-2.143292	-0.018013	-1.882081	-2.156061	-0.184695
9	H	0.600068	2.134645	-0.003114	0.602153	2.138556	-0.009355	0.605681	2.156392	0.143184
10	H	0.600068	-2.134645	-0.003114	0.602153	-2.138556	-0.009355	0.604178	-2.156282	-0.148742
11	N	2.191627	0.000000	0.004756	2.160326	0.000000	0.009983	2.160787	-0.001621	0.013718
12	O	2.759942	1.081637	0.005917	2.781242	1.120208	0.011403	2.705434	0.720249	-0.796342
13	O	2.759942	-1.081637	0.005917	2.781242	-1.120208	0.011403	2.693735	-0.723373	0.830407
14	C	-3.563730	0.000000	0.020795	-3.576161	0.000000	0.031023	-3.528337	0.001744	-0.016109
15	H	-3.970858	0.883612	-0.469934	-3.991130	0.881628	-0.465071	-3.949331	0.933820	-0.390213
16	H	-3.931363	0.000000	1.050184	-3.969821	0.000000	1.056358	-3.865241	-0.092318	1.030446
17	H	-3.970858	-0.883612	-0.469934	-3.991130	-0.881628	-0.465071	-3.946674	-0.853485	-0.545827

Table B6: Geometric coordinates for 3-NT.

		neutral			anion			cation		
atom		x (Å)	y (Å)	z (Å)	x (Å)	y (Å)	z (Å)	x (Å)	y (Å)	z (Å)
1	C	1.2877414	-0.805175	-0.001116	-0.680714	0.088479	-0.020257	1.311614	-0.777659	0.037013
2	C	1.253483	0.581711	-0.059203	0.418706	-0.804855	-0.037250	1.269975	0.581758	0.003890
3	C	0.028695	1.242320	-0.051252	1.719869	-0.335908	-0.001589	-0.010654	1.248361	-0.056618
4	C	-1.137286	0.473005	0.013237	1.961347	1.049051	0.052459	-1.198480	0.460450	-0.080160
5	C	-1.086540	-0.914055	0.070927	0.876472	1.933925	0.069339	-1.126620	-0.904881	-0.045780
6	C	0.135698	-1.572965	0.064667	-0.427874	1.478946	0.034116	0.138939	-1.551586	0.014002
7	H	2.183058	1.128221	-0.111048	0.203241	-1.862342	-0.078937	2.187731	1.154326	0.022821
8	H	-2.099608	0.970041	0.016864	2.977784	1.424882	0.080794	-2.155787	0.961043	-0.125638
9	N	2.598956	-1.484791	-0.012104	-1.983419	-0.396239	-0.056483	2.629411	-1.473363	0.099447
10	O	3.600205	-0.787994	-0.074314	-2.175959	-1.660933	-0.105363	3.614042	-0.768257	0.117961
11	O	2.606304	-2.704773	0.041904	-2.956296	0.435176	-0.040014	2.589818	-2.687210	0.125789
12	H	-2.002783	-1.486484	0.119318	1.061507	3.002424	0.111014	-2.023255	-1.508758	-0.063311
13	H	0.206731	-2.648329	0.106998	-1.271383	2.151424	0.046636	0.218875	-2.630268	0.042287
14	C	-0.042016	2.745693	-0.098883	2.880125	-1.301520	-0.020492	-0.052696	2.716500	-0.091686
15	H	0.932957	3.182897	-0.307636	2.532469	-2.334208	-0.062859	0.533820	3.088030	-0.944204
16	H	-0.392048	3.150691	0.853180	3.505134	-1.194455	0.871727	0.469349	3.126786	0.784789
17	H	-0.737068	3.083763	-0.868835	3.529558	-1.130630	-0.884895	-1.059928	3.118502	-0.137898

Table B7: Mulliken charges for 4-NT.

atom		neutral	anion	cation
1	C	-0.122255	-0.191114	-0.082199
2	C	-0.118533	-0.152249	-0.055972
3	C	0.032732	0.052421	0.071003
4	C	-0.118533	-0.152249	-0.055698
5	C	-0.122255	-0.191114	-0.083975
6	C	0.005708	0.067078	0.134576
7	H	0.129416	0.063226	0.190649
8	H	0.129416	0.063226	0.190711
9	H	0.165522	0.104450	0.205290
10	H	0.165522	0.104450	0.205138
11	N	0.418444	0.325207	0.417648
12	O	-0.310440	-0.511815	-0.186473
13	O	-0.310440	-0.511815	-0.187549
14	C	-0.231988	-0.255719	-0.180267
15	H	0.091037	0.059735	0.130281
16	H	0.105610	0.066548	0.155913
17	H	0.091037	0.059735	0.130924

Table 8: Mulliken charges for 3-NT**.**

atom		neutral	anion	cation
1	C	0.012392	0.068427	0.000679
2	C	-0.130191	-0.212420	-0.031919
3	C	0.050876	0.101108	0.104378
4	C	-0.149122	-0.244480	-0.083992
5	C	-0.092194	-0.094643	-0.040087
6	C	-0.140103	-0.215556	-0.008491
7	H	0.155848	0.096187	0.216822
8	H	0.130670	0.060153	0.191768
9	N	0.423657	0.332320	0.452895
10	O	-0.309170	-0.509246	-0.248612
11	O	-0.308609	-0.509488	-0.249042
12	H	0.138538	0.071268	0.205631
13	H	0.166522	0.105516	0.232976
14	C	-0.236450	-0.251055	-0.172605
15	H	0.086815	0.065863	0.152639
16	H	0.102987	0.068014	0.152747
17	H	0.097533	0.068032	0.124211

Table B9: IR peaks for 4NT.

	neutral		cation	
mode	ν_{harm} (cm^{-1})	ν_{anharm} (cm^{-1})	ν_{harm} (cm^{-1})	ν_{anharm} (cm^{-1})
1	3227.365	3080.772	3217.902	3087.505
2	3227.371	3101.029	3217.181	3101.233
3	3177.069	3031.729	3203.295	3087.069
4	3176.272	3047.512	3200.459	3090.398
5	3113.123	2976.942	3140.095	2907.525
6	3085.109	2946.405	3062.073	2726.252
7	3030.057	2978.692	2952.889	2775.309
8	1645.549	1608.463	1656.527	1582.679
9	1642.510	1600.123	1508.274	1474.134
10	1579.525	1540.083	1495.639	1450.153
11	1532.498	1498.804	1484.698	1431.046
12	1493.460	1463.857	1478.348	1436.932
13	1491.114	1462.911	1429.503	1398.260
14	1440.515	1418.583	1412.366	1383.814
15	1418.173	1402.693	1394.591	1339.676
16	1374.205	1342.628	1365.528	1313.836
17	1351.034	1329.034	1346.197	1309.748
18	1332.991	1306.721	1283.657	1263.773
19	1233.240	1203.655	1256.258	1230.598
20	1205.406	1191.087	1218.267	1193.795
21	1136.017	1123.474	1161.399	1141.546
22	1123.868	1100.147	1138.770	1103.298
23	1066.046	1045.803	1026.605	1022.712
24	1037.893	1024.019	1021.406	998.721
25	1011.793	993.673	1003.491	982.423
26	1004.781	997.521	994.022	960.910
27	999.500	965.817	982.701	968.772
28	877.537	866.797	853.076	837.532
29	866.024	850.655	822.583	811.222
30	856.887	837.409	809.988	790.256
31	802.152	790.686	774.799	763.328
32	762.398	755.173	741.541	737.722
33	707.116	693.730	689.347	684.840
34	650.150	642.879	604.324	596.667
35	626.052	616.794	565.435	563.489
36	533.985	522.262	515.189	514.027
37	483.897	478.309	371.161	363.522
38	422.871	416.341	367.690	360.217
39	361.599	357.984	336.650	329.870
40	359.627	361.981	303.726	326.669
41	283.917	286.258	215.660	215.614
42	220.830	220.425	164.413	177.195
43	107.564	119.991	80.451	70.643
44	55.301	59.812	58.734	46.172
45	25.283	3.290	18.308	-173.842

Table B10. IR peaks for 3NT.

	neutral		cation	
mode	ν_{harm} (cm^{-1})	ν_{anharm} (cm^{-1})	ν_{harm} (cm^{-1})	ν_{anharm} (cm^{-1})
1	3232.063	3089.568	3216.877	3108.291
2	3217.783	3103.626	3210.238	3086.484
3	3192.180	3079.304	3207.704	3081.731
4	3168.489	3021.929	3202.277	3087.522
5	3115.432	2971.084	3156.448	3012.879
6	3083.206	2882.206	2997.453	2814.940
7	3033.296	2973.586	2974.450	2807.556
8	1660.683	1619.706	1669.742	1592.100
9	1625.124	1580.819	1629.218	1575.715
10	1588.695	1559.371	1535.608	1496.716
11	1520.163	1488.866	1483.679	1450.077
12	1501.861	1498.591	1458.322	1426.141
13	1488.841	1414.991	1415.976	1339.223
14	1459.962	1427.246	1396.835	1359.174
15	1420.997	1412.750	1361.550	1328.593
16	1375.669	1348.541	1355.489	1316.108
17	1350.746	1327.347	1326.402	1293.463
18	1321.699	1287.056	1283.789	1258.981
19	1238.238	1210.800	1255.201	1228.310
20	1192.388	1172.692	1202.632	1179.783
21	1116.225	1084.197	1097.517	1070.629
22	1111.884	1096.197	1051.852	1033.185
23	1071.051	1049.386	1039.091	1024.266
24	1025.587	1029.328	1011.116	985.758
25	1013.514	944.520	1007.355	990.954
26	1010.848	1021.309	985.670	970.739
27	965.319	939.898	950.902	934.887
28	923.082	902.627	931.596	906.036
29	919.435	913.627	899.529	885.068
30	829.805	813.351	803.027	791.826
31	820.370	809.340	786.784	774.446
32	756.280	745.410	735.683	726.769
33	693.271	690.580	612.999	603.164
34	688.650	681.013	580.982	583.596
35	557.052	548.018	543.542	539.878
36	508.939	446.401	487.975	483.043
37	505.584	532.615	427.481	433.231
38	438.424	432.388	377.963	376.885
39	398.360	391.717	374.867	374.709
40	357.072	351.616	341.899	340.603
41	217.864	207.282	200.137	202.379
42	210.718	204.126	153.341	152.074
43	162.293	158.405	143.319	142.505
44	47.473	28.976	58.939	40.272
45	12.206	-1841.069	32.222	25.410

Chapter 6: Probing coherent vibrations of organophosphorus radical cation with femtosecond time-resolved mass spectrometry.

Optimized geometries

Table C1: Geometry coordinates for DMMP and DMMP$^+$.

Element	Neutral			Cation		
	x	y	z	x	y	z
P	-0.014798	0.499741	0.174628	-0.000054	0.507481	0.083585
O	-0.964243	-0.411597	-0.778099	-0.000174	0.320753	1.654961
O	-0.710834	1.225992	1.257092	-0.000293	2.181018	-0.50882
O	1.08155	-0.531014	0.780944	-0.000293	2.1878	-1.600081
C	-2.130662	-1.058085	-0.233213	-0.892614	2.68898	-0.138944
C	0.84338	1.505777	-1.056917	0.891867	2.689262	-0.138945
C	1.815132	-1.468547	-0.016988	1.334372	-0.148877	-0.41047
H	-1.842344	-1.867369	0.441681	-1.334314	-0.149246	-0.410504
H	-2.748836	-0.338469	0.304087	1.909402	-1.481877	-0.179937
H	-2.676687	-1.464684	-1.082457	1.499939	-1.9225	0.726636
H	1.282463	0.894782	-1.846899	1.684189	-2.083067	-1.058767
H	0.129842	2.198884	-1.503579	2.978904	-1.32328	-0.085238
H	1.62781	2.078782	-0.560029	-1.908927	-1.482438	-0.180021
H	1.150056	-2.030548	-0.676427	-1.683859	-2.083377	-1.05906
H	2.579006	-0.959497	-0.611399	-1.499035	-1.923143	0.726317
H	2.30177	-2.149918	0.678811	-2.978439	-1.324143	-0.084918

Table C2: Geometry coordinates for DEMP and DEMP$^+$

Element	Neutral			Cation		
	x	y	z	x	y	z
P	-0.022449	-0.860151	0.194661	-0.03881	0.769557	0.067858
O	1.38272	-0.107128	0.430131	1.335906	0.164358	-0.351514
O	-0.50713	-1.567862	1.399328	-1.311939	0.18232	-0.662125
O	-0.974237	0.348067	-0.331251	-0.347882	0.40432	1.567596
C	3.178925	1.463471	0.224519	1.916702	-1.198381	-0.14098
C	1.935461	0.907476	-0.438178	-1.908783	-1.176146	-0.629734
C	0.218942	-1.918157	-1.257594	0.021392	2.502551	-0.323454
C	-2.377147	0.426661	0.026239	3.396458	-1.044255	0.094692
C	-2.826268	1.865924	-0.116637	-3.073997	-1.207402	0.329998
H	3.919434	0.677758	0.388537	1.69084	-1.742316	-1.05821
H	3.627797	2.233223	-0.410102	1.39898	-1.654265	0.703418
H	2.934863	1.911452	1.189867	-1.126367	-1.893511	-0.381458
H	2.176669	0.456565	-1.407384	-2.219335	-1.321162	-1.66552
H	1.182885	1.682835	-0.597168	0.840815	2.965376	0.229384
H	0.566348	-1.346503	-2.12004	0.188644	2.633856	-1.393795
H	0.948924	-2.69276	-1.017128	-0.923633	2.965797	-0.036913
H	-0.726986	-2.399479	-1.512246	3.88239	-0.547635	-0.746157
H	-2.502883	0.061056	1.046745	3.600728	-0.485295	1.00921
H	-2.940073	-0.229729	-0.645384	3.837448	-2.039137	0.200741
H	-2.27077	2.516841	0.562195	-2.737993	-1.043539	1.357758
H	-2.679661	2.225392	-1.137903	-3.822337	-0.456602	0.07293
H	-3.890119	1.948741	0.12433	-3.547348	-2.191099	0.275947

Table C3: Geometric coordinates for DIMP and DIMP$^+$.

Element	Neutral x	y	z	Cation x	y	z
P	-0.047796	1.047264	-0.205076	0.016549	1.035087	-0.148835
O	1.257769	0.210018	-0.669302	-1.34235	0.295558	-0.429419
O	-0.671371	1.727078	-1.36267	-0.018879	1.309494	1.402404
O	-0.989666	-0.013013	0.583312	1.325369	0.239822	-0.458487
C	3.370265	-0.159369	0.447494	-2.623375	-1.678717	-0.919996
C	2.062828	-2.049648	-0.625069	-2.941775	-0.408444	1.273431
C	1.99479	-0.741698	0.149953	-1.977606	-0.911604	0.218752
C	0.47548	2.116208	1.157475	0.031164	2.475582	-1.194905
C	-3.329225	0.008263	-0.095129	3.136829	-0.349566	1.06126
C	-2.028836	-0.781589	-0.106885	1.988124	-0.921345	0.25849
C	-2.127138	-2.117374	0.611476	2.38972	-1.893895	-0.831313
H	3.295757	0.779913	1.000066	2.784123	0.354305	1.81836
H	3.959916	-0.858387	1.047632	3.652817	-1.164551	1.574831
H	3.910432	0.035589	-0.482291	3.857888	0.153254	0.413879
H	2.616063	-2.803967	-0.058165	-1.890299	-1.982683	-1.668389
H	1.062383	-2.438098	-0.826085	-3.089474	-2.579905	-0.513883
H	2.567336	-1.898694	-1.582623	-3.398857	-1.082866	-1.404205
H	1.443132	-0.901161	1.082451	-3.435128	-1.263012	1.742561
H	0.900315	1.541725	1.982225	-2.417968	0.151926	2.051947
H	1.218239	2.823401	0.785436	-3.71121	0.228166	0.832522
H	-0.388725	2.67177	1.523527	-1.164167	-1.485136	0.667471
H	-3.206148	0.95824	-0.61651	0.043345	2.172663	-2.242995
H	-4.119225	-0.558202	-0.597224	-0.860658	3.071392	-0.996311
H	-3.649826	0.205064	0.931959	0.923218	3.065414	-0.978277
H	-1.70594	-0.936073	-1.141053	1.228223	-1.350586	0.914302
H	-1.175038	-2.651937	0.585093	1.526966	-2.243669	-1.400538
H	-2.409674	-1.972267	1.657614	3.105305	-1.439237	-1.518568
H	-2.884895	-2.747309	0.137482	2.866021	-2.762834	-0.37047

Vibrational frequency

Table C4: Vibrational frequencies for DMMP and DMMP$^+$ with associated mode intensities. Experimental reference[161,164]; computational ion reference.[40]

Mode	Expt. (cm -1)	Neutral (cm-1)	Int. (km/mol)	Ion ref. (cm -1)	Int. (km/mol)	Ion (cm -1)	Int. (km/mol)
		71.08	1.215	19.27	0.00	12.43	0.001
		85.4	0.704	69.54	0.23	68.83	0.037
		97.11	0.023	84.03	2.96	84.12	0.787
		128.24	0.635	99.72	2.46	98.32	0.686
		178.08	0.383	133.60	4.54	133.85	1.280
		189.38	3.479	154.69	0.77	159.95	0.135
		204.26	0.924	166.52	15.15	166.40	4.086
		276.23	0.085	204.71	10.28	204.37	2.796
		287.26	3.677	253.09	3.46	253.22	0.924
CPO3 wag	398	397.87	9.165	271.82	8.01	271.93	2.162
O2P=O bend	468	433.09	4.433	346.10	10.01	346.17	2.699
CPO3 wag	500	482.78	9.752	471.50	26.80	471.49	7.181
O-P-O bend	712	672.73	2.711	659.12	24.98	659.07	6.710
O-P-O bend	786	759.26	40.796	760.83	0.64	760.81	0.168
P-C str	818	793.6	36.127	766.97	4.70	766.84	1.255
P-CH3 rock	894	922.86	7.419	864.02	13.13	863.96	3.517
P-CH3 rock	912	937.99	35.145	934.66	15.19	935.34	4.086
COPOC str	1037	1056.41	100.000	952.94	34.93	954.07	9.448
COPOC str	1064	1076.41	64.606	1044.26	180.21	1043.92	48.492
O-CH3 rock	1152	1181.6	0.262	1065.54	371.47	1065.01	100.000
O-CH3 rock	1152	1184.52	0.439	1165.06	2.74	1164.95	0.680
O-C stretch	1183	1202.9	4.157	1168.16	0.20	1167.98	0.056
O-C stretch	1183	1203.46	5.640	1193.50	31.98	1193.56	8.904
P=O str	1250	1275.09	76.116	1193.89	17.05	1193.72	4.732
PC-H bend	1380	1360.66	12.204	1375.94	32.59	1374.53	8.331
PC-H bend	1418	1472.61	1.575	1454.26	17.40	1455.65	4.511
PC-H bend	1418	1479.49	1.616	1454.42	10.49	1456.31	2.559
H-C-H bend		1485.92	0.389	1476.73	3.58	1476.11	1.226
H-C-H bend		1489.49	0.356	1478.22	4.47	1477.63	1.178
H-C-H bend	1450	1507.92	2.742	1481.76	13.10	1481.81	3.263
H-C-H bend	1463	1515.3	1.698	1491.56	0.64	1491.50	0.176
H-C-H bend	1463	1518.03	4.173	1502.53	7.20	1502.83	1.595
H-C-H bend	1463	1521.15	2.048	1507.95	59.09	1507.91	15.692
OC-H3 str	2848	3031.4	15.030	3059.30	16.93	3059.09	4.576
OC-H3 str	2848	3044.28	14.677	3078.34	0.53	3078.18	0.144
PC-H3 str	2848	3055.89	0.757	3079.80	7.36	3079.65	1.996
OC-H3 str	2951	3100.5	9.906	3149.72	6.74	3149.84	1.777
OC-H3 str	2951	3120.45	7.639	3150.15	5.39	3150.13	1.413
OC-H3 str	2992	3137.23	1.777	3176.98	2.61	3176.84	0.690
OC-H3 str	2992	3140.57	6.394	3177.53	2.66	3177.33	0.664
PC-H3 str	2951	3141.44	0.301	3201.86	1.45	3202.01	0.386
PC-H3 str	2951	3150.11	5.003	3202.33	0.65	3202.51	0.181

Table C5: Vibrational frequencies for DEMP and DEMP$^+$ with associated mode intensities. Experimental reference.[159,164]

Mode	Expt. (cm -1)	Neutral (cm -1)	Int. (km/mol)	Ion (cm -1)	Int. (km/mol)
		16.30	0.333	29.77	0.015
		28.30	0.355	44.66	0.009
		43.62	0.497	60.96	0.311
		69.42	1.088	70.78	0.169
		116.09	0.705	138.92	1.866
		171.88	0.673	147.04	1.375
		192.73	0.479	155.17	0.707
		240.95	0.187	211.98	0.336
		247.68	0.030	241.67	0.498
		263.02	0.713	250.34	0.700
		279.85	0.563	259.06	0.192
		323.72	1.956	263.22	1.245
		332.74	2.139	292.09	2.228
		417.28	4.145	378.42	0.686
CPO3 wag	485	444.55	11.828	440.27	2.766
O-P-O bend	502	480.25	5.021	467.91	5.268
O-P-O bend	715	689.28	1.704	655.65	7.359
P-C str	771	764.67	22.354	709.84	1.504
	806	787.93	28.244	755.85	1.541
		818.99	0.246	813.97	0.657
		821.16	0.077	816.16	1.711
P-CH3 rock	898	917.17	3.836	821.73	0.699
P-CH3 rock	939	927.42	7.797	926.33	4.193
C-C str	965	954.61	50.456	946.71	5.419
	965	968.19	48.592	967.02	6.268
COPOC str	1023	1053.05	100.000	983.21	7.839
COPOC str	1049	1073.88	50.812	1004.12	54.956
O-C str	1099	1123.98	2.263	1034.33	100.000
		1127.89	2.410	1106.47	2.537
CH3 rock	1164	1182.82	0.889	1122.68	2.319
		1185.53	1.120	1165.09	3.104
P=O str	1250	1271.33	68.912	1172.72	1.523
PC-H bend	1314	1318.29	0.060	1305.31	4.221
		1321.01	0.590	1315.02	1.594
		1357.16	9.654	1372.59	7.367
PC-H bend	1390	1409.94	0.377	1386.53	2.133
PC-H bend	1390	1411.10	1.014	1403.12	2.509
H-C-H bend	1420	1433.10	3.940	1420.28	3.704
H-C-H bend	1420	1434.48	5.134	1434.31	4.638
H-C-H bend	1445	1476.03	1.433	1456.81	4.466
H-C-H bend	1480	1481.53	0.966	1459.37	2.494
H-C-H bend	1480	1499.52	1.905	1480.58	1.076
		1500.55	2.311	1488.39	8.464
		1514.16	0.591	1496.04	3.533
		1514.58	1.128	1504.08	0.171
		1535.46	0.792	1510.66	1.705
		1537.12	0.701	1516.83	1.613
CC-H3 str	2863	3025.10	9.404	3037.83	2.609
CC-H3 str	2863	3034.68	10.899	3053.10	0.257
CC-H3 str	2935	3037.73	6.114	3059.91	3.375
CC-H3 str	2935	3040.07	5.129	3078.31	6.861
CC-H3 str	2943	3049.68	1.068	3081.57	1.591
CC-H3 str	2943	3085.45	1.859	3107.71	5.158
C-H2 str	2885	3093.18	0.420	3120.34	1.536
C-H2 str	2885	3103.15	8.794	3126.10	1.180
C-H2 str	2990	3105.26	8.358	3127.48	0.475
C-H2 str	2990	3118.75	9.659	3145.94	2.353
PC-H3 str	2880	3120.76	10.167	3147.30	1.054
PC-H3 str	2990	3129.02	2.329	3151.83	1.923
PC-H3 str	2995	3134.18	1.272	3153.95	0.862

Table C6a. Vibrational frequencies for DIMP and DIMP⁺ with associated mode intensities.

Experimental reference.[160,164]

Mode	Expt. (cm⁻¹)	Neutral (cm⁻¹)	Int. (km/mol)	Ion (cm⁻¹)	Int. (km/mol)
		26.32	0.250	8.90	0.007
		36.26	0.071	24.76	0.001
		53.42	0.032	46.36	0.048
		67.34	0.383	57.49	0.188
		134.11	1.049	105.58	1.360
		140.55	1.241	109.14	0.458
		192.35	0.008	151.44	0.201
		220.60	0.021	161.18	2.273
		221.56	0.058	224.53	0.401
		227.79	0.013	225.03	0.310
		249.05	0.150	226.83	0.462
		256.91	0.707	232.22	0.292
		265.53	0.402	240.44	0.834
		292.69	1.261	268.65	0.132
		346.53	0.252	276.73	0.349
		353.25	0.147	334.40	0.233
		389.72	1.488	356.82	0.671
		415.06	4.963	403.40	0.514
		438.94	2.615	409.51	4.596
	451	462.55	1.742	450.41	0.899
CPO3 wag	504	490.06	7.639	461.96	1.763
O2P=O bend	541	500.48	5.912	465.85	4.488
O-P-O bend	719	690.02	2.159	650.80	13.890
O-P-O bend	748	741.63	8.579	664.81	5.215
P-C str	791	777.52	17.159	749.86	1.229
C-C-C bend	884	880.12	4.982	810.53	1.018
C-C-C bend	884	882.73	8.083	873.89	8.169
P-CH3 rock	899	922.14	7.532	884.06	5.642
P-CH3 rock	917	936.08	32.931	930.01	4.038
C-H bend	938	941.32	3.346	946.16	0.312
C-H bend	938	943.90	1.036	946.91	0.142
		948.99	0.151	949.88	0.273
		952.49	0.185	951.48	0.232
COPOC str	994	973.35	100.000	952.18	0.111
COPOC str	1018	1002.87	68.420	969.67	53.153
O-C3 str	1110	1134.15	7.995	1001.41	100.000
O-C3 str	1115	1135.58	11.181	1097.60	3.849
C-C str	1115	1157.35	2.393	1103.01	3.943
C-C str	1115	1161.69	2.923	1147.50	3.343
C-C str	1177	1204.26	6.260	1156.33	2.151
C-C str	1183	1206.19	2.781	1192.30	2.080
P=O str	1251	1266.82	54.292	1200.19	1.130
C-H bend	1350	1358.40	8.470	1357.22	3.329
PC-H bend	1362	1371.81	0.551	1362.71	14.660
		1372.98	0.883	1364.76	2.867
C-H bend	1385	1398.45	2.779	1372.15	9.333
C-H bend	1390	1399.31	3.394	1376.16	1.442
PC-H bend	1419	1415.64	2.578	1414.62	5.234
PC-H bend	1419	1418.06	4.590	1420.01	6.141
		1431.61	7.521	1430.76	0.534
		1432.66	2.372	1435.13	0.516
H-C-H bend	1453	1474.50	1.259	1459.17	5.255
H-C-H bend	1453	1482.20	1.194	1460.76	2.899
H-C-H bend	1475	1496.22	0.375	1484.44	2.091
H-C-H bend	1475	1496.64	0.377	1489.20	1.329
		1501.61	0.118	1491.95	0.760
		1502.79	0.221	1493.67	0.576
		1510.44	1.795	1499.86	10.238
		1512.09	0.173	1503.72	6.554
		1524.43	2.090	1517.35	0.799
		1528.64	1.753	1519.60	3.957

Table C6b. Continuation of Vibrational frequencies for DIMP and DIMP⁺ with associated mode intensities. Experimental reference.[160,164]

Mode	Expt. (cm -1)	Neutral (cm -1)	Int. (km/mol)	Ion (cm -1)	Int.(km/mol)
		3032.07	4.002	3040.83	1.546
		3033.94	4.644	3045.07	1.023
		3037.94	5.551	3052.13	0.243
		3039.44	3.797	3052.60	0.542
		3040.59	2.390	3061.04	3.156
		3049.28	1.576	3081.46	0.405
		3053.68	0.598	3087.67	3.206
		3093.14	1.582	3111.92	5.528
		3098.34	1.146	3114.58	2.946
		3104.67	12.717	3120.21	2.006
		3104.94	10.055	3120.84	1.015
		3107.86	7.901	3126.26	1.167
		3109.50	8.168	3128.10	2.125
		3114.35	8.609	3134.55	6.457
		3126.96	2.730	3136.97	3.988
		3134.94	1.620	3149.32	0.961
		3139.81	0.892	3153.12	0.714
		3032.07	4.002	3040.83	1.546
		3033.94	4.644	3045.07	1.023
CC-H3 str	2872	3037.94	5.551	3052.13	0.243
CC-H3 str	2872	3039.44	3.797	3052.60	0.542
PC-H3 str	2886	3040.59	2.390	3061.04	3.156
C-H str	2902	3049.28	1.576	3081.46	0.405
C-H str	2913	3053.68	0.598	3087.67	3.206
CC-H3 str	2921	3093.14	1.582	3111.92	5.528
CC-H3 str	2921	3098.34	1.146	3114.58	2.946
CC-H3 str	2921	3104.67	12.717	3120.21	2.006
CC-H3 str	2943	3104.94	10.055	3120.84	1.015
CC-H3 str	2945	3107.86	7.901	3126.26	1.167
CC-H3 str	2945	3109.50	8.168	3128.10	2.125
CC-H3 str	2963	3114.35	8.609	3134.55	6.457
CC-H3 str	2963	3126.96	2.730	3136.97	3.988
PC-H3 str	2986	3134.94	1.620	3149.32	0.961
PC-H3 str	2986	3139.81	0.892	3153.12	0.714

Chapter 7: Conserved vibrational coherence in the ultrafast rearrangement of 2-Nitrotoluene radical cation.

Table D1. Geometry coordinates of 2-NT.

	Neutral			Cation		
C	1.815149	-0.080217	-2.797108	1.85267	-0.088766	-2.829846
C	0.629085	-0.416107	-2.140185	0.622908	-0.395895	-2.145514
C	2.953696	0.317451	-2.112253	2.976015	0.285213	-2.151869
H	3.853706	0.561044	-2.664922	3.893972	0.509557	-2.680122
C	0.654034	-0.310791	-0.745376	0.635429	-0.295168	-0.71273
C	2.939423	0.410229	-0.72635	2.932655	0.389479	-0.743498
H	3.822362	0.722773	-0.182809	3.815915	0.695615	-0.194014
C	1.777371	0.103142	-0.041126	1.738704	0.103734	-0.027139
H	1.717048	0.18096	1.035849	1.700079	0.208607	1.050491
H	1.836401	-0.134148	-3.879952	1.857703	-0.158832	-3.911187
C	-0.565743	-0.837491	-2.952559	-0.556463	-0.778953	-2.936031
H	-0.381612	-0.631967	-4.008184	-0.446546	-0.490815	-3.980423
H	-0.764362	-1.902636	-2.82773	-0.657528	-1.875833	-2.884948
H	-1.471645	-0.312154	-2.647166	-1.490058	-0.39796	-2.516581
N	-0.532054	-0.63747	0.068883	-0.568651	-0.643273	0.078673
O	-1.330051	-1.438218	-0.377638	-1.220738	-1.57532	-0.334963
O	-0.633789	-0.095452	1.151077	-0.767044	0.007558	1.07215

Table D2. Geometric coordinate for *aci*-isomer as INT1r and INT2.

	Int1			Int1r			Int2		
C	1.94176	-0.20306	-2.89292	1.27538	0.166432	-1.762637	0.291309	0.020025	-2.531378
C	0.63815	-0.30408	-2.29384	-0.016142	-0.062464	-1.171902	-1.004884	-0.30347	-2.007069
C	3.06538	0.03234	-2.15268	2.390944	0.427128	-1.019439	1.349634	0.333221	-1.724096
H	4.02787	0.12061	-2.6406	3.343516	0.593411	-1.506031	2.313063	0.571828	-2.156341
C	0.60903	-0.24521	-0.83957	-0.062031	0.001459	0.282213	-1.127359	-0.278593	-0.558259
C	2.97538	0.1762	-0.7517	2.299816	0.479417	0.38575	1.185649	0.345494	-0.325836
H	3.86813	0.37296	-0.17094	3.183282	0.686061	0.977259	2.02484	0.593948	0.312344
C	1.76883	0.04014	-0.1037	1.100012	0.271315	1.02508	-0.028066	0.04609	0.252812
H	1.70473	0.10979	0.97425	1.034999	0.312436	2.103634	-0.137057	0.060092	1.327231
H	2.00421	-0.27829	-3.97197	1.341271	0.125342	-2.843211	0.412362	0.009398	-3.608054
C	-0.45433	-0.29043	-3.12649	-1.054586	-0.31368	-2.033573	-1.998713	-0.603199	-2.907074
H	-1.47829	-0.23735	-2.78144	-2.068974	-0.501237	-1.724035	-3.007492	-0.860017	-2.625784
H	-0.29761	-0.27386	-4.19852	-0.848673	-0.325914	-3.097759	-1.761327	-0.582134	-3.964813
H	-1.24466	-1.81608	-1.21619	-3.013726	-0.549211	1.066666	-3.218696	-0.74603	1.662459
N	-0.53454	-0.46848	-0.08666	-1.199142	-0.187752	1.040608	-2.326378	-0.573622	0.047732
O	-0.67934	-0.11812	1.04632	-1.249568	-0.137019	2.246283	-3.361409	-0.869577	-0.50012
O	-1.59568	-1.11812	-0.64089	-2.342494	-0.450189	0.370202	-2.312067	-0.515878	1.400558

Table D3. Vibrational frequencies for 2-NT neutral in cm⁻¹.

Mode	BPW91	B3LYP	CAM-B3LYP	wB97XD	MP2
1	45	45.4	48.5	55.9	65.7
2	128.7	135.6	139.9	138.4	133.9
3	200.5	211.5	216.5	212.1	195.7
4	223.1	233.1	237.8	234.2	222.8
5	249.2	262.1	267.2	271.4	241.7
6	348.4	362.3	368.2	370.1	346.8
7	378.8	392.2	399	398.8	383.5
8	420.7	437.6	444.6	440.9	416.6
9	476.4	495.3	503.1	497.7	436.9
10	526.4	542.5	552	554	454.6
11	554.3	571.1	579.5	581.4	546.8
12	659.4	681.6	692.6	690.6	594.3
13	682.5	705.9	719.5	717.8	680.7
14	713.2	740.5	754.6	753.7	722
15	771.6	799.7	816.1	816.5	772.2
16	785.5	806.7	820.1	819.2	806.6
17	845.7	877.1	895.5	895.5	823.7
18	848.2	882.2	901.7	897	868.8
19	927.5	967.9	993	985.9	871.9
20	954.2	995.4	1023.2	1016.7	872.6
21	990.2	1023.2	1034.2	1034.4	1027.3
22	1029.4	1068.3	1080.9	1075.4	1058.9
23	1048.9	1075.9	1092.2	1091.5	1076
24	1061.7	1099.2	1121.2	1123.4	1120.1
25	1142.6	1174.7	1191.3	1192.1	1182
26	1162.7	1192.9	1197.2	1202.1	1199.3
27	1194.6	1222.2	1243.4	1244	1247.3
28	1270.1	1309.1	1319.3	1323.6	1315.8
29	1307.9	1343.6	1345.5	1350.5	1410.5
30	1344	1377.4	1442.6	1441.7	1450.4
31	1388.2	1436.2	1448.7	1451.3	1458
32	1426.9	1470.9	1488.8	1484.9	1484.2
33	1454.2	1498.9	1508.9	1509.2	1519.3
34	1469.9	1512.3	1525.4	1528.3	1526.2
35	1473.4	1519.4	1544.8	1543.4	1533.1
36	1530	1596.6	1650.8	1652.5	1633.4
37	1577.5	1625.3	1671.1	1673.1	1663
38	1610.8	1659.9	1708.8	1709.1	1783
39	2989.5	3053.2	3082.4	3072	3089.5
40	3055.6	3115.3	3151.5	3149	3176.6
41	3062.6	3120.6	3153.2	3150.5	3181.7
42	3102.1	3169	3195.8	3192.8	3203.5
43	3116.1	3182.5	3209.3	3207.1	3218.1
44	3129.6	3195.3	3222.1	3220.9	3230.8
45	3157.1	3228.9	3253	3246.9	3246.6

Table D4. Vibrational frequencies for 2-NT cation in cm^{-1}.

	BPW91	B3LYP	CAM-B3LYP	wB97XD	MP2
1	31.9	32.3	48.9	47.9	57.1
2	89.7	94.7	104.7	101.4	105.8
3	103	115.7	159.6	161.7	162.4
4	173.1	180.6	201.3	196.8	195.5
5	182	206	256.5	252	225.2
6	277.2	295.4	355	344.7	321.1
7	301.6	299.7	357.9	348	333.9
8	384.2	396.2	396.4	393	347.2
9	407.3	410.3	414.7	418.4	408.3
10	435.9	461.5	503.2	513.1	445.6
11	501	525.2	520.9	522.1	536
12	629.5	620.4	606.4	604.3	613.7
13	662	680.9	637.2	642.9	688.4
14	699.2	725.9	745.6	746.3	723.2
15	746.2	770.6	778.1	775.4	782.1
16	752	784.3	801.1	801	804.4
17	799.5	829.8	880.3	879	831.3
18	838.8	874.6	910	902.6	880.8
19	939.5	972.7	979.6	970.4	952.6
20	968.6	990.9	996.7	1001.9	1005.4
21	975.9	1010.6	1017.6	1009.8	1026.5
22	988.9	1019.2	1034.7	1030	1035.7
23	1007.3	1023.8	1039.9	1031.8	1058.7
24	1085.1	1113.1	1116.2	1121.8	1116
25	1127.9	1123.2	1129.8	1128.5	1193.8
26	1176.2	1202.7	1197.8	1205	1234.6
27	1192.1	1234.8	1257.5	1260.3	1293
28	1256.5	1270.5	1297.1	1297	1300.4
29	1335.4	1365	1364	1363.4	1371.3
30	1353.6	1385.8	1384.6	1386.6	1412.5
31	1360.4	1401.5	1417.4	1419.4	1426.4
32	1401	1424	1432.3	1439.5	1451.1
33	1410.7	1452.2	1441.6	1444.8	1488.3
34	1418.3	1473.3	1470.9	1468.6	1517.1
35	1442.1	1502.9	1505.7	1513.2	1588.4
36	1467.5	1520.8	1563.7	1561.8	1823.5
37	1489.7	1552	1691.6	1701.7	1862.6
38	1522.4	1585.6	1728.5	1729.3	2489
39	2951	3002.2	3008.9	3002.7	3063.7
40	3006.6	3065.4	3108.3	3106.6	3135.2
41	3093.1	3148.8	3179.9	3175.5	3201.7
42	3136.8	3203.9	3227.6	3224.7	3241.6
43	3144.3	3210.2	3232.2	3229.1	3243.7
44	3149.8	3217	3243.3	3240.2	3253.4
45	3157	3222.1	3247	3245.5	3267

Table D5. Vibrational frequencies (cm^{-1}) and intensities (km mol^{-1}) for *aci*-nitro tautomer in its three geometries with *w*B97XD functional.

Int1		Int1r		Int 2	
Frequency	Intensity	Frequency	Intensity	Frequency	Intensity
86.9	2.5	61.0	0.004	79.8	0.9
108.3	5.8	96.0	0.1	97.4	0.3
211.7	0.5	216.1	6.7	213.8	6.0
241.8	28.1	280.9	0.5	276.9	0.4
292.8	27.5	378.8	14.6	379.5	27.8
375.8	10.2	385.5	15.5	383.0	13.3
390.0	9.2	403.5	3.2	416.5	5.4
416.8	3.3	458.8	15.7	434.3	125.9
466.8	15.7	486.0	119.6	471.0	1.8
543.5	9.5	552.2	2.0	530.6	3.2
561.6	7.9	562.6	4.3	567.0	2.3
615.2	17.3	590.5	2.3	589.4	2.3
642.6	7.6	628.4	27.7	628.8	19.7
657.2	4.4	638.8	9.0	647.1	1.9
725.9	2.3	721.8	0.2	723.5	0.4
763.0	22.1	747.3	1.2	752.6	0.3
794.4	53.3	792.5	51.6	789.0	54.9
873.5	3.0	871.7	0.0	866.9	3.0
901.3	3.2	905.1	2.5	901.8	1.6
984.9	7.9	991.9	2.0	988.2	1.9
1008.5	16.1	1012.0	19.3	1015.3	8.6
1020.8	3.1	1026.8	10.5	1028.4	20.8
1040.2	0.8	1044.0	0.3	1043.3	0.0
1052.9	32.8	1063.7	50.6	1057.4	203.6
1082.5	46.9	1095.4	122.9	1073.5	29.3
1173.3	4.0	1174.6	34.0	1192.1	43.8
1213.3	2.4	1216.7	1.0	1216.4	2.1
1258.4	212.1	1251.9	414.9	1256.0	449.0
1312.7	69.7	1313.2	103.5	1304.3	41.3
1351.5	187.5	1354.6	29.3	1362.6	105.2
1364.0	4.9	1413.2	57.6	1408.3	124.6
1425.4	53.1	1434.6	62.5	1440.6	18.3
1478.7	14.5	1487.6	10.5	1476.7	60.1
1503.5	21.7	1514.9	7.3	1513.1	3.7
1553.7	48.5	1557.9	10.4	1554.0	4.4
1578.5	39.0	1594.7	23.3	1592.4	37.5
1625.0	618.1	1641.1	150.4	1638.2	44.4
1638.5	69.4	1660.8	326.8	1681.8	218.0
3178.8	14.2	3191.9	8.2	3186.5	8.2
3215.4	3.1	3216.3	3.0	3215.3	2.6
3223.6	2.4	3223.9	1.6	3223.5	1.0
3233.7	6.8	3236.0	3.4	3235.5	2.5
3240.9	9.5	3247.6	12.1	3258.5	13.1
3283.5	2.2	3325.0	2.3	3314.7	3.2
3753.3	92.7	3737.7	399.3	3753.4	410.6

Table D6. TDDFT excited states (in eV) and oscillatory strength (f) for neutral 2-NT.

state	BPW91	f	B3LYP	f	CAM-B3LYP	f	wB97XD	f
1	1.3601	0	1.8527	0	2.1389	0	2.131	0
2	3.161	0	3.8659	0.0001	4.174	0.0002	4.169	0.0002
3	3.4354	0	3.9743	0.0318	4.4727	0.0499	4.4696	0.0514
4	3.6081	0.0176	4.3852	0.0766	4.8527	0.17	4.8764	0.1811
5	3.7314	0.03	4.6605	0.2386	5.0669	0.1655	5.0914	0.1515
6	3.8647	0	4.77	0	6.2813	0	6.2311	0
7	4.3461	0.2011	5.2122	0	6.4639	0.0987	6.4511	0.1047
8	4.6019	0.0488	5.7254	0.0089	6.5131	0	6.4903	0
9	5.2245	0	6.0566	0	6.716	0	6.6605	0
10	5.2967	0	6.0642	0.0286	6.7202	0.3125	6.711	0.3141
11	5.4839	0.0008	6.4582	0.2177	7.1179	0.0102	7.1357	0.0108
12	5.6434	0.015	6.5196	0.001	7.2679	0.0015	7.2176	0.0015

Table D7. TDDFT excited states (in eV) and oscillatory strength (f) for neutral 2-NT cation.

state	BPW91	f	B3LYP	f	CAM-B3LYP	f	wB97XD	f
1	0.6161	0.0012	0.692	0.0027	0.9261	0.0006	0.8938	0.001
2	1.2161	0.0009	1.2281	0.0012	1.8505	0.0011	1.8139	0.0016
3	1.7002	0.0003	1.5623	0.0007	1.9943	0.0001	2.049	0.0017
4	1.887	0.0601	1.7842	0.0411	2.084	0.0013	2.094	0.0028
5	2.652	0.0006	2.9459	0.0001	2.7371	0	2.9305	0.0001
6	2.8241	0.0008	3.1661	0.0087	3.2797	0.052	3.3085	0.0498
7	3.0029	0.0185	3.2113	0.0169	3.5003	0.0007	3.4597	0.0005
8	3.2684	0.0018	3.4316	0.0009	3.5221	0.0006	3.5684	0.0018
9	3.4195	0.0026	3.5517	0.0059	3.7558	0.0007	3.7333	0.001
10	3.4423	0.0004	3.7999	0.0008	3.9566	0.0001	3.9886	0.0002
11	3.4975	0.0004	4.0542	0.0087	4.142	0.0029	4.1641	0.0041
12	3.5537	0.0088	4.1136	0.0002	4.4041	0.009	4.5128	0.0093
13	3.7135	0	4.3661	0.0038	4.5164	0.0005	4.5196	0.0022
14	4.0871	0.0029	4.4287	0.0169	4.568	0.0002	4.5717	0.0004
15	4.1621	0.024	4.4712	0.0504	4.8517	0.0209	4.8377	0.0215
16	4.285	0.0089	4.8334	0.0011	5.0166	0.0356	5.0257	0.0317
17	4.3426	0.0007	4.9074	0.0146	5.0835	0.0784	5.1069	0.0892
18	4.3673	0.0004	4.9339	0.0187	5.5396	0.0158	5.5579	0.0101
19	4.5103	0.0017	5.1708	0.027	5.7053	0.0316	5.6874	0.0257
20	4.6054	0.0006	5.492	0.003	5.8703	0.0015	5.9294	0.0003
21	4.7602	0.0395	5.5013	0.0112	5.9952	0.0038	6.0869	0
22	4.8995	0.0002	5.6109	0.003	6.0379	0.0079	6.0924	0.005
23	4.9876	0.0057	5.659	0.0003	6.1131	0	6.1104	0.0079

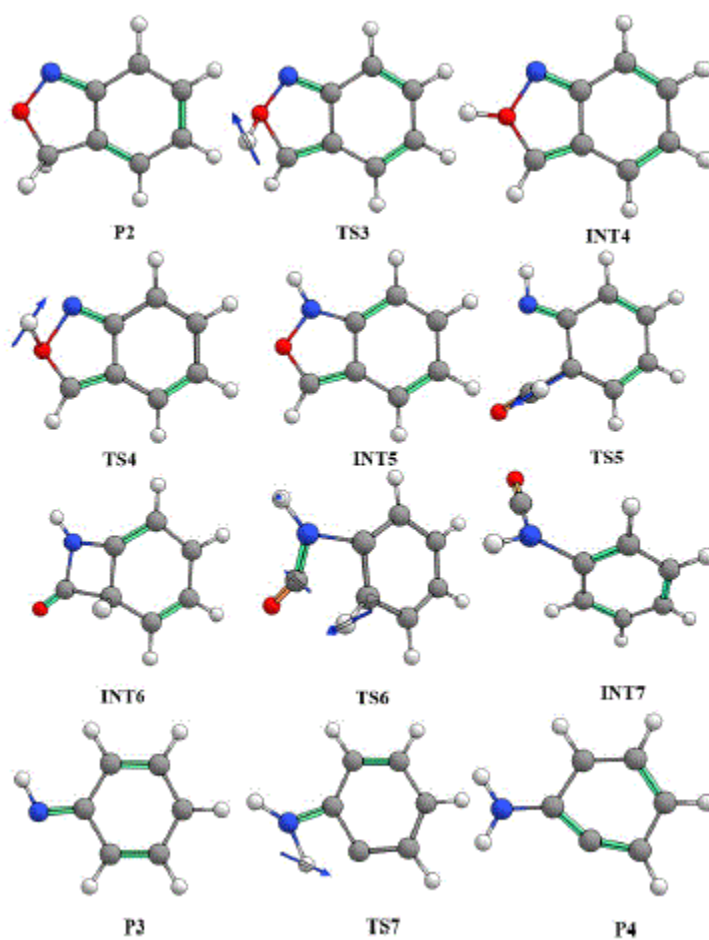# Computed intermediate structures and pathways
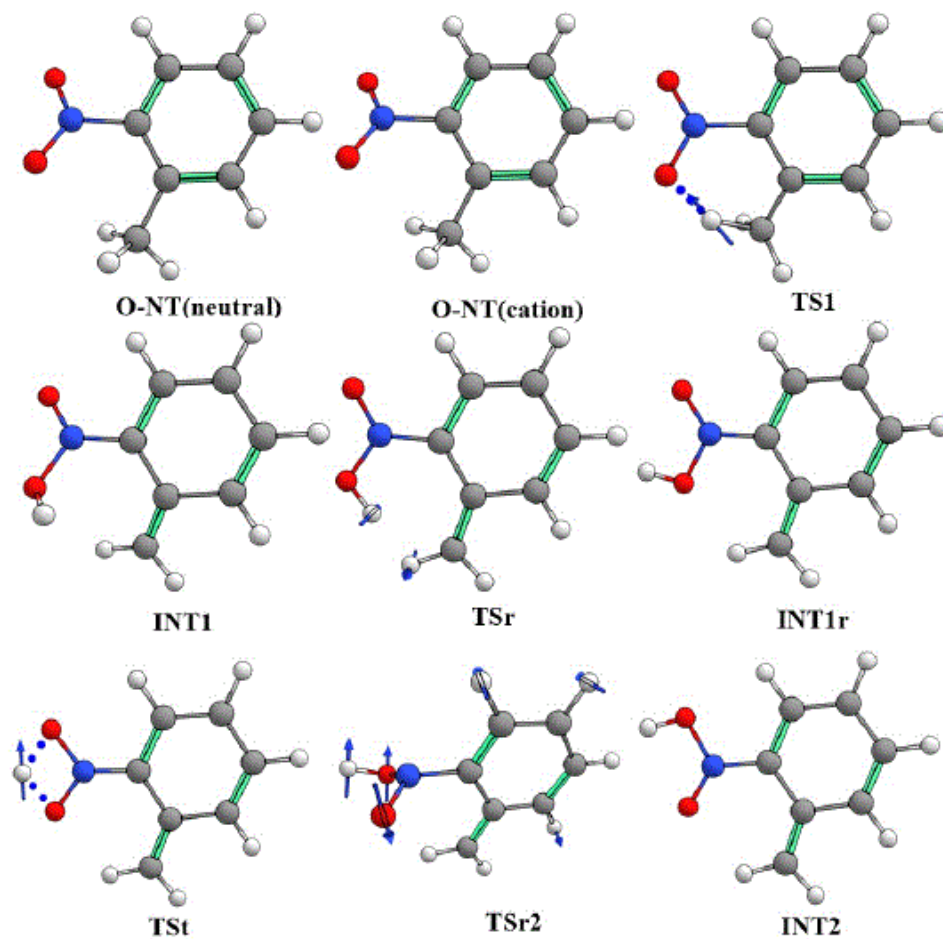
Figure D1. Structure for H-atom attack pathway shown in Figure 7.11 of the main work.
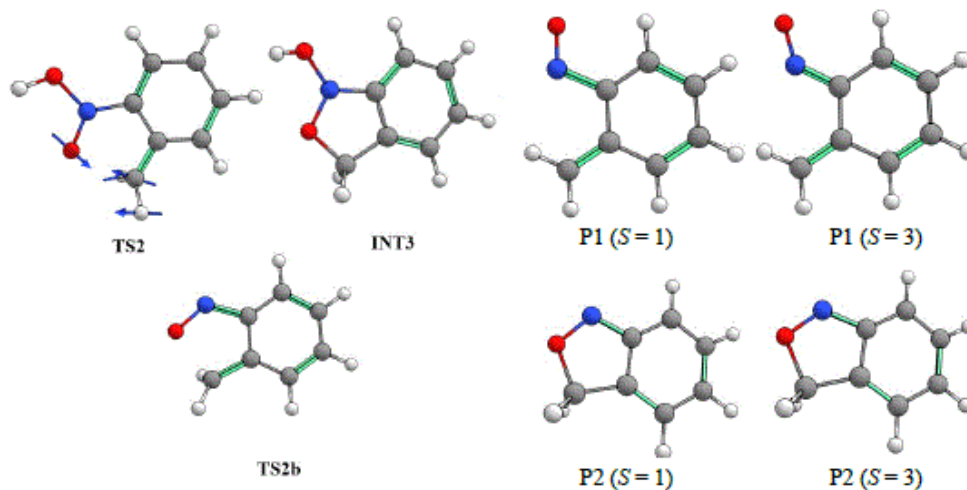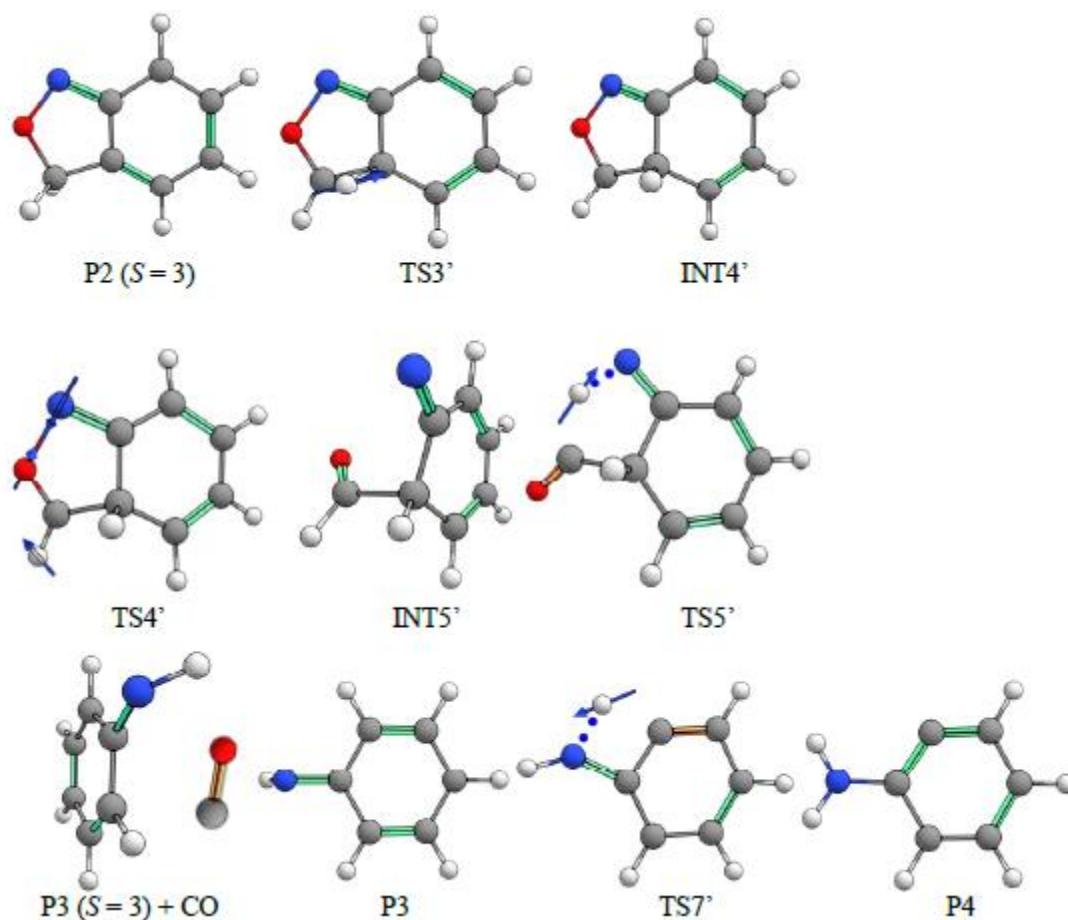
Figure D2. Structures for OH loss pathway shown in Figure 7.14 of the main work.
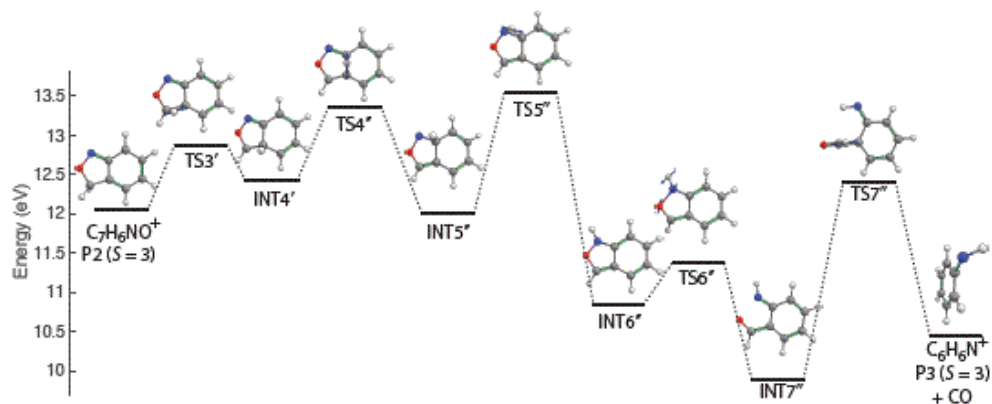

Figure D3. Structures of singlet CO loss pathway shown in Figure 7.15 (a) of the main work.
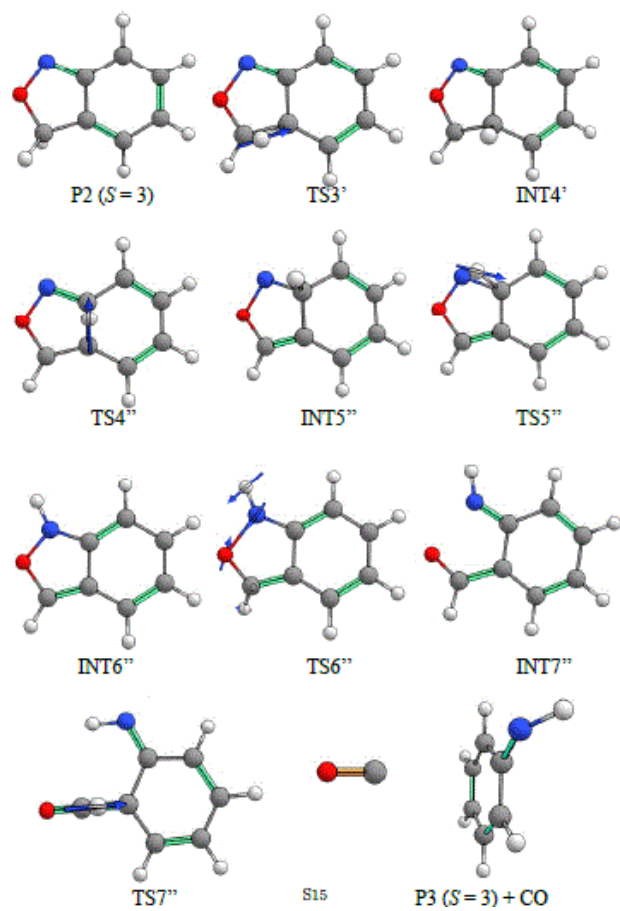
Figure D4. Structures for triplet CO loss pathway shown in Figure 7.15 (b) of the main work.

Figure D5. Mechanism for CO loss from triplet P2 following a pathway similar to the singlet pathway in Figure 7.15 (a) of the main work.

Figure D6. Structure of triplet CO loss pathway shown in Figure 7.15.

Vita

Derrick Ampadu-Boateng was born on January 19, 1983 in Accra, Ghana. He graduated from Wesley Grammar High School in Dansoman, Accra in the year 2000 and received his B.S. in Chemistry from Kwame Nkrumah University of Science and Technology (KNUST), Kumasi in 2006. He received his M.S. in Chemistry from East Tennessee University (ETSU) in Johnson City TN under Dr. Marina Roginskaya in 2014. His master's research was entitled 'Kinetics of Formation and Oxidation of 8-oxo-7,8-dihydroguanine (8oxoG)'. In 2015, he joined Dr. Moore Tibbetts's research group at Virginia Commonwealth University to begin dissertation work for his PhD on 'Probing vibrational wave packet in organophosphorus and nitroaromatic molecules using femtosecond time resolved mass spectroscopy (FTRMS)'.

He has 9 (nine) publications (five first author, one second author and three supporting author). He has presented his research at three scientific meetings.

PUBLICATIONS

Gutsev, Gennady; López Peña, Hugo; McPherson, Shane; **Ampadu Boateng, Derrick**; Ramachandran, Bala; Gutsev, Lavrenty; Tibbetts, Katharine. From Neutral Aniline to Aniline Trication: A Computational and Experimental Study. *J. Phy. Chem. A 2020 published.*

Derrick Ampadu Boateng, Mi' Kayla D. Word, Gennady Lavrenty Gutsev, Puru Jena, and Katharine Moore Tibbetts. *J. Phy. Chem. A.* **2019**, *123,* 1140-1152.

Derrick Ampadu Boateng, Mi' Kayla D. Word, and Katharine Moore Tibbetts. *Molecules*, **2019**, *24*, 509.

Derrick Ampadu Boateng, Tibbetts, K.M. *J.Vis. Exp.* (138), e58263, (**2018**).

Derrick Ampadu Boateng, Gennady Lavrenty Gutsev, Puru Jena, and Katharine Moore Tibbetts, *J. Chem. Phys.* 148, 134305 (**2018**).

Derrick Ampadu Boateng, Gennady Lavrenty Gutsev, Puru Jena, and Katharine Moore Tibbetts, *Phys. Chem. Chem. Phys.,* **2018**, *20*, 4636.

Gennady Lavrenty Gutsev, **Derrick Ampadu Boateng**, Puru Jena, and Katharine Moore Tibbetts, *J. Phys. Chem.* A **2017**, *121*,8414-8424

Marina Roginskaya, Reza Mohseni, **Derrick Ampadu-Boateng** & Yuriy Razskazovskiy (2016): DNA damage by the sulfate radical anion: hydrogen abstraction from the sugar moiety versus one-electron oxidation of guanine, Free Radical Research, DOI: 10.3109/10715762.2016.1166488.

M. Roginskaya, T. J. Moore, **D. Ampadu-Boateng** & Y. Razskazovskiy (2015): Efficacy and site specificity of hydrogen abstraction from DNA 2-deoxyribose by carbonate radicals, Free Radical Research.

PRESENTATIONS

Derrick Ampadu Boateng, Katharine Moore Tibbetts. Probing vibrational wave packet in organophosphorus compounds using femtosecond time resolved mass spectroscopy (FTRMS). *NOBCChE Conference*. St. Louis, MO. November, 21st, 2019

Derrick Ampadu Boateng, Katharine Moore Tibbetts. Probing vibrational wave packet in organophosphorus compounds using femtosecond time resolved mass spectroscopy (FTRMS). *ISMS Conference*. Urbana Champaign, IL. June 18th, 2019

Derrick Ampadu Boateng, Gennady Gutsev, Puru Jena, Katharine Tibbetts. Exploring the dissociation dynamics of radical cations with femtosecond pump-probe spectroscopy: Application to model systems for organophosphorus nerve agents and nitro-based. *American Chemical Society Regional Meeting*. Raleigh NC. November, 2017.